Institute of Mechanics

Doctoral Thesis

Crossings
Deformation, Damage and Optimization

Dipl.-Ing. Dipl.-Ing. Julian Wiedorn, BSc

November 2019

Crossings

Deformation, Damage and Optimization

DISSERTATION

JULIAN WIEDORN

NOVEMBER 2019

zur Erlangung des akademischen Grades

DOKTOR DER MONTANISTISCHEN WISSENSCHAFTEN

an der Montanuniversität Leoben

eingereicht am

Institut für Mechanik

an der Montanuniversitaet Leoben

Contents

List of Figures

Dedicated to my grandparents.

Für meine Großeltern.

Acknowledgements
Danksagung

Niemand kann es von einer simplen Begeisterung zur fertigen Dissertation schaffen ohne dabei viel fachliche und emotionale Unterstützung zu bekommen. Ich hatte das Glück auf eine Gruppe von Menschen zählen zu können, die genau diese Weisheit und Expertise haben und die genau zur richtigen Zeit an Ort und Stelle waren.

- Allen voran möchte ich Univ.-Prof. Thomas Antretter, dem Leiter des Instituts für Mechanik und Hauptbetreuer meiner Arbeit, für die offizielle Betreuung, den regelmäßigen Austausch zu fachlichen Themen während der Dissertation und für die Begutachtung der Arbeit, danken.

  Danke Thomas, vor allem auch für deine Funktion als Wegbereiter. Durch dich bin ich überhaupt zu diesem Thema gekommen!

- Ein weiteres Dankeschön gilt Dr. Werner Daves , Leiter der Projektgruppe Rad/Schiene, der mir durch seine jahrelange Erfahrung im Bereich Rad/Schiene und vor allem Simulation in vielen Bereichen weiterhalf. Seine kollegiale Art bei der täglichen Zusammenarbeit macht die Zeit der Dissertation unvergesslich und setzt die Messlatte für zukünftige Herausforderungen sehr hoch.

  Werner, bei deiner privaten Einführung gleich zu Beginn ist es eigentlich schon um mich geschehen! Danke dafür und für die vielen, auch privaten, Gespräche!

- Thematisch schließt die Arbeit an den Forschungsergebnissen der Dissertation von Dr. Martin Pletz an. Dessen Expertise am Gebiet der Weiche war richtungsweisend und für den erfolgreichen Abschluss der Dissertation wichtig. Seine Fähigkeit schwierigste Themen gelassen und präzise zu vermitteln erleichterte den Einstieg in das Thema und das Schreiben der Publikationen sehr.

  Martin, als Vollblutforscher ist es für dich vielleicht normal immer erreichbar zu sein. Danke dafür! Außerdem weiß ich seitdem auch, dass es sowas wie eine vegane Pizza gibt.

- Das Projekt selbst fand im Rahmen einer Kooperation mit der voestalpine Weichensysteme GmbH statt. Hier möchte ich stellvertretend DI Heinz Ossberger, DI Erik Stocker und DI Uwe Ossberger für die überaus hilfreichen und schnellen Rückmeldungen und die interessanten Diskussionen bei unseren zahlreichen Projektmeetings nennen.

  Ohne euch hätten wir uns sicher das eine oder andere Mal verlaufen. Solche Partner kann man sich nur wünschen!

Außerdem danke ich dem Materials Center Leoben GmbH für die Bereitstellung der Infrastruktur und der fachübergreifenden Expertise. Aber auch meinen Kollegen aus der Simulation für die zahlreichen, nicht nur wissenschaftlichen, Diskussionen (und Kaffeepausen).

Hier alle Namen zu nennen würde den Rahmen dieser Dissertation eindeutig sprengen. Ihr seid immer willkommen und ich freue mich auf einen gemeinsamen Kaffee!

Auch in meinem Freundeskreis fand ich immer wieder Gesprächspartner und Unterstützung. Ihre Ratschläge und Hilfe bei Problemen im Umfeld der Wissenschaft waren für die Fertigstellung der Dissertation in dieser Art und Weise unverzichtbar.

Zum Schluss möchte ich noch meiner Familie danken, meinen Eltern, meinen Geschwistern und meinem Großvater. Für eine allumfassende Unterstützung vor und während meiner Dissertation. Aber auch meiner Großmutter, die maßgeblich dafür verantwortlich ist, wie ich heute bin.

Danke für eigentlich Alles.

Abstract

In this thesis an explicit finite element model for the impact of a wheel on a nose of a railway crossing is introduced. The crucial parameters that describe the dynamic response (contact forces and pressures) of the impact of the wheel on the crossing nose are used to develop a simplified model. This includes (a) geometrical parameters described by the geometry of the crossing and wheel, such as impact angles (movement of the wheel due to the wing rail and crossing nose) and rail radii but also (b) dynamical parameters, such as the velocity of the wheel.

First the influence of those parameters is evaluated performing a parametric study. The simplified model and its results provide a fast way to calculate the dynamic forces and stresses for geometry evaluation and optimization. Including plastic material behavior the deformation of three crossing nose materials (manganese steel, chromium-bainitic steel and tool steel) is predicted. By applying a damage parameter the deformed crossings are then compared and the influence of different axle loads, velocities and wheel types is evaluated. Furthermore, the positive effect of changing the geometry of higher strength steel crossings is discussed. To investigate the severe deformation of manganese steel crossings, explosion-depth hardened manganese crossings are modelled using measured geometries and hardness measurements of crossings in track. Additionally, the observed ability of manganese steel crossings to withstand unfavorable load situations is calculated.

Zusammenfassung

In dieser Arbeit wird ein explizites Finite-Elemente-Modell für den Aufprall eines Rades auf ein Herzstück einer Eisenbahnweiche vorgestellt. Jene Parameter, die das dynamische Verhalten (Kontaktkräfte und -drücke) des Aufpralls des Rades auf die Herzspitze beschreiben, werden bestimmt und für ein vereinfachtes Simulationsmodell adaptiert. Dies umfasst (a) geometrische Parameter, die durch die Geometrie der Weiche und des Rades beschrieben werden, wie Aufprallwinkel (Bewegung des Rades auf der Flügelschiene und des Herzstückes) und Kopfradien des Herzstückes, aber auch (b) dynamische Parameter, wie beispielsweise die Geschwindigkeit des Zuges.

Zunächst wird der Einfluss dieser Parameter in einer parametrischen Studie dargestellt. Das vereinfachte Modell und seine Ergebnisse können dabei als Grundlage dienen, die dynamischen Kräfte und Spannungen zur Bewertung und Optimierung der Geometrie zu berechnen. Unter Berücksichtigung plastischen Materialverhaltens wird die Verformung von drei Herzstückmaterialien (Manganstahl, Chrom-Bainitstahl und Werkzeugstahl) berechnet. Durch Anwenden eines Schadensparameters werden dann die verformten Herzstücke verglichen und der Einfluss verschiedener Achslasten, Geschwindigkeiten und Radtypen bewertet. Darüber hinaus wird der positive Effekt der Änderung der Geometrie höherfester Weichenherzen diskutiert.

Um die starke Verformung von Manganweichen zu untersuchen, werden explosionsgehärtete Manganweichen anhand gemessener Geometrien und Härtemessungen im Detail modelliert und dargestellt. Zusätzlich wird die Fähigkeit von Manganweichen, auf ungünstige Belastungssituationen zu reagieren, untersucht.

Publications

This thesis consists of an extended introduction, a section for the underlying theories and the scientific findings in the appended publications. A full list of all publications that have been written during the thesis is given below.

Wiedorn, J. et al. "Finite element model for predicting the initiation of subsurface damage in railway crossings - A parametric study". In: *Proceedings of the Institution of Mechanical Engineers, Part F: Journal of Rail and Rapid Transit* 233.6 (2019), pp. 614–628. DOI: 10.1177/0954409718797039.

Wiedorn, J. et al. "Investigation of deformation mechanisms in manganese steel crossings using FE models". In: *Tribology International* 138 (2019), pp. 424–434. ISSN: 0301-679X. DOI: https://doi.org/10.1016/j.triboint.2019.06.016. URL: http://www.sciencedirect.com/science/article/pii/S0301679X19303305.

Wiedorn, J. et al. "Numerical assessment of materials used in railway crossings by predicting damage initiation - Validation and application". In: *Wear* 414-415 (2018), pp. 136–150. ISSN: 0043-1648. DOI: https://doi.org/10.1016/j.wear.2018.08.011.

Wiedorn, J. et al. "Simplified explicit finite element model for the impact of a wheel on a crossing - Validation and parameter study". In: *Tribology International* 111 (2017), pp. 254–264. ISSN: 0301-679X. DOI: https://doi.org/10.1016/j.triboint.2017.03.023.

Wiedorn, J. et al. "Using Stress-based Damage Models to Describe Subsurface Damage in Crossings". In: *Proceedings of 11th International Heavy Haul Association Conference*. International Heavy Haul Association, Cape Town, South Africa, 2017.

Wiedorn, J. et al. "A Simplified Dynamic Finite Element Model for the Impact of a Wheel on a Crossing: Validation and Parameter Study". In: *Proceedings of the Third International Conference on Railway Technology: Research, Development and Maintenance*. Ed. by J. Pombo. Civil-Comp Press, Stirlingshire, UK, 2016. DOI: 10.4203/ccp.110.116.

Some ideas and figures of the introduction and theory sections have already appeared in these publications.

Affidavit

I declare in lieu of oath, that I wrote this thesis and performed the associated research myself, using only literature cited in this volume.

Graz, November 2019

Julian Wiedorn

Figure I: A railway crossing

Introduction

General Railway crossings are components of railway switches (often referred to as turnouts or points), a set of mechanical installations in track that guide a train through junctions. Fig. 1 gives an overview of the components of a typical railway switch including the crossing and its parts. Those parts include the wing rails and the crossing nose (or frog).

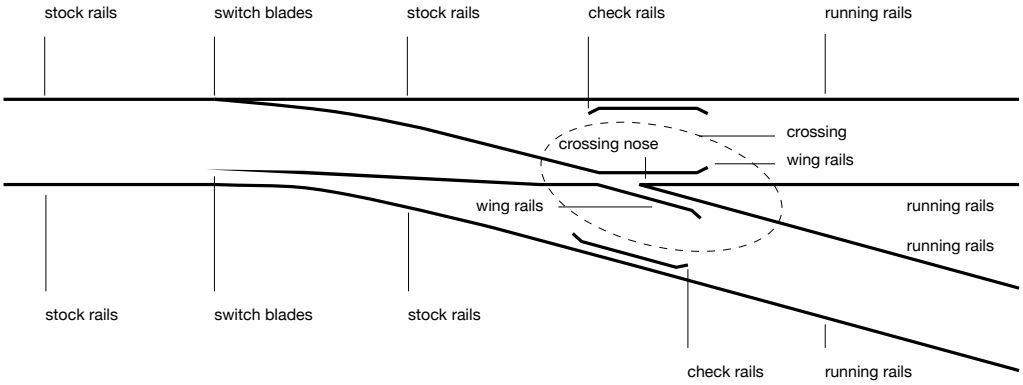

Figure 1: The components of a railway switch (turnout).

Some numbers The importance of the function of turnouts is also reflected in the number of installations: More than 70000 turnouts are installed in Germany, more than 25000 in UK and France and over 10000 in Belgium, Austria and Switzerland.

Although this often means less than one turnout per km, see Table 1[1], their economic impact is significant. Railway switches are known cost-drivers in track networks. In terms of numbers this means 12% of track maintenance and 25% of track renewal are spent for switches in Sweden. A similar number is evaluated in UK by Network Rail: they spend about 17% and 25% for track maintenance and track renewal, respectively[2]. According to the European Innotrack project[3] an average of over 30 % of the total maintenance cost of railways is spent for switches. But those installations do not only increase maintenance effort and installation costs, they also limit the possible railway transportation in terms of reliability and availability. That is also why a lot of investigation is done concerning measurements to

[1] The data for Switzerland is taken from SBB (sbb.ch, multi-tracks are extrapolated manually), for Germany from DB, for Austria from ÖBB and for Belgium, France, Italy, Netherlands, Sweden, UK from the DESTination RAIL project.

[2] E. Kassa et al. *DESTination RAIL: Deliverable 1.3. Presentation on Monitoring Switches and Crossings (turnouts) and tracks*. DESTination RAIL, 2009. URL: www.http://www.destinationrail.eu/

[3] A. Ekberg and B. Paulsson. *Innotrack: Deliverable 1.4.8 Overall Cost Reduction*. Innotrack, 2009. URL: www.innotrack.eu

Country	Track in km	Population S&C
Belgium	6,500	12,200
France	65,100	25,600
Italy	27,100	42,700
Netherlands	6,500	7,800
Sweden	14,900	12,000
UK	31,100	25,800
Germany	60,000	77,000
Switzerland	5,100	14,000
Austria	10,000	13,500

Table 1: Population of turnouts for selected countries in Europe.

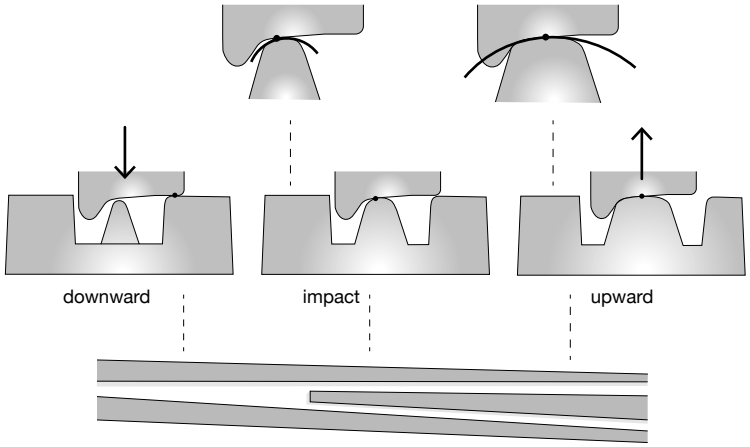

Figure 2: The downward and upward movement and the change of the contact position of the wheel during the transition from the wing rail to the crossing nose.

evaluate the current state of switches and, more importantly, predict possible failures (before they occur).

Types of crossings With regard to the crossing nose, basically two different types of crossings are distinguished: fixed crossings and swingnose crossings. The former ones force the wheel to move over a gap accompanied by a downwards and upwards movement of the wheel. Swingnose crossings have an additional device that allows to move the crossing nose and to close this gap. In this work we investigate fixed crossings as they are the more common type of crossings used in track. Furthermore, their geometrical restrictions entail a more severe loading situation for the crossing nose. Fig. 2 shows the transition of the wheel from the wing rail to the crossing nose in more detail - pointing out the already mentioned more severe and unfavorable load situation.

Loadings on a crossing The design of a fixed crossing forces the wheel to move downwards and upwards (center of Fig. 2), which leads to high contact forces (and also pressures). Due to the high velocities, this behavior describes an impact of the wheel onto the crossing nose. Furthermore, the contact radii of the wheel and the rail change during the transition (top of Fig. 2), which has two effects: (a) the change of the contact position causes slip (and therefore tangential contact stresses) and (b) the smaller contact radii on the crossing nose increase the normal contact pressures. Fig. 3a shows a typical dynamical response of normal contact forces and pressures between the wheel and crossing due to the transition of the wheel. Fig. 3b sketches the radius of the wheel (inspired by a standard ORE 1002) at the contact point of the wheel and the rail and the head radii of the crossing nose. The radius of the second wheel of the axle, however, is assumed to be constant as the wheel is moving steadily on the stock rail.

Slip then occurs due to the sudden change of the wheel radii in

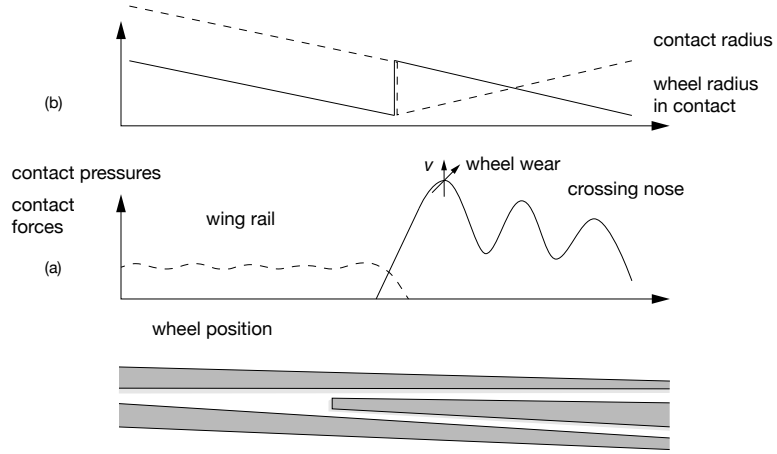

Figure 3: (a) Arising contact forces, pressures and (b) the wheel radius at the contact position due to the transition of the wheel from the wing rail to the crossing nose.

contact with the wing rail / crossing nose and due to wheel radius of the second wheel. Axle loads and speeds, but also the crossing geometry and wheel profiles, i.e. hollow wheels, influence this process (by increasing contact forces and pressures, see Fig. 3a) and can be the reason for severe wear and damage.

Simulation methods Common tools to predict this dynamic process are the multibody simulation (MBS) and the Finite Element (FE) method. The former enables the user to calculate displacements of complex structures very fast by dividing them into a system of rigid and flexible bodies (considering masses and inertias) connected with springs and dashpots. Such crossing models can represent a whole train and several hundred meters of track. The FE method, however, allows to calculate stress and strain fields in the bodies combined with complex material laws to account for e.g. plastic deformations. To investigate mechanisms of damage locally, those results are needed[4]. Early work investigating the dynamic response of turnouts is done by Kassa et al.[5]. By applying additional tools, they calculate contact pressures and stresses[6] and predict wear and damage[7]. They do this by combining MBS and FE models and transferring data from one to the other.

Yan et al.[8] and Wiest et al.[9] use the explicit FE method to calculate the loading on a crossing. With this method they calculate the entire dynamic process and evaluate stresses, strains and plastic deformation at material points within the modelled body. The modelled body is subdivided into smaller parts – finite elements – that represent the volume at those material points. A high resolution, however, increases the calculation time significantly as it depends on the size and number of involved elements. Therefore, the authors use a rail with a kink as simulation model to simplify the crossing and the impact of the wheel. Continuing this work, Pletz et al.[10] calculate the dynamic response using a FE model with realistic crossing geometry, which is validated with track measurements by Ossberger et al.[11]. Pletz et al.

[4] J. Wiedorn et al. "Numerical assessment of materials used in railway crossings by predicting damage initiation - Validation and application". In: *Wear* 414-415 (2018), pp. 136–150. ISSN: 0043-1648. DOI: https://doi.org/10.1016/j.wear.2018.08.011

[5] E. Kassa et al. "Simulation of dynamic interaction between train and railway turnout". In: *Vehicle System Dynamics* 44.3 (2006), pp. 247–258. ISSN: 0042-3114. DOI: 10.1080/00423110500233487

[6] C. Andersson and T. Abrahamsson. "Simulation of Interaction Between a Train in General Motion and a Track". In: *Vehicle System Dynamics* 38.6 (2002), pp. 433–455. ISSN: 0042-3114. DOI: 10.1076/vesd.38.6.433.8345

[7] A. Johansson et al. "Simulation of wheel-rail contact and damage in switches & crossings". In: *Wear* 271.1-2 (2011), pp. 472–481. ISSN: 0043-1648. DOI: 10.1016/j.wear.2010.10.014

[8] W. Yan et al. "Numerical Analysis of the Cyclic Response of a Crossing Component in a Switch". In: *Proceedings of the XIXth Verformungskundliches Kolloquium*. Montanuniversität Leoben, Austria, 2000, pp. 78–83

[9] M. Wiest et al. "Deformation and damage of a crossing nose due to wheel passages". In: *Wear* 265.9-10 (2008), pp. 1431–1438. ISSN: 0043-1648. DOI: 10.1016/j.wear.2008.01.033

[10] M. Pletz et al. "A wheel set/crossing model regarding impact, sliding and deformation - Explicit finite element approach". In: *Wear* 294-295 (2012), pp. 446–456. ISSN: 0043-1648. DOI: 10.1016/j.wear.2012.07.033

[11] U. Ossberger et al. "Validation of a finite element crossing model using measurements at an instrumented turnout". In: *Proceedings of the 23rd Symposium on Dynamics of Vehicles on Roads and Tracks*. Qingdao, China, 2013

are able to simulate the load transfer from the wing rail to the crossing nose and calculate cyclic plastic deformation using simplifications[12]. Furthermore, the findings identify parameters that are needed to calculate a realistic impact of a wheel on a crossing nose. More recent work is done by L. Xin[13] and L. Ma[14] continuing investigating damage on crossing noses using a realistic model geometry.

Introducing a reduced model Due to the limited resolution of models with realistic geometry, in this thesis the approach focuses on developing a simplified model similar to a submodel. Based on previous work, the authors introduce a simplified model and replace the wing rail by a non-linear spring: only the crossing nose is shown as a component. Furthermore, they identify crucial parameters and use them as input for the model creation. This parameters include the geometry of the crossing and wheel, such as impact angles (defined by the movement of the wheel due to wing rail and crossing nose) and their rail head radii. To identify their influences – including dynamical parameters, such as the velocity of the train (wheel) – parametric studies are performed[15]. Furthermore, it is shown that the simplified model yields similar results as the model with realistic geometry (realistic model). Due to the short computational times, the simplified model and its results provide a fast way to calculate the dynamic forces and stresses for geometry evaluation and optimization.

Deformation of crossing nose materials Crossings have their maximum deformation at the position where the wheel transfers the load from the wing rail to the crossing nose. Depending on the type of wheel (and wear) and the geometry of the wing rails, a broad dent is formed, see Fig. 4. There, the depth of the dent depends on the load cycles and, especially, the crossing nose material.

Typical materials used for a crossing and their selection do not follow a specific guideline. There exist crossing noses with manganese steel, which has a very low yield stress but also steels with higher yield stresses, such as the R350HT rail steel or tool steels. Although their mechanical properties seem to be very different, all of them show a good performance in track. Pletz et al. use a realistic model and investigate different crossing nose materials. There, a significant influence of the deformed geometry on the performance, especially for steels with low yield stress, is recognized[16]. To investigate this phenomena in more detail, we adapt the simplified model and use inelastic material behavior. Then, the deformation of three different crossing nose materials is investigated: manganese steel, chromium-bainitic steel and tool steel. These materials are commonly used in crossing noses although their material behavior is rather different: Manganese steel has, as mentioned above, a low yield stress but a distinct work hardening behavior; tool steel and chromium bainitic steel, however, have higher yield stresses, but less work hardening. Based on low cycle fatigue experiments an elastic-plastic material model is introduced and the plastic deformation due to cyclic wheel

[12] M. Pletz et al. "Rolling contact fatigue of three crossing nose materials - Multiscale FE approach". In: *Wear* 314.1-2 (2014), pp. 69–77. ISSN: 0043-1648. DOI: 10.1016/j.wear.2013.11.013

[13] L. Xin et al. "Numerical analysis of the dynamic interaction between wheel set and turnout crossing using the explicit finite element method". In: *Vehicle System Dynamics* 54.3 (2016), pp. 301–327. ISSN: 0042-3114. DOI: 10.1080/00423114.2015.1136424

[14] Y. Ma et al. "Modelling and experimental validation of dynamic impact in 1:9 railway crossing panel". In: *Tribology International* 118 (2018), pp. 208–226. ISSN: 0301679X. DOI: 10.1016/j.triboint.2017.09.036

[15] J. Wiedorn et al. "A Simplified Dynamic Finite Element Model for the Impact of a Wheel on a Crossing: Validation and Parameter Study". In: *Proceedings of the Third International Conference on Railway Technology: Research, Development and Maintenance*. Ed. by J. Pombo. Civil-Comp Press, Stirlingshire, UK, 2016. DOI: 10.4203/ccp.110.116; J. Wiedorn et al. "Simplified explicit finite element model for the impact of a wheel on a crossing - Validation and parameter study". In: *Tribology International* 111 (2017), pp. 254–264. ISSN: 0301-679X. DOI: https://doi.org/10.1016/j.triboint.2017.03.023

[16] M. Pletz et al. "Rolling contact fatigue of three crossing nose materials - Multiscale FE approach". In: *Wear* 314.1-2 (2014), pp. 69–77. ISSN: 0043-1648. DOI: 10.1016/j.wear.2013.11.013

impacts is calculated. In-track measurements of the geometry of crossings validate the calculated plastic surface deformation[17].

Applying a damage criterion Material fatigue represents a common mechanism of material degradation due to cyclic loading: Starting with damage localization and crack initiation it can lead to crack propagation and ultimately failure of a component. Similar to rails, typical damages on crossings include head-checking, spalling or shelling. They are mainly differentiated by their appearance in track but have the presence of cracks in common. Different approaches exist for evaluating fatigue damage, such as Johnson's shakedown method[18] or Burstow's RCF crack initiation model (often referred to as $T - \gamma$ model)[19]. The former one uses normal and tangential forces and material properties to define a shakedown limit and evaluate how likely RCF damage occurs. The latter one additionally considers slip in the contact zone and allows to calculate an index (probability) for RCF damage. Both methods are simple to use because they require little input, but they do not considering the current stresses in the body or the deformed material (i.e. hardening, plastic deformation).

For a more detailed prediction of fatigue lifes approaches that belong to the group of stress-life methods (S-N curves) or crack growth method can be used. Both of them rely on stresses and deformation in the body and on intensive material testing.

To compare the different crossing nose materials a high cycle fatigue criterion by K.D. Van[20] is introduced that belongs to the group of stress-life methods. It assumes a loading in the elastic shakedown regime and uses the stress amplitude and the hydrostatic stresses to predict where and in what direction cracks may initiate[21]. Two material parameter that are evaluated with bending and torsion experiments describe a damage locus: higher hydrostatic pressures increase the critical stress amplitude. Because of its limitations, especially for damage predictions at the surface and the possibility of too conservative results for compressive hydrostatic stresses, several adaptions are proposed[22]. Nevertheless, the criterion is widely used to analyze rail and wheel damage - even in combination with a crack propagation analysis[23]. In this thesis we utilize the DV criterion to calculate

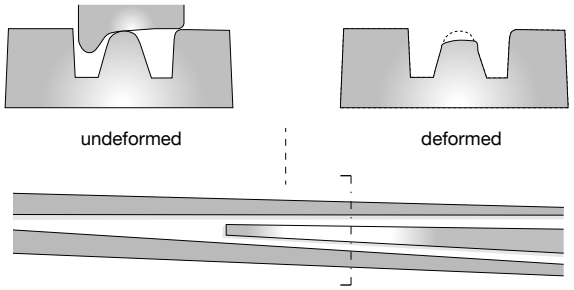

Figure 4: Deformation of a crossing nose due to the transition of wheels.

[17] J. Wiedorn et al. "Using Stress-based Damage Models to Describe Subsurface Damage in Crossings". In: *Proceedings of 11th International Heavy Haul Association Conference*. International Heavy Haul Association, Cape Town, South Africa, 2017; J. Wiedorn et al. "Numerical assessment of materials used in railway crossings by predicting damage initiation - Validation and application". In: *Wear* 414-415 (2018), pp. 136–150. ISSN: 0043-1648. DOI: https://doi.org/10.1016/j.wear.2018.08.011

[18] A. Bower and K. Johnson. "Plastic flow and shakedown of the rail surface in repeated wheel-rail contact". In: *Wear* 144.1 (1991), pp. 1–18. ISSN: 0043-1648. DOI: https://doi.org/10.1016/0043-1648(91)90003-D

[19] M. Burstow. "Whole Life Rail Model Application and Development for RSSB - Development of an RCF Damage Parameter". In: *Rail Safety and Standards Board report* AEATR-ES-2003-832 Issue 1 (2003)

[20] subsequently referred to as DV criterion.

[21] K. Dang Van and B. Griveau. "On a New Multiaxial Fatigue Limit Criterion: Theory and Application: EGF3". In: *Mechanical Engineering Publications*, pp. 476–496

[22] H. Desimone et al. "On the application of Dang Van criterion to rolling contact fatigue". In: *Wear* 260.4-5 (2006), pp. 567–572. ISSN: 0043-1648. DOI: 10.1016/j.wear.2005.03.007; M. Ciavarella et al. "On the Dang Van fatigue limit in rolling contact fatigue". In: *International Journal of Fatigue* 28.8 (2006), pp. 852–863. ISSN: 01421123. DOI: 10.1016/j.ijfatigue.2005.11.002

damage initiation for crossing noses - without any adaptions. The limitations may not apply as we consider plastic deformation. Since we assume a state close to elastic shakedown some of the necessary conditions are not fullfilled. However, the DV concept is applied to compare the different crossing nose materials (considering the plastically deformed geometries) and explain their good performance in track[24].

Manganese steel crossings Cast manganese steel crossings are widely used in turnouts all over the world. The steel is defined by its high manganese content (> 12%) and often referred to as mangalloy or Hadfield steel, after Robert Hadfield - a british metallurgist who discovered manganese steel in 1882[25]. Because of its low yield stress and the repeated wheel impacts, manganese steel experiences large plastic deformations - in contrast to other crossing nose materials. The deformation, however, is accompanied by extensive work hardening: This changes its mechanical properties and microstructure[26] due to twinning induced plasticity (TWIP)[27]. Therefore, the low yield strength and high work hardening capacity characterize its material behavior. As a result, manganese steel shows an extraordinary performance in track that is supported by simulations[28]: The authors explain the positive effect of the deformed (adapted) geometry and predict the benefit when using the adapted geometry for steels with higher yield stresses. Furthermore, they investigate the ability of manganese steel crossings to react to unfavorable load situations[29]. A method that utilizes the deformation behavior of manganese steel, which is also applied to crossings, is pre-hardening by explosives[30]. It increases the wear resistance and strength due to a combination of twinning and slipping near the surface[31].

In general, two effects of plastic deformation can be defined for manganese crossings, but also explosion-depth hardened (EDH) manganese crossings: (1) the positive adaption of the geometry and material to (and due to) the loading in the first few cycles and (2) the long-time behavior with continuing deformation. To explain these deformation mechanisms for EDH manganese steel crossings, we utilize the simplified model. With measured geometries and hardnesses of new and worn EDH manganese steel crossings, we modify the equations for the plastic material law and present these two effects (or stages in the service life of the crossing) using two adaptions of the model. Therefore, a procedure is presented that allows to include (pre-)deformed manganese steel in the simulation model. The model then evaluates the surface deformation, plastic strains and the dynamic response (contact forces and stresses). By showing the evolution of those outputs over wheel impact cycles, we are able to calculate the plastic adaption of a new crossing. Furthermore, statements are made about the long-time behavior of manganese steel crossings[32].

Structure of the thesis The thesis is divided into two parts:

[23] K. Dang Van et al. "Elastoplastic analysis of repeated moving contact application to railways damage phenomena". In: *Wear* 196.1-2 (1996), pp. 77–81. ISSN: 0043-1648. DOI: 10.1016/0043-1648(95)06864-3; K. Dang Van and M. H. Maitournam. "On some recent trends in modelling of contact fatigue and wear in rail". In: *Wear* 253.1-2 (2002), pp. 219–227. ISSN: 0043-1648. DOI: 10.1016/S0043-1648(02)00104-7; A. Ekberg et al. "An engineering model for prediction of rolling contact fatigue of railway wheels". In: *Fatigue & Fracture of Engineering Materials and Structures* 25.10 (2002), pp. 899–909. ISSN: 8756-758X. DOI: 10.1046/j.1460-2695.2002.00535.x; A. Ekberg et al. "Wheel/rail rolling contact fatigue – Probe, predict, prevent". In: *Wear* 314.1-2 (2014), pp. 2–12. ISSN: 0043-1648. DOI: 10.1016/j.wear.2013.12.004

[24] J. Wiedorn et al. "Numerical assessment of materials used in railway crossings by predicting damage initiation - Validation and application". In: *Wear* 414-415 (2018), pp. 136–150. ISSN: 0043-1648. DOI: https://doi.org/10.1016/j.wear.2018.08.011

[25] G. Tweedale et al. "Sir Robert Abbott Hadfield F. R. S. (1858-1940) and the dicovery of manganese steel". In: *Notes and Records of the Royal Society of London* 40.1 (1985), pp. 63–74. ISSN: 1743-0178. DOI: 10.1098/rsnr.1985.0004

[26] O. Bouaziz et al. "High manganese austenitic twinning induced plasticity steels: A review of the microstructure properties relationships". In: *Current Opinion in Solid State and Materials Science* 15.4 (2011), pp. 141–168. ISSN: 13590286. DOI: 10.1016/j.cossms.2011.04.002

[27] L. Chen et al. "Some aspects of high manganese twinning-induced plasticity (TWIP) steel, a review". In: *Acta Metallurgica Sinica (English Letters)* 26.1 (2013), pp. 1–15. ISSN: 1006-7191. DOI: 10.1007/s40195-012-0501-x

[28] J. Wiedorn et al. "Numerical assessment of materials used in railway crossings by predicting damage initiation - Validation and application". In: *Wear* 414-415 (2018), pp. 136–150. ISSN: 0043-1648. DOI: https://doi.org/10.1016/j.wear.2018.08.011

[29] J. Wiedorn et al. "Finite element model for predicting the initiation of subsurface damage in railway crossings - A parametric study". In: *Proceedings of the Institution of Mechanical Engineers, Part F: Journal of Rail and Rapid Transit* 233.6 (2019), pp. 614–628. DOI: 10.1177/0954409718797039

Part 1 describes the mechanical foundations needed to perform the research and

Part 2 presents a selection of published journal papers.

TO PART 1

Chapter 1 states the equations of continuum mechanics - the kinematics, deformations, stresses and balance laws.

Chapter 2 explains the used material models and their physical and mathematical formulations

Chapter 3 gives the numerical discretization, the finite element method, the finite elements and the solution methods

Chapter 4 then explains the different contact formulations and the numerical implementation

Chapter 5 includes the description of the damage criterion. There, the criterion is explained mechanically and the finite element implementation and necessary mathematical routines are shown

RESEARCH, FINDINGS AND OUTLOOK Due to the high loads on crossings, and especially crossing noses, compared to the other parts of the rail network, they are of special interest. This is associated with increased safety issues and high maintenance costs, which in turn causes additional costs for the operator. Although the optimization of crossings is of great importance, research in this area has only increased in the last decade. This may be due to the similarity and variety of research topics in the field of rails, but also due to the complexity that a crossing entails.

In order to achieve progress, from a mechanical point of view, the knowledge of the resulting loads on the crossing nose due to the passing of a train is particularly important. Therefore, forces and stresses are evaluated by measurement and simulation. The simulation, however, enables to react to and identify problems in advance and can be a useful tool when it comes to optimization – already during the planning phase. The measurement, on the other hand, can be additionally used to validate the simulation results.

State-of-the-art Previous work by Wiest et al., Pletz et al. and Kassa et al. investigated the dynamic response of the impact of a wheel on a crossing using simulation models. These models made it possible to identify the loads on a crossing nose and calculate the resulting forces and, to a certain extent, also stresses – for the first time. However, they have their advantages and limits: The two methods (and the models based on it) allow to investigate different mechanisms during the impact of a wheel on a crossing. Therefore, two directions of research have developed: (a) the calculation of the detailed dynamic response combined with simplified methods for the material degradation using

[30] F. Zhang et al. "Microstructure and Properties of Purity High Mn Steel Crossing Explosion Hardened". In: *ISIJ International* 48.12 (2008), pp. 1766–1770. ISSN: 0915-1559. DOI: 10.2355/isijinternational.48.1766

[31] F. C. Zhang et al. "Explosion hardening of Hadfield steel crossing". In: *Wear* 26.2 (2010), pp. 223–229. ISSN: 0043-1648. DOI: 10.1179/174328408X363263

[32] J. Wiedorn et al. "Investigation of deformation mechanisms in manganese steel crossings using FE models". In: *Tribology International* 138 (2019), pp. 424–434. ISSN: 0301-679X. DOI: https://doi.org/10.1016/j.triboint.2019.06.016. URL: http://www.sciencedirect.com/science/article/pii/S0301679X19303305

the multi-body simulation and (b) the simulation of a simplified dynamic response with a detailed modeling of the material degradation (plastic deformation) of a crossing using the finite element method. Therefore, a detailed investigation of the mechanisms of the cyclic deformation and, based on this, an assessment criterion for crossings is still missing.

Current Research and Findings This work focuses on the material degradation of a crossing nose and represents a first step towards understanding the deformation behavior of different crossing nose materials. This is done with models of the group of the finite element method. In comparison to previous work, the dynamics, occurring stresses and deformation during the impact are modeled in more detail. In order to cover the dynamic response of the system including a high resolution of the arising stresses and strains, crucial parameters for the dynamic process are investigated. These parameters are taken from measured geometries and are then used to build a simplified model for the crossing nose. This not only provides a tool for calculating the dynamic response fast, but it can also be used for prediction of the service life, as planning tool during the design phase and for material development.

Furthermore, material behavior of tool steel and chromium-bainitic steel is added to the simulation model and the material model for manganese steel is adapted to allow for the calculation of explosion-depth hardened crossing noses.

Then, the cyclic deformation of new and worn crossing nose geometries due to the impact of differently worn wheels is shown. There, the stages of plastic deformation of manganese steel crossings and their ability to react on unfavourable loads are explained for the first time. Intensive fatigue testing of these materials allow then the application of a multiaxial fatigue criterion: it is used as assessment for crossing nose materials.

Thus, in this work, with the proposed simplified model, the new material models and the stress-based damage criterion the influence of

- various crossing geometries (by reducing them to their crucial parameters),
- dynamic parameters, such as velocity of the wheel,
- mechanical parameters, such as different crossing nose materials,
- on arising forces, stresses, deformation and damage initiation

is studied.

Questions Therefore, questions about the following topics will be answered:

Q1 Geometry optimization – using a pre-deformed crossing nose geometry

Q2 Material selection – for crossing noses using a damage criterion

Q3 Deformation mechanisms – especially of a high work hardening steel (manganese steel)

Outlook Although the major findings in this thesis provide a deeper insight into deformation and damage of crossings, there are still many topics that are untouched and require intensive research work. A focus should be put on a detailed characterization of the material, especially when considering damage/crack initiation and propagation. Common rail and crossing materials suffer from severe deformation during their service life that affects the material properties significantly. In addition to changes in fracture toughness and crack propagation, also anisotropies are introduced that are not considered in simulation models yet. The Dang-Van damage criterion allows for qualitative analysis and is certainly an appropriate method for specific applications. However, the mentioned effects resulting from the high contact load between wheel and rail and its deformation can not be taken into account. In order to create a physically correct basis and to consider the effects caused by deformation, more precise investigations are needed using methods in the area of high deformation testing such as high pressure torsion (HPT). This also applies to a precise characterization of explosion-depth hardened (or highly deformed) manganese steel.

Furthermore, other components of the turnout, such as wing rails and, especially switch blades suffer similar damages as crossing noses due to high loads. Research on switch blades, however, has rarely been performed yet. Therefore, future work may include the investigation of these components with similar or – based on the current results and advances – modified methods. Above all, the behavior of the entire system has to be considered too.

Part I

Fundamentals

Figure II: A moving train

1

Continuum Mechanical Foundation

This chapter states the continuum mechanical foundation needed for the following research results, see Paper A to D. It contains a short summary of the mechanical background including all the ingredients - definitions, procedures and variables - needed to develop a numerical method for solving engineering problems, such as the finite element method. First we discuss the kinematics of large displacements and introduce strain measures and stresses. On this basis, balance laws are stated. The constitutive law used in the papers, the finite element discretization - especially the formulation of the weak form - and the implementation concept for contact of continuum bodies is discussed in the following chapters. For an in-depth discussion of continuum mechanics standard literature, i.e. by Holzapfel[1], Wriggers[2] or Mase et al.[3] should be consulted.

[1] G. A. Holzapfel. *Nonlinear solid mechanics: A continuum approach for engineering*. Repr. Chichester: Wiley, 2010. ISBN: 9780471823193

[2] P. Wriggers. *Nonlinear Finite Element Methods*. Berlin, Heidelberg: Springer Berlin Heidelberg, 2008. DOI: 10.1007/978-3-540-71001-1

[3] G. Thomas Mase, Ronald E. Smelser, George E. Mase. *Continuum Mechanics for Engineers, Third Edition*. CRC Press, 2009. ISBN: 9781420085396. DOI: 10.1201/9781420085396

1.1 KINEMATICS, DEFORMATIONS AND STRESSES

The kinematic relations are explained by considering a homogeneous body Ω with the surface S described by continuously distributed material points $P \in \Omega$ in the Euclidean point space $\mathbb{E}^3$, see Fig. 1.1. A body is placed by mapping material points in $\mathbb{E}^3$ with the mapping function ϕ. The mapping of the whole body can then be described with $\phi(\Omega) = \{\phi(P)|P \in \Omega\}$ and is called configuration. To describe motions and deformations, two configurations are considered, the reference configuration and the current configuration. With ϕ the location at a time t of a particle $\boldsymbol{P}$ (being the position vector of the reference configuration) can be calculated

$$\boldsymbol{p} = \phi(\boldsymbol{P}, t). \tag{1.1}$$

Figure 1.1 shows a graphical representation of the body in its reference configuration Ω and current configuration $\mathfrak{b}$ and at a chosen time t. The current configuration is calculated with Eq. 1.1: points described by the vectors $\boldsymbol{p}$ are created from the vectors of the reference configuration $\boldsymbol{P}$. The displacement $\boldsymbol{u}$ between the two configurations - the difference of their positions in space - is described with

$$\boldsymbol{u}(\boldsymbol{P}, t) = \boldsymbol{p}(\boldsymbol{P}, t) - \boldsymbol{P}. \tag{1.2}$$

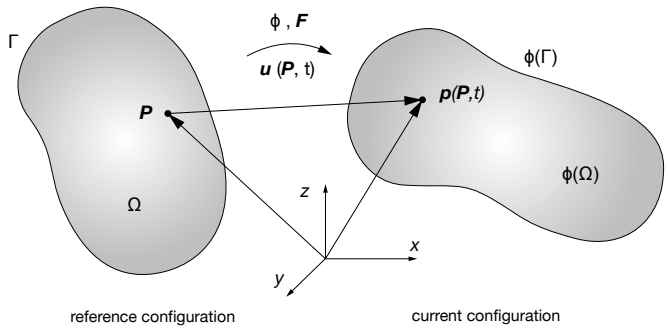

Figure 1.1: Graphical representation of the kinematics of a body in reference and current configuration

There, the displacements $\boldsymbol{u}$ not only consist of a motional but also a deformational component. Furthermore, they are of particular interest as they represent the unknown variables, which have to be calculated, in the numerical investigation in this thesis.

As the passing of a wheel on a crossing is a dynamic process, we need the deriviates in time of the kinematic component $\boldsymbol{p}$. They are calculated with

$$\boldsymbol{v}(\boldsymbol{P}, t) = \frac{\partial \boldsymbol{p}(\boldsymbol{P}, t)}{\partial t} \tag{1.3}$$

and

$$\boldsymbol{a}(\boldsymbol{P}, t) = \frac{\partial \boldsymbol{v}(\boldsymbol{P}, t)}{\partial t} \tag{1.4}$$

where $\boldsymbol{v}$ represents the velocity and $\boldsymbol{a}$ the acceleration. To describe the deformations locally, we consider a material line in the reference $\partial \boldsymbol{P}$ and current $\partial \boldsymbol{p}$ configuration. This gives us the deformation gradient $\boldsymbol{F}$ with

$$\boldsymbol{F} = \frac{\partial \boldsymbol{p}}{\partial \boldsymbol{P}} \tag{1.5}$$

As a strain measure, the Green-Lagrange strain tensor $\boldsymbol{E}$ is introduced, which refers to the reference configuration and is defined by

$$\boldsymbol{E} = \frac{1}{2}(\boldsymbol{F}^{\mathrm{T}}\boldsymbol{F} - \boldsymbol{I}) = \frac{1}{2}(\boldsymbol{C} - \boldsymbol{I}) \tag{1.6}$$

where $\boldsymbol{C} = \boldsymbol{F}^{\mathrm{T}}\boldsymbol{F}$ is the right Cauchy-Green tensor and $\boldsymbol{I}$ the unit tensor. For the strain measure of the current configuration the left Cauchy-Green tensor $\boldsymbol{b} = \boldsymbol{F}\boldsymbol{F}^{\mathrm{T}}$ is used.

While the strain of infinite small volume elements of a continuous material is measured in the reference configuration with the Green-Lagrange strain tensor $\boldsymbol{E}$, a stress measure is used to express the internal forces acting in the body. The relationship between the stress vector in the current configuration $\boldsymbol{t}$ on a surface at a point P and the stress tensor σ is uniquely defined by Cauchy's stress theorem with

$$\boldsymbol{t} = \sigma \boldsymbol{n} \tag{1.7}$$

where $\boldsymbol{n}$ is the unit normal vector of the surface. Depending on the context, different stress measures are used. In current configuration, the stresses may be represented by the Cauchy stresses σ, whereas in the reference configuration by the second Piola-Kirchhoff stress $\boldsymbol{S}$.

Other stress measures include the unsymmetric first Piola-Kirchhoff stress $\boldsymbol{PK}$ and the Kirchhoff stress tensor $\boldsymbol{\tau}$.

Using push-forward and pull-back operations[4], the different stress measures can be obtained. The relationship between the different measures can be summarized with

$$\boldsymbol{\tau} = J\ \boldsymbol{\sigma} = \boldsymbol{F}\ \boldsymbol{PK}^{\mathrm{T}} = \boldsymbol{F}\ \boldsymbol{S}\ \boldsymbol{F}^{\mathrm{T}} \tag{1.8}$$

where J is the determinant of the deformation gradient tensor $\boldsymbol{F}$.

When considering small displacements (small displacement theory or infinitesimal strain theory), simplifications can be made. There, the material and spatial coordinates are similar and their gradients approximately equal. Therefore, strains and stresses can be described - independent of their configuration - with a strain measure $\boldsymbol{\epsilon}$ and a stress measure $\boldsymbol{\sigma}$, respectively.

[4] In continuum mechanics push-forward and pull-back operations relate different configurations. The operators represent a mapping between different spaces. Therefore, quantities in the current configuration are the push-forward of quantities in the reference configuration. Analogously, quantities in the reference configuration are the pull-back of quantities in the current configuration.

1.2 BALANCE LAWS, BOUNDARY CONDITIONS, STRONG AND WEAK FORMS

To describe the mechanical behavior of continuum materials, fundamental laws are introduced as physical relationships. One representation of these laws is called balance laws and include the balance of mass, momentum and energy. Balance laws become the local (stronger) form of the conservation laws – often referred to as continuity equations when including additional sources and sinks.

The balance of mass in the current (Eulerian) configuration is described with

$$\dot{\rho} + \rho\ \nabla \cdot \boldsymbol{v} = 0 \tag{1.9}$$

where ρ is the density, $\dot{\rho}$ its time derivative, describing the change of the density, and $\boldsymbol{v}$ the particle velocity. The balance of momentum is divided into a linear and an angular momentum. The balance of the linear momentum[5] is

$$\rho\ \dot{\boldsymbol{v}} - \nabla \cdot \boldsymbol{\sigma} - \rho\ \boldsymbol{b} = 0 \tag{1.10}$$

with the derivative of the velocity (acceleration) $\dot{\boldsymbol{v}}$, the Cauchy stresses $\boldsymbol{\sigma}$ and the body forces per volume $\boldsymbol{b}$. The balance of angular momentum[6] forces the stress tensor to be symmetric with

$$\boldsymbol{\sigma} = \boldsymbol{\sigma}^{\mathrm{T}} \quad . \tag{1.11}$$

As a last equation in its local form, the balance of energy (First law of thermodynamics) is written as

$$\rho\ \dot{e} - \boldsymbol{\sigma} : (\nabla \boldsymbol{v}) + \nabla \cdot \boldsymbol{q} - \rho\ s = 0 \quad . \tag{1.12}$$

$\dot{e}$ is the material derivative (time rate of change) of the internal density per unit volume, $\boldsymbol{q}$ is the heat flux and s the rate of energy that is created in the body (source). Because of its importance in continuum mechanics, the velocity gradient tensor $\nabla \boldsymbol{v}$ is referred to as $\boldsymbol{l}$ and, by using the deformation gradient $\boldsymbol{F}$, it can be calculated with $\boldsymbol{l} = \nabla \boldsymbol{v} =$

[5] As represented here, the balance of linear momentum is often referred to as Cauchy's first law of motion.

[6] Often referred to as Cauchy's second law of motion.

$\dot{\boldsymbol{F}}\boldsymbol{F}^{-1}$. In modern engineering applications, the balance of energy is mainly used to check the physical correctness of the results.Within this context often the second law of thermodynamics is mentioned. However, due to its importance for constitutive equations, it stated in its special form as Clausius-Duhem inequality in Chapter 2.

To calculate the reaction of the material to a load, another set of equations are needed, which are called constitutive equation(s). They present a relation of stresses σ to deformations by stating that the stresses are a function of the deformations:

$$\sigma \approx \sigma(\boldsymbol{F}) \qquad . \tag{1.13}$$

A detailed discussion on the constitutive equations used in this thesis is presented in Chapter 2.

To solve initial and boundary value problems, conditions have to be added to the equations. Initial conditions are usually specified at the time of the problem (t_0; $t := 0$) with

$$\boldsymbol{u}(t_0) =: \boldsymbol{u}_0 \qquad \text{and} \qquad \boldsymbol{v}(t_0) =: \boldsymbol{v}_0 \tag{1.14}$$

for the displacements $\boldsymbol{u}$ and the velocity $\boldsymbol{v}$, respectively. Boundary conditions, however, are specified on the boundary of the body - they provide a solution in some region of space and are – in comparison to initial value problems – independent of time. Because of their common use in engineering applications, the following boundary conditions are distinguished:

$$\boldsymbol{u} = \boldsymbol{u}_{\mathbf{d}} \quad \text{on} \quad \phi(\mathrm{S_u}) \qquad \text{and} \qquad \boldsymbol{t} = \sigma\, \boldsymbol{n} \quad \text{on} \quad \phi(S_\sigma) \tag{1.15}$$

The former one, the Dirichlet boundary condition (or first-type), specifies displacements along a boundary - the so-called Dirichlet boundary $\mathrm{S_u}$. The latter one is a Neumann boundary condition (second-type) which specifies the derivative of the solution along a boundary - the Neumann boundary S_σ. A typical example for Neumann boundary conditions in solid mechanics are external forces or stresses acting on the surface.

After numerical discretization, these constraints are often referred to as single-point constraints (SPC) as they specify values for specific points. Problems in modern engineering applications often consist of initial conditions, boundary conditions and other variations, which includes for example mixed conditions, complicated functions on boundaries and multi-points constraints (MPC). In this work contact constraints that belong to the group of MPC, are used on several occasions and discussed in Chapter 4.

Figure III: A deformed crossing

2

Constitutive Equations

One aim of this work is the evaluation of the damage and deformation of the railway crossing caused by the wheels of the switching train. The deformed geometry and material is decisive for the occurring forces and stresses. To account for this behavior, a non-linear material model has to be employed. Apart from geometry and contact, this is a source of nonlinearity that significantly influences the computational time of the simulation.

The constitutive equations in this work and their implementation are taken from the work of Simo[1], Souza[2] or Chen[3] and can be reviewed there in further detail.

For the calculation of the wheel's impact on the crossing, two materials are considered: the material of the wheel and of the crossing. The material response of the wheel is considered to be purely linear-elastic, whereas the material response of the crossing behaves elastic-plastically.

In this chapter, the linear theory is used to describe the constitutive equations: considering plasticity at small strains (infinitesimal plasticity) limits the range of applicability and validity, but allows for an additive strain decomposition. This simplifies the equations and allows for a better understanding.

[1] Simo J.C. and Hughes T. J. R. *Computational Inelasticity*. Vol. 7. New York: Springer-Verlag, 1998. ISBN: 0-387-97520-9. DOI: 10.1007/b98904

[2] E. A. de Souza Neto et al. *Computational methods for plasticity: Theory and applications*. Chichester: John Wiley & Sons, 2008. ISBN: 9780470694527. DOI: 10.1002/9780470694626

[3] W.-F. Chen and D.-J. Han. *Plasticity for structural engineers*. Ft. Lauderdale, FL: J. Ross Publ, 2007. ISBN: 9781932159752

2.1 ELASTICITY

Following the infinitesimal strain theory, the strain tensor is calculated with

$$\boldsymbol{\epsilon} = \frac{1}{2}(\boldsymbol{F} + \boldsymbol{F}^{\mathrm{T}} - \boldsymbol{I}) \qquad . \tag{2.1}$$

where $||\boldsymbol{F}|| \ll 1$. As already mentioned in Section 1, in case of small strains, the different stress measures coincide and are now denoted to as stress $\boldsymbol{\sigma}$.

In order to establish the physical basis for material behavior in continuum mechanics, a special form of the second law of thermodynamics is used, the Clausius-Duhem inequality. In its local form, ignoring the influence of temperature, the equation simplifies to

$$\mathfrak{D} = \boldsymbol{\sigma} \ : \dot{\boldsymbol{\epsilon}} - \rho\dot{\psi} \geq 0 \tag{2.2}$$

where σ are stresses, $\dot{\epsilon}$ the strain deformation rate, its product $\sigma : \dot{\epsilon}$ the local stress power, ψ the free Helmholtz energy and ρ the current density. In case of finite deformation $\dot{\epsilon}$ is replaced by $\boldsymbol{d}$, the symmetric part of the deformation velocity gradient $\boldsymbol{l}$ with the Cauchy stresses as stress measure. For both materials, the free Helmholtz energy is a function of the elastic deformation gradient, as it represents the usable work of the system.

In elasticity, all the work supplied by external sources is recoverable, meaning $\mathfrak{D} = 0$ and after several simplifications the stresses can be obtained from the free energy with

$$\boldsymbol{\sigma} = \frac{\partial \psi}{\partial \boldsymbol{\epsilon}} \tag{2.3}$$

where $\boldsymbol{\epsilon}$ is the strain tensor. A similar result can be obtained when proposing the linear Hooke's law with $\boldsymbol{\sigma} = \boldsymbol{C} : \boldsymbol{\epsilon}$, where $\boldsymbol{C}$ is the elasticity tensor with its usual symmetries[4]. Then, $\mathfrak{D}$ in Eq. 2.2 becomes 0, which expresses the assumption of full recoverable energy.

[4] A. Bertram and A. Krawietz. "On the introduction of thermoplasticity". In: *Acta Mechanica* 223.10 (2012), pp. 2257–2268. ISSN: 0001-5970. DOI: 10.1007/s00707-012-0700-6

Elastic materials derived from a strain energy function are usually referred to as hyperelastic materials. In this thesis, linear Hooke's law is used to describe the elastic material response of the wheel during the impact on the crossing. There exist different ways to derive its expressions - mainly caused by the historical development of the law. Similar to other materials, a strain energy function can be defined for the generalized Hooke's law with

$$\psi(\boldsymbol{\epsilon}) = \frac{1}{2}\lambda \ \mathrm{Tr}(\boldsymbol{\epsilon})^2 + \mu \ \boldsymbol{\epsilon} : \boldsymbol{\epsilon} \tag{2.4}$$

where λ and μ are material parameters - called the first and second Lamé parameters. In engineering applications often the elastic modulus E and Poisson's ratio ν are used. They can be calculated with

$$E = \frac{\mu(3\lambda + 2\mu)}{\lambda + \mu} \quad \text{and} \quad \nu = \frac{\lambda}{2(\lambda + \mu)} \quad . \tag{2.5}$$

By using the relationship shown in Eq. 2.3 the following expression can be derived for the stresses $\boldsymbol{\sigma}$

$$\boldsymbol{\sigma} = \lambda \ \mathrm{Tr}(\boldsymbol{\epsilon}) \ \boldsymbol{I} + 2\mu\boldsymbol{\epsilon} \tag{2.6}$$

where $\boldsymbol{I}$ is the idendity tensor. The same result can be evaluated when starting with the generalized Hooke's law - $\boldsymbol{\sigma} = \boldsymbol{C} : \boldsymbol{\epsilon}$, where $\boldsymbol{C}$ is the fourth order stiffness tensor - including symmetries of the tensor and isotropy. Fig. 2.1 shows the stress-strain response of a linear-elastic material with its stored, recoverable strain energy ψ. In this thesis the elastic deformations of the wheel are not of interest and assumed to be rather small in comparison to the ones of the crossing nose.

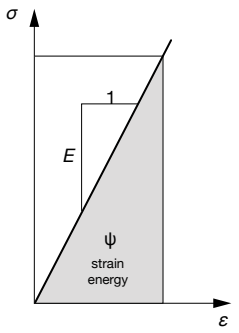

Figure 2.1: Linear-elastic response of a material and its strain energy ψ

2.2 PLASTICITY

If a certain load of a component is exceeded, the material of the component loses the ability to react elastically. This leads to an

irreversible deformation of the material - plastic deformation. Fig 2.2 shows a uniaxial stress-strain curve for a typical metal loaded until failure. After reaching the yield stress σ_y, the stresses have to be continuously increased to drive the deformation of the material due to material hardening. In addition to material hardening, other

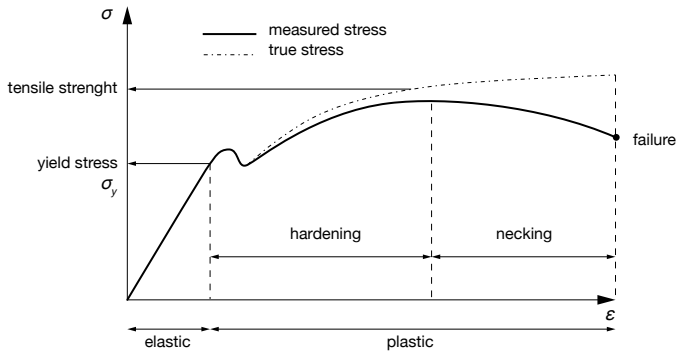

Figure 2.2: Example of an uniaxial stress-strain curve of a typical metal. After reaching the elastic limit, the specimen further deforms until failure.

effects are visible, such as the Lüders elongation after reaching the elastic limit: a drop of the yield stress that is caused by the formation of a localized band of plastic deformation. After the band passed through the material the deformation proceeds uniformly. Usually this deformation is not considered in simulations.

Rails and especially crossings are heavily loaded by the passing wheels. The high loads of the trains are transmitted through a small contact surface into the rails. This leads to plastic deformation of the contacting partners. Furthermore, the repeated cyclic contact and the complex loading situations can cause other behavior, such as the Bauschinger effect – a change in the elastic limit due to the direction of the plastic deformation – or elastic or plastic shakedown and ratcheting. Fig. 2.3 shows different mechanisms of cyclic deformation.

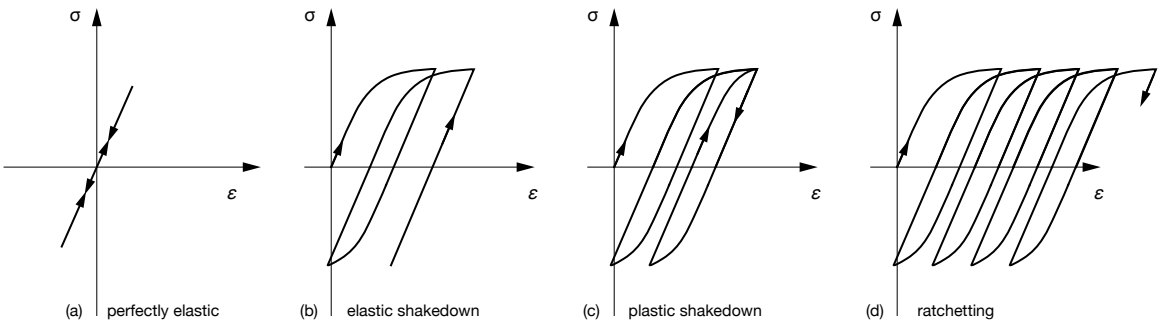

Figure 2.3: Cyclic deformation of materials caused by different mechanisms due to complex loading situation: (a) perfectly elastic, (b) elastic shakedown, (c) plastic shakedown and (d) ratchetting

Therefore, we use elastic-plastic material behavior for the crossing nose during the passing of the wheel.

Mathematical Formulation

The following requirements are needed for the mathematical formulation of plasticity:

DECOMPOSITION OF THE STRAINS When using small deformation theory the strains are decomposed additively

$$\epsilon = \epsilon^{\mathbf{e}} + \epsilon^{\mathbf{p}} \tag{2.7}$$

where $\epsilon^{\mathbf{e}}$ is the reversible elastic part and $\epsilon^{\mathbf{p}}$ the irreversible plastic part of the strains.

ELASTIC LAW The elastic law is needed to relate the stresses and strains in the elastic regime. In this thesis we use Hooke's law

$$\sigma = \boldsymbol{C} \ : \epsilon \qquad . \tag{2.8}$$

YIELD CRITERION The yield function

$$f(\sigma, H) \tag{2.9}$$

then describes the limit of the elastic range. It depends on the current stress state σ and scalar or tensorial hardening variables H. This also includes the yield condition (elastic limit) with

$$f(\sigma, H) = 0 \tag{2.10}$$

and the assumption of being in the elastic range when

$$f(\sigma, H) < 0 \tag{2.11}$$

The loading and unloading condition can be described respectively with

$$\dot{\sigma} : \frac{\partial f}{\partial \sigma} \geq 0 \quad \text{and} \quad \dot{\sigma} : \frac{\partial f}{\partial \sigma} < 0 \tag{2.12}$$

where $\dot{\sigma}$ describes the material time ρ of the stresses.

FLOW RULE To determine the evolution of the plastic strain (direction of the plastic flow), a flow rule is introduced in its general form with

$$\dot{\epsilon}_{\mathbf{p}} = g(\epsilon, \sigma, H, \dot{\epsilon}) \tag{2.13}$$

Conditions that are often used in metal plasticity are Drucker's[5] (and Hill's[6]) stability postulates. They are a strong condition for the internal energy and state that the internal energy can only increase. The criterion leads to the normality condition that states the direction of plastic deformation is normal to the yield surface and further restricts the function for the yield surface. A graphical representation of the flow rule including plastic potential and flow direction is shown in Fig. 2.5.

The consistency condition (Prager) is another equation, which is needed to solve the set of constitutive equations. It states that the

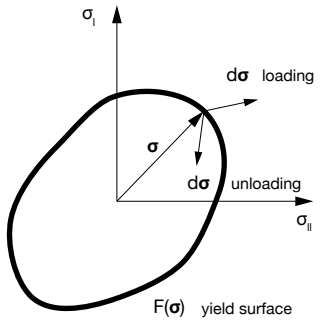

Figure 2.4: The yield surface f and the loading and unloading criterion.

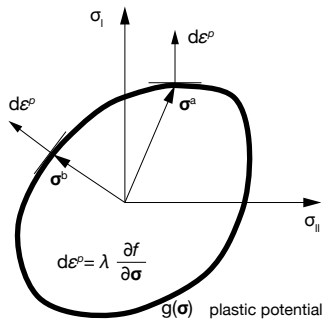

Figure 2.5: The plastic potential g ($= f$ for associated flow rules) for a convex surface (convexity) and the direction of plastic flow normal to the surface of plastic potential (normality).

[5] D. Drucker. "A definition of a stable inelastic material". In: *ASME Journal of Applied Mechanics* 26 (1959), pp. 101–195.

[6] R. Hill. "A general theory of uniqueness and stability in elastic-plastic solids". In: *Journal of the Mechanics and Physics of Solids* 6.3 (1958), pp. 236–249. ISSN: 00225096. DOI: 10.1016/0022-5096(58)90029-2

stress state during plastic deformation must remain on the yield surface with

$$\dot{f} = 0 \qquad . \tag{2.14}$$

To meet the yield criterion and ensure that the stress-state lies on the yield surface a plastic multiplier λ is introduced. Using the plastic multiplier λ and the yield function f as plastic potential g, the flow rule becomes

$$\mathrm{d}\boldsymbol{\epsilon_p} = \mathrm{d}\lambda \frac{\partial f}{\partial \boldsymbol{\sigma}} \tag{2.15}$$

where $d\lambda > 0$. Flow rules that use the yield function as plastic potential are called associated flow rules ($g = f$). There, the direction of the plastic strain increment vector is normal to the yield surface f (given by $\frac{\partial f}{\partial \boldsymbol{\sigma}}$).

Reformulating the admissible states of plastic flow, the following conditions have to be met to evaluate $\boldsymbol{\epsilon_p}$ from Eq. 2.15 for any stress $\boldsymbol{\sigma}$:

$$\dot{\lambda} \geq 0 \qquad , \qquad f \leq 0 \qquad \text{and} \qquad \dot{\lambda} f = 0. \tag{2.16}$$

These restrictions are called Karush Kuhn Tucker[7] (KKT) conditions and are used in several engineering and mathematical problems for solving optimization tasks. As a last step the consistency condition (Eq. 2.14) can be described with

$$\dot{\lambda}\dot{f} = 0 \qquad \text{if} \qquad f = 0. \tag{2.17}$$

[7] W. Karush. "Minima of Functions of Several Variables with Inequalities as Side Constraints". PhD thesis. Chicago, Illinois: University of Chicago, 1939; H. W. Kuhn and A. W. Tucker. "Nonlinear Programming". In: *Proceedings of the Second Berkeley Symposium on Mathematical Statistics and Probability*. Berkeley, Calif.: University of California Press, 1951, pp. 481–492

HARDENING As seen in Fig. 2.2 the deformation behavior of metals includes mechanisms such as hardening. A general form of hardening can be introduced with

$$\dot{H} = h(\boldsymbol{\epsilon}, \boldsymbol{\sigma}, H, \dot{\boldsymbol{\epsilon}}) \qquad . \tag{2.18}$$

It describes the change of the yield surface (expansion, translation). These hardening rules are needed for the material to react to the complex loading situations as shown in Fig. 2.3. Typical hardening mechanisms (or rules) to describe this behavior are isotropic (Fig. 2.6a) and kinematic (Fig. 2.6b) hardening, which may occur alone or in a mixed mode (Fig. 2.6c). The former introduces an expansion of the yield surface with increasing stresses, whereas the latter introduces a translation of the yield surface according to the occurring stresses in the stress space. Fig. 2.6 shows all mechanisms in a principal stress space.

2.3 MATERIAL MODEL

For the crossing models in this paper, cyclic hardening models are used. As mentioned above, they are able to describe the material response of the complex loading situation during wheel-rail contact. The material response of the wheel, however, is described with a simple linear elastic material law, see Section 2.1. In this section, a detailed description of the plastic behavior - on the basis of the

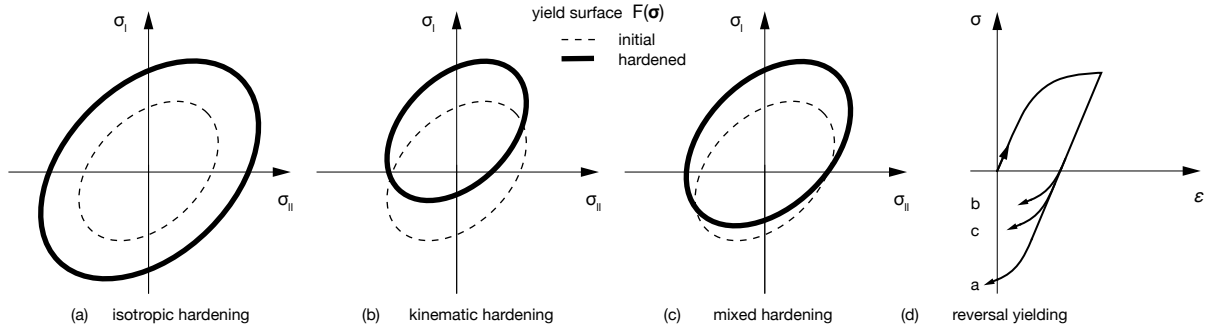

Figure 2.6: Two types of hardening, kinematic and isotropic, alone and in a mixed mode. Their response is shown in terms of loading (stress-strain) curves (d) and yield surface changes: (a), (b) and (c).

previous section - is stated: the yield and failure criteria / plastic potential and the hardening model.

By using the additive decomposition of the strain tensor, see 2.3, 2.6 and Eq. 2.7, the stresses can be described with

$$\boldsymbol{\sigma} = \frac{\partial \psi(\boldsymbol{\epsilon} - \boldsymbol{\epsilon}_{\mathbf{p}})}{\partial \boldsymbol{\epsilon}} = \boldsymbol{C} : (\boldsymbol{\epsilon} - \boldsymbol{\epsilon}_{\mathbf{p}}). \tag{2.19}$$

where $\boldsymbol{C}$ is the stiffness tensor that - including all symmetries for fully isotropic material - can be described by two parameters, the Lamé parameters (λ and μ or E and ν, see Eq. 2.4). For the yielding of the material, the von Mises yield function is used. It is a common criterion for ductile material, such as metals, and uses the second invariant of the stress J_2

$$J_2 = \frac{1}{2}\mathrm{Tr}(\boldsymbol{s}^2) = \frac{1}{2}\boldsymbol{s} : \boldsymbol{s} \tag{2.20}$$

where $\boldsymbol{s}$ are the deviatoric stresses. They are defined with

$$\boldsymbol{\sigma} = \boldsymbol{s} + \frac{1}{3}\mathrm{Tr}(\boldsymbol{\sigma})\boldsymbol{I} = \boldsymbol{s} + \frac{1}{3}I_1\boldsymbol{I} \tag{2.21}$$

where $\boldsymbol{I}$ is the identity tensor and I_1 the first stress invariant. The yield function then follows with

$$f(\boldsymbol{\sigma}) = \sqrt{3J_2} - \sigma_0 = \sqrt{\frac{3}{2}\boldsymbol{s} : \boldsymbol{s}} - \sigma_0 \tag{2.22}$$

where σ_0 is the yield stress of the material, evaluated through material testing. A graphical representation of the criterion is shown in Fig. 2.7. In principal stress coordinates the criterion describes a cylinder along the hydrostatic axis σ_h (Fig. 2.7a). When represented by all principal stresses (three principal axes) on the deviatoric plane (or Π plane), the cylinder appears as circle (Fig. 2.7b). Fig. 2.6 shows the initial yield criterion (dotted line) when considering two principal stresses.

The scalar representation of the ocurring stresses is commonly used in engineering applications and called von Mises or effective stresses

$$\sigma_\mathrm{Mises} = \sqrt{\frac{3}{2}\boldsymbol{s} : \boldsymbol{s}} \quad . \tag{2.23}$$

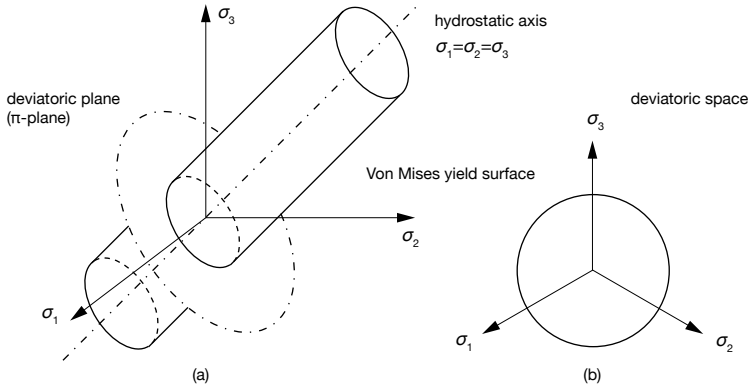

Figure 2.7: A 3D representation of the yield surface described by the von Mises function in the space of principal stresses. σ_1, σ_2 and σ_3 represent the principal stresses. The Π plane is the deviatoric plane - its normal is defined by the hydrostatic axis σ_h.

Furthermore, the criterion is often referred to as maximum distortion strain energy criterion as the second stress invariant J_2 is independent of the first stress invariant I_1 and therefore, independent of the hydrostatic stresses $\sigma_h = \frac{1}{3} I_1$.

To consider the mixed hardening behavior, the von Mises yield condition of the material adapts to

$$f(\boldsymbol{\sigma}, \boldsymbol{\epsilon_p}) = \sqrt{\frac{3}{2}(\boldsymbol{s} - \boldsymbol{\alpha_d}) : (\boldsymbol{s} - \boldsymbol{\alpha_d})} - \sigma_0 \tag{2.24}$$

where $\boldsymbol{\alpha_d}$ is the deviatoric part of the backstresses $\boldsymbol{\alpha}$ to describe kinematic hardening. The evolution of the yield surface caused by isotropic hardening is included in the current yield stress σ_0 which may depend on the plastic strains $\boldsymbol{\epsilon_p}$.

Similar to the effective stresses in Eq. 2.23, effective plastic strains or equivalent plastic strains ϵ_p are defined[8].

$$d\epsilon_p = \sqrt{\frac{2}{3} d\boldsymbol{\epsilon_p} : d\boldsymbol{\epsilon_p}} \quad . \tag{2.25}$$

They are needed for the kinematic and isotropic hardening functions. Here, a non-linear isotropic and kinematic hardening model based on the work of Chaboche is taken[9]. The evolution of the backstresses $\boldsymbol{\alpha}$ is described with

$$d\boldsymbol{\alpha} = \sum_{k=1}^{N} C_k d\epsilon_p \frac{1}{\sigma_0}(\boldsymbol{\sigma} - \boldsymbol{\alpha}) - \gamma_k \boldsymbol{\alpha_k} d\epsilon_p \tag{2.26}$$

where C_k and γ_k are material parameters and k is an arbitrary number needed to define the number of parameters to fit the model to the results evaluated through material testing. An exponential evolution law to describe isotropic hardening for the current yield stress σ_0 is used

$$\sigma_0 = \sigma_y + Q_\infty (1 - e^{-b\epsilon_p}) \tag{2.27}$$

with the material parameters Q_∞, b and the initial yield stress σ_y.

[8] In common software applications these strains are referred to as accumulated equivalent plastic strains.

[9] J.-L. Chaboche. "Constitutive equations for cyclic plasticity and cyclic viscoplasticity". en. In: *International Journal of Plasticity* 5.3 (Jan. 1989), pp. 247–302. ISSN: 07496419. DOI: 10.1016/0749-6419(89)90015-6; J.-L. Chaboche. "A review of some plasticity and viscoplasticity constitutive theories". en. In: *International Journal of Plasticity* 24.10 (Oct. 2008), pp. 1642–1693. ISSN: 07496419. DOI: 10.1016/j.ijplas.2008.03.009

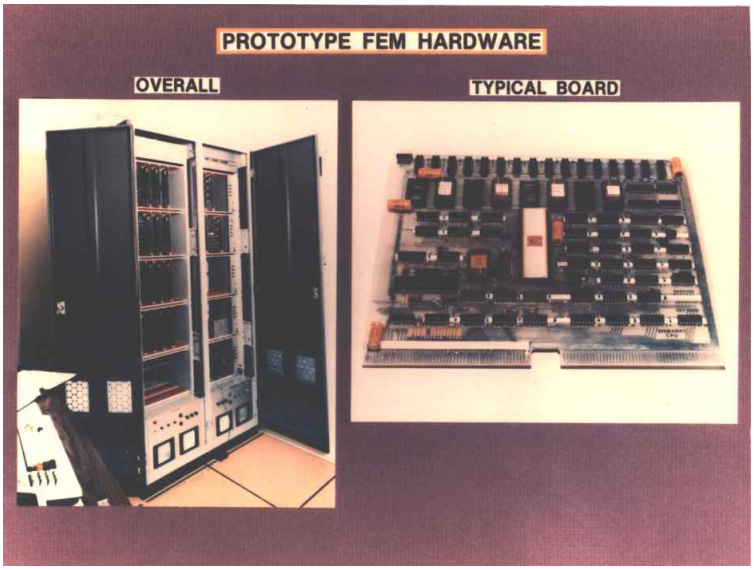

Figure IV: The Finite Element Machine

3

Finite Element Discretization

To solve the initial and boundary value problem the finite element method (FEM) is used. The numerical method subdivides the problem - on the basis of the set of equations mentioned in the previous chapters - into smaller parts, called finite elements. These elements are built of nodes that are connected through mechanical models and equations. The simple equations that describe these elements are then assembled again into a large system of equations to describe the entire mechanical problem. A numerical solution of the problem is then found by solving the full set of equations using implicit and explicit methods. The derivation of the method is taken from Bathe[1], Wriggers[2] and Chen[3] and can be reviewed there in further detail.

As a first step the strong form of the balance of momentum, see Eq. 1.10, is taken and multiplied by a virtual displacement $\delta \boldsymbol{u}$ and integrated over its solution space Ω.

$$\int_{\phi(\Omega)} \delta \boldsymbol{u}\, \rho\, \dot{\boldsymbol{v}}\, \mathrm{d}v = \int_{\phi(\Omega)} \delta \boldsymbol{u}\, (\nabla \cdot \boldsymbol{\sigma} + \rho\, \boldsymbol{b})\, \mathrm{d}v \tag{3.1}$$

We now transform Eq. 3.1 using the Gauss theorem to obtain the weak form of the balance equation[4]

$$\underbrace{\int_{\phi(\Omega)} \delta \boldsymbol{u}\, \rho\, \dot{\boldsymbol{v}}\, \mathrm{d}v}_{\delta W_{\text{kin}}} + \underbrace{\int_{\phi(\Omega)} \nabla \delta \boldsymbol{u} : \boldsymbol{\sigma}\, \mathrm{d}v}_{\delta W_{\text{int}}} = \underbrace{\int_{\phi(\Omega)} \delta \boldsymbol{u}\, \rho \boldsymbol{b}\, \mathrm{d}v + \int_{\phi(S_\sigma)} \delta \boldsymbol{u}\, \boldsymbol{t}\, \mathrm{d}a}_{\delta W_{\text{ext}}} \tag{3.2}$$

where $\nabla \delta \boldsymbol{u}$ represents the virtual strains $\delta \boldsymbol{\epsilon}$. The last term in Eq. 3.2 describes the surface integral of the applied boundary forces (Neumann), the natural boundary conditions. As the displacement boundary conditions (Dirichlet) still have to be met by the trial solutions (or virtual displacement field), they are referred to as essential boundary conditions. This not only reduces the order of the derivatives of the given equation but is also a weaker requirement: the residuum of the approximated solution is set to zero by multiplying by the virtual displacements and integrating the residual over the whole domain.

[1] K.-J. Bathe and P. Zimmermann. *Finite-Elemente-Methoden*. ger. 2., vollst. neu bearb. und erw. Aufl. OCLC: 51700169. Berlin: Springer, 2002. ISBN: 9783540668060

[2] P. Wriggers. *Computational Contact Mechanics*. Berlin, Heidelberg: Springer Berlin Heidelberg, 2006. DOI: 10.1007/978-3-540-32609-0

[3] W.-F. Chen and D.-J. Han. *Plasticity for structural engineers*. Ft. Lauderdale, FL: J. Ross Publ, 2007. ISBN: 9781932159752

[4] The weak form is also called the principle of virtual displacements, which is equivalent of the principle of virtual work.

3.1 SPATIAL DISCRETIZATION

In addition to the approximation of the primary variables (the displacements), the finite element method also approximates the geometry by finite elements. The body Ω can then be described by

$$\Omega \approx \Omega^h = \bigcup_{e=1}^{N} \Omega_e \tag{3.3}$$

where Ω^h is the approximated body and Ω_e its smaller parts, see Fig. 3.1.

For the finite element approximation, the variable fields used in Eq. 3.2 have to be discretized. The displacements, the virtual displacements and the acceleration are approximated with

$$\boldsymbol{u}_e(\boldsymbol{X}, t) = \boldsymbol{N}_\mathbf{e}(\boldsymbol{X})\ \boldsymbol{v}_e(t) \tag{3.4}$$

$$\delta\boldsymbol{u}_e(\boldsymbol{X}, t) = \boldsymbol{N}_\mathbf{e}(\boldsymbol{X})\ \delta\boldsymbol{v}_e(t) \tag{3.5}$$

$$\boldsymbol{a}_e(\boldsymbol{X}, t) = \boldsymbol{N}_\mathbf{e}(\boldsymbol{X})\ \ddot{\boldsymbol{v}}_e(t) \tag{3.6}$$

where $\boldsymbol{N}_\mathbf{e}(\boldsymbol{X})$ is a shape or ansatz function in its local (element-wise) coordinate system $\boldsymbol{X}$. As already mentioned the degrees of freedom of an element is given at nodes. Therefore, $\boldsymbol{v}_e$, $\delta\boldsymbol{v}_e$ and $\ddot{\boldsymbol{v}}_e$ are the unknown nodal quantities - the displacement, its virtual representation and the acceleration. The gradient of the deformation in Eq. 3.2 is calculated with

$$\nabla\delta\boldsymbol{u}_e(\boldsymbol{X}, t) = \frac{\partial \boldsymbol{N}_\mathbf{e}(\boldsymbol{X})}{\partial \boldsymbol{x}}\delta\boldsymbol{v}_e(t) = \boldsymbol{B}_e(\boldsymbol{X})\ \delta\boldsymbol{v}_e(t) \tag{3.7}$$

with the kinematic $\boldsymbol{B}$-operator. To allow for the deriviation of the shape function N_e, an inverse Jacobian takes care of the coordinate system mismatch from local coordinates $\boldsymbol{X}$ to global coordinates - $\boldsymbol{p}$ or $\boldsymbol{P}$ (if differentiated between current and reference configuration). The Jacobian is defined then with $\boldsymbol{j}_\mathbf{e} = \frac{\partial \boldsymbol{p}}{\partial \boldsymbol{P}}$ and $\boldsymbol{J}_\mathbf{e} = \frac{\partial \boldsymbol{P}}{\partial \boldsymbol{p}}$ for the current and reference configuration, respectively.

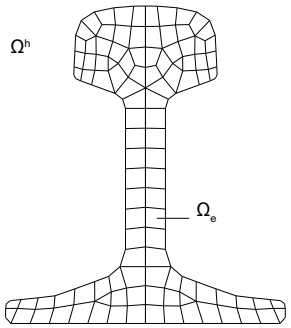

Figure 3.1: A body (rail) discretized into finite elements (Ω_e) and assembled to represent an FE simulation model (Ω^h).

NOTE In this step also the usual matrix representation of the variables for the finite method is introduced.

In this thesis three dimensional elements on the basis of eight node brick elements with standard integration are used (C3D8), see Fig. 3.2.

This element has linear shape functions according to

$$N_I(\boldsymbol{X}) = \frac{1}{2}(1 + X_1 C_1)\ \frac{1}{2}(1 + X_2 C_2)\ \frac{1}{2}(1 + X_3 C_3) \tag{3.8}$$

where I is a number between 1 and 8 that represents the number of the node, cp. Fig. 3.2. X_1, X_2 and X_3 are the components of the vector $\boldsymbol{X}$ and C_1, C_2 and C_3 the components of the vector $\boldsymbol{C}$ that describes the position of the current node I.

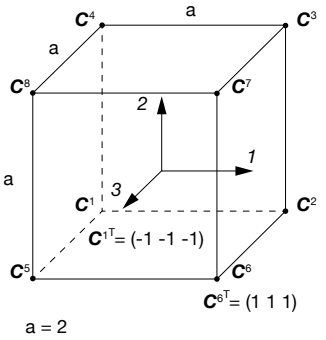

Figure 3.2: The eight node brick element with and its internal node numbering and the position vector $\boldsymbol{C}$.

Then, the equations defined for each element are assembled and Eq. 3.2 rewritten to

$$\delta \boldsymbol{v} \; (\boldsymbol{M}\ddot{\boldsymbol{v}}(t) - \boldsymbol{f}_{\text{ext}}(t) + \boldsymbol{f}_{\text{int}}(\boldsymbol{v}, t)) = 0 \tag{3.9}$$

where $\boldsymbol{f}_{\text{int}}$ represents the internal nodal forces with

$$\boldsymbol{f}_{\text{int}} = \bigcup_{e=1}^{N} \int \boldsymbol{B}_{\mathbf{e}}^{\mathbf{T}}(\boldsymbol{v}, t) \; \boldsymbol{\sigma}(\boldsymbol{v}, t) \; \mathrm{d}v \tag{3.10}$$

$\boldsymbol{f}_{\text{ext}}$ the external nodal forces with

$$\boldsymbol{f}_{\text{ext}} = \bigcup_{e=1}^{N} \int \boldsymbol{N}^{\mathbf{T}} \; \rho \boldsymbol{b} \, \mathrm{d}v + \int \boldsymbol{N}^{\mathbf{T}} \; \boldsymbol{t} \, \mathrm{d}a \tag{3.11}$$

and $\boldsymbol{M}$ the mass matrix with

$$\boldsymbol{M} = \bigcup_{e=1}^{N} \int \boldsymbol{N}^{\mathbf{T}} \; \boldsymbol{N} \; \rho \, \mathrm{d}v \qquad . \tag{3.12}$$

With the appropriate choice of test functions or virtual displacements, the equations defined above result in an equivalent finite element system of equations as follows

$$\boldsymbol{M}\ddot{\boldsymbol{v}}(t) = \boldsymbol{f}_{\text{ext}}(t) - \boldsymbol{f}_{\text{int}}(\boldsymbol{v}, t) \qquad . \tag{3.13}$$

In case of geometrically linear analysis (small deformation) and linear elasticity, the product $\boldsymbol{B} \; \boldsymbol{\sigma}$ in Eq. 3.10 can replaced by $\boldsymbol{K}^{\mathbf{e}}$ the stiffness matrix with

$$\boldsymbol{K}^{\mathbf{e}} = \boldsymbol{B}_{\mathbf{e}}^{\mathbf{T}} \; \boldsymbol{C} \; \boldsymbol{B}_{\mathbf{e}} \tag{3.14}$$

by using $\boldsymbol{\sigma} = \boldsymbol{C} \; : \; \boldsymbol{\epsilon}$ and $\boldsymbol{\epsilon} = \boldsymbol{B} \; \boldsymbol{v}$. In case of finite deformation and incremental plasticity, the integrals, deformations and stresses have to be evaluated in respect to the chosen configurations and are a source of non-linearity[5].

Those quantities in the finite element solution that are calculated through integration, such as stresses and strains, are evaluated at specific positions in the element: integration or Gauss points. In general we differentiate between full and reduced integration. In the FE models in this thesis elements with reduced integration are used (c3D8R). In case of 8 node brick elements (C3D8) and reduced integration the number of integration points drops from 8 to only 1 point, see Fig. 3.3. This prevents locking effects and reduces the numerical effort of the simulation.

HOURGLASSING A disadvantage is the possible occurrence of hourglassing, a deformation of the element that represents no energy change (zero energy mode), see Fig. 3.4.

To avoid this problem, an enhanced hourglassing control is used that is implemented in the FE software Simulia ABAQUS[6]. This method gives an increased resistance against hourglassing for nonlinear material behavior, as applied in this thesis. It uses stiffness coefficients that are based on the enhanced assumed strain method. Stiffness formulations usually generate (hourglass) forces depending on the nodal displacement that are responsible for the hourglass modes (local increase of the stiffness).

[5] P. Wriggers. *Computational Contact Mechanics*. Berlin, Heidelberg: Springer Berlin Heidelberg, 2006. DOI: 10.1007/978-3-540-32609-0

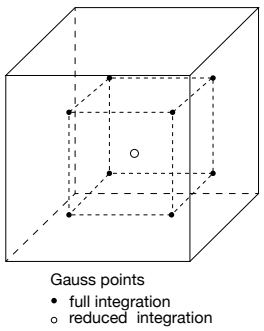

Figure 3.3: The eight node brick element with and gauss points with standard integration (C3D8) and reduced integration (C3D8R).

[6] *Simulia ABAQUS Documentation*. Providence, RI, USA.: Dassault Systemes

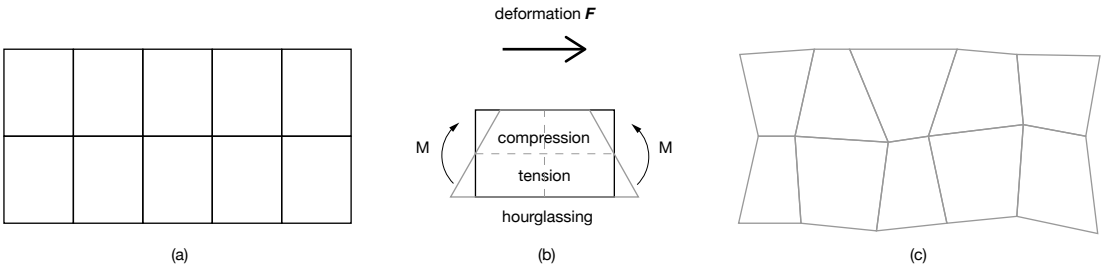

Figure 3.4: An (a) undeformed and (b) deformed 2D finite element mesh with hourglassing due to reduced element integration. (c) shows the modes for one element and the non-detection of strains at the integration point.

COMPUTATIONAL EFFICIENCY Different methods are used to reduce the computational effort. A common method is to reassemble the existing matrices in the FE system of equations in a computationally efficient way. In general, this is done for the mass matrix $\boldsymbol{M}$, where a diagonal matrix is obtained by dividing the total mass to the nodes of the finite element (diagonalization). This so called lumped mass matrix can then be simply stored as a vector[7].

A widely used method for the efficient storage of symmetric and banded sparse matrices, such as the tangent / stiffness matrix $\boldsymbol{K}$ is the application of the skyline storage scheme[8]. In this method only entries in a fixed distance from the matrix diagonal are stored (half bandwith). Renumbering the rows and columns optimizes the existing matrix to obtain the lowest possible skyline.

[7] K. H. Huebner. *The finite element method for engineers*. 4. ed. New York, NY: Wiley, 2001. ISBN: 0471370789

[8] I. S. Duff et al. *Direct Methods for Sparse Matrices*. Oxford University Press, 2017. ISBN: 9780198508380. DOI: 10.1093/acprof:oso/9780198508380.001.0001

3.2 SOLUTION METHODS

In this thesis, explicit and implicit solution methods are used. The former simulates the dynamic impact of the wheel on the crossing nose and the latter one is used for the relaxation step in between the impact cycles. There, the wheel is removed from the model and the crossing is fixed in space to achieve a state of static equilibrium. Paper C and D gives a more detailed explanation of these two models.

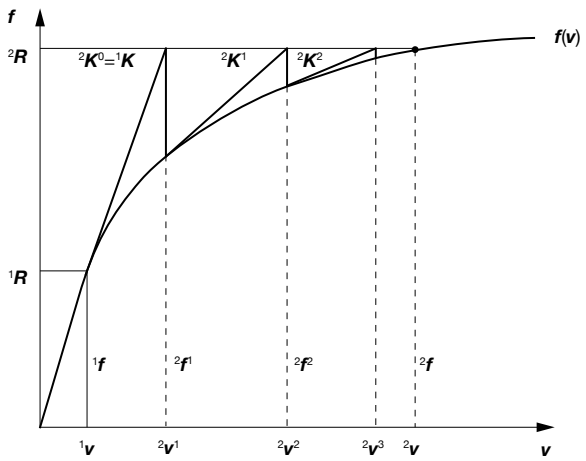

Figure 3.5: The Newton-Raphson scheme for solving shown for several iteration steps: v_1^1, v_1^2, v_1^3 to reach v_2. The Jacobian $\boldsymbol{K}^i$ has to be calculated in each iteration step.

Both models use nonlinear solution methods to solve the system of equations. A typical implicit solution method is Newton's method. Considering the fact that implicit methods in this thesis are used for static analyses only, the first term in Eq. 3.13 ($\boldsymbol{M}\ \ddot{\boldsymbol{v}}(t)$) is equal to 0 and the system of equation is simplified to

$$f(v) = 0 \tag{3.15}$$

where f combines all the forces $f(v) = f_{\text{ext}} - f_{\text{int}}(v)$. Newton's method uses iterative steps to solve the non-linear equations of the finite element system. To show the approximation steps, Eq. 3.15 is rewritten using the current approximation of the displacement v^{i} and the error to the exact solution $e^{\text{i}+1}$

$$f(v^{\text{i}} + e^{\text{i}+1}) = 0 \qquad . \tag{3.16}$$

By using the Taylor series for expanding f around the approximated solution and neglecting all higher order terms, we obtain

$$f(v^{\text{i}}) + \frac{\partial f}{\partial v}(v^{\text{i}})\ (v^{\text{i}+1} - v^{\text{i}}) = 0 \tag{3.17}$$

where $v^{\text{i}+1} - v^{\text{i}} = \Delta v^{\text{i}+1} = e^{\text{i}+1}$. The system of equation simplifies then to

$$\boldsymbol{K}^{\text{i}}\ e^{\text{i}+1} = -f^{\text{i}} = f^{\text{i}}_{\text{int}} - f_{\text{ext}} \tag{3.18}$$

where $\boldsymbol{K}^{\text{i}}$ is the Jacobian or tangential stiffness matrix ($\frac{\partial f}{\partial v}(v^{\text{i}})$) and f^{i} stands for the current forces ($f(v^{\text{i}})$), both at iteration step i.

The full iteration scheme is then completed with

$$v^{\text{i}+1} = v^{\text{i}} + e^{\text{i}+1} \qquad . \tag{3.19}$$

The current displacement $v^{\text{i}+1}$ is then used as new displacement in Eq. 3.17 (instead of v^{i})). This iteration continues until the convergence criterion is satisfied: a sufficiently small $e^{\text{i}+1}$. Figure 3.5 shows the iteration procedure schematically.

A disadvantage of this method is that the Jacobian matrix has to be calculated for each iteration step. A common modification to reduce the computational effort is to omit this step. The modified Newton Raphson method (or initial stress method) uses the initial stiffness (Jacobian matrix) for all iteration steps. There Eq. 3.17 can be rewritten

$$\boldsymbol{K}^{0}\ e^{\text{i}+1} = f^{\text{i}} \tag{3.20}$$

for all iteration steps i where $\boldsymbol{K}^{0}$ is the stiffness matrix evaluated at the beginning of the iteration process ($i = 0$). Fig. 3.6 shows this procedure.

Because of the lower convergence rate of this method, often a compromise of these methods is used, a Quasi-Newton method. The Broyden-Fletcher-Goldfarb-Shanno (BFGS) algorithm belongs to this group of methods[9]. This matrix update method uses a lower rank matrix to update the inverse of the current stiffness matrix $\boldsymbol{K}^{\text{i}}$. Its

[9] C. G. Broyden. "The Convergence of a Class of Double-rank Minimization Algorithms 1. General Considerations". In: *IMA Journal of Applied Mathematics* 6.1 (1970), pp. 76–90. ISSN: 0272-4960. DOI: 10.1093/imamat/6.1.76

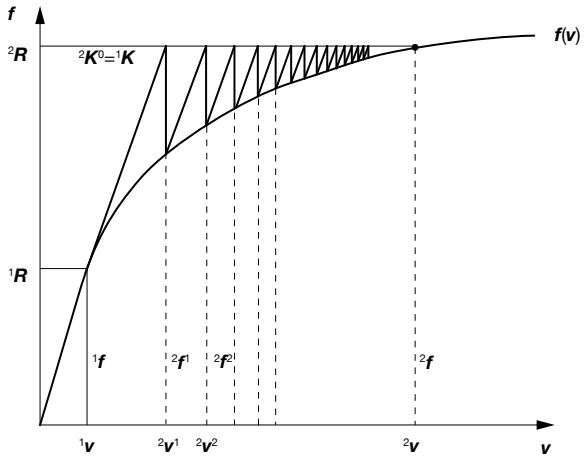

Figure 3.6: The modified Newton-Raphson scheme for solving shown for several iteration steps: v_1^1, v_1^2, v_1^3 to reach v_2. The Jacobian $\boldsymbol{K}^{\mathrm{i}}$ is calculated in the first iteration step which increases the number of iterations.

construction is based on the previous displacement increment $\Delta \boldsymbol{v}^{\mathrm{i}}$ (or $\boldsymbol{e}^{\mathrm{i}}$), the out of balance force vector $\boldsymbol{f}_{\mathrm{ob}}^{\mathrm{i}}$ with

$$\boldsymbol{f}_{\mathrm{ob}}^{\mathrm{i}} = \boldsymbol{f}_{\mathrm{ext}} - \boldsymbol{f}_{\mathrm{int}}^{\mathrm{i}} \tag{3.21}$$

and its increment $\Delta \boldsymbol{f}_{\mathrm{ob}}^{\mathrm{i}}$

$$\Delta \boldsymbol{f}_{\mathrm{ob}}^{\mathrm{i}} = \boldsymbol{f}_{\mathrm{ob}}^{\mathrm{i}-1} - \boldsymbol{f}_{\mathrm{ob}}^{\mathrm{i}} \quad . \tag{3.22}$$

The approximation of the Jacobian matrix is then updated with

$$[\boldsymbol{K}^{\mathrm{i}}]^{-1} = \boldsymbol{A}^{\mathrm{i}-1}\ [\boldsymbol{K}^{\mathrm{i}-1}]^{-1}\ \boldsymbol{A}^{\mathrm{i}-1} \tag{3.23}$$

where $\boldsymbol{A}$ is a modification matrix which depend on the vectors $\Delta \boldsymbol{v}^{\mathrm{i}}$ and $\boldsymbol{f}_{\mathrm{ob}}^{\mathrm{i}}$. The iteration scheme includes then the calculation of the displacement increment $\Delta \boldsymbol{v}^{\mathrm{i}}$ with

$$\Delta \boldsymbol{v}^{\mathrm{i}} = [\boldsymbol{K}^{\mathrm{i}-1}]^{-1}\ \boldsymbol{f}_{\mathrm{ob}}^{\mathrm{i}-1} \tag{3.24}$$

for every iteration i with an updated modification matrix.

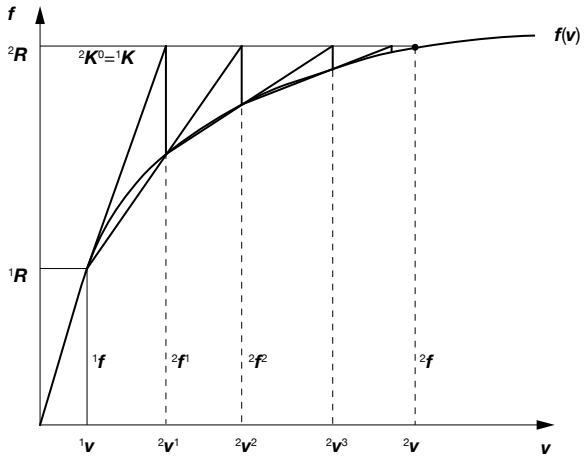

Figure 3.7: The quasi Newton-Raphson scheme for solving shown for several iteration steps: v_1^1, v_1^2, v_1^3 to reach v_2. The Jacobian $\boldsymbol{K}^{\mathrm{i}}$ is updated in each iteration step based on the previous result.

For the calculation of the dynamic impact of the wheel on the crossing an explicit procedure is used. In comparison to the static

analysis using implicit procedures, the accelerations $\ddot{\boldsymbol{v}}(t)$ are non-zero and calculated for every increment. By using the modified Euler method[10] (MEM) for the explicit time integration, the equation of motion can be described with central difference approximations

$$\dot{\boldsymbol{v}}^{i+\frac{1}{2}} = \dot{\boldsymbol{v}}^{i-\frac{1}{2}} + \frac{\Delta t^{i+1} + \Delta t^{i}}{2} \ddot{\boldsymbol{v}}^{i} \tag{3.25}$$

$$\boldsymbol{v}^{i+1} = \boldsymbol{v}^{i} + \Delta t^{i+1}\, \dot{\boldsymbol{v}}^{i+\frac{1}{2}} \tag{3.26}$$

where $\dot{\boldsymbol{v}}$ is the velocity and $\ddot{\boldsymbol{v}}$ the acceleration. Unlike implicit methods, for every update of the variables, the values used in the equation are taken from the previous increment - $\dot{\boldsymbol{v}}^{i-\frac{1}{2}}$ and $\ddot{\boldsymbol{v}}^{i}$. The needed accelerations are calculated using Eq. 3.13 with

$$\ddot{\boldsymbol{v}}^{i} = \boldsymbol{M}^{-1} \left(\boldsymbol{f}^{i}_{\text{ext}} - \boldsymbol{f}^{i}_{\text{int}} \right) \tag{3.27}$$

where $\boldsymbol{M}^{-1}$ is the lumped mass matrix as described above.

[10] G. D. Hahn. "A modified Euler method for dynamic analyses". In: *International Journal for Numerical Methods in Engineering* 32.5 (1991), pp. 943–955. ISSN: 0029-5981. DOI: 10.1002/nme.1620320502

Stability

As explicit procedures depend on results of the previous step, small time increments have to be chosen to guarantee a stable calculation. This limitation has a physical meaning too: the chosen timestep has to be able to resolve the shock waves moving through the solid. The limit for the time increment Δt is described by the Courant number (or CFL number after Courant-Friedrichs-Lewy[11]) with

$$\Delta t \leq \frac{2}{\omega_{\max}} = \min_{\forall e} \frac{L_e}{c_d} \tag{3.28}$$

where $\omega_{\max}$ is the maximum eigenvalue, L_e the characteristic length and c_d the wave speed of the material for all elements. This relation can be calculated using a simple linear oscillator.

[11] R. Courant et al. "Über die partiellen Differenzengleichungen der mathematischen Physik". In: *Mathematische Annalen* 100.1 (1928), pp. 32–74. DOI: 10.1007/BF01448839

For problems including non-linearities, such as plasticity and contact, no exact stability criterion exists: Even if Eq. 3.28 holds, other instabilities, i.e. mechanical, can occur. As an alternative, the stability of the energy is considered, in particular the energy balance of kinetic, internal and external energy for each time step.

Mass Scaling

Since the time step depends on the size of the element, high computational effort is required for very small elements. As the FE mesh often involves a few very small elements that have negligible influence on the result, the explicit method adjusts the mass to obtain higher time steps and therefore reduce the computational effort: This is called mass scaling. This can be done by increasing the wave speed c_d by artificially increasing the density ρ with

$$c_d = \sqrt{\frac{E}{\rho}} \tag{3.29}$$

where E is Young's modulus. With Eq. 3.28, Δt can then be decreased and the computational effort reduced.

In case of variable mass scaling, additional mass is introduced into the affected elements without changing the dynamics of the system. In the simulation, a target value was selected for the time step and the affected elements were adjusted automatically. As a first check of the system dynamics, the changed mass of the entire system can be used.

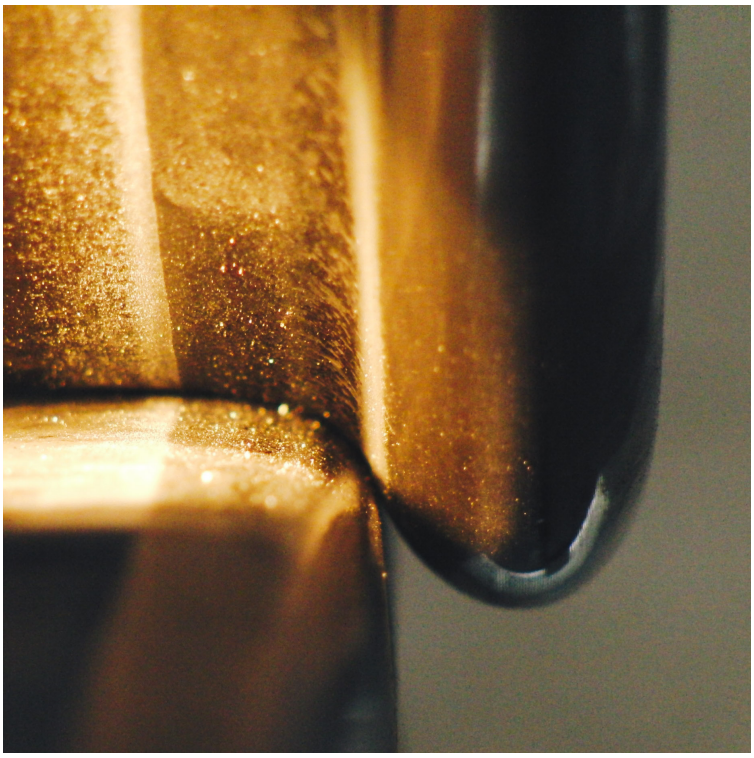

Figure V: A wheel in contact with a rail

With permission of the photographer.

4

Contact

An essential part of the simulation of the wheel impact on the rail or crossing nose is the treatment of the contact between the moving and deforming bodies or surfaces. This is another source of non-linearity since the touching bodies have to be in balance in each time step. In addition, the contact simulation involves other numerical elaborate methods, such as finding the contact points. In case of a rolling/sliding of wheel on a rail, finite sliding formulations are needed to consider the constantly changing contact. This increases, next to finite deformation and material non-linearity, the computational effort significantly.

In an explicit time integration algorithm, the procedure works as follows: In each time step, the involved bodies are separated - without consideration of contact - and the dynamic balance is calculated. The resulting penetrations are corrected at the end of the time step. Contact search algorithms find the contact position of the bodies. After detection - at the end of the time step - the resulting penetration is corrected to avoid any overlaps. Contact forces then act between the affected surfaces.

The basics for classic contact mechanical theories can be taken from Johnson[1]. The presented mechanical description of the contact and its numerical implementation is based on the work of Wriggers[2], Erhart[3] and Konyukhov et al.[4].

[1] K. L. Johnson. *Contact mechanics*. eng. 9. print. OCLC: 250004367. Cambridge: Cambridge Univ. Press, 2003. ISBN: 9780521347969

[2] P. Wriggers. *Computational Contact Mechanics*. Berlin, Heidelberg: Springer Berlin Heidelberg, 2006. DOI: 10.1007/978-3-540-32609-0

[3] T. Erhart. *Strategien zur numerischen Modellierung transienter Impaktvorgänge bei nichtlinearem Materialverhalten: Zugl.: Stuttgart, Univ., Diss., 2004*. Vol. Nr. 44. Bericht / Institut für Baustatik der Universität Stuttgart. Stuttgart: Inst. für Baustatik, 2004. ISBN: 3000154434

[4] A. Konyukhov and R. Izi. *Introduction to computational contact mechanics: a geometrical approach*. Wiley series in computational mechanics. Chichester, West Sussex: Wiley, 2015. ISBN: 9781118770641

4.1 KINEMATICS, CONTACT INTERFACE AND STRESSES

In order to develop a framework for the implementation of contact in the simulation, the kinematics in the area of contact - the contact boundary - are stated. For the description, Fig. 4.1 shows two exemplary bodies, called master and slave, in the current configuration that approach, and, afterwards, touch each other. Their possible contact boundary, $\phi^M(\Gamma_C^M)$ and $\phi^S(\Gamma_C^S)$ for the master and slave body, respectively, are considered together with $\phi(\Gamma_C)$. There, Γ is used for surfaces represented in the reference configuration and $\phi^M(\Gamma)$ in current configuration. The contact boundary is added to the existing

conditions to describe the boundaries of the body with

$$\phi(\Gamma) = \phi(\Gamma_u) \cup \phi(\Gamma_\infty) \cup \phi(\Gamma_C) \quad . \tag{4.1}$$

$\phi(\Gamma_u)$ and $\phi(\Gamma_\sigma)$ are the Dirichlet and Neumann boundary, respectively, cp. Eq 1.15. To find the position of the closest neighbour of a

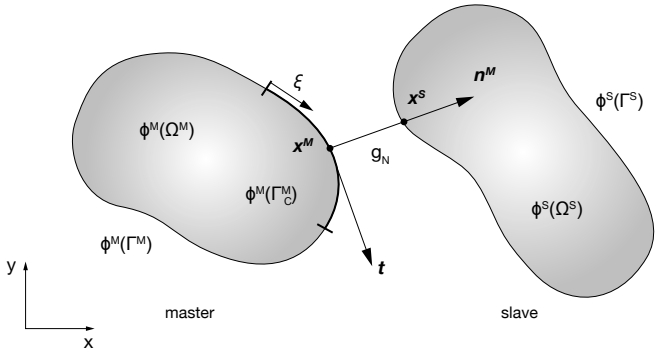

Figure 4.1: The kinematics of two approaching bodies. By finding the shortest distance, the contact in $\boldsymbol{x}^{\mathbf{M}}$ and $\boldsymbol{x}^{\mathbf{S}}$ on the master and slave body, respectively, is evaluated.

node on the slave surface on the master body the shortest distance between them has to be evaluated with

$$||\boldsymbol{x}^{\mathbf{S}} - \boldsymbol{x}^{\mathbf{M}}|| = \min_{\boldsymbol{x}^{\mathbf{M}} \in \phi^{\mathrm{M}}(\Gamma_C^{\mathrm{M}})} ||\boldsymbol{x}^{\mathbf{S}} - \boldsymbol{x}^{\mathbf{M}}(\xi)|| \quad . \tag{4.2}$$

This is done for all points on the slave surface $\boldsymbol{x}^{\mathbf{S}} \in \phi^{\mathrm{S}}(\Gamma_C^{\mathrm{S}})$ with a parametrized master surface $\phi^{\mathrm{M}}(\Gamma_C^{\mathrm{M}})$. It is described by $\boldsymbol{x}^{\mathbf{M}}(\xi)$ where ξ represents the running variable along the slave surface.

After finding $\boldsymbol{x}^{\mathbf{M}}$ the penetration/distance function g_N can be defined with

$$g_N = (\boldsymbol{x}^{\mathbf{S}} - \boldsymbol{x}^{\mathbf{M}})\ \boldsymbol{n}^{\mathbf{M}} \tag{4.3}$$

where $\boldsymbol{n}^{\mathbf{M}}$ is the normal vector to the point $\boldsymbol{x}^{\mathbf{M}}$ on the master surface.

g_N can be used during the contact search algorithm (or in combination with the penalty method) defining different conditions

$$g_N = \begin{cases} > 0 & \text{no contact} \\ = 0 & \text{contact} \\ < 0 & \text{slave node is penetrating the master body} \end{cases} \tag{4.4}$$

Fig. 4.2 shows a graphical representation of these conditions. Furthermore, it describes the non-penetration condition - the kinematic constraint needed for solving contact problems - with

$$g_N \geq 0 \quad . \tag{4.5}$$

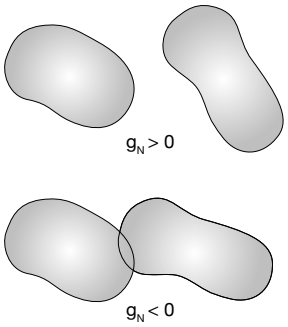

Figure 4.2: A graphical representation of penetration showing the penetration/distance function g_N.

Similar to the penetration function for normal contact, for tangential contact the relative movement of the touching bodies can be used. There, the length of the sliding distance g_T of the slave point $\boldsymbol{x}^{\mathbf{S}}$ on the master surface is calculated with

$$g_T = \int_{\xi_0}^{\xi_e} || \boldsymbol{t} ||\, \mathrm{d}\xi \tag{4.6}$$

where $\boldsymbol{t}$ is the tangential vector on the master surface at the point in contact, ξ_0 and ξ_e describe the path of the slave point $x^{\mathbf{S}}$ on the master surface, i.e. in parametrized form. For describing the tangential contact, the kinematic conditions are often described in terms of velocities. In absence of interpenetration the tangential velocity $\dot{g}_{\mathbf{T}}$ is equivalent to the slip rate $\gamma_{\mathbf{T}}$ with

$$\dot{g}_{\mathbf{T}} = \gamma_{\mathbf{T}} = v^{\mathbf{M}} - v^{\mathbf{S}} \tag{4.7}$$

where $v^{\mathbf{M}}$ and $v^{\mathbf{S}}$ are the velocities of the master and slave surface points in contact. $v^{\mathbf{M}} - v^{\mathbf{S}}$ illustrates the relative tangential velocity.

Normal contact and pressure

As a result of the contact of the two bodies contact stresses, contact pressure and tangential stresses occur on the contact interface. In this thesis, a hard contact formulation is used, which means no use of constitutive equations in the contact zone. With the geometrical non-penetration constraint, the contact pressure part follows directly from the contact stresses. There, we differentiate the following cases

$$\begin{aligned} p_{\mathrm{N}} = 0 \quad \text{for } g_{\mathrm{N}} < 0 \quad \text{no contact} \\ g_{\mathrm{N}} = 0 \quad \text{for } p_{\mathrm{N}} > 0 \quad \text{contact} \end{aligned} \tag{4.8}$$

where p_{N} is the contact pressure. A graphical representation of this formulation is shown in Fig. 4.3. Here, a similar formulation as the KKT conditions in incremental plasticity can be used

$$g_{\mathrm{N}} \geq 0 \quad , \quad p_{\mathrm{N}} \leq 0 \quad \text{and} \quad p_{\mathrm{N}}\, g_{\mathrm{N}} = 0. \tag{4.9}$$

the so-called Hertz-Signorini-Moreau conditions.

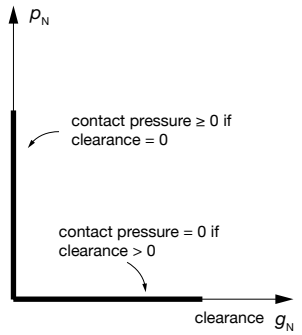

Figure 4.3: A graphical representation of the hard contact formulation used in this thesis.

Tangential contact and stresses

Similar to normal contact pressures during normal contact, tangential stresses occur when the wheel is rolling on the rail or crossing nose. Tangential stresses significantly influence the state of stress inside the component, the resulting (plastic) deformation and the tribological behavior.

A frequently used constitutive equation that is also used in this thesis is the law of Coloumb. It seperates sticking and slipping by limiting the tangential stresses and forces, see Fig. 4.4.

This limit depends on the occurring contact pressures or forces. The tangential stresses $\boldsymbol{t}_{\mathbf{T}}$ can then be described with

$$\boldsymbol{t}_{\mathbf{T}} = -\mu\, |p_{\mathrm{N}}|\, \frac{\dot{\boldsymbol{g}}_{\mathbf{T}}}{||\dot{\boldsymbol{g}}_{\mathbf{T}}||} \quad \text{if} \quad ||\boldsymbol{t}_{\mathbf{T}}|| > \mu p_{\mathrm{N}} \tag{4.10}$$

where μ is the friction coefficient - a coefficient that depends on the material pairing.

To describe an advanced tangential behavior, the friction coefficient can also be a function of different variables, such as an equivalent slip rate $\dot{\gamma}_{\mathrm{eq}}$, the contact pressures p_{N} or the temperature Θ.

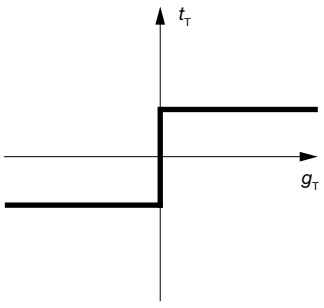

Figure 4.4: A graphical representation of Coloumb's friction law

4.2 IMPLEMENTATION - FORMULATIONS AND ENFORCEMENT

For the implementation of contact in finite element simulations, different formulations and numerical methods are needed. There, the discretization of the body into elements requires a special treatment of the contact kinematics and contact conditions, cp. Eq. 4.8 to Eq. 4.10. This includes contact discretization formulations and enforcement methods. Common formulations for the discretization of the contact include

- NTS: Node-To-Surface (3D) or Node-To-Segment (2D) and
- STS: Surface-To-Surface (3D) or Segment-To-Segment (2D).

When using the traditional node-to-surface (NTS) method, single nodes of the slave surface (called node-based surface) interact with a point of projection of the master surface. There, penetration of a slave node into the master surface is restricted but penetration of master nodes into the slave surface may occur. Surface-to-surface (STS) contact considers both surfaces and minimizes the penetration. This is done by including adjacent slave nodes. In Fig. 4.5, both types of discretization and the involved nodes are shown in 2D.

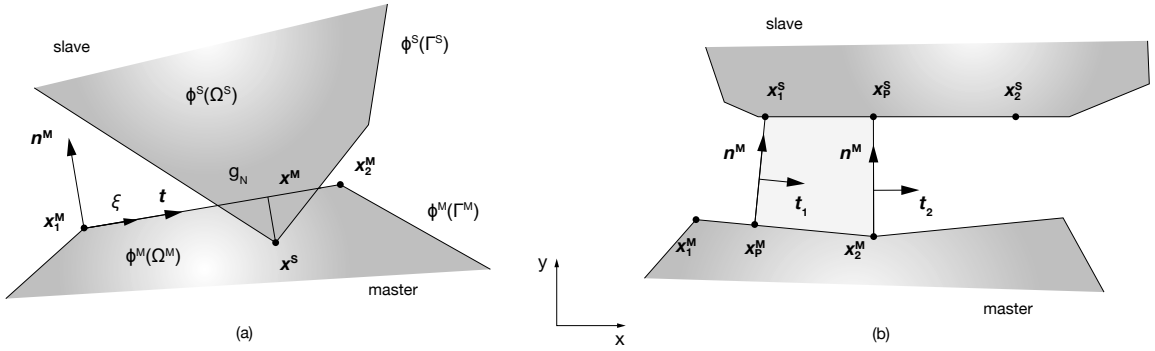

Figure 4.5: Two discretization methods: (a) Node-To-Surface (NTS) and (b) Surface-To-Surface (STS). Both methods are represented in 2D.

The kinematic relations of the NTS discretization in Fig. 4.5a can be taken from Section 4.1, see Fig. 4.1: $\boldsymbol{x}_1^{\mathbf{M}}$ and $\boldsymbol{x}_2^{\mathbf{M}}$ represent nodes on the master surface and $\boldsymbol{x}^{\mathbf{S}}$ the node in contact on the slave surface. The vectors $\boldsymbol{n}$ and $\boldsymbol{t}$ are the normal and tangent of the master surface and ξ the variable describing the parametrization of the master surface.

Fig. 4.5b shows the segmentation of the surface for a STS contact discretization - in this case a mortar method. The grey segment represents one mortar segment that is defined by the four nodes: the nodes $\boldsymbol{x}_1^{\mathbf{M}}$ and $\boldsymbol{x}_2^{\mathbf{M}}$ of the master and slave surface, respectively, and their protections on each others surface $\boldsymbol{x}_{\mathbf{P}}^{\mathbf{S}}$ and $\boldsymbol{x}_{\mathbf{P}}^{\mathbf{M}}$. Contact constraint enforcement is then performed on this segment.

The stricter enforcement of non-penetration for surface-to-surface contact makes the calculation less susceptible to severe transition from coarse to fine mesh and results in more accurate results[5]. As surface stresses represent the occurring loads on rails and crossings a surface-to-surface discretization is chosen.

[5] *Simulia ABAQUS Documentation*. Providence, RI, USA.: Dassault Systemes

There exist different (numerical) methods for the contact enforcement in finite element simulations. We distinguish three types in this thesis:

- The penalty method
- The Lagrange multiplier method (or direct method) and
- The kinematic contact algorithm[6].

[6] An implicit corrector method referred to as kinematic contact algorithm in Simulia Abaqus/Explicit (*Simulia ABAQUS Documentation*)

The first two methods and their implementation are presented especially for static calculations. The latter one is a special method and presented for dynamic calculations using explicit methods. There, the contact is solved using an implicit method (with the Penalty or Lagrange mulitplier method) and the dynamic response of the system using an explicit method.

4.2.1 Penalty method and Lagrange multiplier method

To solve boundary value problems including contact restrictions with the finite element method, equations similar to the weak form as in Eq. 3.2 have to be evaluated. This includes the variational formulation of the contact conditions stated in Eq. 4.8 and 4.9. As seen in Eq. 3.2, the variational formulation leads to an equality. However, including the HSM constraints, cp. Eq. 4.9, the weak formulation leads to a variational inequality - a source of non-linearity even when considering small strains and linear elasticity. For the sake of simplicity, an active set strategy is chosen, which means that the contact is considered to be known: This enables us to write the weak form as equality and update the principle of virtual work, cp. Eq. 3.2, for both bodies and include the involved contact interface with

$$\sum_{i=1}^{2}(\delta W^{i}_{kin} + \delta W^{i}_{int} - \delta W^{i}_{ext}) + \delta W_{con} = 0 \qquad . \tag{4.11}$$

δW_{con} represents the additional term due to contact, all the other terms are considered for all bodies in contact ($N = 2$). For the penalty method δW_{con} becomes

$$\delta W^{P}_{con} = \int_{\Gamma_C} \epsilon_N \, g_N \, \delta g_N + \epsilon_T \, \boldsymbol{g_T} \, \delta \boldsymbol{g_T} \, \mathrm{d}A \tag{4.12}$$

where ϵ_N and ϵ_T are penalty parameters for the normal and tangential contact with $\epsilon_N, \epsilon_T > 0$. They represent stiffnesses that allow the bodies to penetrate each other. High values for ϵ_N and ϵ_T minimize the possible penetration but lead to an ill-conditioned numerical problem. During slip, the term $\epsilon_T \, g_T$ in Eq. 4.12 becomes $\boldsymbol{t_T}$ according to Eq. 4.10. Using the penalty method to solve the contact problems allows minor penetration but does not add any degree of freedom to the set of equations.

Another common method is the Lagrange multiplier method. There, Lagrange multipliers λ are added to the equation to fulfill

the contact constraints as additional degree of freedom with

$$\delta W_{\text{con}}^{\text{L}} = \int_{\Gamma_{\text{C}}} \lambda_{\text{N}}\, \delta g_{\text{N}} + \boldsymbol{\lambda_{\text{T}}}\, \delta \boldsymbol{g_{\text{T}}}\, \mathrm{d}A + \underbrace{\int_{\Gamma_{\text{C}}} \delta\lambda_{\text{N}}\, g_{\text{N}} + \delta\boldsymbol{\lambda_{\text{T}}}\, \boldsymbol{g_{\text{T}}}\, \mathrm{d}A}_{\text{enforcement of constraints}} \quad (4.13)$$

where λ_{N} and λ_{T} represent the Lagrange multipliers. The equation is divided into the virtual work of the normal and tangential penetration functions and the enforcement of the constraints. In case of pure slip, the term $\boldsymbol{\lambda_{\text{T}}}$ is known and replaced by $\boldsymbol{t_{\text{T}}}$.

For the implementation in the used finite element method, the above mentioned principles have to be discretized. For the penalty method, this is done for the gap function g_{N}, the tangential counterpart $\boldsymbol{g_{\text{T}}}$ and their variations δg_{N} and $\delta \boldsymbol{g_{\text{T}}}$. For simplicity, only normal contact is considered here. The discretization of δg_{N} is shown using a surface discritization via shape functions (similar to Eq. 3.4-3.6) with

$$g_{\text{N}}^{\text{e}} = \boldsymbol{N}(\boldsymbol{\xi})\ \boldsymbol{g_{\text{N}}} \quad (4.14)$$

where $\boldsymbol{g_{\text{N}}}$ are the nodal values of the gap functions. The gap functions at the contact zone can be related to the nodal displacements $\boldsymbol{v_{\text{e}}}$ - depending on the discretization (e.g. node-to surface, surface-to-surface). Therefore, after integration of the penalty contact contribution, see Eq. 4.12, we define the following relation for the gap functions using the vector $\boldsymbol{C_{\text{e}}}$ with

$$g_{\text{N}}^{\text{e}} = \boldsymbol{C_{\text{e}}}\ \boldsymbol{v_{\text{e}}} \quad (4.15)$$

for each contact element. This is done for every element associated to contact constraints and summarized into a matrix $\boldsymbol{C}$. With this matrix the contact contributions can be assembled to the global finite element system of equations. Eq. 4.11 then becomes

$$\delta \boldsymbol{v}\ (\boldsymbol{f}_{\text{int}}(\boldsymbol{v}) - \boldsymbol{f}_{\text{ext}} + \epsilon_{\text{N}} \boldsymbol{C}\ \boldsymbol{C}^{\text{T}}\ \boldsymbol{v}) = 0 \quad (4.16)$$

where $\epsilon_{\text{N}} \boldsymbol{C}\boldsymbol{C}^{\text{T}}\boldsymbol{v}$ is the contribution due to penalty contact, see Eq. 4.12.

For the Lagrange multiplier method - additionally to the gap function g_{N} and $\boldsymbol{g_{\text{T}}}$ and their variations - the Lagrange multipliers ($\boldsymbol{\lambda_{\text{T}}}$ and λ_{N}) and their variations have to be discretized. In analogy to the penalty method, normal contact only is considered here and the gap functions are combined in the global constraint matrix $\boldsymbol{C}$. Due to the additional degrees of freedom - the Lagrange multipliers $\boldsymbol{\lambda}$ - updating Eq. 4.11 by considering Eq. 4.13 leads to

$$\begin{aligned} \delta \boldsymbol{v}\ (\boldsymbol{f}_{\text{int}}(\boldsymbol{v}) - \boldsymbol{f}_{\text{ext}} + \boldsymbol{C}\ \boldsymbol{\lambda}) &= 0 \\ \delta \boldsymbol{\lambda} (\boldsymbol{C}\ \boldsymbol{v}) &= 0 \end{aligned} \quad . \quad (4.17)$$

This system of equations includes the contact constraints. To evaluate the correct constraints before, the contacting elements have to be found by using search algorithms. Then, using update algorithms, the arising contact stresses are calculated iteratively to enforce equilibrium and constraint conditions.

4.2.2 *Kinematic contact algorithm*

The kinematic contact algorithm is a special method used for explicit simulations, as already explained in the introduction section. There, contact is not considered at the beginning. After checking for penetrations, contact is considered by "correcting" the nodal displacements at the interfaces implicitly. The following principle is introduced by Kane et al.[7].

[7] C. Kane et al. "Finite element analysis of nonsmooth contact". In: *Computer Methods in Applied Mechanics and Engineering* 180.1 (1999), pp. 1–26. ISSN: 0045-7825. DOI: 10.1016/S0045-7825(99)00034-1

For this algorithm, Eq. 3.13 is updated to

$$\boldsymbol{M}\ddot{\boldsymbol{v}}(t) = \boldsymbol{f}_{\mathbf{ext}}(t) - \boldsymbol{f}_{\mathbf{int}}(v,t) - \boldsymbol{f}_{\mathbf{con}}(t) \quad . \tag{4.18}$$

where $\boldsymbol{f}_{\mathrm{con}}$ represent additional forces (corrector forces) due to the contact between the bodies. To seperate the contact from the dynamic simulation, the acceleration $\ddot{\boldsymbol{v}}$ is decomposed with

$$\ddot{\boldsymbol{v}}(t) = \ddot{\boldsymbol{v}}_{\mathbf{int}}(t) + \ddot{\boldsymbol{v}}_{\mathbf{con}}(t) \quad . \tag{4.19}$$

There, $\ddot{\boldsymbol{v}}_{\mathbf{int}}$ represents the internal part and $\ddot{\boldsymbol{v}}_{\mathbf{con}}$ the external part due to the contact. They are defined with

$$\ddot{\boldsymbol{v}}_{\mathbf{int}}(t) = \boldsymbol{M}^{-1}(\boldsymbol{f}_{\mathbf{ext}}(t) - \boldsymbol{f}_{\mathbf{int}}(t)) \quad \text{and} \quad \ddot{\boldsymbol{v}}_{\mathbf{con}}(t) = \boldsymbol{M}^{-1}\boldsymbol{f}_{\mathbf{con}}(t) \tag{4.20}$$

where the internal acceleration $\ddot{\boldsymbol{v}}_{\mathbf{int}}$ is calculated from the balance of external and internal forces, cp. Eq. 3.27, and the contact acceleration $\ddot{\boldsymbol{v}}_{\mathbf{con}}$ from the contact forces. The equations of motions for the explicit method using the MEM, cp. Eq. 3.25 and 3.26 in Section 3.2 are then updated to

$$\dot{\boldsymbol{v}}^{\mathbf{n+1}} = \dot{\boldsymbol{v}}^{\mathbf{n}} + \boldsymbol{\Delta t}\ \ddot{\boldsymbol{v}}^{\mathbf{n}}_{\mathbf{int}} + \boldsymbol{\Delta t}\ \ddot{\boldsymbol{v}}^{\mathbf{n+1}}_{\mathbf{con}} \tag{4.21}$$

$$\boldsymbol{v}^{\mathbf{n+1}} = \boldsymbol{v}^{\mathbf{n}} + \Delta t\ \dot{\boldsymbol{v}}^{\mathbf{n}} + \Delta t^2\ \ddot{\boldsymbol{v}}^{\mathbf{n}}_{\mathbf{int}} + \Delta t^2\ \ddot{\boldsymbol{v}}^{\mathbf{n+1}}_{\mathbf{con}} \tag{4.22}$$

where $\dot{\boldsymbol{v}}^{\mathbf{n+1}}$ represents the velocity of the next time step and $\boldsymbol{v}^{\mathbf{n+1}}$ the displacements. In comparison to the standard approach, the velocities $\Delta t\ \ddot{\boldsymbol{v}}^{\mathbf{n+1}}_{\mathbf{con}}$ and displacements $\Delta t^2\ \ddot{\boldsymbol{v}}^{\mathbf{n+1}}_{\mathbf{con}}$ due to contact are added. The algorithm first calculates the velocities and displacements without any additional part due to contact. The resulting penetrations are then corrected by calculating the contact forces $\boldsymbol{f}_{\mathbf{con}}$ and from them, their accelerations $\ddot{\boldsymbol{v}}^{\mathbf{n+1}}_{\mathbf{con}}$. This is denoted by using the current accelerations with index $n+1$ for their calculations. The forces are evaluated using implicit methods, such as the Lagrange multiplier method, as stated in the previous section.

4.2.3 *Calculation of contact stresses and forces*

The calculation of the contact stresses depends on the contact formulation and constraint enforcement method. The discretization within the finite element method usually reduces the mechanical equations stated in Eq. 4.12-4.15 to specific points (or nodes) for each element. This is then the position where the Penalty method or Lagrange multiplier method enforces the contact constraints. Due to the integration in Eq. 4.12 and Eq. 4.13, the nodal contact pressures become nodal

contact forces. In case of the penalty method, the contact pressures are calculated by multiplying the penalty stiffnesses ϵ with the displacements (or gap functions). For the Lagrange multiplier method, the contact pressures can be read directly from the Lagrange multipliers λ.

Often contact pressures for each element are calculated a posteriori by dividing the contact forces by the area of the contact element: in case of 3D surface-to-surface contact this is the surface area of the element. Usually one value for contact pressures can be evaluated per element. The resulting contact pressures[8] are then constant for the surface of the element. The contact pressures mentioned in the attached papers are calculated using a similar principle.

By adding up the nodal contact forces, the overall contact forces for the whole system can be calculated. These forces give a good indication of a systems reaction to the arising dynamics. They are of special interest in this thesis, as the transition of a wheel from the wing rail to the crossing nose is a dynamic process. There, the movement of the wheel represents an impact on the crossing nose. The reaction due to the impact can be described very well by the resulting contact forces[9]. During the impact of the wheel the contact forces increase significantly and decrease slowly afterwards.

[8] In the attached papers contact pressures are calculated and called contact pressures p. In the commercial FE software these pressures are denoted as *CPRESS*.

[9] Similar to the contact pressures we present these forces as contact forces F in the attached papers. Furthermore, we evaluated its maxima around the impact position on the crossing nose referred to as $F_{\max}$

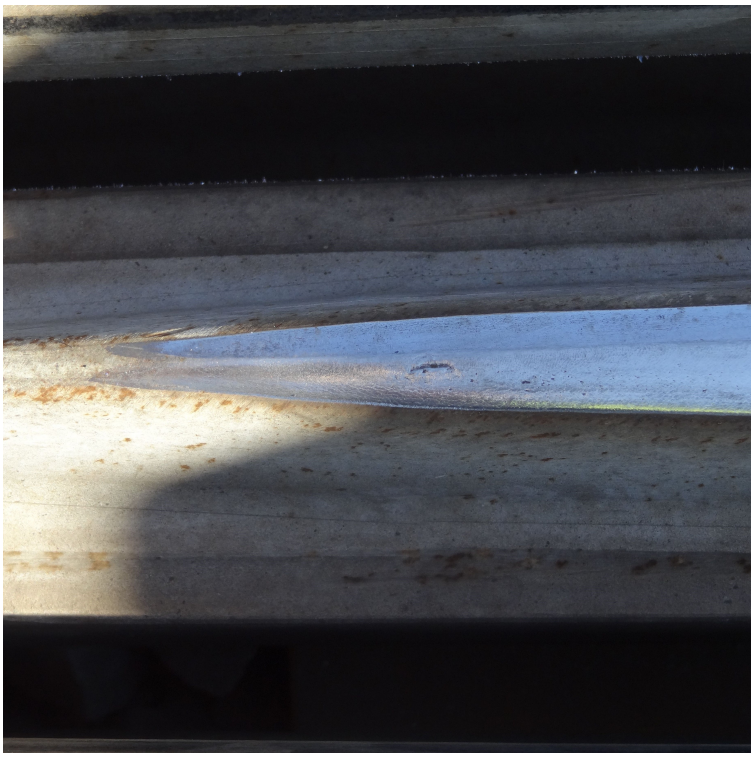

Figure VI: A damaged crossing nose

With permission of the photographer.

5

Damage

Turnouts and especially crossing noses suffer damage similar as in rails, which are caused by the load of the rolling stock. Due to the contact of the wheel and rail, the force is transmitted through a small contact area. As a result high contact stresses arise that are the reason for various types of damage. Because of the geometrical restrictions of crossings – especially fixed crossings – more severe loading situations occur: higher contact pressures and an increase of slip. This causes tighter service intervals and shorter service lives in comparison to rails.

Mechanisms and Defects Typical damage mechanisms in crossings (and rails) include plastic deformation, wear and fatigue – mechanisms that occur together and interact with each other. Fatigue-related defects, however, are very common and are classified as rolling contact fatigue (RCF) defects. There, due to cyclic loading, damage is localized, which can lead to crack initiation, propagation and failure of the component. Typical defects that belong to this group (according to UIC) include head-checking, spalling, shelling and squats. Fig. 5.1a and b show typical head-checks and squats on rails, respectively. Although their appearance in-track is different, they may be related and arise due to the cyclic loading. Furthermore, both of them have the presence of cracks in common.

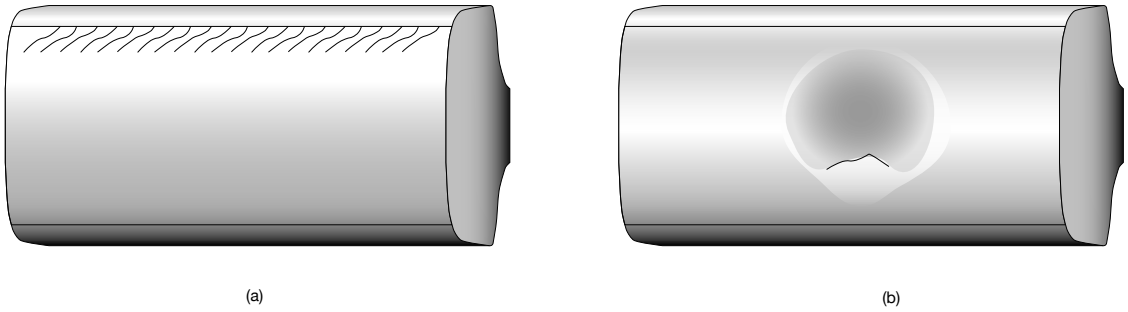

Figure 5.1: Typical rail damage due to RCF: (a) head-checks and (b) squats.

Squats Due to their lack of predictability, squats differ from other rail defects: cracks may also play a role in their initiation, but unlike

head-checks, their occurrence is not regular and cannot be predicted easily. While preventive maintenance can be planned for head checks, this is not possible for squats. Furthermore, to avoid any safety issues, major maintenance measures have to be put in action quickly.

Predicting Fatigue To predict fatigue damage for rails and crossings, different methods are used. One of the first approaches has been introduced by Johnson and is called shakedown method or map[1], see Fig. 5.2a. There, using Hertz's hypothesis, a normalized vertical load (or contact stresses) and the traction coefficient of the contacting partners describe the material response. The estimation includes four types of behavior: elastic, elastic and plastic shakedown and ratcheting. Material properties, such as the yield stress, then define their limits. If the shakedown limit is exceeded, RCF cracks may initiate.

[1] A. Bower and K. Johnson. "Plastic flow and shakedown of the rail surface in repeated wheel-rail contact". In: *Wear* 144.1 (1991), pp. 1–18. ISSN: 0043-1648. DOI: https://doi.org/10.1016/0043-1648(91)90003-D

Another approach is proposed by Burstow and is called RCF crack initiation model[2], see Fig. 5.2b. It uses the $T-\gamma$ number, the product of the tangential forces and the slip in the contact area and is often referred to as $T-\gamma$ model. This number represents an energy, initially used for the prediciton of wear. Therefore, it is often referred to as wear number. An index for RCF damage is then calculated by combining $T-\gamma$ with a non-linear damage function. The damage function divides the probability of RCF damage into three different areas: Very low $T-\gamma$ values represent insufficient energy for the RCF initiation, very high $T-\gamma$ values result in wear instead. The area in between represents a transition with increasing and – after reaching a maximum – decreasing probabilty for RCF initiation.

[2] M. Burstow. "Whole Life Rail Model Application and Development for RSSB - Development of an RCF Damage Parameter". In: *Rail Safety and Standards Board report* AEATR-ES-2003-832 Issue 1 (2003)

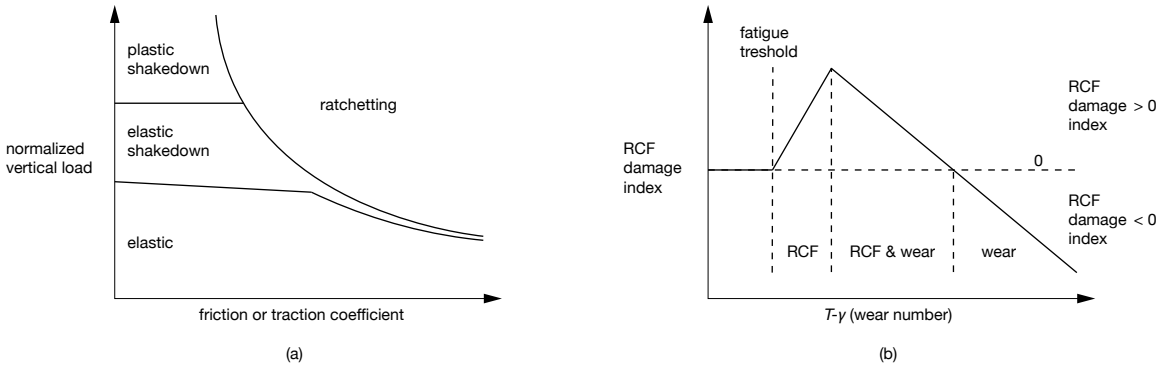

Figure 5.2: Simple approaches for the prediction of fatigue: (a) the shakedown map of Johnson's shakedown method shows four different material behaviors: elastic, elastic and plastic shakedown and ratcheting. (b) Burstow's RCF initiation model states the probability for RCF damage initiation (RCF damage index) using $T-\gamma$ values.

Both methods are simple to use because they require little input, but they do not consider the current stresses in the body or the deformed material (i.e. hardening or plastic deformation).

For a more detailed prediction of fatigue lifes, approaches that belong to the group of stress-life methods (S-N curves) or crack growth method can be used. They both rely on stresses and deformations in the body and on a detailed material description by intensive material testing.

S-N methods use S-N curves that are often generated for uniaxial

or simple multiaxial loading. Therefore, a criterion has to be defined for more complex loading situations.

Crack growth methods assume initial cracks that tend to grow after reaching a treshold value due to cyclic loading. A common equation that gives the rate of crack growth as a function of the stresses near the crack tip is defined by Paris and referred to as Paris' law[3]. After considering a critical crack length, the number of cycles until failure can be evaluated.

[3] P. Paris and F. Erdogan. "A Critical Analysis of Crack Propagation Laws". In: *Journal of Basic Engineering* 85.4 (1963), p. 528. DOI: 10.1115/1.3656900. URL: https://doi.org/10.1115/1.3656900

Fatigue criterion To calculate the tendency of different crossing materials to damage based on their fatigue strength, a criterion of the group of stress-life methods is used. The high cycle fatigue criterion by K.D. Van uses shear stresses and hydrostatic stresses in the body and fatigue limits evaluated with shear-torsion and tension-compression testing. For the calculation of the criterion the resulting stresses during the cyclic impact of the wheel on the crossing nose are used. Parts of the following description can be found in a similar way in the attached papers – Paper B[4] and Paper C[5].

[4] J. Wiedorn et al. "Numerical assessment of materials used in railway crossings by predicting damage initiation - Validation and application". In: *Wear* 414-415 (2018), pp. 136–150. ISSN: 0043-1648. DOI: https://doi.org/10.1016/j.wear.2018.08.011

[5] J. Wiedorn et al. "Finite element model for predicting the initiation of subsurface damage in railway crossings - A parametric study". In: *Proceedings of the Institution of Mechanical Engineers, Part F: Journal of Rail and Rapid Transit* 233.6 (2019), pp. 614–628. DOI: 10.1177/0954409718797039

5.1 FATIGUE CRITERION - THEORY

K.D Van's multiaxial fatigue criterion[6] for the high cycle regime is used to consider the nucleation of fatigue cracks. The macroscopic phenomenon of fatigue crack initiation is considered at critical zones of stress concentration.

[6] K. Dang Van and B. Griveau. "On a New Multiaxial Fatigue Limit Criterion: Theory and Application: EGF3". In: *Mechanical Engineering Publications*, pp. 476–496

The criterion uses local stresses - as calculated in the simulation - based on the macroscopic stress cycle. This is done by using the local loading path of microscopic stresses in the stabilized state (after elastic shakedown) over the entire duration of loading. The assumptions include that cracks usually occur in intragranular slip bands inside a macro-volume.

Two material parameters that are evaluated experimentally by bending and torsion experiments are needed to consider the multiaxiality in the criterion. The equivalent stresses $\tau_{eq,dv}$ are calculated in every cycle as

$$\tau_{eq,dv} = \tau_a(t) + \alpha_{dv}\sigma_h(t) \tag{5.1}$$

with the shear stress amplitude τ_a, the hydrostatic stress σ_h, the current time t during one loading cycle and the Dang-Van material parameter α_{dv}, which is calculated using

$$\alpha_{dv} = \frac{\tau_f - \frac{\sigma_f}{2}}{\frac{\sigma_f}{3}} \tag{5.2}$$

with τ_f and σ_f standing for the shear-torsion and tension-compression fatigue limits, respectively. Damage is predicted if

$$\tau_{eq,dv} > \tau_f \quad . \tag{5.3}$$

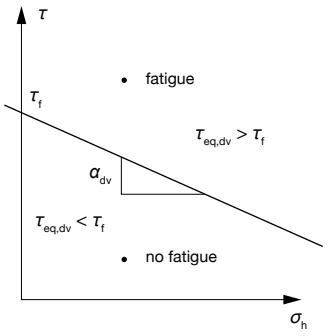

Figure 5.3: Graphical representation of the Dang-Van damage criterion. α_{dv} and τ_f are DV material parameters.

Figure 5.3 shows a graphical representation of the threshold limit of the Dang-Van damage criterion. The fatigue limit is represented

by the solid line, cp. Eq. 5.1 and Eq. 5.3. If the equivalent stress $\tau_{eq,dv}$ of a state of stress - defined by the shear stress amplitude τ_a and hydrostatic stresses σ_h - is above this limit ($\tau_{eq,dv} > \tau_f$), fatigue damage is expected.

Damage parameter

To compare loading cycles we transform the equation and introduce the Dang-Van (DV) damage variable P_{dv}[7] with

$$P_{dv} = \max_{0 \le t \le T} \frac{\tau_a(t)}{\tau_f - \alpha_{dv}\sigma_h(t)} \quad . \tag{5.4}$$

where T is the total time period for one impact cycle ($t \in T$). A P_{dv} value above 1 indicates damage initiation and a P_{dv} value below 1 indicates no damage initiation. In the DV damage model τ_f represents the critical shear stress at a hydrostatic stress $\sigma_h(t)$ of 0 and α_{dv} multiplied by the current hydrostatic stresses σ_h its shift ($\tau_{eq,dv}$).

The criterion calculates damage using shear stress amplitudes. Therefore, a median stress $\boldsymbol{\sigma_{mid}}$ has to be found. This is accomplished by using an optimization algorithm with the objective function

$$\min \max ||\sigma_{ij,d}(t) - \sigma_{ij,mid,d}|| \tag{5.5}$$

where $||.||$ is the Mises norm; the subscript d indicates deviatoric stresses. For the equation the Einstein summation over repeated indices is used. The routine minimizes the largest von Mises stress occurring during the total time period T. For a validation, we took stresses from Bernasconi et al.[8] and calculated a difference of less than 1% when comparing $||\boldsymbol{\sigma_{mid}}||$ to the one evaluated in the paper. The stress amplitude $\boldsymbol{\sigma_{a,d}}(t)$ at any time t is then defined as

$$\boldsymbol{\sigma_{a,d}}(t) = \boldsymbol{\sigma_d}(t) - \boldsymbol{\sigma_{mid,d}} \quad . \tag{5.6}$$

On this basis, the shear stress amplitude can be obtained with

$$\tau_a(t) = \frac{1}{2}\max(|\sigma_{1,a}(t) - \sigma_{2,a}(t)|, |\sigma_{1,a}(t) - \sigma_{3,a}(t)|, |\sigma_{2,a}(t) - \sigma_{3,a}(t)|) \tag{5.7}$$

where $\sigma_{1,a}$, $\sigma_{2,a}$ and $\sigma_{3,a}$ are the first, second and third principal stresses of the stress amplitude tensor $\boldsymbol{\sigma_a}$.

5.2 SOLUTION METHODS AND IMPLEMENTATION

The above mentioned principle is implemented as part of the post-processing. The stresses are taken from the results of the FE simulation. The calculation of $\boldsymbol{\tau_a}(t)$, P_{dv} and the optimization routine is performed in Wolfram Mathematica©[9]. The mid stresses σ_{mid} are evaluated by solving Eq. 5.5.

Optimization routine The optimization routine uses a differential evolution method[10] of the group of direct search methods. In comparison to gradient-based methods, these methods do not process

[7] The Dang-Van damage variable P_{dv} and its maximum per (impact) cycle $P_{dv,max}$ is calculated in the attached papers.

[8] A. Bernasconi and I. V. Papadopoulos. "Efficiency of algorithms for shear stress amplitude calculation in critical plane class fatigue criteria". In: *Computational Materials Science* 34.4 (2005), pp. 355–368. ISSN: 09270256. DOI: 10.1016/j.commatsci.2005.01.005

[9] *Mathematica Documentation*. Champaign, IL, USA.: Wolfram Research

[10] R. Storn. "On the usage of differential evolution for function optimization". In: *1996 Biennial Conference of the North American Fuzzy Information Processing Society, NAFIPS*. ed. by M. H. Smith. Piscataway, N.J.: Institute of Electrical and Electronics Engineers, 2002, 1996, pp. 519–523. ISBN: 0-7803-3225-3. DOI: 10.1109/NAFIPS.1996.534789

derivative information. Therefore, they converge more slowly but are more robust and tolerant to the presence of noise. The differential evolution method uses an adaptive search procedure based on candidate solutions. In each iteration step, randomly chosen candidates are combined to generate a new solution. The inadequate solutions are then discarded and the procedure is repeated until a termination criterion is met.[11] Because of this simple principle, the differential evolution method is one of the faster methods using the evolution strategy and known to be robust. Fig. 5.4 shows the mutation scheme in a 2D parametric space. The old parameters are represented as vectors, i.e. $\boldsymbol{X}_\mathbf{p}^\mathbf{1}$, $\boldsymbol{X}_\mathbf{p}^\mathbf{2}$ and $\boldsymbol{X}_\mathbf{p}^\mathbf{3}$ and the function is expressed as contour lines on its 2D parameter space.

[11] The principle is similar to the one of biological evolution where the natural selection works according to the survival of the fittest principle. The recombination of solutions can then be seen as mutations.

The optimum - in this case a minimum - is reached in the middle of the circles. The three randomly sampled parameter vectors are then combined using an additional scaling factor F to create a new perturbed vector, which - if the resulting vector is closer to the optimum - becomes a new parameter vector $\boldsymbol{V}^\mathbf{1}$. This pertubation is performed randomly for all parameters.

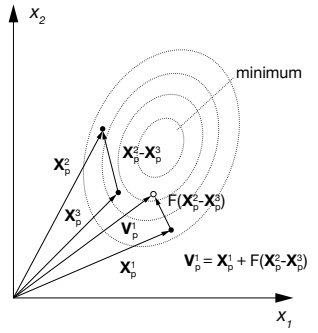

Figure 5.4: Graphical representation of the mutation scheme of a Differential Evolution method.

The FE implementation

Eq. 5.5 is then solved with this routine for a chosen number of elements around the position of interest (impact position for wheel impact on the crossing) of the finite element simulation results. We choose a sufficiently high number of time steps for each time period T, where the stresses are obtained, to get accurate results for the stress amplitude $\sigma_{\mathbf{a,d}}(t)$ and thus P_{dv}.

A sketch of the evaluation routine for the damage initiation value P_{dv} is presented in Figure 5.5a to c. Fig. 5.5a shows a discretized

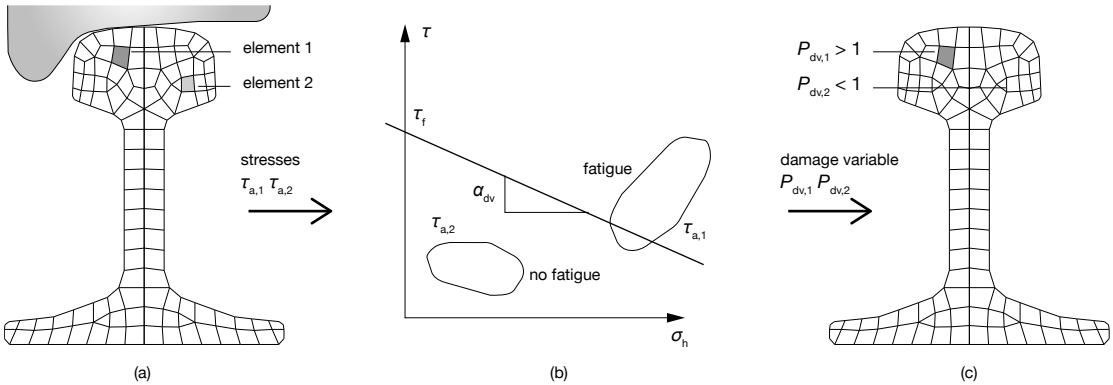

Figure 5.5: The evaluation routine for the DV damage criterion. For several elements the stress cycles are used for calculating the damage initiation value P_{dv} using the DV parameters α_{dv} and τ_{f}.

rail in contact with a wheel. The rail is loaded by the wheel: Two positions in the rail (element 1 and element 2) are chosen at a specific time t_{j} during the contact of the wheel. The dark colored element closer to the surface represents a more severe state of stress than the lower element. The stresses of both elements are evaluated at every $t \in T$. In this thesis the stress distribution due to the impact of a wheel on the crossing nose is taken. As described above, we then calculate the mid stress for those positions to evaluate the shear stress

amplitude $\tau_a(t)$ (see equation 5.7).

Fig. 5.5b shows the hydrostatic stresses $\sigma_h(t)$ and shear stress amplitudes $\tau_a(t)$ for all $t \in T$ (one loading cycle), see $\tau_{a,1}$ and $\tau_{a,2}$ for position 1 and 2, respectively. The solid line represents an exemplary damage locus of the Dang-Van criterion defined by α_{dv} and σ_f. Shear stresses that are above the damage locus indicate damage initiation. With equation 5.4, the DV damage variable P_{dv} is then calculated – as the maximum offset of the stress amplitude to the Dang-Van damage locus, see the solid line in Fig. 5.5b. Therefore, the stress cycle of element 1 indicates fatigue, whereas no fatigue is observed at position 2.

Fig. 5.5c shows the discretized rail and the chosen elements. Instead of stresses, see Fig. 5.5a, the colored elements represent the calculated DV damage variable P_{dv} when fatigue damage is calculated. As the stress cycle of element 1 indicates fatigue damage, the calculated damage variable $P_{dv,1}$ is higher than 1 (represented by the colored element). For element 2, however, no fatigue is calculated ($P_{dv,2} < 1$). The routine is repeated for every element in the chosen evaluation area.

Bibliography

Andersson, C. and Abrahamsson, T. "Simulation of Interaction Between a Train in General Motion and a Track". In: *Vehicle System Dynamics* 38.6 (2002), pp. 433–455. ISSN: 0042-3114. DOI: 10.1076/vesd.38.6.433.8345.

Bathe, K.-J. and Zimmermann, P. *Finite-Elemente-Methoden*. ger. 2., vollst. neu bearb. und erw. Aufl. OCLC: 51700169. Berlin: Springer, 2002. ISBN: 9783540668060.

Bernasconi, A. and Papadopoulos, I. V. "Efficiency of algorithms for shear stress amplitude calculation in critical plane class fatigue criteria". In: *Computational Materials Science* 34.4 (2005), pp. 355–368. ISSN: 09270256. DOI: 10.1016/j.commatsci.2005.01.005.

Bertram, A. and Krawietz, A. "On the introduction of thermoplasticity". In: *Acta Mechanica* 223.10 (2012), pp. 2257–2268. ISSN: 0001-5970. DOI: 10.1007/s00707-012-0700-6.

Bouaziz, O. et al. "High manganese austenitic twinning induced plasticity steels: A review of the microstructure properties relationships". In: *Current Opinion in Solid State and Materials Science* 15.4 (2011), pp. 141–168. ISSN: 13590286. DOI: 10.1016/j.cossms.2011.04.002.

Bower, A. and Johnson, K. "Plastic flow and shakedown of the rail surface in repeated wheel-rail contact". In: *Wear* 144.1 (1991), pp. 1–18. ISSN: 0043-1648. DOI: https://doi.org/10.1016/0043-1648(91)90003-D.

Broyden, C. G. "The Convergence of a Class of Double-rank Minimization Algorithms 1. General Considerations". In: *IMA Journal of Applied Mathematics* 6.1 (1970), pp. 76–90. ISSN: 0272-4960. DOI: 10.1093/imamat/6.1.76.

Burstow, M. "Whole Life Rail Model Application and Development for RSSB - Development of an RCF Damage Parameter". In: *Rail Safety and Standards Board report* AEATR-ES-2003-832 Issue 1 (2003).

Chaboche, J.-L. "A review of some plasticity and viscoplasticity constitutive theories". en. In: *International Journal of Plasticity* 24.10 (Oct. 2008), pp. 1642–1693. ISSN: 07496419. DOI: 10.1016/j.ijplas.2008.03.009.

Chaboche, J.-L. "Constitutive equations for cyclic plasticity and cyclic viscoplasticity". en. In: *International Journal of Plasticity* 5.3 (Jan. 1989), pp. 247–302. ISSN: 07496419. DOI: 10.1016/0749-6419(89)90015-6.

Chen, L. et al. "Some aspects of high manganese twinning-induced plasticity (TWIP) steel, a review". In: *Acta Metallurgica Sinica (English Letters)* 26.1 (2013), pp. 1–15. ISSN: 1006-7191. DOI: 10.1007/s40195-012-0501-x.

Chen, W.-F. and Han, D.-J. *Plasticity for structural engineers*. Ft. Lauderdale, FL: J. Ross Publ, 2007. ISBN: 9781932159752.

Ciavarella, M. et al. "On the Dang Van fatigue limit in rolling contact fatigue". In: *International Journal of Fatigue* 28.8 (2006), pp. 852–863. ISSN: 01421123. DOI: 10.1016/j.ijfatigue.2005.11.002.

Courant, R. et al. "Über die partiellen Differenzengleichungen der mathematischen Physik". In: *Mathematische Annalen* 100.1 (1928), pp. 32–74. DOI: 10.1007/BF01448839.

Dang Van, K. and Griveau, B. "On a New Multiaxial Fatigue Limit Criterion: Theory and Application: EGF3". In: *Mechanical Engineering Publications*, pp. 476–496.

Dang Van, K. and Maitournam, M. H. "On some recent trends in modelling of contact fatigue and wear in rail". In: *Wear* 253.1-2 (2002), pp. 219–227. ISSN: 0043-1648. DOI: 10.1016/S0043-1648(02)00104-7.

Dang Van, K. et al. "Elastoplastic analysis of repeated moving contact application to railways damage phenomena". In: *Wear* 196.1-2 (1996), pp. 77–81. ISSN: 0043-1648. DOI: 10.1016/0043-1648(95)06864-3.

Desimone, H. et al. "On the application of Dang Van criterion to rolling contact fatigue". In: *Wear* 260.4-5 (2006), pp. 567–572. ISSN: 0043-1648. DOI: 10.1016/j.wear.2005.03.007.

Drucker, D. "A definition of a stable inelastic material". In: *ASME Journal of Applied Mechanics* 26 (1959), pp. 101–195.

Duff, I. S. et al. *Direct Methods for Sparse Matrices*. Oxford University Press, 2017. ISBN: 9780198508380. DOI: 10.1093/acprof:oso/9780198508380.001.0001.

Ekberg, A. and Paulsson, B. *Innotrack: Deliverable 1.4.8 Overall Cost Reduction*. Innotrack, 2009. URL: www.innotrack.eu.

Ekberg, A. et al. "An engineering model for prediction of rolling contact fatigue of railway wheels". In: *Fatigue & Fracture of Engineering Materials and Structures* 25.10 (2002), pp. 899–909. ISSN: 8756-758X. DOI: 10.1046/j.1460-2695.2002.00535.x.

Ekberg, A. et al. "Wheel/rail rolling contact fatigue – Probe, predict, prevent". In: *Wear* 314.1-2 (2014), pp. 2–12. ISSN: 0043-1648. DOI: 10.1016/j.wear.2013.12.004.

Erhart, T. *Strategien zur numerischen Modellierung transienter Impaktvorgänge bei nichtlinearem Materialverhalten: Zugl.: Stuttgart, Univ., Diss., 2004*. Vol. Nr. 44. Bericht / Institut für Baustatik der Universität Stuttgart. Stuttgart: Inst. für Baustatik, 2004. ISBN: 3000154434.

G. Thomas Mase, Ronald E. Smelser, George E. Mase. *Continuum Mechanics for Engineers, Third Edition*. CRC Press, 2009. ISBN: 9781420085396. DOI: 10.1201/9781420085396.

Hahn, G. D. "A modified Euler method for dynamic analyses". In: *International Journal for Numerical Methods in Engineering* 32.5 (1991), pp. 943–955. ISSN: 0029-5981. DOI: 10.1002/nme.1620320502.

Hill, R. "A general theory of uniqueness and stability in elastic-plastic solids". In: *Journal of the Mechanics and Physics of Solids* 6.3 (1958), pp. 236–249. ISSN: 00225096. DOI: 10.1016/0022-5096(58)90029-2.

Holzapfel, G. A. *Nonlinear solid mechanics: A continuum approach for engineering*. Repr. Chichester: Wiley, 2010. ISBN: 9780471823193.

Huebner, K. H. *The finite element method for engineers*. 4. ed. New York, NY: Wiley, 2001. ISBN: 0471370789.

Johansson, A. et al. "Simulation of wheel-rail contact and damage in switches & crossings". In: *Wear* 271.1-2 (2011), pp. 472–481. ISSN: 0043-1648. DOI: 10.1016/j.wear.2010.10.014.

Johnson, K. L. *Contact mechanics*. eng. 9. print. OCLC: 250004367. Cambridge: Cambridge Univ. Press, 2003. ISBN: 9780521347969.

Kane, C. et al. "Finite element analysis of nonsmooth contact". In: *Computer Methods in Applied Mechanics and Engineering* 180.1 (1999), pp. 1–26. ISSN: 0045-7825. DOI: 10.1016/S0045-7825(99)00034-1.

Karush, W. "Minima of Functions of Several Variables with Inequalities as Side Constraints". PhD thesis. Chicago, Illinois: University of Chicago, 1939.

Kassa, E. et al. *DESTination RAIL: Deliverable 1.3. Presentation on Monitoring Switches and Crossings (turnouts) and tracks*. DESTination RAIL, 2009. URL: www.http://www.destinationrail.eu/.

Kassa, E. et al. "Simulation of dynamic interaction between train and railway turnout". In: *Vehicle System Dynamics* 44.3 (2006), pp. 247–258. ISSN: 0042-3114. DOI: 10.1080/00423110500233487.

Konyukhov, A. and Izi, R. *Introduction to computational contact mechanics: a geometrical approach*. Wiley series in computational mechanics. Chichester, West Sussex: Wiley, 2015. ISBN: 9781118770641.

Kuhn, H. W. and Tucker, A. W. "Nonlinear Programming". In: *Proceedings of the Second Berkeley Symposium on Mathematical Statistics and Probability*. Berkeley, Calif.: University of California Press, 1951, pp. 481–492.

Ma, Y. et al. "Modelling and experimental validation of dynamic impact in 1:9 railway crossing panel". In: *Tribology International* 118 (2018), pp. 208–226. ISSN: 0301679X. DOI: 10.1016/j.triboint.2017.09.036.

Mathematica Documentation. Champaign, IL, USA.: Wolfram Research.

Ossberger, U. et al. "Validation of a finite element crossing model using measurements at an instrumented turnout". In: *Proceedings of the 23rd Symposium on Dynamics of Vehicles on Roads and Tracks*. Qingdao, China, 2013.

Paris, P. and Erdogan, F. "A Critical Analysis of Crack Propagation Laws". In: *Journal of Basic Engineering* 85.4 (1963), p. 528. DOI: 10.1115/1.3656900. URL: https://doi.org/10.1115/1.3656900.

Pletz, M. et al. "A wheel set/crossing model regarding impact, sliding and deformation - Explicit finite element approach". In: *Wear* 294-295 (2012), pp. 446–456. ISSN: 0043-1648. DOI: 10.1016/j.wear.2012.07.033.

Pletz, M. et al. "Rolling contact fatigue of three crossing nose materials - Multiscale FE approach". In: *Wear* 314.1-2 (2014), pp. 69–77. ISSN: 0043-1648. DOI: 10.1016/j.wear.2013.11.013.

Simo J.C. and Hughes T. J. R. *Computational Inelasticity*. Vol. 7. New York: Springer-Verlag, 1998. ISBN: 0-387-97520-9. DOI: 10.1007/b98904.

Simulia ABAQUS Documentation. Providence, RI, USA.: Dassault Systemes.

Souza Neto, E. A. de et al. *Computational methods for plasticity: Theory and applications*. Chichester: John Wiley & Sons, 2008. ISBN: 9780470694527. DOI: 10.1002/9780470694626.

Storn, R. "On the usage of differential evolution for function optimization". In: *1996 Biennial Conference of the North American Fuzzy Information Processing Society, NAFIPS*. Ed. by M. H. Smith. Piscataway, N.J.: Institute of Electrical and Electronics Engineers, 2002, 1996, pp. 519–523. ISBN: 0-7803-3225-3. DOI: 10.1109/NAFIPS.1996.534789.

Tweedale, G. et al. "Sir Robert Abbott Hadfield F. R. S. (1858-1940) and the dicovery of manganese steel". In: *Notes and Records of the Royal Society of London* 40.1 (1985), pp. 63–74. ISSN: 1743-0178. DOI: 10.1098/rsnr.1985.0004.

Wiedorn, J. et al. "Finite element model for predicting the initiation of subsurface damage in railway crossings - A parametric study". In: *Proceedings of the Institution of Mechanical Engineers, Part F: Journal of Rail and Rapid Transit* 233.6 (2019), pp. 614–628. DOI: 10.1177/0954409718797039.

Wiedorn, J. et al. "Investigation of deformation mechanisms in manganese steel crossings using FE models". In: *Tribology International* 138 (2019), pp. 424–434. ISSN: 0301-679X. DOI: https://doi.org/10.1016/j.triboint.2019.06.016. URL: http://www.sciencedirect.com/science/article/pii/S0301679X19303305.

Wiedorn, J. et al. "Numerical assessment of materials used in railway crossings by predicting damage initiation - Validation and application". In: *Wear* 414-415 (2018), pp. 136–150. ISSN: 0043-1648. DOI: https://doi.org/10.1016/j.wear.2018.08.011.

Wiedorn, J. et al. "Simplified explicit finite element model for the impact of a wheel on a crossing - Validation and parameter study". In: *Tribology International* 111 (2017), pp. 254–264. ISSN: 0301-679X. DOI: https://doi.org/10.1016/j.triboint.2017.03.023.

Wiedorn, J. et al. "Using Stress-based Damage Models to Describe Subsurface Damage in Crossings". In: *Proceedings of 11th International Heavy Haul Association Conference*. International Heavy Haul Association, Cape Town, South Africa, 2017.

Wiedorn, J. et al. "A Simplified Dynamic Finite Element Model for the Impact of a Wheel on a Crossing: Validation and Parameter Study". In: *Proceedings of the Third International Conference on Railway Technology: Research, Development and Maintenance*. Ed. by J. Pombo. Civil-Comp Press, Stirlingshire, UK, 2016. DOI: 10.4203/ccp.110.116.

Wiest, M. et al. "Deformation and damage of a crossing nose due to wheel passages". In: *Wear* 265.9-10 (2008), pp. 1431–1438. ISSN: 0043-1648. DOI: 10.1016/j.wear.2008.01.033.

Wriggers, P. *Computational Contact Mechanics*. Berlin, Heidelberg: Springer Berlin Heidelberg, 2006. DOI: 10.1007/978-3-540-32609-0.

Wriggers, P. *Nonlinear Finite Element Methods*. Berlin, Heidelberg: Springer Berlin Heidelberg, 2008. DOI: 10.1007/978-3-540-71001-1.

Xin, L. et al. "Numerical analysis of the dynamic interaction between wheel set and turnout crossing using the explicit finite element method". In: *Vehicle System Dynamics* 54.3 (2016), pp. 301–327. ISSN: 0042-3114. DOI: 10.1080/00423114.2015.1136424.

Yan, W. et al. "Numerical Analysis of the Cyclic Response of a Crossing Component in a Switch". In: *Proceedings of the XIXth Verformungskundliches Kolloquium*. Montanuniversität Leoben, Austria, 2000, pp. 78–83.

Zhang, F. C. et al. "Explosion hardening of Hadfield steel crossing". In: *Wear* 26.2 (2010), pp. 223–229. ISSN: 0043-1648. DOI: 10.1179/174328408X363263.

Zhang, F. et al. "Microstructure and Properties of Purity High Mn Steel Crossing Explosion Hardened". In: *ISIJ International* 48.12 (2008), pp. 1766–1770. ISSN: 0915-1559. DOI: 10.2355/isijinternational.48.1766.

Part II

Papers

Paper A

Simplified explicit finite element model for the impact of a wheel on a crossing - Validation and parameter study

AUTHORS

Julian Wiedorn[1], Werner Daves, Uwe Ossberger, Heinz Ossberger, Martin Pletz

[1] **corresponding author**

JOURNAL

Published in Tribology International (ISSN: 0301-679X).

ABSTRACT

An explicit finite element (FE) model for the impact of a wheel on the crossing nose of a rigid crossing with simplified model geometry is introduced. It can calculate the dynamic forces as well as the elastic/plastic stress and strain fields in the crossing nose. The model is based on impact angles and rail head radii that are automatically extracted from measured wheel and crossing geometries. Results of this model with elastic material behavior are compared to results of FE models with realistic crossing geometry and a scheme for checking the applicability of the simplified model is presented. The model thus provides a fast, automated and validated method to calculate dynamic forces and stress-based damage indicators for crossings.

CONTRIBUTION

Responsible for the development of the method.
Carried out the numerical simulations.
Wrote most parts of the paper.

Tribology International 111 (2017) 254–264

Contents lists available at ScienceDirect

Tribology International

journal homepage: www.elsevier.com/locate/triboint

Simplified explicit finite element model for the impact of a wheel on a crossing – Validation and parameter study

Julian Wiedorn[a,*], Werner Daves[a], Uwe Ossberger[b], Heinz Ossberger[b], Martin Pletz[c]

[a] Materials Center Leoben Forschung GmbH, Leoben, Austria
[b] Voestalpine VAE GmbH, Zeltweg, Austria
[c] Department of Polymer Engineering and Science, Montanuniversitaet Leoben, Austria

ABSTRACT

An explicit finite element (FE) model for the impact of a wheel on the crossing nose of a rigid crossing with simplified model geometry is introduced. It can calculate the dynamic forces as well as the elastic/plastic stress and strain fields in the crossing nose. The model is based on impact angles and rail head radii that are automatically extracted from measured wheel and crossing geometries. Results of this model with elastic material behaviour are compared to results of FE models with realistic crossing geometry and a scheme for checking the applicability of the simplified model is presented. The model thus provides a fast, automated and validated method to calculate dynamic forces and stress-based damage indicators for crossings.

1. Introduction

Railway switches are an important part of railway structure as they ensure a guided transition from one track to another. Fixed crossings, as shown in Fig. 1, feature a discontinuity on the rail – they have to provide a transition of the wheel from one rail to another without any moving parts. The transition of the wheel from the wing rail to the crossing nose (or vice versa) occurs with a vertical movement (down- and upwards), which causes an impact with increased contact forces and stresses. It is thus a challenge to design crossings with long service life, as the transition is influenced by the crossing and wheel geometry, the passing direction, the crossing support and load parameters such as the train velocity and the axle load. In the regions of the transition, some slip between the wheel and the rail part occurs, which can also contribute to damage in the crossing [1]. Due to geometric restrictions of rigid crossings, the crossing nose has a small head radius at its tip, where high contact forces cause very high contact pressures, i.e. in case of worn wheels [2].

The dynamic process of the wheel during this transition is characterized by the contact radii and the vertical wheel movement along the running direction. Fig. 1b shows the vertical displacement of the wheel as it runs over a crossing. For the facing move (the wheel impacts on the crossing nose), the wheel lowers its position (red line) until it reaches the crossing nose, where it is forced to move upwards (black line). This changes the direction of the wheel velocity and causes an impact of the wheel on the crossing nose. The change of velocity direction can be described by an impact angle α_{Impact}. The impact angle, the contact radius of wing rail and crossing nose can be evaluated according to the geometry of the wheel and the crossing. However, the calculation of the arising forces and pressures is more complicated. Common methods for calculating this impact and associated loads are multi body system (MBS) simulations and dynamic finite element (FE) methods.

The MBS method provides a fast tool to analyse complex dynamical systems by dividing them into rigid bodies, springs and dashpots. With an extension, even beams and more complex mechanical structures can be used. Such crossing models can represent a whole train and some hundred meters of track. A MBS model for the loading of turnouts was developed by Kassa et al. [3]. With additional tools, the local loads such as contact pressure and stresses can be calculated [4,5]. In Refs. [6] and [7], wear and damage were predicted by combining MBS models and FE tools. In these models, obtained stress/strain fields and plastic deformation have to be transferred from MBS to a FE model, introducing possible errors and the need for validation.

Explicit FE models incorporate the entire dynamic process and the full stress/strain fields and they are able to model plastic deformations and the contact between different parts. The calculation time, however, is considerably higher than for MBS models, which limits the size of the modelled region. Yan et al. [8] first modelled the crossing's loading using an explicit FE model with simplified geometry. Wiest et al. [9] studied cyclic plastic deformation with a similar model which predicted fatigue and wear and incorporated plastic material behaviour (kine-

* Corresponding author.
E-mail address: Julian.wiedorn@mcl.at (J. Wiedorn).

http://dx.doi.org/10.1016/j.triboint.2017.03.023
Received 20 January 2017; Received in revised form 14 March 2017; Accepted 16 March 2017
Available online 18 March 2017

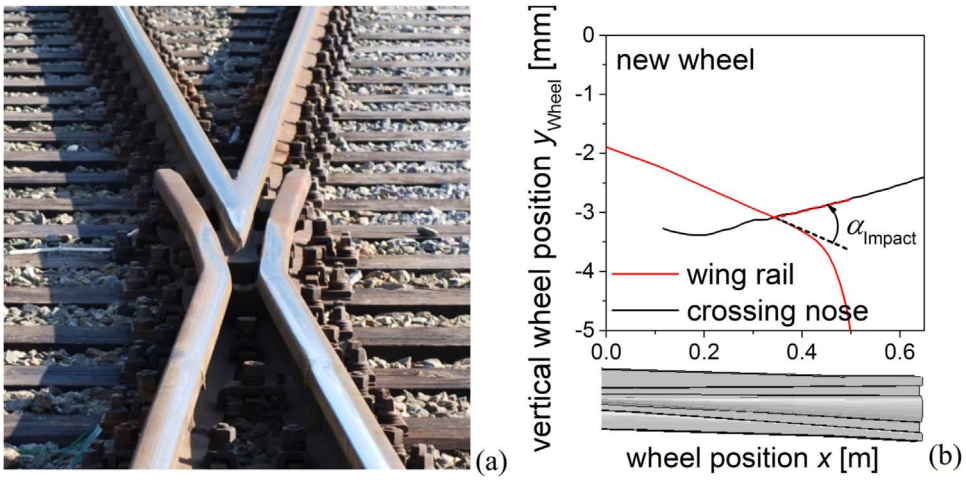

Fig. 1. (a) Typical crossing nose. (b) The vertical displacement position of a new wheel and the descriptive impact angle α_{Impact}.

matic hardening) for different crossing materials. On the basis of these models, Pletz et al. introduced a FE model with realistic crossing geometry [10]; the model was then improved and validated with track measurements in Ref. [11]. The difference between the velocity vector of the wheel on wing rail and crossing nose (impact angle α_{Impact}) was identified as a crucial parameter for the arising impact forces [12]. With a multi-scale approach, plastic cyclic deformations and crack driving forces were calculated in Ref. [13]. These models showed the positive effect of plastic deformation on reducing the contact stress loading of crossings. An explicit FE model with realistic crossing geometry was developed and validated in terms of acceleration measurements in Ref. [14].

Although FE crossing models with realistic modelled geometry (crossing length of about 4.5 m) are able to calculate the full stress/elastic-plastic strain fields, their use is computationally limited, since one cycle requires hours of computation time and hundreds or thousands of cycles are required. It thus needs simplifications, as was done in Ref. [13]. The crossings geometry was simplified in Ref. [15] to calculate dynamic forces faster, similar to the one already introduced earlier [9], but it was able to compare its results to the FE models with realistic geometry [10].

In this work, a simplified crossing model is developed to calculate vertical contact forces and stresses more quickly and automatically. The model is similar to one proposed in Ref. [15], but assumes the wheel to be initially running on a contact spring representing the wing rail/wheel contact. The impact angle α_{Impact} and the contact radius of the wing rail and crossing nose are extracted from crossing and wheel geometry and are input for the FE model. The only other parameters are wheel mass, crossing's bedding and train speed. The results of the simplified model are compared to results of extended FE models to show its range of validity, i.e. in which cases a geometric extraction of α_{Impact} and of contact radii can be correctly used.

2. Finite element modelling

The explicit finite element model is built up using parameters extracted from the wheel/crossing geometry. These parameters are the impact angle α_{Impact} and the contact radii of wing rail (r_{wr}) and crossing nose (r_{cn}) at the position of the impact. The following sections describe how these parameters are extracted from the geometry and how the finite element model is set up.

2.1. Geometric analysis for FE model input

The input for this geometric analysis is a list of coordinates for the surface points of a wheel and crossing. These coordinates can either be extracted from CAD geometries or measured. Here, the coordinates are extracted from the geometry of an existing finite element crossing model. In the following, the calculation of the impact angle α_{Impact}, the wing rail radius r_{wr}, and the crossing nose head radius r_{cn} based on these geometries will be described.

Fig. 2 shows the geometry of wheel (unworn 1002 profile: *new wheel*) and crossing (type EW-60E1-CENTRO-500-1:12). The wheel is placed at a certain longitudinal position over the crossing and the cross-sections are extracted. Note that a certain lateral position of the wheel is assumed, e.g. determined by the check-rails in the crossing panel. In this cross-section, the vertical distance of wheel and rail can be calculated as Δd. The contact radius for the crossing nose or wing rail can also be extracted from these cross-sections. This analysis is done for a range of longitudinal wheel positions to develop Δd, r_{wr}, and r_{cn}.

To analyse the cross-sections, the point lists of the crossing surface and wheel surface are imported to Wolfram Mathematica [16], where they are linearly interpolated. The wheel, however, is defined by the outer surface of its cross-section, as shown in Fig. 2.

Fig. 3 shows typical wheel and crossing cross-sections with the lateral coordinate z and the vertical coordinate y. The points defining the wheel profiles and the points of the crossing surface are denser in regions of contact and coarser in regions where there is no contact. For each point of the wheel and frog along the z-direction, the distance in y-direction is calculated. The minimum of these differences gives the shortest distance Δd. For the lateral contact radius of the crossing nose or wing rail, a circle is fitted through the points on the surface. This circle has to touch the contact point (at the shortest distance Δd). Since the radius changes along the profile, the fitted radius depends on the number of used surface points. For this reason, a weighted fit is realized. For 10 nodes (approximately 5 mm on both sides of the

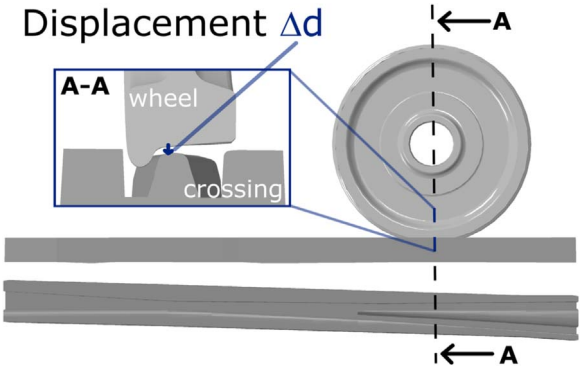

Fig. 2. Schematic routine for geometry evaluation using realistic wheel and crossing.

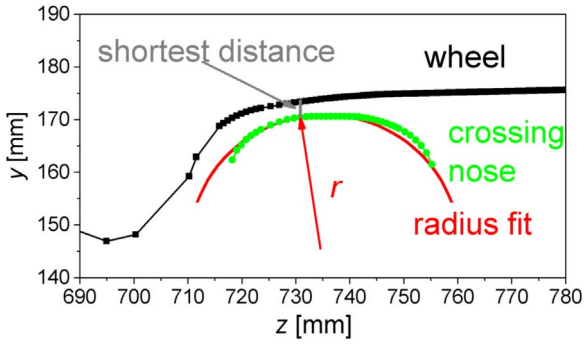

Fig. 3. A relevant cross-section - wheel (black) and crossing nose (green) - represented by their surface points. The red circle shows the interpolation of the contact radius of the crossing nose and the grey line the shortest distance between points of the wheel and the crossing nose.

contact point), the quadratic error of the radius is formulated and summed up with weighting factors: The weighting factors are defined as 1 in the central point and decrease linearly with the distance from the central point and become 0 in the outer points. This error sum is then minimized to obtain the radius.

This procedure for extracting the Δd values can be used to obtain the relative vertical position y_{wheel} of the wheel on the corresponding cross-sections of the crossing. This vertical position y_{wheel} is plotted in Fig. 4 for several positions along the longitudinal direction (wheel position x) separately for the wing rail and the crossing nose, plotted as a solid and a dashed line, respectively. Where the lines for wing rail and crossing nose intersect, the impact position x_{Impact} is calculated. The head radii of the wing rail (r_{wr}) and the crossing nose (r_{cn}) at this position are then used in the finite element model. To determine the impact angle α_{Impact}, the vertical wheel position y_{wheel} of the wing rail and the crossing nose are fitted linearly from the impact position to 20 mm before (wing rail) or after (crossing nose) the impact position. The angle between these two lines corresponds to the impact angle α_{Impact}.

2.2. Explicit finite element model

The explicit FE model now uses the parameters extracted from the measured crossing geometry to calculate dynamic forces and stress/strain fields as the wheel impacts onto the crossing. These parameters are the impact angle α_{Impact}, the crossing nose head radius r_{cn} and the head radius of the wing rail r_{wr}. The model is developed with the commercial finite element package ABAQUS/Explicit. The geometry of the model is shown in Fig. 5. As can be seen, the model uses a simplified wheel (cylindrical running surface) and a simplified crossing nose (extruded cross-section). The wheel radius in the model is set to

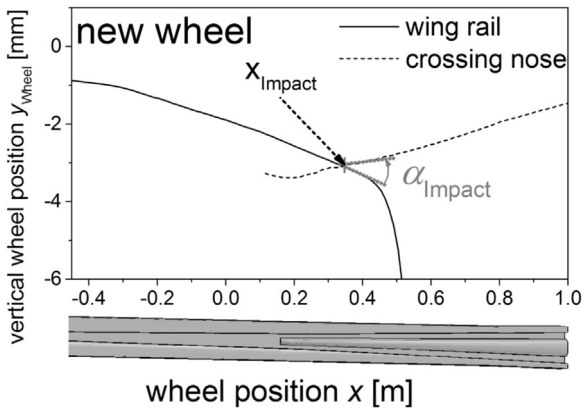

Fig. 4. The vertical wheel position y_{wheel} for the wing rail (solid line) and crossing nose (dashed line) for a new wheel.

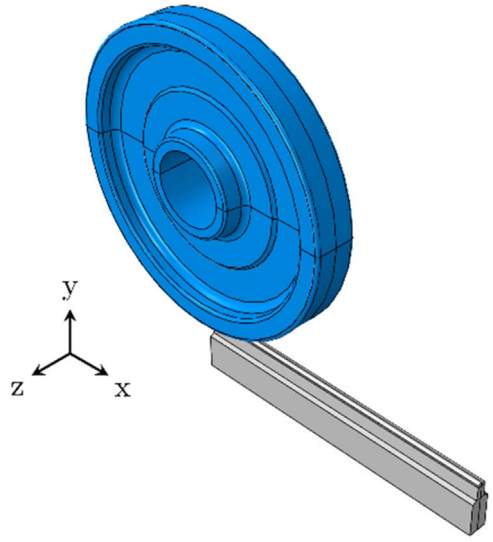

Fig. 5. Geometry of the finite element model.

0.476 m. The used geometry of the wheel rim is provided in Ref. [10]. To obtain the impact angle α_{Impact} in the model, the wheel initially runs horizontally and the crossing nose is extruded under an angle α_{Impact} to the horizontal/longitudinal direction.

In addition to the solid parts shown in Fig. 5, some springs and dashpots are used in the model. A scheme of the mechanical system is drawn in Fig. 6. A reference point is introduced at the center of the wheel, which is rigidly connected to the inner surface of the wheel rim. Loads and displacements of the wheel are applied to this reference point. Two further reference points are introduced above and below the wheel, the first for the primary suspension and the latter one for the spring mimicking the contact of wheel and the wing rail. Together with the wheel, both are forced to move at a constant velocity of either 75 km/h, 160 km/h or 250 km/h in the x-direction. A spring/dashpot support is used in this model to account for the rail pads, sleepers, ballast and ground with a spring constant k_{r} of 90 kN/mm and a dashpot constant d_{r} of 250,000 Ns/m. The lower surface of the rail and the lower end of the contact spring are both rigidly connected to this spring-dashpot support. Bending of the rail is thus constrained and has to be accounted by the bedding spring. The mass of the rail is set to be 680 kg, which corresponds with the mass used in existing FE models with realistic geometry [10]. The primary suspension of the wheel is

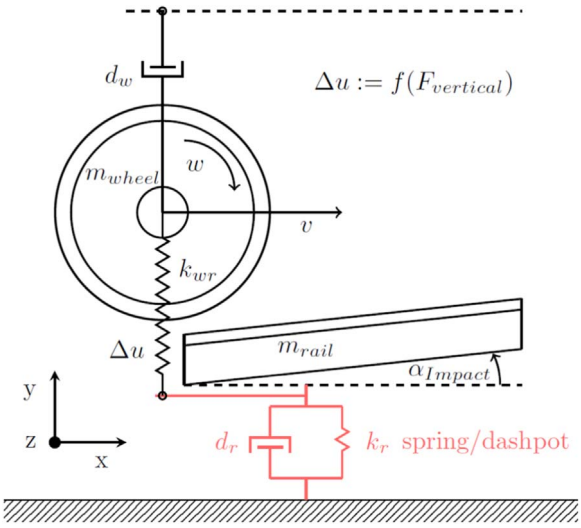

Fig. 6. Mechanical system of the finite element model. The bottom of the rail is rigidly connected to a spring/dashpot combination support (red) in the vertical direction.

Table 1
The material parameters used in the model.

Property	Wheel: elastic material	Rail: elastic material
Young's modulus [GPa]	210	190
Poisson's ratio [-]	0.3	0.3
Density [kg/m³]	7800	7800

modelled with a dashpot (dashpot constant d_w of 53 kNs/m) that connects the central point of the wheel to the upper reference point as in Ref. [10]. The total mass of the wheel is set to 1025 kg.

Wheel and crossing are modelled with linear elastic material behaviour. The elastic parameters of wheel and crossing are given in Table 1. Plastic deformations are not accounted for in the model.

To account for the contact of the wheel to the wing rail before it impacts onto the crossing nose, a vertical, non-linear spring representing the wing rail (see Fig. 6.) is introduced. If compressed, it produces a force according to Hertz formulas and in tension it produces a force of 0. The wheel initially runs on this spring, which is released as the impact onto the crossing nose leads to an upward movement of the wheel. The displacement w of this nonlinear spring is defined by simplifying the static Hertz formulas for two crossed cylinders [2,17]:

$$w = 1.31\left[1-\left(\frac{R_W - R_{WR}}{R_W + R_{WR}}\right)^2\right]^{0.23}\sqrt{\frac{F_C^2}{R_V}\left(\frac{1-\mu_c^2}{E_V}\right)^2}, \quad (1)$$

with $R_v = 2\frac{R_W R_{WR}}{R_W + R_{WR}}$ and $E_v = 2\frac{E_W E_{WR}}{E_W + E_{WR}}$ for $R_w \leq R_{WR}$, where R_W and R_{WR} are the radii of the wheel, respectively the wing rail, F_C is the normal contact force, μ_c the Poisson's ratio and E_W and E_{WR} the Young's modulus. This force/displacement function depends on wheel and wing rail radius. While the wheel radius is assumed to be constant, the wing rail radius depends on the longitudinal wheel position. For simplicity, a constant radius of the wing rail at the position of the impact is taken for the calculations.

The Hertz formulas can also be used to show the influence of using a cylindrical running surface for the wheel. As can be seen in Fig. 3, the wheel also has a contact radius in the lateral direction. For the position of the impact, these radii are evaluated as 0.15 m, 0.31 m and 0.36 m for the new, worn and hollow wheel, respectively. The corresponding head radius values of the crossing nose shown in Table 3. We can now show the differences in the maximum contact pressures p_0, the lateral half contact length a_0 and the longitudinal half contact length b_0 between the cylindrical running surface and the actual contact radii. For that, we use a normal load of 80 kN and elastic material properties given in Table 1 for both contact partners. We then calculate the error we get by using the cylindrical running surface as for (p_0, a_0, b_0) as (+7%, −1%, +8.4%), (+2.5%, −1%, +3%) and (+4%,−1%, +5%) for the new, worn and hollow wheel, respectively. This shows that the geometric simplification of the model overestimate the contact pressures by up to 7%, underestimates the lateral contact length by about 1% and overestimates the longitudinal contact length by up to 8.4% for the typical load cases.

The crossing nose geometry is based on the standard design of EN 13674-1:60E1 rails. It is mainly described by the head radius r, which is extracted from the wheel/crossing geometry. Fig. 7 shows geometries and cross-sections with head radii r of 100 mm (Fig. 7b) and 30 mm (Fig. 7c). This definition results in narrower rails with smaller rail head radii, which correspond with the crossing nose geometry. The contact of the wheel and the rail surfaces is modelled by a kinematic contact algorithm using the ABAQUS option "*hard contact*". For the tangential interaction, a penalty algorithm is used. The coefficient of friction is set to 0.3, which is a typical value of dry wheel/rail friction.

The model uses eight-node brick elements with reduced integration (C3D8R). To improve the calculation time, the wheel and rail parts are subdivided and meshed independently. Fixed-motion constraints reconnect the parts with different element sizes. The surfaces in contact use elements with an edge length of 3 mm for the model calculating the impact forces [9] and 0.5 mm for calculating the contact stresses [18]. The total number of elements in the model with a crossing nose head radius r of 20 mm is thus about 130,000 (wheel: 90,000; rail: 40,000) to calculate the contact forces and about 270,000 (wheel: 120,000; rail: 150,000) for the contact stresses. The number of elements increases

Table 2
The chosen model parameters for the parametric study.

Parameter	Value
Velocity v [km/h]	75, 160, 250
Impact angle α_{Impact} [mrad]	3, 4.5, 7, 9 (validation: 5.1, 8.4, 30.5)
Crossing nose head radius r [mm]	15, 16, 20, 30, 45, 60, 100
Wing rail head radius r_{wr} [mm] (contact spring)	100

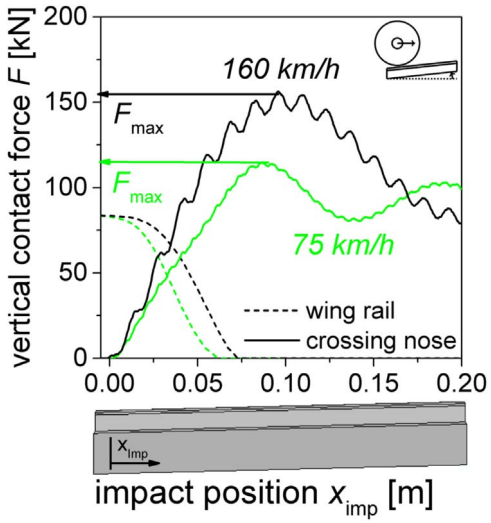

Fig. 8. Impact model results of the vertical contact forces F plotted over the wheel position for the different wheel positions. The impact angle α_{Impact} is set to 5.1 mrad and the crossing nose head radius to 20 mm. The maximum vertical contact force during the impact is referred to as the impact force F_{max}.

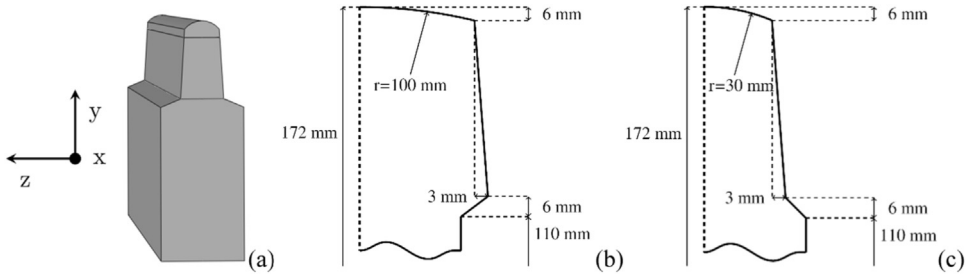

Fig. 7. Cross-sections of the rail: (a) whole geometry, (b) schematic sketch of the upper part with radius r of 100 mm and (c) schematic sketch of the upper part with radius r of 30 mm.

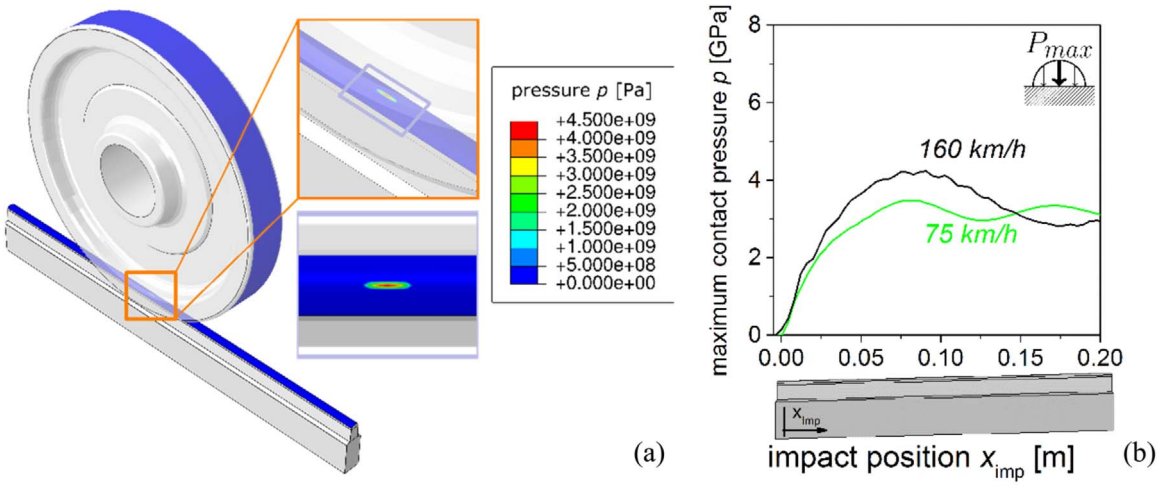

Fig. 9. Contour plot of the contact pressure p for an impact angle α_{Impact} of 5.1 mrad, train speed of 160 km/h and a crossing nose head radius of 20 mm at the time of the maximum occurring p values.

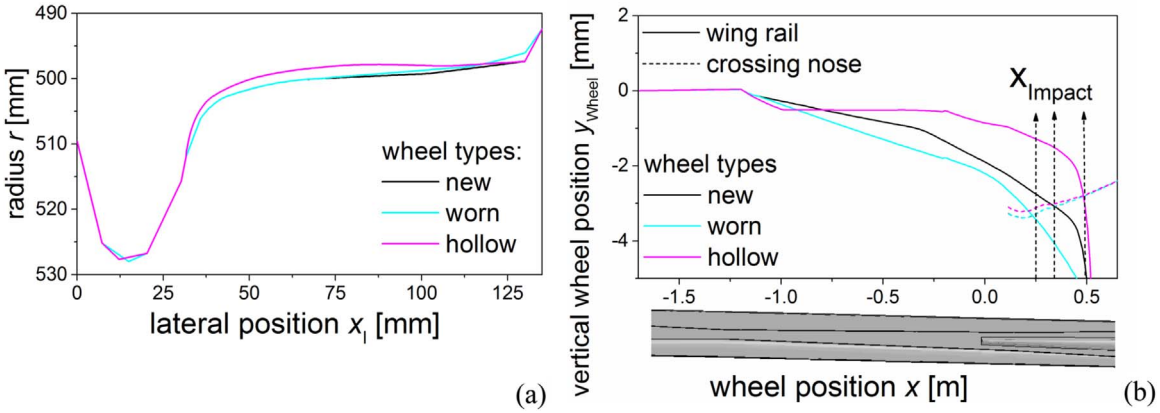

Fig. 10. a) Profiles of the three chosen wheels (new, worn and hollow) and b) the trajectories of those wheel profiles running along the wing rail and the crossing nose geometry.

Table 3
Parameters for the validation of the model.

	Wheel Type		
Parameters	**New**	**Worn**	**Hollow**
Impact angle α_{Impact} [mrad]	5.1	8.4	30.5
Head radius – crossing nose [mm]	20	16.1	30.2
Head radius – wing rail [mm]	100	72	8

with increasing head radii and impact angles.

The varied parameters and their range in the parametric study are shown in Table 2. Three velocities are studied and the impact angle α_{Impact} is varied between 3 and 9 mrad. For the crossing nose head radius, values between 15 mm and 100 mm are used. The wing rail radius, which determines the stiffness of the contact spring, is held constant at 100 mm.

3. Results and discussion

3.1. General results of the model

Fig. 8 shows the vertical contact force F and the arising maximum contact pressures calculated in the impact model for an impact angle α_{Impact} of 5.1 mrad and a crossing nose head radius of 20 mm. Results for train speeds of 75 km/h and 160 km/h are shown. The results are plotted over the longitudinal position of the wheel, called the *impact position* x_{imp}, with the origin at the position of the first contact of the wheel with the crossing nose. Previous work of the authors [10] has shown that the first impact is crucial in terms of the crossing's loading and damage, so here only the first of two or more peaks of the contact forces is considered.

In Fig. 8, for x_{imp} below 0, the wheel runs only on the wing rail with a vertical force denoted by the dashed lines. Starting at x_{imp} of 0, the vertical load is transferred to the crossing nose. Until a x_{imp} value of about 0.06 m, the wheel contacts both wing rail and crossing nose. For x_{imp} values higher than 0.06 m, the wheel runs solely on the crossing nose and a peak in the F values occurs. The F value of the first peak of this impact will be called impact force F_{max} and is drawn in Fig. 8 for train speeds v of 75 km/h and 160 km/h. The F_{max} value considerably increases with the increase of the train speed: from 115 kN to 156 kN for 75 km/h and 160 km/h, respectively.

Fig. 9a shows a contour plot of the contact pressure p between the wheel and the crossing nose for a velocity of 160 km/h and a new wheel. Note that the model uses elastic material data for wheel and rail. The axis of the contact patch has a length of 22 mm and a width of 4.1 mm. The maximum contact pressure p is 4.23 GPa in this case. The maximum p values as the wheel impacts onto the crossing nose (i.e. for different impact positions x_{imp}) are plotted in Fig. 9b for a train speed of 75 km/h and 160 km/h. Similar peaks can be seen in Fig. 8 for the p values as well as for the F values. The contact pressures reach maximum values of 3.47 GPa and 4.23 GPa for 75 km/h and 160 km/h, respectively. Note that these contact pressure values are very high and would be considerably lower when using elastic/plastic material behaviour in the model since the plastic deformation of the crossing nose would increase the size of the contact patch.

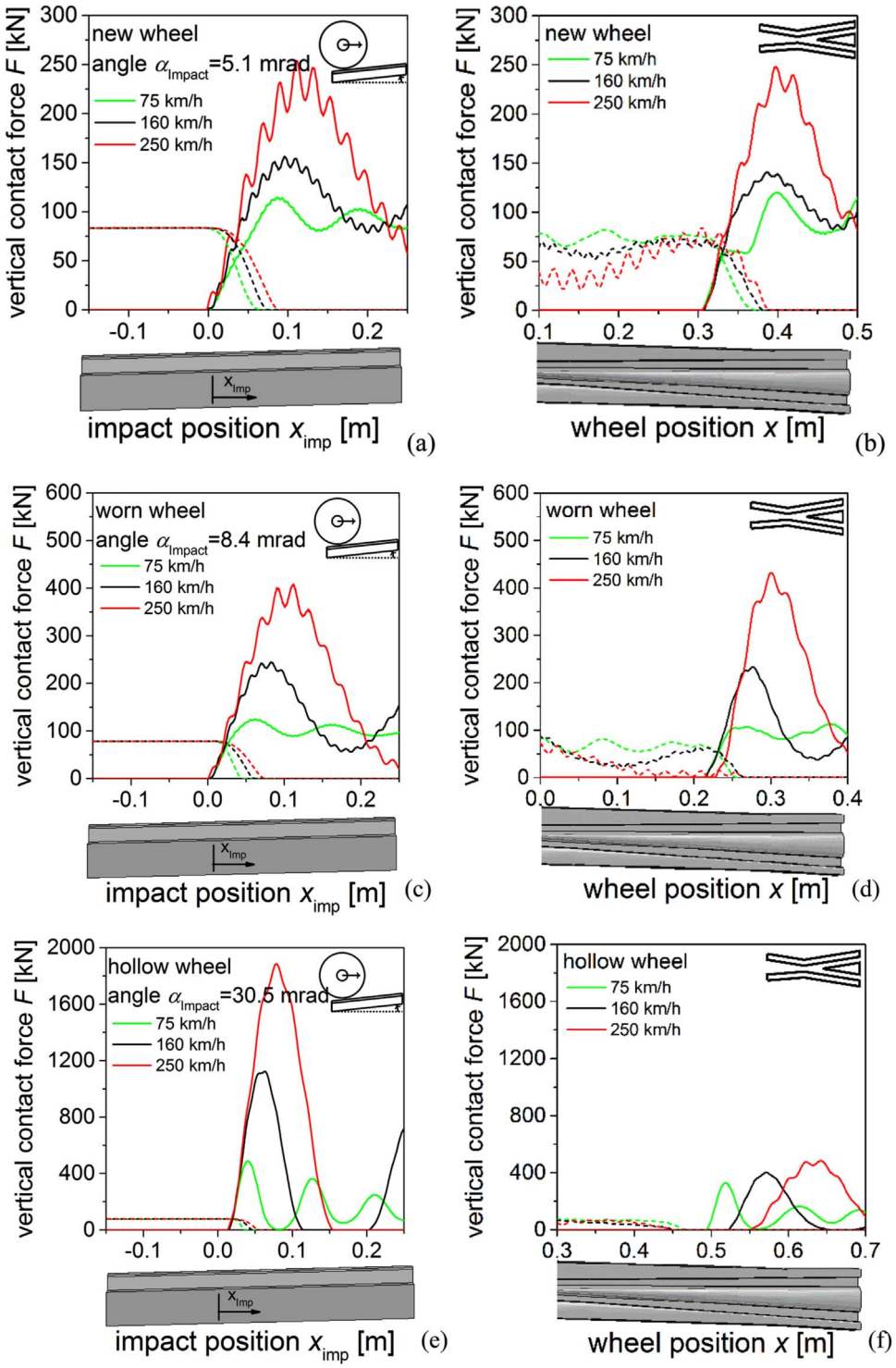

Fig. 11. The contact forces *F* as the wheel impacts onto the crossing nose with spring/dashpot support and a static load of 79.7 kN for the simplified model ((a), (c), (e)) and the model with realistic geometry ((b), (d), (f)) for a new ((a), (b)), worn ((c), (d)), and hollow ((e), (f)) wheel. The dashed lines represent forces at the wing rail and the solid lines at the crossing nose.

3.2. Model validation

To assess how well the simplified model can describe a realistic situation compared to models with realistic crossing geometry [11], which have been validated with track measurements in Refs. [10] and [11], a range of/several model parameters, e.g. impact angle and crossing nose head radius, have to be compared. Three different wheel profiles, shown in Fig. 10a, are used in the realistic and simplified model. These wheel types will be referred to as *new* wheel (initial 1002 wheel profile), *worn* wheel (wear "away" from the flange) and *hollow* worn wheel. For the simplified model, the first step is a geometrical analysis of wheel and crossing. The result of the wheel trajectories through the crossing of the three wheels is shown in Fig. 10b. The solid curves depict the trajectories of the wheel on the wing rail and the dashed the trajectories on the crossing nose. At the intersection of these curves, the impact occurs. The impact angle, wing rail radius and crossing nose radius are extracted at these locations according to the method described in Section 2.1.

Table 4
Comparison of the maximum vertical contact forces for new/worn/hollow wheel.

		Train Speed					
		75 km/h		160 km/h		250 km/h	
		simplified model	realistic model	simplified model	realistic model	simplified model	realistic model
Max. vertical contact Force F_{max} [kN]	New wheel	115	120	156	141	254	248
	Worn wheel	125	107	244	234	409	432
	Hollow wheel	490	329	1123	405	1886	432

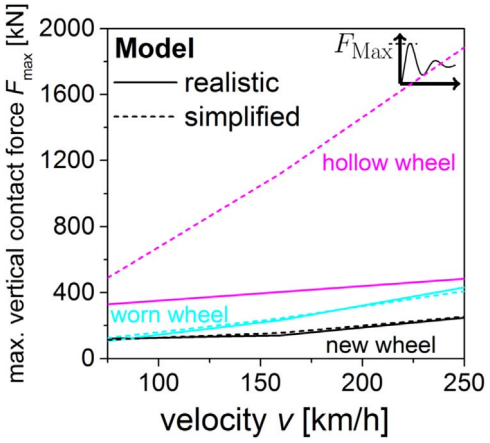

Fig. 12. The impact forces F_{max} calculated in the realistic and simplified model plotted over the train speed v.

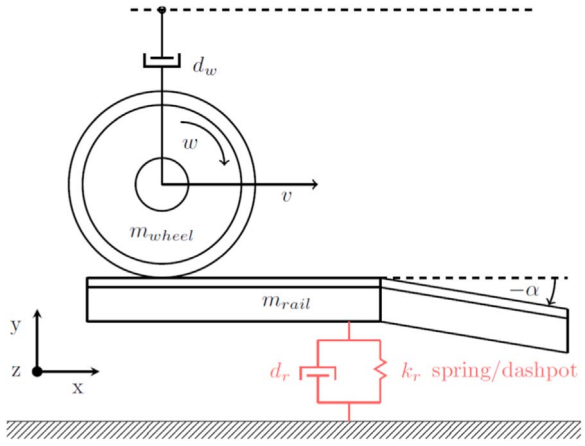

Fig. 13. Mechanical system of the finite element model for the investigation of the model limitations. The bottom of the rail is rigidly connected to a spring/dashpot combination support (red) in the vertical direction.

As a result of different degradation of the three wheel profiles, the wheel undergoes different vertical displacements, which not only change the impact angles, but also the impact positions and contact radii. Until a wheel position x of about −1.25 m, the three wheels exhibit a similar vertical displacement. At x of about −1.25 m, the wing rail branches outwards, which leads to a downward movement of the wheels determined by their conicity (which is highest for the worn wheel and lowest for the hollow wheel). Up to a wheel position x of about −0.4 m, the hollow wheel shows the lowest downward movement, but at this position its trajectory has an abrupt and steep downward movement. In terms of the impact angles defined in Section 2.1, this leads to a very high impact angle α_{Impact} of 30.5 mrad. As shown in Table 3, the impact angles of the worn wheel and the new wheel are considerably lower with 8.4 mrad and 5.1 mrad, respectively. As for intersections of the wing rail and crossing nose trajectories, the worn wheel calculates this impact geometrically at x=0.25 m. The new wheel and the hollow wheel have their geometrically calculated impact positions at 0.35 m and 0.5 m, respectively. Table 3 shows the fitted contact radius of crossing nose and wing rail at these positions. The impact positions determine the fitted contact radius – the sooner the impact, the bigger the contact radius at the wing rail and smaller the contact radius on the crossing nose. The simplified model uses the values reported in Table 3 for wing rail and crossing nose and an infinite contact radius in the longitudinal direction.

Fig. 11 compares the vertical contact force results of the simplified model and the realistic model for the above wheel profiles and train speeds of 75 km/h, 160 km/h and 250 km/h. The train speed v is denoted by the line colors: Green for a speed of 75 km/h, black for 160 km/h and red for 250 km/h. In the right column of Fig. 11, i.e. Fig. 11b, d, f, vertical contact force results of the realistic model are plotted over the wheel position. The wheel runs from left to the right in the diagrams. In the figures on the left, i.e. Fig. 11a, c, e, the vertical contact force results of the simplified model are plotted over the *impact position*. This *impact position* is defined so that it has its origin at the position of first contact of the wheel with the crossing nose. An earlier impact of a wheel is thus only represented by changed impact angle and contact radius, but the impact – and the longitudinal position of the impact - are not intended to correspond in the simplified and realistic model.

Fig. 11a and Fig. 11b show the contact force results for the new wheel. In the simplified model (Fig. 11a), the wheel initially runs on the contact spring that represents the wing rail with the static wheel load. At an impact position of 0, the wheel initially makes contact with the crossing nose and the contact force on the wing rail declines. At the same time, the contact force on the crossing nose increases and reaches a maximum value F_{max}. This maximum force increases with increasing train speeds. The results of the realistic model for the new wheel (Fig. 11b) reveal a similar picture, except for oscillations of the contact forces at the wing rail before the impact. This is due to the full wing rail geometry used in the realistic model. Considering the impact of the wheel on the crossing nose, the models show quite good agreement in the F_{max} values and the oscillation frequencies. The results for the models with a worn wheel are shown in Fig. 11c and Fig. 11d. Again, the peaks of the contact forces show quite good agreement between the two models for all three train speeds. For the hollow wheel results shown in Fig. 11e and Fig. 11f, the simplified model calculates considerably higher contact forces at the impact than the realistic model.

The maximum contact forces reached on the crossing nose F_{max} for the cases shown in Fig. 11 are listed in Table 4. For the new wheel, the F_{max} values of the two models differ less than 10%. For the worn wheel, the maximum difference of the F_{max} values of the two models is 17% for a train speed of 75 km/h. The F_{max} values for the hollow wheels are considerably higher in the simplified model than in the realistic model.

Fig. 12 shows the impact forces F_{max} of the two models plotted over the train speed for the three wheel profiles (black for the new wheel, cyan for the worn wheel and magenta for the hollow wheel). The good fit of the two models for the new and worn wheel can be seen. The discrepancy for the hollow wheel is very distinct and increases/

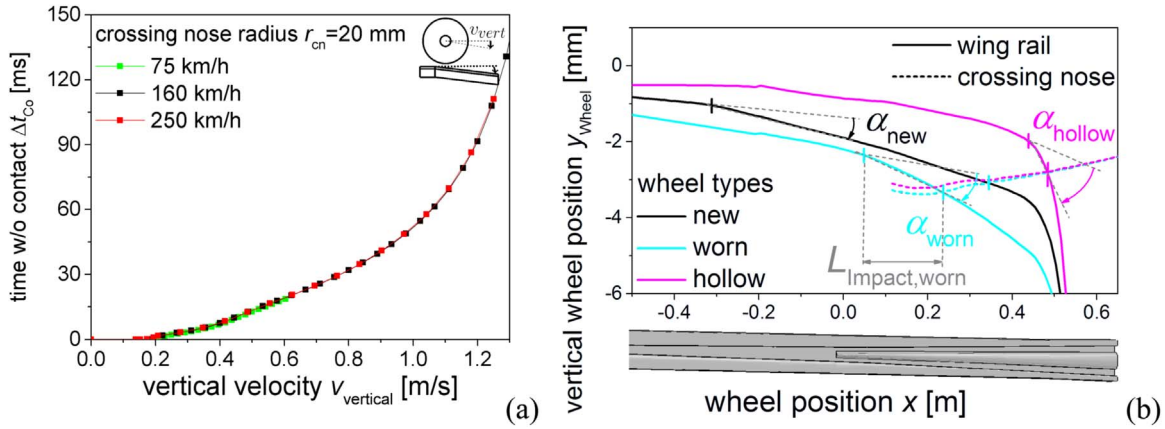

Fig. 14. (a) Time Δt_{Co} to establish contact after a geometry change at the wing rail for different vertical velocities $v_{vertical}$. (b) The geometrical change α (downward movement) for new (black), worn (cyan) and hollow (magenta) wheel and the distance to the impact position L_{Impact} for the worn wheel.

Table 5
$v_{vertical}$ and Δt_{Impact} for new, worn and hollow wheel.

	Train Speed					
	75 km/h		**160 km/h**		**250 km/h**	
	$v_{vertical}$ [m/s]	Δt_{Impact} [ms]	$v_{vertical}$ [m/s]	Δt_{Impact} [ms]	$v_{vertical}$ [m/s]	Δt_{Impact} [ms]
New wheel	0.0346	31	0.0738	14.6	0.115	9.3
Worn wheel	0.075	10	0.16	4.5	0.25	2.8
Hollow wheel	0.385	6.2	0.822	3	1.28	1.9

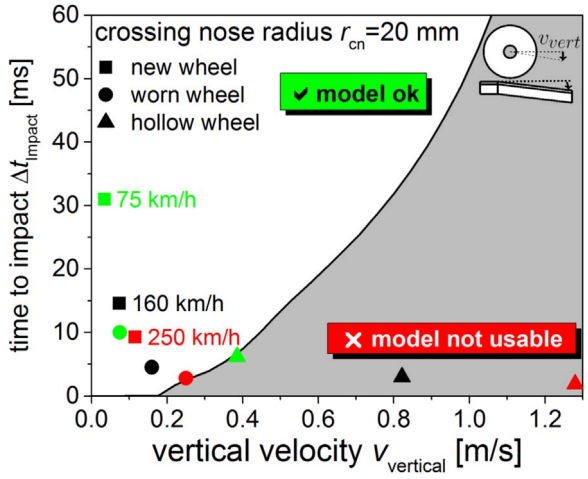

Fig. 15. Vertical velocity $v_{vertical}$ and lift-off time Δt_{Impact} (time from the downward kink to the impact) for the validation load cases (new, worn and hollow wheel profile and train speeds of 75 km/h, 160 km/h and 250 km/h). The grey area shows the region where the wheel has lifted off the wing rail and has not contacted the wing rail again at the time of the impact onto the crossing nose.

becomes greater with increasing train speed v. The discrepancy for the hollow wheel can be explained by the assumption in the simplified model that the wheel is running on the wing rail as it impacts onto the crossing nose and that the impact angle can be extracted geometrically as shown in Fig. 4. For the hollow wheel, these assumptions are not valid, as can be seen in Fig. 11f. For all three train speeds, the wheel is lifted off the wing rail before it impacts onto the crossing nose.

3.3. Limits of the model

As seen in the comparison of the simplified and realistic model results in Section 3.2, the simplified model is not able to predict the dynamic behaviour for hollow wheels. This is because the simplified model assumes that the wheel follows the path of the geometrically evaluated vertical displacement. Under real conditions, the wheel is able to lift off from the rail if it cannot follow the wing rail geometry, due to its inertia. Important parameters for losing contact with the wing rail before the impact are:

- the negative (downward) angle α in the wheel trajectories,
- train speed,
- wheel mass,
- bedding and mass of the crossing

To investigate if the wheel lifts off the wing rail, we developed a model similar to the simplified model but with a downward kink in the geometry. This model is similar to the model introduced in Ref. [15] and is illustrated in Fig. 13. It uses the same bedding, crossing and wheel mass as the simplified model. Also boundary conditions and contact algorithms are similar to the simplified model.

In some cases (particularly for high train speeds v and big angles α) the wheel lifts off and makes contact with the rail again after a time Δt_{Co}. To find a general dependency of the lift-off case for the investigated bedding, wheel mass and crossing mass, the train speed v and the angle can be combined to a vertical velocity $v_{vertical}$ that defines abrupt change in vertical velocity for the wheel to follow the wing rail geometry:

$$v_{vertical} = v \tan(\alpha) \tag{2}$$

Fig. 14a shows the dependence of the time without contact of wheel on the rail Δt_{Co} on the vertical velocity $v_{vertical}$. It can be seen that the curves for the three different velocities (75 km/h, 160 km/h and 250 km/h) overlap, which shows that choosing Δt_{Co} and $v_{vertical}$ allows a velocity independent plot of those values. This means that for a certain crossing/wheel combination, not only the impact angle and contact radii for the impact should be extracted from the geometry, but also the last downward kink in the wing rail trajectory (the change of the angle α and the distance to the impact position, L_{Impact}). In

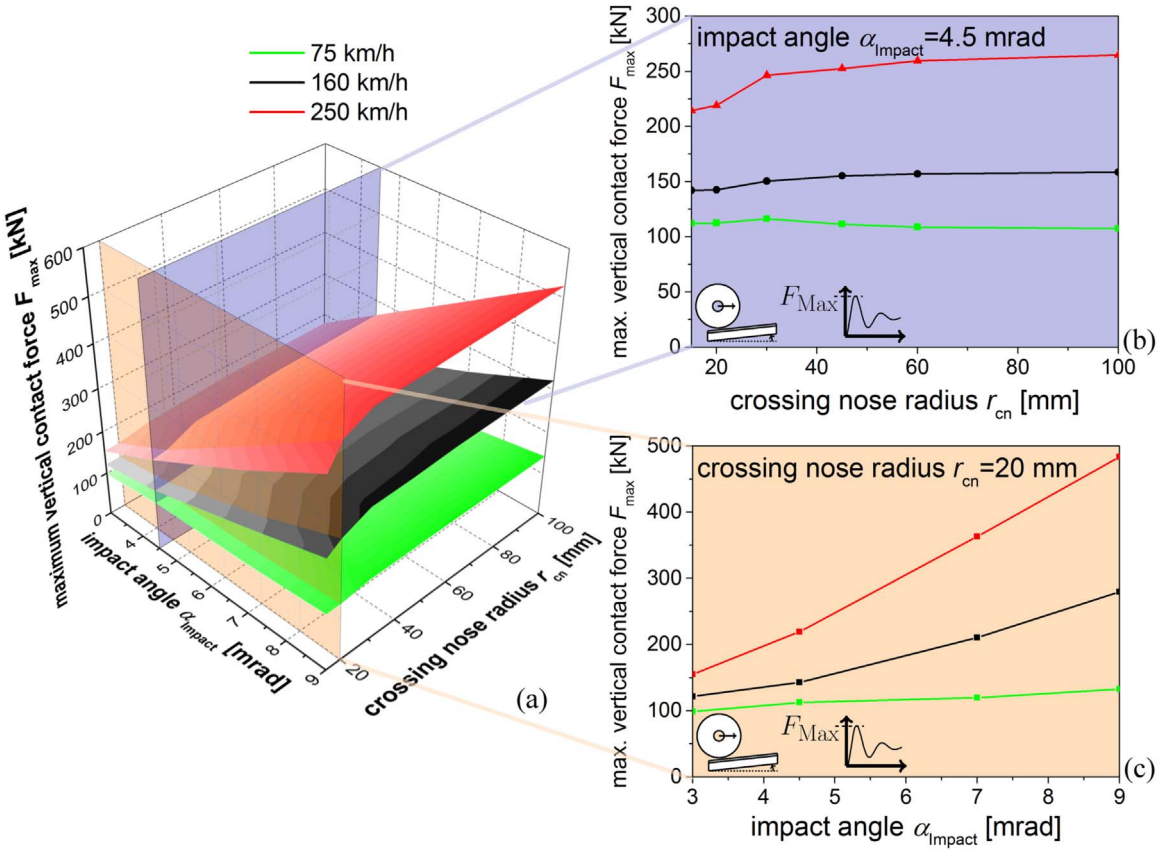

Fig. 16. Maximum contact forces F_{max} calculated for different velocities, crossing nose head radii and impact angles α_{Impact} in (a) a 3D surface plot, (b) 2D plot over crossing nose head radii (purple) for a constant α_{Impact} of 4 mrad and (c) 2D plot over the impact angles (orange) with a constant r of 20 mm.

Fig. 14b, these angles are drawn as α_{new}, α_{worn} and α_{hollow} for the corresponding wheels used in the validation section. From the angles α, the vertical velocity $v_{vertical}$ can be calculated for all velocities. From the positions of the downward kinks in Fig. 14b, also the L_{Impact} values can be extracted – Fig. 14b shows L_{Impact} for the worn wheel. Fig. 14b shows that this L_{Impact} correlates with the unevenness of the wheel wear for the worn wheel – The kink is situated where the worn part of the worn wheel comes into contact with the wing rail, see Fig. 10a. For the worn wheel, L_{Impact} is the very small length where the wheel would fall onto the crossing nose. From those L_{Impact} values, a division by the train speed v gives the associated time Δt_{Impact}. All parameters for the load cases of the validation section are listed in Table 5.

Fig. 15 shows the line of Fig. 14a again, but additionally the Δt_{Impact} values for the three wheel profiles and train speeds. The Δt_{Co} values (line) divides the graph in a non-critical (upper) and critical (lower: grey) area for the Δt_{Impact} values (points). In the critical area, the wheel lifts off at the wing rail and is not in contact again until it impacts onto the crossing nose ($\Delta t_{Co} > \Delta t_{Impact}$). This means that for points lying in the grey area, the simplified model introduced in this work is not valid and the wheel loses contact. The points of the new wheel lie in the non-critical area for all velocities, whereas the worn wheel reaches the transition zone of the critical area for a velocity of 250 km/h. The calculated contact forces of the realistic model for v=250 km/h show that the worn wheel is almost lifting off, but does not fully lose contact. However, this seems to have a very small influence on the impact force, see Fig. 11c. For the hollow wheel, all three velocities lie in the region where the model is not valid. This corresponds well with the discrepancies seen in Figs. 11 and 12, between the simplified and realistic model for the hollow wheel.

For the used masses and bedding of the crossing, Fig. 15 can thus be used to check the validity of the simplified model and can be incorporated into the geometric analysis.

3.4. Impact force: Influence of train speed, impact angle and crossing nose head radius

Fig. 16 shows the impact force F_{max} results of the simplified model for varied values of the train speed v, crossing nose head radius r_{cn} and impact angle α_{Impact}. Fig. 16a provides an overview of all data in a 3D plot with the surfaces representing velocities of 75 km/h (green), 160 km/h (black) and 250 km/h (red). A cut through the surfaces at an impact angle α_{Impact} of 4.5 mrad is plotted in Fig. 16b to show the F_{max} dependency on the crossing nose head radius r. Fig. 16c plots a cut through the F_{max} surface at a crossing nose head radius r of 20 mm and thus shows the dependency of F_{max} on the impact angle. The F_{max} values vary only little with changing r values. At 250 km/h, there is a clear drop of F_{max} with low r values, which can be explained by a lower contact stiffness that can reduce impact forces. Concerning the impact angle α_{Impact}, there is a clear increase of F_{max} values with increasing α_{Impact} values. This effect becomes more distinct with increasing velocities. At a train speed of 75 km/h, F_{max} increases from 99 kN to 133 kN with increasing α_{Impact} from 3 mrad to 9 mrad, whereas at 250 km/h, F_{max} values increase from 155 kN to 484 kN for the same α_{Impact} values. For the used wheel mass and crossing support, F_{max} values can thus be interpolated from the data shown in Fig. 16.

3.5. Maximum contact pressure: influence of train speed, impact angle and crossing nose head radius

Fig. 17 shows the results for the maximum contact pressures p_{max} similar to the plot of the impact forces in Fig. 16. The dependency of train speed v, crossing nose head radius r_{cn} and impact angle α_{Impact} on p_{max} are shown. Fig. 17a shows a surface plot of p_{max} for the three used velocities of 75 km/h (green), 160 km/h (black) and 250 km/h (red). Figs. 17b and c shows the 2D plots of p_{max} plotted over the crossing

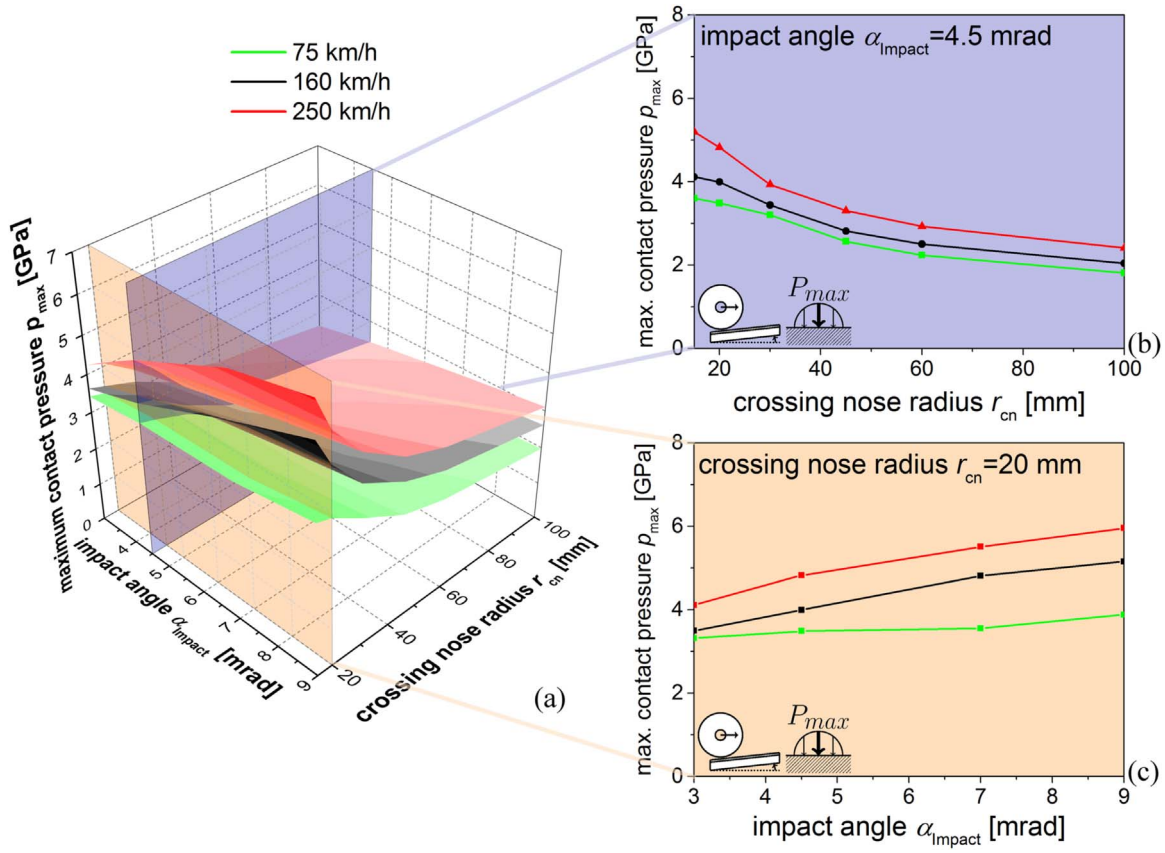

Fig. 17. Maximum contact pressure p_{max} during the impact calculated for different velocities, crossing nose head radii r_{cn} and impact angles α_{Impact} in (a) a 3D surface plot, (b) 2D plot over crossing nose head radii (purple) for a constant α_{Impact} of 4 mrad and (c) 2D plot over the impact angles (orange) with a constant r_{cn} of 20 mm.

nose head radius r_{cn} and the impact angle α_{Impact}, respectively. In Fig. 17b, it can be seen that there is a distinct influence of the crossing nose head radius r_{cn} on the p_{max} values – the lower r_{cn} gets, the higher are the p_{max} values. This corresponds to dependencies described by the Hertz formulas [2], where a smaller contact radius for a constant normal force leads to smaller contact areas and higher contact pressures. Note that for crossing materials with low initial hardness but high work hardening capability, such as the widely used Manganese steel, these contact pressures would cause plastic deformations that will reduce the p_{max} values. For crossing materials with high hardness, wear could have a similar effect but only after many cycles of loading.

Increasing the impact angle α_{Impact} also increases the p_{max} values, as shown in Fig. 17c. This effect is more distinct for higher train speeds. At a train speed of 75 km/h, p_{max} increases from 3.3 to 3.9 GPa with an increase of α_{Impact} from 3 mrad to 9 mrad. For a train speed of 250 km/h, the p_{max} values increase from 4.1 to 6 GPa in the same α_{Impact} range.

4. Conclusion

Based on existing finite element crossing models with realistic crossing geometry, a model with simplified geometry was developed. The calculation times are reduced from several hours to less than one hour, while being able to describe the impact forces quite accurately. In this simplified model, the crossing nose is modelled as an extruded profile meshed with finite elements and the wing rail is modelled as a nonlinear contact spring. The elastic/plastic stress and strain fields in the crossing can thus be directly calculated and used to calculate profile degradation due to plastic deformation and stress-based damage parameters. The inclination of the crossing nose (defining the impact angle), the crossing nose head radius and the wing rail head radius (for calculating the stiffness of the contact spring) are extracted from the wheel and crossing geometries. For a typical rigid crossing and three types of wheels (*new* profile, *hollow*-worn profile and wheel with increased conicity- the *worn* wheel), parameters for the simplified model were obtained from a geometric analysis. It is shown that:

a) the impact angle is lowest for the *new* wheel, slightly higher for the *worn* wheel and highest for the *hollow* wheel;
b) compared to the new wheel, the impact occurs earlier for the worn wheel and later for the hollow wheel;
c) the head radius at the impact position is thus lowest for the worn wheel and highest for the hollow wheel.

These three wheel profiles are used to validate the simplified crossing model by comparing results for three velocities (75 km/h, 160 km/h and 250 km/h) to results of the crossing model with realistic geometry. The comparison shows that:

a) there is a very good agreement of impact force results between simplified and realistic model at all used velocities for new and worn wheels;
b) the existing oscillations of the vertical contact forces between wing rail and wheel before the impact seem to have only a small influence on the impact force;
c) it is necessary to model the wing rail with a spring to account for the simultaneous contact of the wheel with wing rail and crossing nose; and
d) for the hollow worn wheel, the simplified model gives considerably higher values of the impact force than the realistic model. This overestimation is due to an assumption that the vertical wheel movement follows the trajectories defined by wheel and crossing geometry and the wheel cannot lift off the wing rail (which it does for the hollow wheel).

Because of these discrepancies between simplified and realistic model results, a scheme for checking the applicability of the simplified model has been developed. The scheme can tell whether the wheel will lose contact with the wing rail before the impact on the crossing nose. The presented diagrams are valid for a certain wheel mass, static load and crossing bedding, but can be recalculated for other values of wheel mass, static load and other beddings of the crossing.

The impact angles, head radius of wing rail and crossing nose and velocities were varied to show the dependencies of impact force and maximum arising contact pressure on these parameters. The model shows that:

a) the impact force and maximum contact pressure increase with increasing velocities. The increase of impact forces is more distinct for high impact angles;
b) the impact force and maximum contact pressure increase with increasing impact angles. The dependency is more pronounced for high velocities whereas for a velocity of 75 km/h this increase is very small;
c) decreasing the crossing nose head radius leads to lower impact forces as the contact stiffness is reduced; and
d) decreasing the crossing nose head radius also leads to smaller contact areas and thus to higher contact pressures.

The presented model provides an automated and fast tool for calculating the impact forces and elastic/plastic stress and strain fields in the crossing. This tool will allow for a study of cyclic plastic deformation and damage based on stress fields. Furthermore, the model can be automated to characterize measured crossing profiles and optimize crossing geometries to reduce impact forces and arising contact pressures.

Acknowledgements

Financial support by the Austrian Federal Government (in particular from Bundesministerium für Verkehr, Innovation und Technologie and Bundesministerium für Wissenschaft, Forschung und Wirtschaft) represented by Österreichische Forschungsförderungsgesellschaft mbH and the Styrian and the Tyrolean Provincial Government, represented by Steirische Wirtschaftsförderungsgesellschaft mbH and Standortagentur Tirol, within the framework of the COMET Funding Programme is gratefully acknowledged.

References

[1] Ekberg A, Kabo E. Fatigue of railway wheels and rails under rolling contact and thermal loading—an overview. Contact Mech Wear Rail/Wheel Syst 2005;258(7–8):1288–300.
[2] Hertz H. Über die Berührung fester elastischer Körper. J für die reine und Angew Math 1881;92:156–71.
[3] Kassa E, Andersson C, Nielsen JC. Simulation of dynamic interaction between train and railway turnout. Veh Syst Dyn 2006;44(3):247–58.
[4] KALKER JJ. A fast algorithm for the simplified theory of rolling contact. Veh Syst Dyn 2007;11(1):1–13.
[5] Andersson C, Abrahamsson T. Simulation of interaction Between a train in general motion and a track. Veh Syst Dyn 2010;38(6):433–55.
[6] Nicklisch D, Kassa E, Nielsen J, Ekh M, Iwnicki S. Geometry and stiffness optimization for switches and crossings, and simulation of material degradation. Proc Inst Mech Eng, Part F: J Rail Rapid Transit 2010;224(4):279–92.
[7] Johansson A, Pålsson B, Ekh M, Nielsen JC, Ander MK, Brouzoulis J, Kassa E. Simulation of wheel–rail contact and damage in switches & crossings. Wear 2011;271(1–2):472–81.
[8] Yan WY, Antretter T, Fischer FD, Blumauer H, editors. Numerical Analysis of the Cyclic Response of a Crossing Component in a Switch. Leoben, Austria: Verformungskundliches Kolloquium XIX; 2000.
[9] Wiest M, Daves W, Fischer FD, Ossberger H. Deformation and damage of a crossing nose due to wheel passages: contact mechanics and wear of rail/Wheel systems - CM2006. Wear 2008;265(9–10):1431–8.
[10] Pletz M, Daves W, Ossberger H. A wheel set/crossing model regarding impact, sliding and deformation—explicit finite element approach. Wear 2012;294–295:446–56.
[11] Ossberger, U., Pletz, M., Eck, S., Daves, W. (eds) (2013) *Validation of a finite element crossing model using measurements at an instrumented turnout*. In: Proceedings of the 23rd Symposium on Dynamics of Vehicles on Roads and Tracks, Qingdao, China.
[12] Pletz M, Daves W, Ossberger H. Understanding the Loading of Railway Crossings. *Railway Gazette International*, **August Issue**; 2015.
[13] Pletz M, Daves W, Yao W, Ossberger H. Rolling contact fatigue of three crossing nose materials—Multiscale FE approach In: Proceedings of the 9th International Conference on Contact Mechanics and Wear of Rail / Wheel Systems, Chengdu, 2012. *Wear*, **314** (1–2), 69–77; 2014.
[14] Xin L, Markine VL, Shevtsov IY. Numerical analysis of the dynamic interaction between wheel set and turnout crossing using the explicit finite element method. Veh Syst Dyn 2016;54(3):301–27.
[15] Wiedorn J, Daves W, Ossberger H, Pletz M. A Simplified Dynamic Finite Element Model for the Impact of a Wheel on a Crossing: Validation and Parameter Study, in *In: Proceedings of the Third International Conference on Railway Technology: Research, Development and Maintenance* (ed J. Pombo), Cagliari, Sardinia, Italy. Civil-Comp PressStirlingshire, UK; 2016.
[16] Research Wolfram. *Mathematica, Version 11.0*, Champaign, Illinois; 2016.
[17] Kunz J. Kontaktprobleme und ihre praktische Lösung. Konstruktion 2009;61:54–8.
[18] Zhao X, Li Z. The solution of frictional wheel–rail rolling contact with a 3D transient finite element model: Validation and error analysis In: Proceedings of the 8th International Conference on Contact Mechanics and Wear of Rail / Wheel Systems, Florence, 2009. *Wear*, **271** (1–2), 444–452; 2011.

Paper B

Numerical assessment of materials used in railway crossings by predicting damage initiation - Validation and application

AUTHORS

Julian Wiedorn[1], Werner Daves, Uwe Ossberger, Heinz Ossberger, Martin Pletz

[1] **corresponding author**

JOURNAL

Published in Wear (ISSN: 0043-1648).

ABSTRACT

The Dang Van damage criterion is utilized to predict (subsurface) damage initiation in railway track crossing components. A simplified, explicit finite element model is used to calculate the cyclic impact of a wheel on a crossing nose (frog point). The model is applied to an elastic and to three elastic-plastic materials (manganese steel, chromium-bainitic steel and tool steel). These three materials deform differently, and that difference affects the loading on the crossing after a period of time in use. Plastic deformation is calculated and validated with measurements. The damage parameter (Pdv) is then calculated to compare the damage initiation tendency of the three materials with their plastically deformed shapes. The positive effect of changing the geometry of higher strength steel crossings is also discussed.

CONTRIBUTION

Responsible for the development of the method.
Carried out the numerical simulations.
Wrote most parts of the paper.

Wear 414–415 (2018) 136–150

Contents lists available at ScienceDirect

Wear

journal homepage: www.elsevier.com/locate/wear

Numerical assessment of materials used in railway crossings by predicting damage initiation – Validation and application

Julian Wiedorn[a,*], Werner Daves[a], Uwe Ossberger[b], Heinz Ossberger[b], Martin Pletz[c]

[a] Materials Center Leoben Forschung GmbH, Leoben, Austria
[b] voestalpine VAE GmbH, Zeltweg, Austria
[c] Department of Polymer Engineering and Science, Montanuniversitaet Leoben, Austria

ABSTRACT

The Dang Van damage criterion is utilized to predict (subsurface) damage initiation in railway track crossing components. A simplified, explicit finite element model is used to calculate the cyclic impact of a wheel on a crossing nose (frog point). The model is applied to an elastic and to three elastic-plastic materials (manganese steel, chromium-bainitic steel and tool steel). These three materials deform differently, and that difference affects the loading on the crossing after a period of time in use. Plastic deformation is calculated and validated with measurements. The damage parameter (P_{dv}) is then calculated to compare the damage initiation tendency of the three materials with their plastically deformed shapes. The positive effect of changing the geometry of higher strength steel crossings is also discussed.

1. Introduction

Crossings (frog points) are a key part of the track system: they allow gauge corner intersections of two different track routes. Depending on their design and type, high forces can occur during the transition of the wheel from one rail to the other. Especially fixed crossings, which have a design-related gap, are of particular interest, see Fig. 1. This design forces the wheel to move downwards and upwards (1–3 at the top in Fig. 1), which leads to high contact forces and an impact of the wheel onto the crossing nose. Furthermore, the contact radii of the wheel and the rail change during the transition (2–3 at the bottom in Fig. 1), which cause slip and can also increase the contact stresses due to the small head radii of the crossing nose. Axle loads and speeds, but also the crossing geometry and wheel profiles, i.e. hollow wheels [1], influence this process and can be the reason for severe wear and damage [2].

Common tools to predict this dynamic process are the multi-body simulation (MBS) and the Finite Element (FE) method. The former enables the user to analyze complex structures very fast by dividing them into a system of rigid and flexible bodies and calculating their displacements. The FE method, however, allows to calculate stress and strain fields in the bodies with complex material laws to account for e.g. plastic deformations. To investigate mechanisms of damage locally, those results are needed.

Kassa et al. [3] developed a MBS model to calculate the dynamic response of a turnout. With additional tools, they calculated contact pressure and stresses. To predict wear and damage, they overcame the main disadvantage of MBS models and accounted for plastic deformation and evaluated stresses and strains in the body. Simplified FE models are added to the analysis chain and data is transferred between these methods.

Yan et al. [4] and Wiest et al. [5] used the explicit FE method to calculate the loading on a crossing. This method can calculate the entire dynamic process and evaluate stresses, strains and plastic deformation at a material point within the body. For a high resolution, however, a high number of small elements is needed, which increases the calculation times significantly. Therefore, the authors used a geometrically simplified crossing: a kink on a rail accounts for the downward and upward movement of the wheel during the impact. In [6], Pletz et al. introduced a crossing model with realistic geometry, which was validated with track measurements in [7]. They were able to include the load transfer from the wing rail to the heavily loaded crossing nose and identified crucial parameters for the impact. To calculate the cyclic deformation of the crossing nose and crack driving forces, they then used a multiscale approach and investigated the behavior of typical crossing nose materials in [8]. More recently, L. Xin developed crossing model similar to the one of Pletz et al. [6] and validated its results with acceleration measurements in [9].

To study the cyclic behavior of crossings in more detail, Wiedorn et al. [10,11] developed a simplified crossing model that is able to simulate the impact of a wheel in just a few hours. He focused on the deformation of the crossing nose and simplified the wing rail to a nonlinear contact spring. Its input parameters were evaluated from a given geometry and the FE model is built automatically. In [12], Y. Ma introduced another strategy to optimize calculation times: to simulate the

* Corresponding author.
E-mail address: Julian.wiedorn@mcl.at (J. Wiedorn).

https://doi.org/10.1016/j.wear.2018.08.011
Received 10 January 2018; Received in revised form 12 August 2018; Accepted 15 August 2018
Available online 18 August 2018
0043-1648/

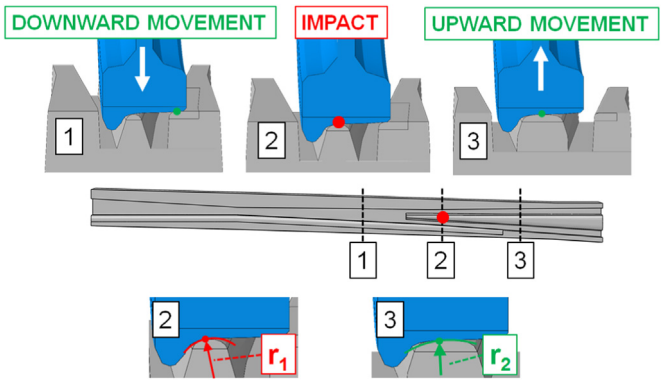

Fig. 1. Downward and upward movement of the wheel (1–3 at the top) and changing radii in contact during the impact on a realistic crossing (2–3 at the bottom). The symbols r_1 and r_2 indicate the lateral contact radius of the crossing nose at the position of contact.

dynamic behavior of 1:9 crossings, he adapeds the FE mesh to data evaluated in pre-processing.

Nevertheless, with the simplified model from [10], it is possible to perform cyclic plastic calculations easily and allows the application of stress-based damage models for different crossing noses.

Van [13] introduced a damage criterion for the multi-axial high cycle fatigue regime for ball bearings. He assumes a loading in the elastic shakedown regime and used he stress amplitude and the hydrostatic stresses to give an indication where and in what direction damage, such as cracks, may initiate. The Dang-Van (DV) criterion can predict this damage. It uses one parameter to describe the dependence of the critical stress amplitude on the hydrostatic pressures: higher hydrostatic pressures increase the critical stress amplitude. However, for the deformation near crossing surfaces (µm region) the criterion may miss crucial mechanisms for the crack initiation, which should be considered: There ratcheting is commonly the dominating damage mechanism and is responsible for the initiation of surface initiated cracks as e.g. head checks, see [14]. Nevertheless, in [15], the author applied the criterion on rails using cyclic plasticity and loads the rail by repeatedly moving contact stresses. Using this method, Van analyzed typical rail damages in [16], such as shelling or head-checking. To study crack propagation they combined crack initiation with a Paris law at the evaluated position of damage [17].

In [18] and [19], Ekberg uses the proposed criterion for subsurface damage evaluation as part of a universal predictive damage model for wheels. It is described as a typical damage mechanism for fatigue failure in absence of macroscopic defects in a depth of about 3–10 mm below the wheel thread. There the requirements for the application, i.e. the absence of ratcheting, seem satisfied.

The DV criterion is highly recognized in the field of wheel/rail contact mechanics, although there are some limitations, especially for damage at the surface, which have to be considered. Desimone et al. [20] mentioned the disagreement of the criterion for negative stress ratios and proposes a different failure limit: a constant value replaces the increasing damage limit in the regime of compressive hydrostatic stresses. Ciavarella et al. confirmed the possibility of too conservative values under RCF, depending on the contact and slip conditions [21]. In [22], the authors explained over-optimistic fatigue limits due to the influence of the hydrostatic component of the stress in particular cases and proposed an integration of Weibull-like theories [23].

For the application to crossings in this paper, the authors use the classical approach of the Dang-Van criterion without the change of the failure limit, which is mentioned before. The presented conclusions should be valid for a change of the failure limits, too. As we consider plastic deformation and calculate a state close to elastic shakedown, we assume that the limitations of the use of the DV criterion do not apply.

On this basis, we utilize the simplified model from [10] to calculate a series of cycles and obtain the stress-fields for the DV damage calculations. To capture the impact, especially the plastic deformation, stresses and strains in more detail, and keep the advantage of short calculation times, we extend the simplified model. The model uses the contact radii and vertical displacements over a chosen distance from a given geometry and creates the crossing nose geometry according to this data. It is then possible to calculate several cycles with a more realistic geometry and include the variation of different worn wheels. Similar to [24], we perform 55 cycles using three different elastic-plastic material models for typical crossing materials. We then calculate the Dang-Van damage parameter P_{dv} for all cycles for an area close to the impact position to show its development during the geometrical adaption of the crossing. Additionally, the model calculates the dynamic response of the same geometry and impact positions but elastic material behavior. Then, contact forces, stresses and damage of the last 5 plastic cycles (including the material hardening and residual stresses) are compared to the elastic cycles. Together with plastic deformation and residual stresses, we point out the influence of the cyclic plastic material deformation on the calculated damage parameter P_{dv}. Therefore, the influence of both, the geometry change and developed residual stresses are analyzed.

2. Damage: concept, materials and experimental evaluation

Within this section, we introduce the theoretical background of the DV criterion, its implementation in the FE model and validation. Furthermore, the determination of parameters from experiments is described and the DV damage parameters for the investigated materials are stated.

2.1. Theory and implementation

The multiaxial fatigue criterion of Van [13] considers the nucleation of fatigue cracks. The criterion assumes that the initiation of fatigue cracks takes place at critical zones of stress concentration. It is developed for the high cycle regime and uses the stabilized (after elastic shakedown) microscopic variables instead of the calculated macroscopic ones. This is done by using the local loading path at each time based on the macroscopic stresses in the body. The assumptions include that cracks usually occur in intragranular slip bands inside a macro-volume. As critical stress zones for typical slip conditions of our calculations often appear underneath the surface, subsurface damage is initiated.

The criterion uses two material parameters, which are evaluated experimentally. The equivalent stresses $\tau_{eq,dv}$ are calculated in every cycle as

$$\tau_{eq,dv}(t) = \tau_a(t) + \alpha_{dv}\sigma_h(t), \tag{1}$$

with the shear stress amplitude τ_a, the hydrostatic stress σ_h, the current time t during one loading cycle and the Dang-Van material parameter α_{dv}, which is calculated using

$$\alpha_{dv} = \frac{\tau_f - \frac{\sigma_f}{2}}{\frac{\sigma_f}{3}}. \tag{2}$$

with τ_f and σ_f standing for the shear-torsion and tension-compression fatigue limits, respectively. Damage is predicted if

$$\tau_{eq,dv} > \tau_f.$$

By transforming the equation, the Dang-Van damage variable P_{dv} can be introduced as

$$P_{dv} = \max_{0\le t\le T} \frac{\tau_a(t)}{\tau_f - \alpha_{dv}\sigma_h(t)}. \tag{3}$$

We evaluate the damage criterion for every cycle (wheel impact) with the total time period T for one impact cycle ($t \in T$). A P_{dv} value

above 1 indicates damage initiation and a P_{dv} value below 1 indicates no damage initiation

In the DV damage model τ_f stands for the critical shear stress at a hydrostatic stress σ_h of 0 and α_{dv} multiplied by the current hydrostatic stresses σ_h its shift ($\tau_{eq,dv}$).

The criterion calculates damage using stress amplitudes. Therefore, a median stress σ_{mid} has to be found. We do this by using a min-max optimization algorithm solving

$$\min(\max\|\sigma_{ij,d}(t) - \sigma_{ij,mid,d}\|), \quad (4)$$

where ||.|| is the Mises norm. The subscript d indicates deviatoric stresses and ij the Einstein notation. The routine minimizes the largest von Mises stress occurring during the total time period T. For a validation, we took stresses from [25] and calculated a difference of less than 1% when comparing $||\ \sigma_{mid}\ ||$ to the one evaluated in the paper.

The stress amplitude $\sigma_{ij,a,d}(t)$ for every time t is then defined as

$$\sigma_{ij,a,d}(t) = \sigma_{ij,d}(t) - \sigma_{ij,mid,d}, \quad (5)$$

On this basis, the shear stress amplitude can be calculated with

$$\tau_a(t) = \frac{1}{2}\max(|\sigma_{1,a}(t) - \sigma_{2,a}(t)|, |\sigma_{1,a}(t) - \sigma_{3,a}(t)|, |\sigma_{2,a}(t) - \sigma_{3,a}(t)|), \quad (6)$$

The calculation of $\tau_{,a}(t)$ and P_{dv} is performed in Wolfram Mathematica© as part of post-processing for a chosen number finite elements around the impact position. We choose a sufficiently high number of time steps for each time period T, where the stresses are obtained, to get accurate results for the stress amplitude $\sigma_{ij,a,d}(t)$ and thus P_{dv}.

2.2. Materials and experimental evaluation of the damage parameters

We use three materials for the damage evaluation: Manganese steel, chromium-bainitic steel and tool steel. Manganese steel has the lowest initial yield stress in combination with a distinct work hardening behavior and high values of elongation and tensile strength. Tool steel, however, has the highest yield stress and ultimate strength at lower elongation values and good fracture toughness. Third, the chromium bainitic steel is an enhanced railway steel with increased yield stress and increased elongation at fracture compared to standard perlitic railway steel grades.

We performed rotational bending and alternating torsion experiments for manganese steel (rolled, solution annealed, quenched), tool steel (forged, quenched and tempered) and chromium bainitic steel (rolled, naturally cooled, tempered). Each test was done with 25 polished specimens with a diameter of 5 mm and evaluated according to ASTM E739 standard [26] in combination with the arcsine-sqrt(P) method in the fatigue endurance regime. In the tests, up to 10 million load cycles were applied and the evaluated parameters are based on 50% probability of failure at the fatigue endurance limit, see Fig. 2a.

Table 1
The parameters for the DV damage criterion.

Materials	DV parameters	
	τ_f [MPa]	α_{dv} [-]
Chromium bainitic steel (CB)	375	0.07
Tool steel (TS)	500	0.11
Manganese steel (Mn)	278	0 (− 0.06)

Fully reversed testing (R = -1) is done to evaluate the fatigue parameters. This adds additional safety to the evaluation, since multi-axial stresses occur in wheel/rail contact mechanics, but usually in the pressure regime. With Eq. (2), the DV parameter α_{dv} is then calculated. Table 1 shows the needed parameters to calculate Dang-Van damage variable P_{dv}, see Eq. (3), for each investigated material. A graphical representation of the DV criterion is shown in Fig. 2b.

The negative α_{dv} indicates that the DV criterion is maybe not well-suited for the manganese steel, as it is opposed to the common observations: increasing hydrostatic stresses, decreases the damage initiation P_{dv}. The reason is the high fatigue resistance observed for rotational bending but not for alternating torsion. There the fatigue limit reaches values as high as the yield stress. Therefore, the measured parameter α_{dv} for the manganese steel crossing is corrected to 0.0. These effects can be explained by the plastic deformation of the manganese steel in the tests: the plastic deformation and thus the material properties are different for alternating torsion and rotational bending.

3. Finite element modeling

This section describes the chosen geometry and loads of the crossing, which mimic different wheel profiles. The input parameters of the FE model and its evaluation is stated. Furthermore, the simplifications and developments of the FE model, that are taken from [10], are explained and the materials and the loads are shown.

3.1. Geometric parameter evaluation for the FE model

The procedure used for evaluating the input parameters for the model is based on that in [10], but further developed. Starting from a known wheel and crossing geometry, we take the profile of the wheel and the crossing profile, i.e. described by point lists. Similar to [10], this work investigates three different wheel profiles: worn, new and hollow wheel, to vary impact positions, see Fig. 3b. We took the geometry of an existing FE crossing model, which is based on an EW-60E1- 500-1:12 CENTRO crossing type and the new wheel uses an ORE S1002 profile.

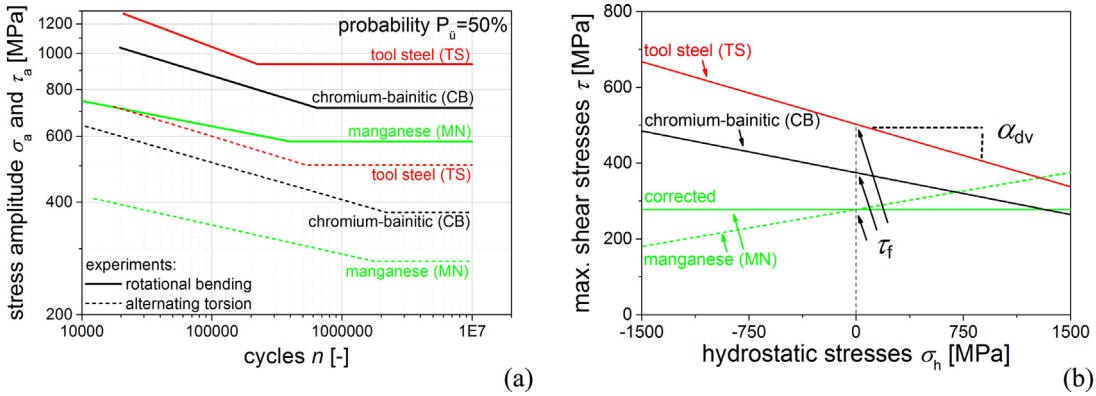

Fig. 2. a) The fatigue limits for rotational bending and alternating torsion evaluated from experiments and (b) a graphical representation of the DV damage locus.

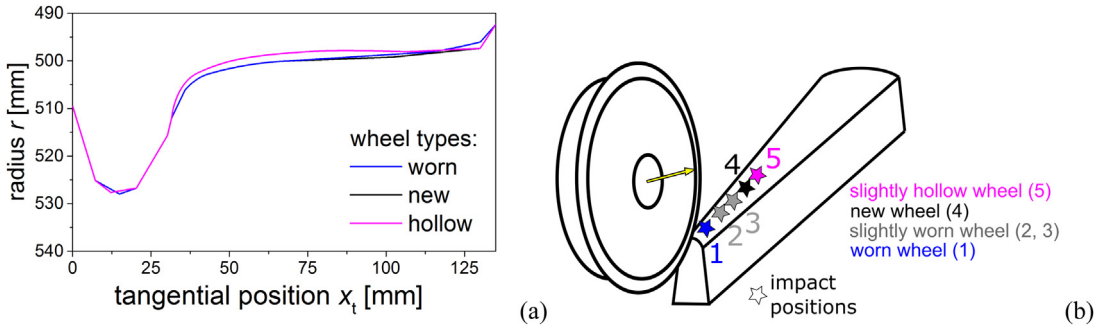

Fig. 3. a) Profiles of the three chosen wheels (new, worn and hollow) and b) a sketch of its impact position on the crossing.

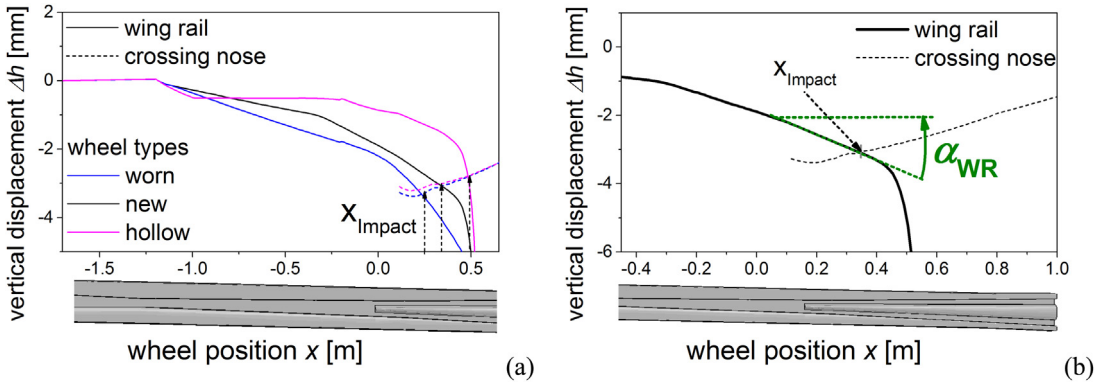

Fig. 4. a) The trajectories of the chosen wheel profiles running along the wing rail and the crossing nose geometry and (b) a detail view of the downward movement on the wing rail of a new wheel.

By moving the wheel profiles along the crossing surface, we evaluate the vertical displacement statically. Fig. 4a shows the displacements for the investigated wheels. The vertical displacement of the wheel on the wing rail and crossing nose are investigated separately (cp. solid and dotted lines in Fig. 4a). The intersection of the wheel positions is called impact position x_{Impact}. Due to the state of wear of the wheels, the impact positions and the contact positions in tangential direction are different, which means an earlier and belated impact of the worn and hollow wheel, respectively. This goes along with different wheel trajectories: when comparing the downward movement of the hollow and worn wheel to the new wheel, the wheel shows a much higher displacement on a shorter distance. To take this into account, we define a downward angle α_{WR} – see Fig. 4b. We use a linear curve fit through the closest points on the wing rail at x_{Impact}, see the dotted green line in Fig. 4b.

At the same time, we evaluate the contact radius at the impact position on the wing rail as r_{WR}. For the crossing nose, we choose more positions to describe the crossing nose surface. This is done by fitting a radius in an area around the contact position of the wheel and crossing nose or wing rail, see [10].

To describe the loads of the crossing nose from the wheel trajectories we now use:

- the downward angle on the wing rail α_{WR},
- the impact position x_{Impact}, and
- the contact radius r_{WR} on the wing rail at x_{Impact}.

Fig. 5 shows the evaluated parameters for the given geometry: the green line shows the wheel downward angle and the purple line the wing rail head radius r_{WR} taken at the impact positions. Three points define the lines:

- the worn wheel with the earliest impact positions at $x_{Impact} = 1.42$ m,
- the new wheel at $x_{Impact} = 1.54$ m (at the kink in Fig. 5) and

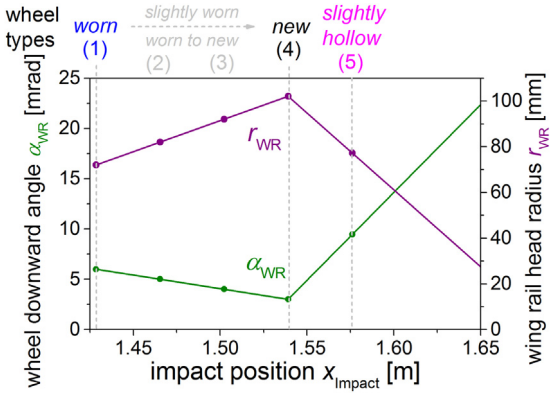

Fig. 5. The selected load cases (wheel downward angle α_{WR} and wing rail head radius r_{WR}) according to the geometry evaluation. Two wheels are chosen in between the worn and new wheel: slightly worn #1 and #2.

- the hollow wheel after $x_{Impact} = 1.65$ m, which is not shown in the graph.

To vary the loads for our cyclic calculations, we add two points in between the worn and hollow wheel – slightly worn #1 and slightly worn #2 - and one point with a similar distance at $x_{Impact} = 1.6$ m, which replaces the extreme case of a fully hollow wheel – a slightly hollow wheel. We used Wolfram Mathematica [27] for the static evaluation of the input parameters.

Two functions describe the crossing nose geometry, see Fig. 6:

- the crossing nose height $h(x)$ and
- the crossing nose head radius $r_{cn}(x)$.

The similar displacements for all wheels enable us to take the same

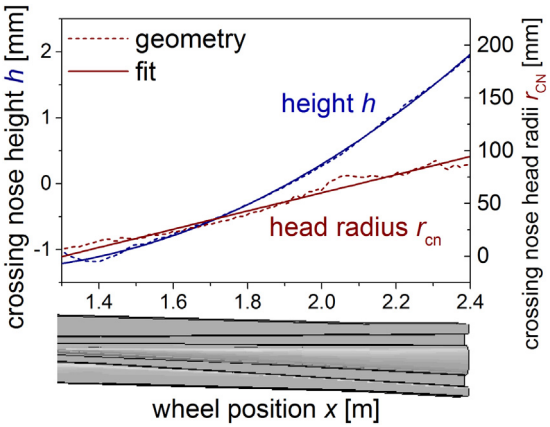

Fig. 6. The geometrical input for the simplified model: the height h and head radius r_{cn} over the wheel positions x. The dotted lines are evaluated geometrically from a given geometry and the solid lines represent fits used in the model.

data for all wheel profiles. Furthermore, they account for the crossing nose height with

$$h(x) = h_{basis} + \Delta h(x), \tag{7}$$

where h_{basis} is a constant height, $\Delta h(x)$ is the vertical displacements and x is the wheel position along the crossing.

In Fig. 6, the dotted lines represent $h(x)$ and $r_{cn}(x)$ that were evaluated from the geometric analysis. To reduce the dependent parameters, a least square fit determines a quadratic and a linear curve for the crossing nose height and head radius, respectively, plotted in Fig. 6 as solid lines. The model uses these functions for the geometry.

3.2. Finite element model

Fig. 7a shows the simplified FE model implemented in SIMULIA Abaqus [28], which uses the extracted data shown in Section 2.1. For the crossing nose, the geometry – defined by the crossing nose head radius $r_{cn}(x)$ and the crossing nose height $h(x)$ – is built up automatically according to the fits in Fig. 5.

The other parameters, such as the downward angle α_{WR}, the impact position x_{Impact} and a nonlinear contact spring k_{wr}, which depend on the radius in contact of the wing rail [29], define the load cases of the model, cp. Fig. 5 for the evaluated data. Fig. 7b shows these parameters as part of the mechanical model. The boundary conditions, the wheel geometry and its masses are taken from [10]. The wheel damper d_w is set to 53 kNs/m and the values for the spring/dashpot support d_r / k_r are 250,000 Ns/m and 90 kN/mm. The velocity of the wheel is 120 km/h and the vertical static load is set to 80 kN. The slip of the wheel, due to the second wheel and changing contact radii during the transition, is neglected. The wheel radius is 0.478 m and its weight is 1025 kg.

We investigate three different material, in terms of their elastic-pastic behavior:

a. manganese steel (MN),
b. chromium-bainitic steel (CB) and
c. tool steel (TS).

The order of these materials corresponds to the increasing yield stress of the materials: rather low for manganese steel and high for tool steel. Stress-strain curves for simple tensile tests and one cycle of load with a strain amplitude of 1.1% are shown in Fig. 8a and b, respectively. The solid lines show the results from the experiments and the dotted lines are taken from a simulation using the material models shown in Table 2.

The simulation model uses a cyclic Chaboche model with combined isotropic and kinematic hardening. The elasto-plastic model uses three to five backstresses to describe the kinematic hardening behavior. R_0 is the initial yield stress, Q and B are the parameters for isotropic and C_i and D_i for kinematic hardening. The wheel, however, is modeled using linear-elastic material. This is chosen because of the lack of available data about the material state (hardening) of the wheels. When calculating the impact of a wheel on a tool steel crossing, the plastic deformation may be overestimated. Table 2 shows the input data for the model.

For the cyclic calculation, each load cycle consists of two calculations:

- an explicit dynamic model, see Fig. 7b, for the impact and
- an implicit static model for relaxation of the elastic waves (dynamic strains and stresses) in the rail.

In the explicit model, the wheel initially runs with a constant velocity on a contact spring simulating wing rail. It moves downwards according to the angle α_{WR} and impacts onto the crossing nose at the impact position x_{Impact}. Then, the wheel runs on the crossing nose for about 0.8 m. This event causes oscillations of the contact force between

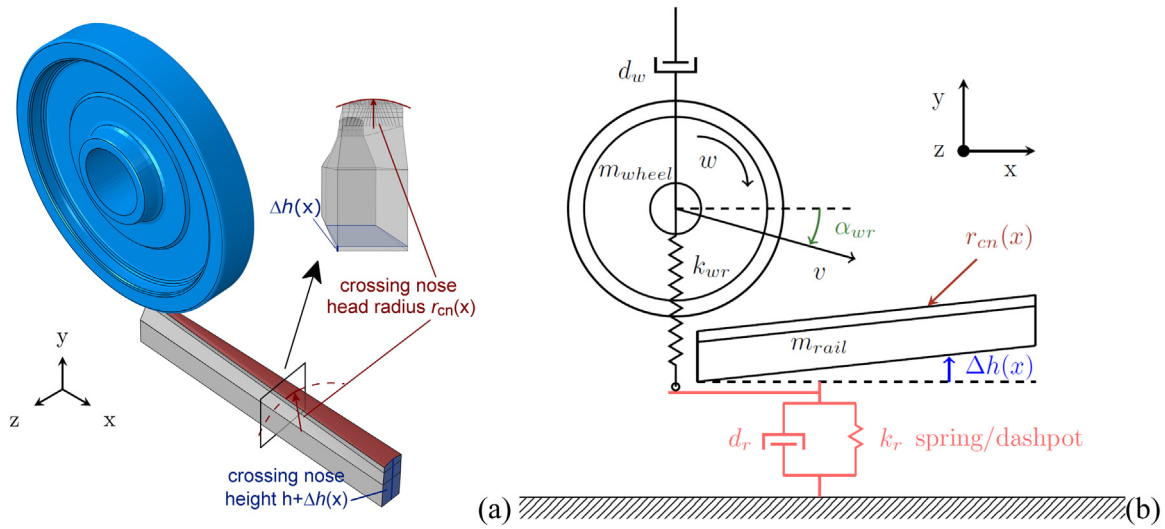

Fig. 7. (a) The geometry of the finite element model and (b) the mechanical system of the finite element model. The bottom of the rail is rigidly connected to a spring/dashpot combination support in the vertical direction.

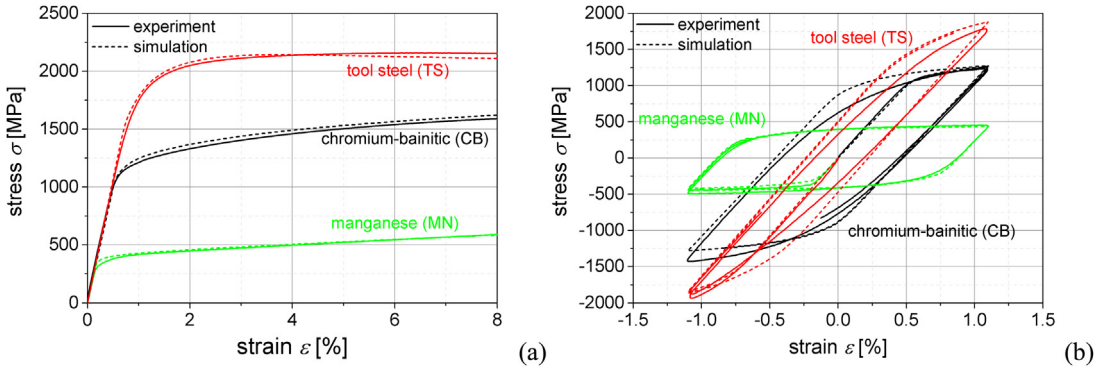

Fig. 8. Experimental and simulated stress-strain curve for a tensile test and one cycle of load with a strain amplitude of 1.1% for all plastically deforming materials: manganese steel, chromium-bainitic steel and tool steel.

Table 2
The material parameters used in the model.

Property	Wheel/Rail: elastic material	Rail: plastic material		
		MN	CB	TS
Young's modulus [GPa]	210	201	200	214
Poisson's ratio [-]	0.3	0.3	0.3	0.3
Density [kg/m^3]	7800	7800	7800	7800
R_0 [MPa]	–	200	950	1400
Q [MPa]	–	250	− 80	− 150
B [-]	–	3	1	10
C_1 [GPa]	–	1000	1200	1100
D_1 [-]	–	10000	10000	7500
C_2 [GPa]	–	40	80	150
D_2 [-]	–	400	800	610
C_3 [GPa]	–	2	15	55
D_3 [-]	–	3	200	140
C_4 [GPa]	–	–	10000	–
D_4 [-]	–	–	10	–
C_5 [GPa]	–	–	2	–
D_5 [-]	–	–	1	–

the wheel and the crossing nose. After the impact, the crossing nose and its material state are transferred to the implicit static model. There, the crossing nose is moved to its initial position and all stress waves vanish. Now the wheel is moved again to its impact position as calculated for the next cycles. The material state of the relaxed crossing is then transferred to the explicit model.

The model repeats this procedure for every cycle to account for the accumulating residual stresses and plastic deformations. In this paper, this results in 110 simulations – 55 implicit and 55 explicit – for each material.

We implemented the variation of the loads, based on the different wheel profiles (see Fig. 5) with the following loading order. The model uses a sequence of 5 different loads (worn wheel: *1*; slightly hollow wheel: *2*, slightly hollow wheel: *3*, new wheel: *4*, slightly hollow wheel: *5*, cp. Figs. 3b and 5) and repeats them until the demanded cycles are reached. In this paper, this means 11 times the sequence: 1, 2, 3, 4, 5.

To minimize simulation errors, enhanced hourglassing is used for the reduced integration elements (C3D8R), according to recommendations in [28]. For the contact between the wheel and the rail, we use a kinematic algorithm and a coefficient of friction of 0.3. The elements in contact have an edge length of less than 1 mm, which results in a total number of elements of about 105,000 for the rail and 83,000 for the wheel. In [30], Zhao et al. shows the accuracy of different element sizes in contact. He compares them to the analytical Hertz solution and postulates an error of less than 5% for elements of about 1.5 mm. Thus, the chosen edge length for the study in this paper of about 1 mm can accurately model the contact between the wheel and rail.

The model calculates 55 cycles and evaluates contact forces and pressures for the last 5 cycles (51st to 55th). Additionally, we analyze the same outputs for an elastic crossing using (i) a new geometry and (ii) a deformed geometry for the five load cases: (ii) uses the geometry of the deformed crossing with manganese material at the end of the 50th cycle. As part of post-processing, we then apply the routine in Section 2.1 to calculate damage initiation for those simulations. There, we assume a state close to elastic shakedown and investigate this assumption by evaluating the influence of the continuing plastic deformation.

4. Results and discussion

In this section, we show the calculated contact forces, pressures, plastic deformation and the Dang-Van damage parameter P_{dv} of crossings using elastic and plastic material behavior. The plastic alters the geometry and thus the damage parameter P_{dv}. This allows us to relate the contact forces to the downward angle of the wheel on the wing rail α_{WR} and the P_{dv} values to the contact pressures. The evolution of P_{dv} for all materials is shown and the influence of residual stresses and plastic deformation explained.

4.1. Elastic calculation: contact forces, stresses and damage

The following section shows model results for linear-elastic material behavior of the crossing nose. Fig. 9a shows the vertical contact forces F during the impact. The increasing impact positions x_{Impact} from worn to hollow wheel shift the dynamic response of each wheel. The impact of the new wheel has the smallest maximum vertical contact force with values around 125 kN and the hollow wheel around the highest contact forces with 280 kN. This is due to the small downward angle α_{WR} for the new wheel and the rather high α_{WR} for the slightly hollow wheel. The contact forces of the worn wheels (1–3) are lower according to the wing rail downward angle α_{WR}.

Fig. 9b shows the contact pressures p during the impact. Again, the curves are shifted according to their impact position x_{Impact}, but their maximum values do not fully correspond to the downward angles α_{WR}. The maximum contact pressure arise for the worn wheel with about 4.3 GPa and the minimum for the new wheel with 3.1 GPa. According to Hertz [1], the contact pressures depend on the forces, but also the contact radii: small forces decrease and small radii increase the contact pressures. Although the contact force is rather low for the worn wheel, the contact radius on the tip of the crossing nose is very small, which increases the pressures significantly. Furthermore, the large contact radius at the belated impact position of the slightly hollow wheel decreases the contact pressures and its maximum to a value close to but less than the worn wheel, although the contact forces for the slightly hollow wheel are much higher than for the worn wheel.

Fig. 10 shows the calculated Dang-Van damage values P_{dv} for all

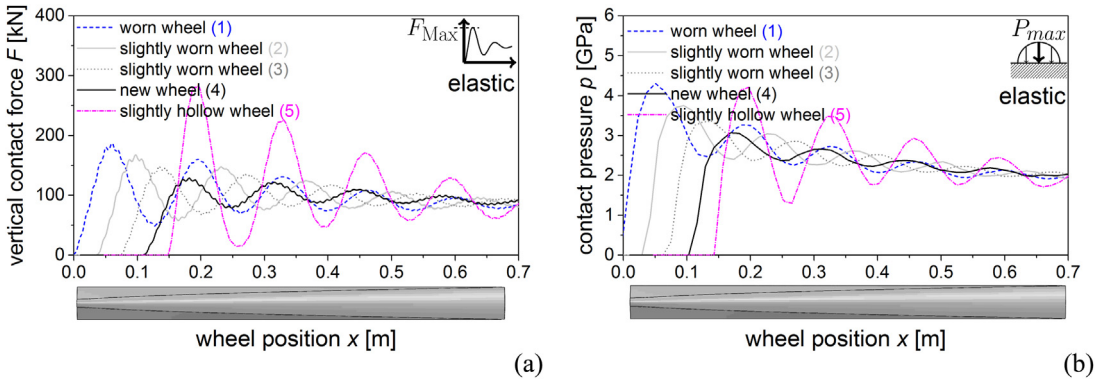

Fig. 9. (a) The contact forces F and (b) the contact pressures p as the wheel impacts onto the crossing nose with a static load of 79.7 kN. Five different types of wheels are shown: worn (1-blue dashed), slightly worn #1 (2- solid light gray) and #2 (3- dotted gray), new (4-solid black) and slightly hollow (5-dashed-dotted magenta).

wheel types: worn (1), slightly worn #1 (2) and #2 (3), new (4) and slightly hollow (5) and a plot where they are combined. Areas with a color from yellow to red have P_{dv} values larger than 1, which indicates damage initiation. Areas of blue or green color indicate regions where P_{dv} is lower than 1, which indicates no damage initiation. The values use the evaluation routine from Section 2.1 and the DV material parameters for tool steel (cp. Table 1). The illustration of the wheel and the rail on top indicates the taken area for the evaluation of the damage values. It has a length of about 20 cm and a depth of 3 cm and it is shifted according to the impact position of each wheel. The last plot at the bottom is a combination of all wheels. There, we took the maximum values of all load cases in each evaluated element – max($P_{dv,i}$), where $P_{dv,i}$ is a list of the P_{dv} values of all wheel types.

The arrows and colored areas point out the evaluated area of each wheel, i.e. the blue area: it starts at the beginning of the crossing and covers more than half of the chosen area. Whenever two or more colored areas overlay each other, we take the maximum value for the combined (last) plot, i.e. at the area of the last white arrow, the damage values of all 5 wheels overlay and the maximum has to be evaluated – max ($P_{dv,\ worn}$, $P_{dv,\ slightly\ worn\ 1}$, $P_{dv,\ slightly\ worn\ 2}$, $P_{dv,\ new}$, $P_{dv,\ slightly\ hollow}$).

Similar to the contact stresses, the impact of the worn and slightly hollow wheel show the highest maximum P_{dv} values – up to 1.4 for the worn wheel. The new wheel has the lowest P_{dv} value with around 1.0. As the DV damage criterion depends on the stresses in the body, it is easy to retrace its dependence on the contact pressures. The maximum P_{dv} value, however, is further away from the surface for the slightly hollow wheel and closer to the surface for the worn wheel. From the worn to the new wheel, P_{dv} and the affected depth is decreasing, with about 1.2 at a depth of 0.9 mm and 1.1 at 1 mm, respectively. The maximum P_{dv} values of each wheel are shown in Fig. 11b. Fig. 11a shows the evaluated areas (similar to Fig. 10) with the position of the maximum values – indicated with colored points. We take the maximum values and refer to them as $P_{dv,max}$ Fig. 11b. It shows decreasing

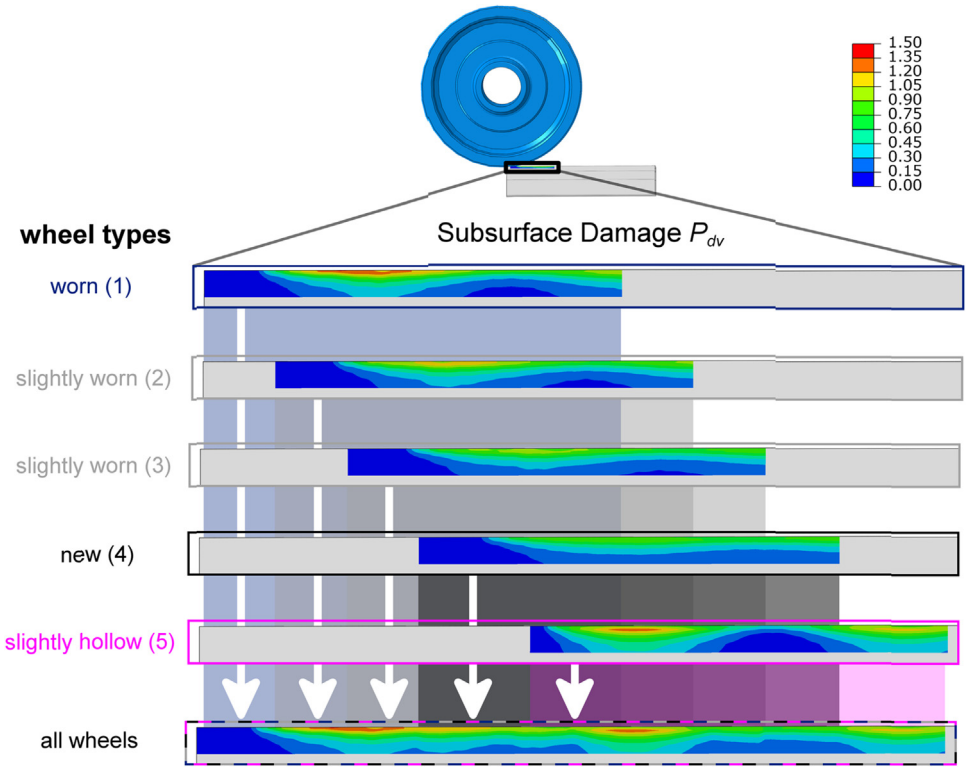

Fig. 10. Damage parameter P_{dv} for all wheels (worn (1), slightly worn ((2) and (3)), new (4) and slightly hollow (5)) and a combined plot showing the maximum P_{dv} values of all wheels.

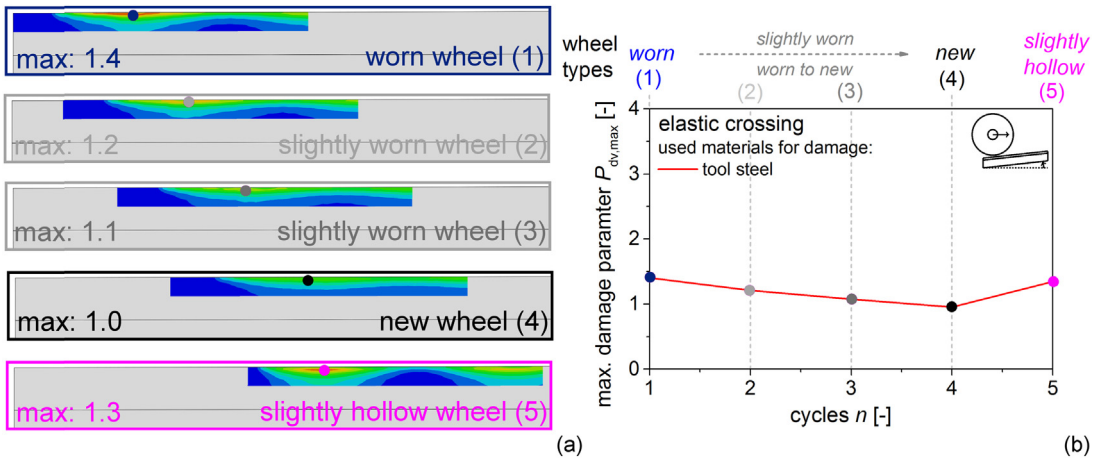

Fig. 11. The maximum damage for each wheel underneath the surface (subsurface) (right: worn to slightly hollow – 1–5) and its position during the impact (left).

values from worn to the new wheel and increasing values from the new to the hollow wheel, as described before. To discuss the calculated damage parameter P_{dv} in this paper, we use the combined plot of all wheels in Fig. 10 and the $P_{dv,max}$ plot of Fig. 11b.

Furthermore, when comparing the $P_{dv,max}$ over the cycles or wheel types, as shown Fig. 11b, to the downward angles α_{WR} in Fig. 5 in Section 3.1, we see that $P_{dv,max}$ and the downward angle α_{WR} of the wing rail show a similar tendency. The difference for the slightly hollow wheel is due to the larger head radius of the crossing nose at its impact position, which reduces the contact pressures.

4.2. Plastic calculation: contact forces, stresses and deformation

Within this section, the results of the model with plastic material behavior for all materials (manganese steel, chromium-bainitic steel and tool steel) are shown. We evaluate the vertical contact forces F and the contact pressure p for the last 5 cycles of the simulations (cycle 51st to 55th). Fig. 12 shows the contact forces F - (a), (c), (e) and (g) - and contact pressures p - (b), (d), (f) and (h). The results of the model with linear elastic behavior are shown in (a) and (b), whereas (c) and (d) shows the results for elastic-plastic material behavior of manganese steel, (e) and (f) of chromium-bainitic steel and (g) and (h) of tool steel.

The 5 plotted cycles (51st to 55th) correspond to different worn wheels: the solid blue line, the solid light gray and dashed dark gray lines, the solid black line and the dashed-dotted magenta line represent the worn (1), the slightly worn (2) and (3), the new (4) and the slightly hollow (5) wheel, respectively. When comparing the plastic calculation to the elastic one, we can see the effect of the plastic deformation on the dynamic forces and stresses.

The manganese crossings show the biggest change of the dynamic contact force over the simulated cycles, see Fig. 12c. Its impact positions are shifted not only due to the different wheels but also because of the plastically deformed geometry of the crossing, which causes a dent in the area around the impact positions. For the 51st to the 53rd cycle, the second peak of the vertical contact forces increases and becomes higher than the first due to the plastic deformation. There, the highest forces can be found for the slightly worn wheel (2) and the worn wheel (1) with values about 220 kN and 250 kN, respectively. The normal (4) and the hollow wheel (5), however, reach impact forces up to 200 kN and 220 kN at the first peak. When comparing the results to the one of the elastic crossing (cp. Fig. 12a), we see a slight increase of the maxima of all wheels, except for the slightly hollow wheel (5). The chromium-bainitic crossing (Fig. 12e) shows a similar behavior of the contact forces as the ones of the elastic crossing. The maximum contact force for the hollow wheel in the 55th cycle, however, reduces from 290 kN in the elastic calculation to 260 kN. The dynamic contact forces for the crossing with tool steel, cp Fig. 12g, behave similarly to the ones of elastic crossing too, except for the new wheel (4), which just has one small peak at the beginning, and the slightly hollow (5) wheel, where the maximum contact force increases up to 350 kN. The reason is the deformation of the crossing nose that creates a dent at the impact position of the hollow wheel, see Fig. 13. The high yield stresses of the tool steel crossing results in a local, but small deformation directly at the impact position. The small variety of differently worn wheels (and impact positions) – only 5 positions are chosen - enhances this effect and, together with the hardening of the material, prevents then further deformation around the dent. Impacts of more differently worn wheels or a small variation of the impact positions would spread the deformation of the crossing nose more smoothly.

Fig. 12d shows the contact pressures p for the manganese crossing. They have an average value of about 1.2 GPa and reach a maximum of about 1.5 GPa. Similar to its vertical contact forces, we see a belated impact due to the plastic deformation of the crossing. This adaption causes a reduction of 2.5 GPa when comparing the pressures of the slightly hollow wheel (magenta line) with the one of the elastic crossing (Fig. 12b: 4 GPa).

For, the chromium-bainitic crossing in Fig. 12f the maximum contact pressures for all wheels are around 3 GPa at the first peak after the impact, except the new wheel (4) with 2.5 GPa. In comparison to the crossing with elastic material, the maximum contact pressures decrease about 1 GPa for the impact of the worn (1) and hollow wheel (5) and 0.5–0.8 GPa for the impact of the new (4) and slightly worn wheels (2) and (3).

The contact pressures between the wheel and the crossing nose using tool steel material behavior, see Fig. 12h, show the lowest changes in comparison to the elastic crossing (Fig. 12b). The new wheel (4) has the lowest contact pressure with less than 3 GPa and the values for the slightly worn wheel (2) and (3) are 3.4 and 3.6 GPa, respectively. The maximum contact pressure of the impact of the worn wheel reduces to 3.9 GPa and for the slightly hollow wheel, it increases, similar to the contact force, about 0.25 GPa up to 4.2 GPa. The adaption potential of the contact pressures behaves according to the yield stress of the material: the tool steel has the highest values and the smallest changes and the manganese steel has the smallest values, showing a reduction of maximum contact pressures of 1.5 GPa. The chromium-bainitic crossing is in between those crossings and shows a reduction of the contact pressures after 50 cycles of up to 1 GPa.

Fig. 14 shows the crossing nose deformation due to the cyclic impacts of the wheels for all materials: the green, black and red lines represent the manganese steel, chromium-bainitic steel and tool steel crossings, respectively. The height is taken from the simulation model along the running direction of the wheel on the crossing nose. The

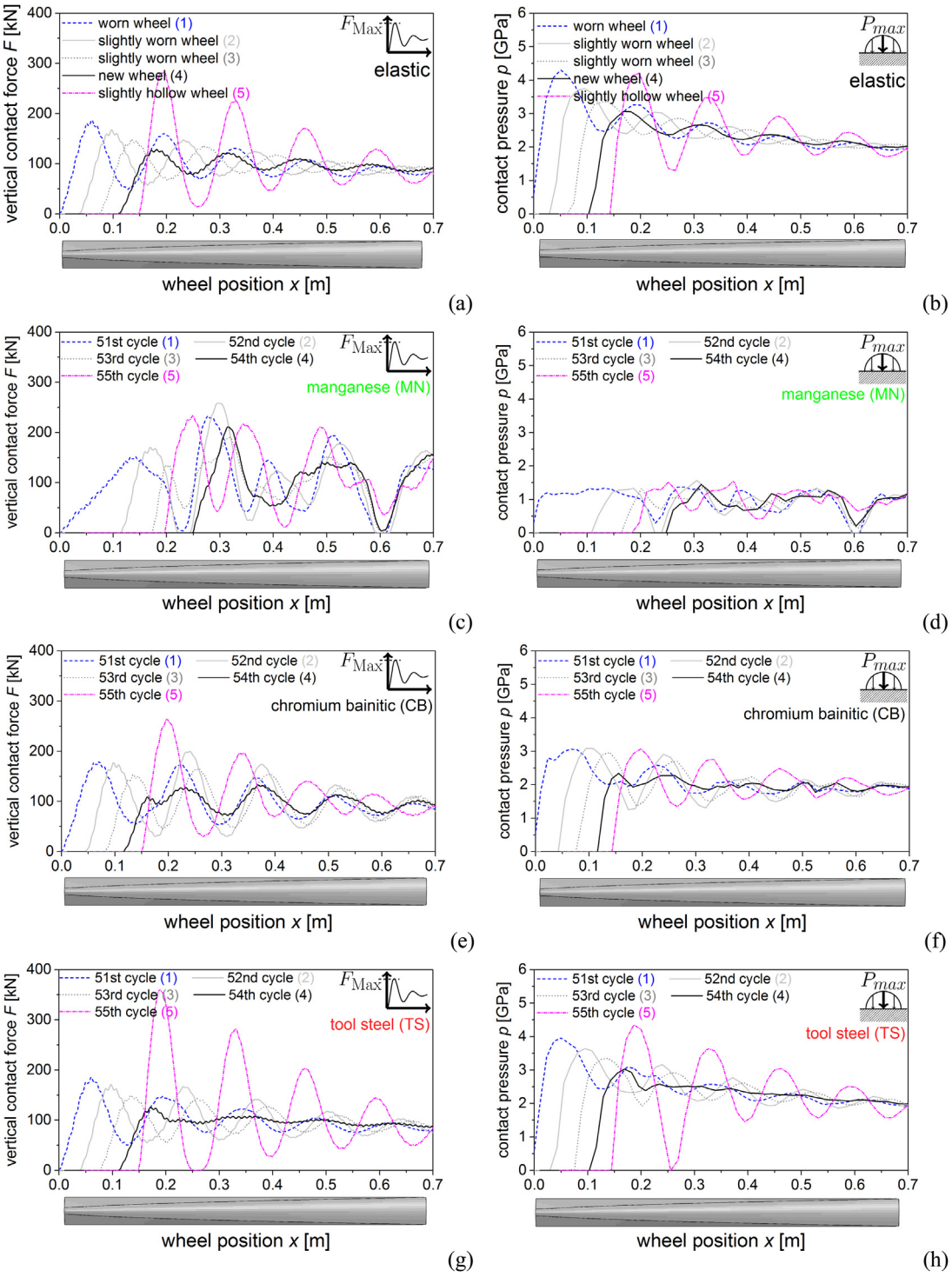

Fig. 12. The vertical contact forces F as the wheel impacts onto the crossing nose with spring/dashpot support and a static load of 79.7 kN for the crossing with (a) elastic and the used plastic materials ((c), (e), (g)) for the last 5 cycles (51–55). (b), (d), (f) and (g) show the contact pressure p during the impact of the wheel for the elastic and all used plastic materials, respectively.

crossing nose height after 55 cycles and its undeformed geometry (gray dotted line) is plotted in Fig. 14a. We see the highest height change Δy_{cn} (the difference of the undeformed height and the height of the deformed geometry) for all crossings directly after the impacts of the wheels between x = 0.05 m and x = 0.4 m.

Because of the high height change Δy_{cn} of the manganese steel, the impact position of the wheel shifts to the right. The reason is the linear downward movement of the wheel (cp. α_{WR} in Section 2.1), which does not change over the cycles. The previous impact cycles, however, "remove" the existing material due to plastic deformation. Fig. 14b shows a cross-sectional view of the manganese crossing at the position of the maximum Δy_{cn} (x = 0.315 m) after 55 cycles: it reaches a value of 0.7 mm. The chromium-bainitic steel and the tool steel have a maximum displacement (height change) of about 0.07 mm and 0.03 mm, respectively.

Fig. 15 shows the height displacement Δy_{cn} plotted over the simulated cycles. The chromium-bainitic steel and tool steel show a flat line with almost no height displacement increment after the first cycles. The

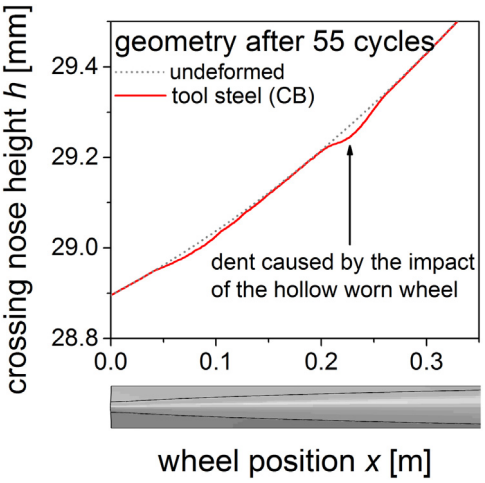

Fig. 13. Detail of the crossing nose deformation of the tool steel crossing.

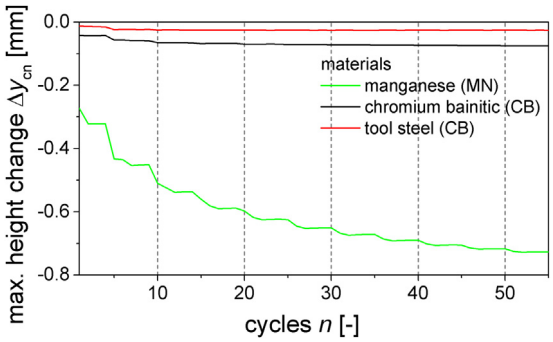

Fig. 15. The maximum height change Δy_{cn} of the crossing for all 55 cycles. The max. height change $\Delta y_{cn,max}$ for manganese steel in the last cycle is marked in Fig. 13. The results are shown for all materials: manganese, chromium bainitic and tool steel.

manganese crossing, however, starts with a very high height change Δy_{cn} of nearly 0.3 mm, shows a decreasing increment, reaches a value of about 0.7 mm after 55 cycles. The simulation still calculated minor height changes in the last cycles. In contrast, for chromium-bainitic steel and tool steel, we can assume a situation very close to elastic shakedown after 55 cycles. In our model, these deformations are purely caused by plastic deformations of the crossings. Therefore, Fig. 16 shows the accumulated equivalent plastic strains ((a), (b) and (c)) and the residual stresses in longitudinal direction ((d), (e) and (f)) for all materials after 55 cycles. The cutted area of the evaluation is similar to the one of the damage in Section 3.1.

As expected, the deformed manganese crossing (Fig. 16a) shows the highest accumulated equivalent plastic strains with values up to 30%. There are plastic strains throughout the depth of the plastically defined area. The chromium-bainitic steel crossing reaches acc. equiv. pl. strain values of about 6.5% close to the surface within the area around the impact position, see Fig. 16b. At the right end of the cutted area - after the impact positions of the different wheels - few elements reach acc. equiv. pl. strains up to 15%. This is due the recurring contact of different wheels at this position – an artefact that would be prevented if the number of worn wheels is increased These elements are outside the shown area and therefore not shown in Fig. 16. The tool steel (Fig. 16c) shows the smallest plastic strains with about 1.5% in the area, where the worn (1) and slightly hollow wheel (5) impacts.

Fig. 16d to f shows the residual stresses in the longitudinal direction σ_{xx}. Generally, the plastic deformations cause compressive residual stresses in regions of contact. Their minima in the cutted view are in the area of the impact positions of the wheels: −500 MPa for the manganese steel, −750 MPa for the chromium-bainitic steel, and - 490 MPa for the tool steel. The chromium-bainitic steel crossing, however, has higher values after the impact positions (see blue dots at the right end of the evaluated area: −1 GPa). In some areas of the manganese steel crossing nose positive residual stresses occur at the surface. When loaded cyclically this changes the stress ratio, which influences the crack growth behavior. Furthermore, for typical cracks at the surface of rails and crossing, this results in a mode 1 (opening) component for the fracture loading.

These positions and their depth correspond to the positions of high accumulated equivalent plastic strains in (a)-(c). The manganese crossing shows compressive residual stresses of about −150 MPa down to a depth of about 3 cm for the evaluated area around the impacts (yellow area). For the chromium- bainitic crossing and tool steel crossing similar values can be found in a maximum depth of about 0.65 cm and 0.55 cm, respectively. Both are around the impact position of the slightly hollow wheel.

4.3. Validation of the geometry adaption

The main feature of this work is the calculation of the cyclic plastic deformation of the crossing nose as this leads to a geometrical adaption that can change the loading of the crossings significantly. Thus, considering the plastic deformation is crucial for the material assessment of crossing noses. For validation, we compare the calculated deformations due to plastic deformation at the surface after 55 cycles with surface measurements of crossings in track published in [31]. To minimize the effects of wear, the earliest profile measurements after the installation

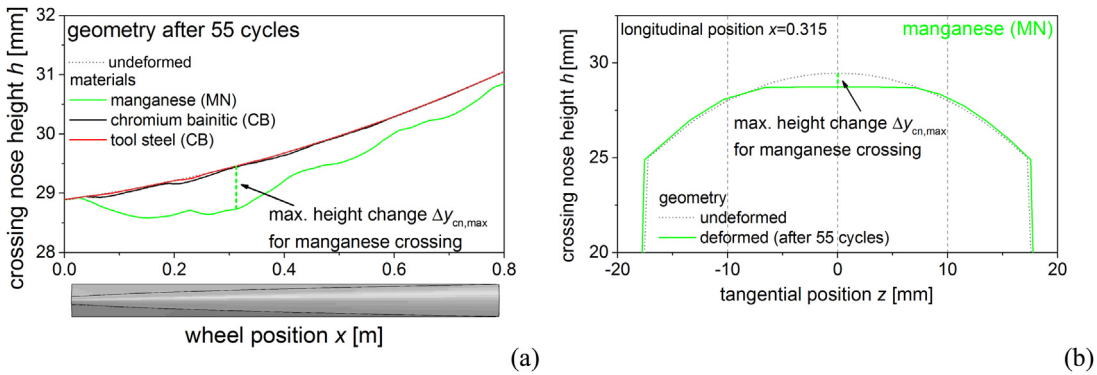

Fig. 14. (a) The crossing nose height h after 55 cycles for all materials: manganese (solid green), chromium bainitic (solid black) and tool steel (solid red) and (b) a crossectional view of the deformed (solid) and undeformed (dotted) geometry of the crossing using manganese material at the position of its maximum (x = 0.315 m).

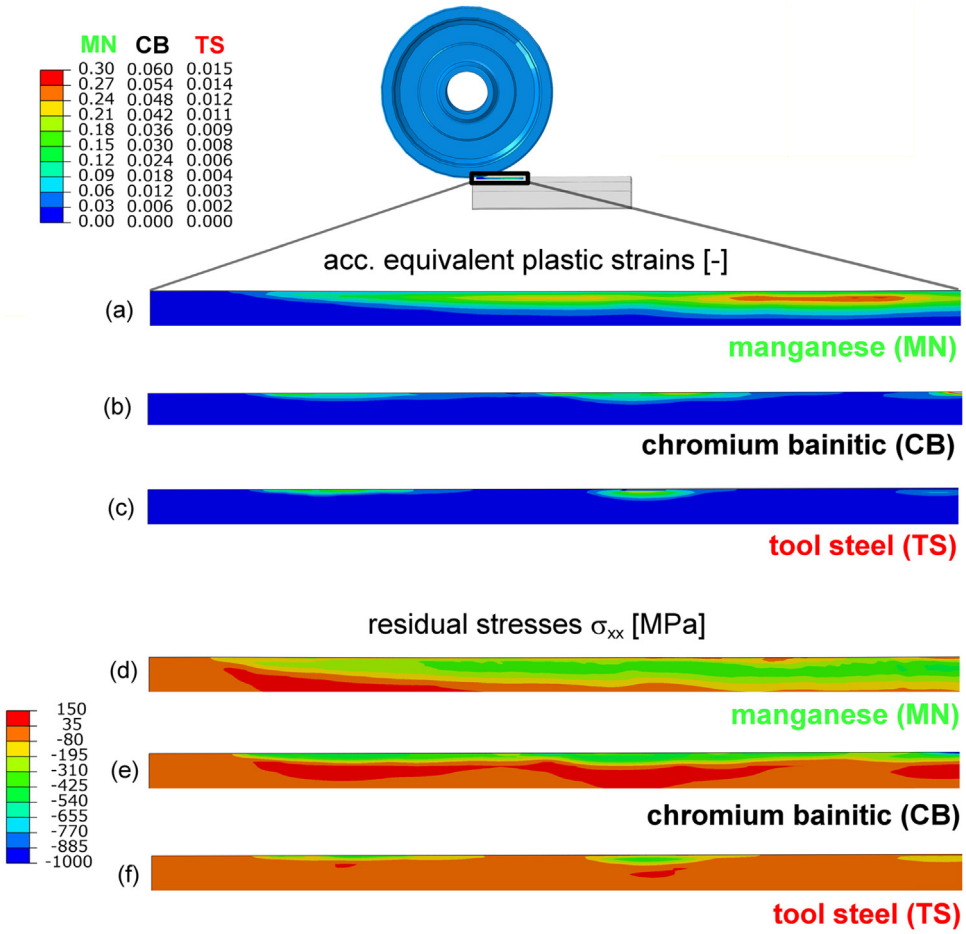

Fig. 16. Accumulated equivalent plastic strains - (a), (b) and (c) - and residual stresses in longitudinal direction σ_{xx} – (d), (e) and (f) - for crossings with manganese steel chromium-bainitic steel and tool steel, respectively.

in track are taken: a total amount of 3.5–4 MGT passed each crossing. Fig. 17 shows superimposed 2D plots of cross-sections for a crossing with (a) manganese steel, (b) chromium-bainitic steel and (c) tool steel. Positive values (0 mm to +1 mm: red) indicate a decrease and negative values (-1–0 mm: blue) indicate an increase of the surface height in comparison to the undeformed state.

Fig. 18 compares the height change Δy_{cn} of the simulation after 55 cycles (solid line) with the measurements (points): (a) represents the crossing with manganese steel, (b) chromium-bainitic steel and (c) tool steel. The height change Δy_{cn} is taken at the contact position of the crossing nose and wheel (wheel position) over a distance of 0.4 m on the crossing nose after the impact

Deformation trends between the three investigated materials show a good agreement of the simulations and measurements. The decreasing height change from manganese to chromium-bainitic and tool steel of both, the simulation and measurements, can be seen clearly and their difference (cp. the lines and dots) are in a reasonable range.

In our model, we are able to calculate the first impact cycles, whereas the measured crossings were loaded more frequently. Therefore, the model considers the plastic deformation, as this occurs

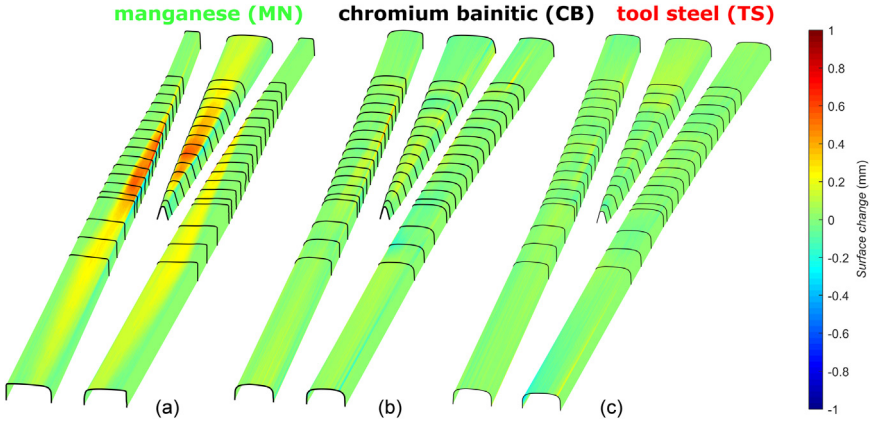

Fig. 17. Surface change for measured crossing geometries with (a) manganese (MN), (b) chromium bainitic (CB) and (c) tool steel (TS).

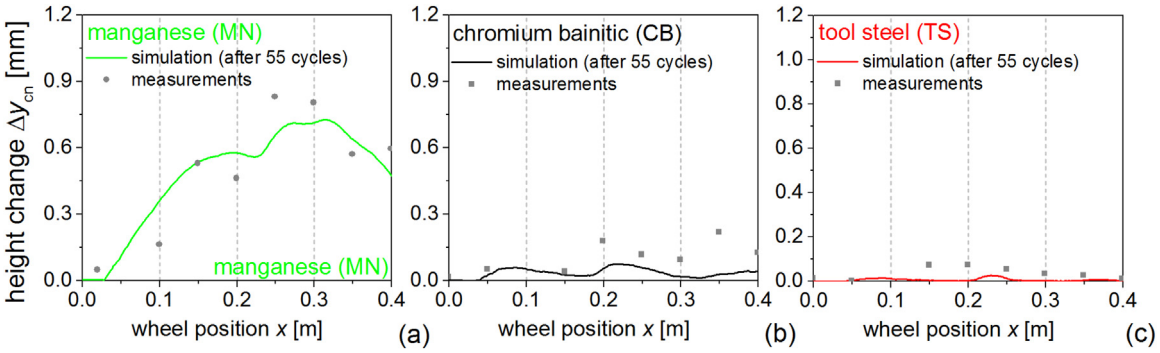

Fig. 18. The height change Δy_{cn} of the crossing nose after 55 cycles for (a) manganese (MN), (b) chromium bainitic (CB) and (c) tool steel (TS). The wheel position describes different positions in the running direction on the crossing nose. Note for manganese steel: In comparison to the crossing nose in the simulation model, the measurements were performed on an explosion-hardened crossing.

mainly in the first cycles, but it is limited to include other effects, such as wear. Furthermore, the initial geometry of the measured crossings are slightly different and the wheel loads of the passing trains and the profiles of the wheels are wide-spread, which is not covered in the simulation. Considering these inaccuracies, it is possible to track the differences of the simulation and measurements. The measurements of the manganese crossing were performed on an explosion-hardened crossing, whereas the crossing in the simulation model has no pre-deformation. Therefore, additional deformation is calculated in the model, which may explain why manganese steel shows the least differences. The crossings with chromium-bainitic (b) and tool steel (c), however, show larger differences. However, the measurements confirm the calculated deformation trends of the simulations, which allows for a comparison of the materials.

4.4. Damage initiation parameter P_{dv}: comparison and influences

In this section, we evaluate the damage initiation parameter P_{dv} for all crossings with plastic material behavior. In comparison to the results of the elastic crossing, a “run-in” condition is assumed. Therefore, we take the plastically deformed crossing after 50 cycles. By applying the DV criterion on the last 5 cycles, we can investigate the damage initiation for the different wheels including both, the deformed crossing and material history. The criterion is applied after the simulation in a post-processing routine and evaluates the impact of the current cycle (wheel type). We attempt to reach a near steady-state load case in cycle 50–55 and calculate the P_{dv} values for the stresses in those cycles. Using the graphical presentation of Fig. 10 in Section 3.1, Fig. 19 shows a combined plot of 5 different wheels (and cycles) for the three plastic crossings and one elastic crossing for comparison: (a) manganese steel, (b) chromium-bainitic steel, (c) tool steel and (d) the elastic steel crossing using the damage material parameters (α_{DV} and τ_f) of tool steel. In the combined plot of the crossing noses using plastic material models, we evaluated P_{dv} for the last 5 cycles (51st to 55th). The wheel and crossing nose above indicates the evaluated area. The damage parameter P_{dv} for the chromium-bainitic crossing and the tool steel

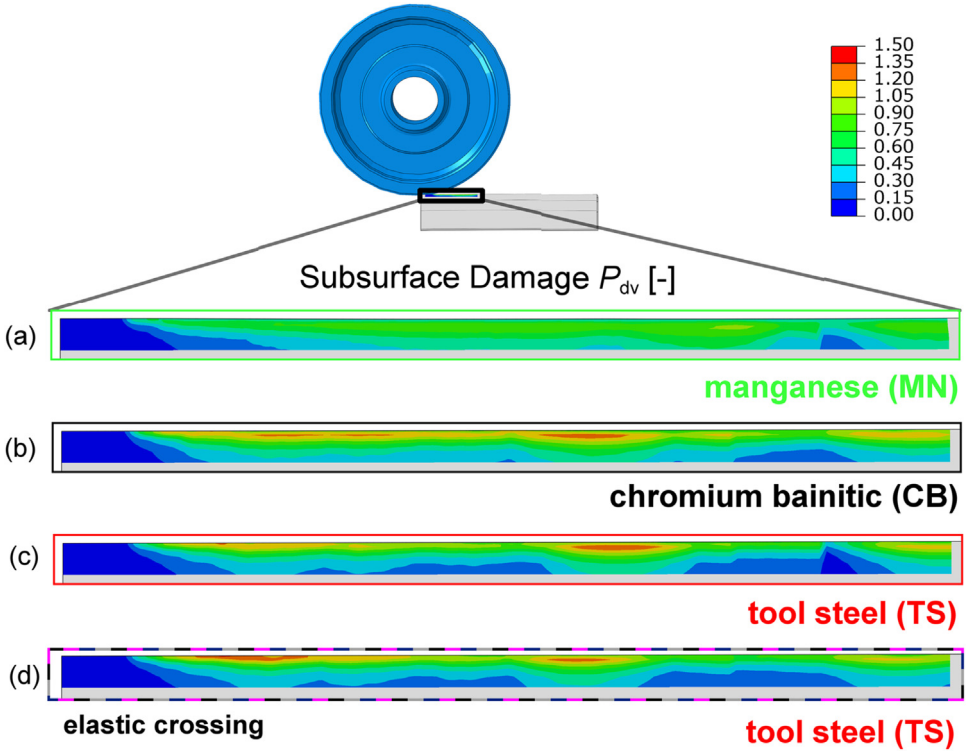

Fig. 19. Damage initiation P_{dv} for all wheels combined (worn, slightly worn #1 and #2, new and slightly hollow) for plastic material behavior of (a) manganese (MN), (b) chromium bainitic (CB), (c) tool steel (TS) and elastic material behavior with experimental DV parameters of tool steel.

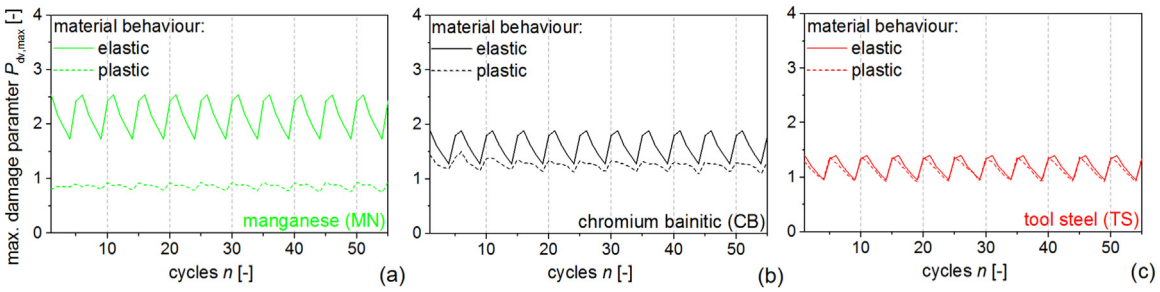

Fig. 20. The maximum damage $P_{dv,max}$ for each cycle for (a) manganese (MN), (b) chromium bainitic (CB) and (c) tool steel (TS).

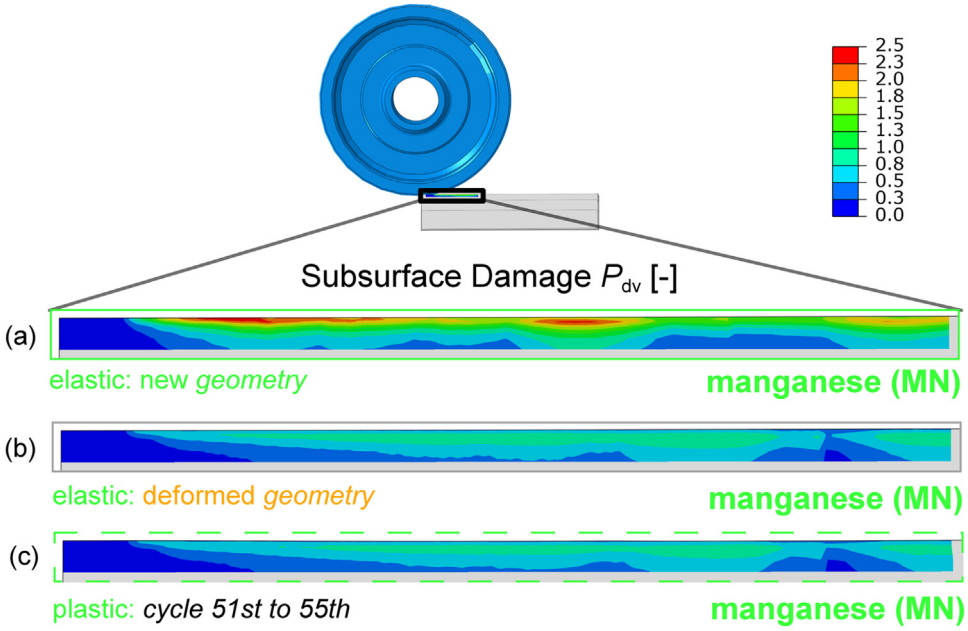

Fig. 21. Damage parameter P_{dv} for all wheels combined (worn, slightly worn, new and slightly hollow #1 and #2) with manganese damage values for (a) elastic material behavior with new geometry, (b) elastic material behavior with deformed geometry and (c) plastic material for cycle 51–55.

crossing have maximum values of about 1.5 and the manganese steel crossing about 1.0. All maxima are at the impact position of the worn (1) and slightly hollow wheel (5) at the beginning and in the right part of the cutted area in Fig. 19. The contour plot of the elastic crossing (d) shows no big changes to the one using the plastic material behavior of tool steel (c).

Fig. 20 shows the evolution of maximum damage initiation parameter $P_{dv,max}$ over the simulated cycles n for the crossings using plastic (dotted lines) and elastic (solid lines) material behavior. The recurring pattern (zig-zag) is due to the loading of the crossing with different wheels: it starts with a worn (1), ends with a slightly hollow (5) wheel and then starts all over again, as explained in Section 2.2.

The solid and dotted lines of the tool steel crossing in Fig. 20c confirm the similar P_{dv} values of the elastic and plastic crossing from Fig. 21c and d. For the crossing with manganese steel (Fig. 20a) and chromium-bainitic steel (Fig. 20b) a larger drop of the damage parameter $P_{dv,max}$ of the plastic (dotted) to the elastic results (solid) can be seen. The $P_{dv,max}$ values for the manganese crossing using elastic material behavior vary between 2.7 (worn (1) and slightly hollow wheel (5)) and 1.6 (new wheel (4)), whereas the model with plastic material behavior shows maxima between 0.8 and 1. The $P_{dv,max}$ values for chromium-bainitic steel drop from 1.9 (elastic) to 1.5 (plastic). Two reasons can explain this behavior:

1. The plastic deformation of the crossing flattens the crossing, which reduces the contact radius and increases the contact area. This lowers the contact forces and pressures, especially for manganese steel, see Fig. 12 and Fig. 14. This reduces the occurring stresses in the body and, therefore, the stress amplitude, which is used in the DV criterion.
2. The occurring residual stresses, which also contribute to this effect (see Sec. 3.3).

The DV material parameters, see Table 1, behave similarly to the yield stress: They are low for manganese steel and high for tool steel. The plastic deformation enables a positive adaption of the stresses in the crossing, an effect that is more distinct for materials with lower yield stress. In case of the manganese crossing, the $P_{dv,max}$ values are equal or less than 1.0, which is a reduction of more than 1.5 compared to the P_{dv} values of the crossing with elastic material behavior.

$P_{dv,max}$ over the cycles (and plastic deformation) for the plastic materials (dotted lines in Fig. 20), however, seems to be constant. The $P_{dv,max}$ values of the crossing with tool steel (Fig. 20c) shows almost no change over the simulated cycles and the values of the crossing with chromium-bainitic steel shows a reduction at the beginning and does not vary after half of the cycles. $P_{dv,max}$ of manganese crossing, however, has similar values (about 0.8) for all wheels at the beginning. Then, the zig-zag pattern of the $P_{dv,max}$ caused by the different wheels evolve. In the last cycles steady values for all wheels are reached. This result suggests a condition close to the elastic shakedown and will be

discussed in more detail in Section 4.5

4.5. Study: influence of material history on damage initiation

To evaluate the influence of the material history (residual stresses and hardening) and the small but - in some areas - continuing plastic deformation on the DV criterion, we create a model using the plastically deformed geometry of the manganese crossing after the 50th cycle with elastic material behavior. The model calculates the impact of the different worn wheels. We then evaluate the damage parameter P_{dv} using the DV material parameters of manganese steel and compare the results to the P_{dv} values of

- the manganese crossing with the plastic material (cycles 51st to 55th) and
- the crossing with elastic material and adapted geometry

Fig. 21 shows the damage parameter P_{dv} in a contour plot for the manganese crossing: (a) is the crossing with elastic material and new geometry, (b) the crossing with elastic material and deformed geometry and (c) the crossing with plastic material behavior (cycles 51st to 55th).

The P_{dv} values of the elastic crossing with the adapted geometry (b) show small changes to the one using the plastic material behavior (c). They are similar and at the same position. For both, the maximum P_{dv} values are around 1. The P_{dv} values for the elastic crossing, however, are slightly higher (an increase of about 0.04–0.1) compared to the effects of the deformed geometry, which means that there is a reduction due to the residual stresses and material hardening. This means, that the influence of the material history on the Dang-Van criterion is found to be low in comparison to the influence of the deformed geometry. Furthermore, this suggests that, even for manganese steel crossings, where the highest plastic deformation occurs, a condition close to the elastic shakedown has been achieved

Fig. 22a shows the maximum damage parameter $P_{dv,max}$ for the last five cycles for the material and geometry combinations mentioned before. It shows the higher maximum values $P_{dv,max}$ of the elastic crossing with adapted geometry (solid orange line) compared to the plastic one (dotted green line) and the elastic crossing with new geometry (solid green).

The same comparison is done for chromium-bainitic steel in Fig. 22b and tool steel in Fig. 22c. The orange line represents $P_{dv,max}$ of the adapted geometry of manganese steel with elastic material behavior. P_{dv} is calculated using the DV material parameters for chromium-bainitic steel and tool steel, respectively (see Table 1). Now, the effect of an adapted geometry on the damage parameter P_{DV} for higher strength steels, which do not plastically adapt in the first 55 cycles, can be studied.

For chromium-bainitic steel, see Fig. 22b, the $P_{dv,max}$ values of the crossing with the adapted geometry are less than 1 (orange dashed-dotted). They reduce about 0.5 for all cycles compared to $P_{dv,max}$ of the crossing with plastic material (black dotted) and about 1 for the first and last cycle for the crossing with elastic material (black solid).

Fig. 22c shows $P_{dv,max}$ of about 0.5 for all cycles for tool steel and the adapted geometry of manganese steel (orange dashed-dotted). This is a reduction of about 0.9 for the first and last cycle, when compared to the tool steel crossing with a new geometry and elastic (red solid) and plastic (red dotted) material behavior (it drops from 1.4 to 0.5). For both steels the adapted geometry clearly shows a positive influence: their damage values are less than 1, which means no damage initiation according to the DV criterion. Compared to manganese steel, the Dang-Van material parameters (α_{DV} and τ_f) of high strength steels are much higher. This is the reason for the significant reduction of the P_{dv} values compared to the ones of manganese steel with the run-in geometry.

5. Conclusion

The observed performance of three different materials (manganese steel, chromium-bainitic steel and tool steel) used in railway crossings is explained and a methodology for material selection is presented. To investigate this problem the Dang-Van (DV) damage criterion is applied on cyclically loaded and deformed crossings. As a result of modeling and analysis, the major findings concerning differences in the wear and damage of the three steels are:

(a) For all materials, the impact of a worn and slightly hollow wheel showed the highest damage initiation values P_{dv}, the new wheel showed the lowest ones.
(b) For all materials, a reduction of the damage initiation value P_{dv} for the plastically deformed crossings is observed when comparing it to the impact on an undeformed crossing with elastic material. This effect decreases with increasing yield stress of the materials.
(c) The crossing with manganese steel shows the lowest P_{dv} values. The higher strength steels show higher values. Neglecting the plastic deformation, the crossing with manganese steel has the highest damage values, due to the low DV material parameters. The geometry adaption of the manganese crossing is found to be the main reason for low P_{dv} values, due to the decrease of loads.
(d) The influence of residual stresses on the damage initiation values P_{dv} is found to be negligible in comparison to the reduction caused by the plastic deformation.
(e) Suggestions are made on how to reduce the initiation P_{dv} (and occurring stresses) for high strength steels. If the deformed geometry of the manganese crossing is used for steels with a high yield stress, which do not plastically adapt, the calculations show a significant reduction of P_{dv} values.

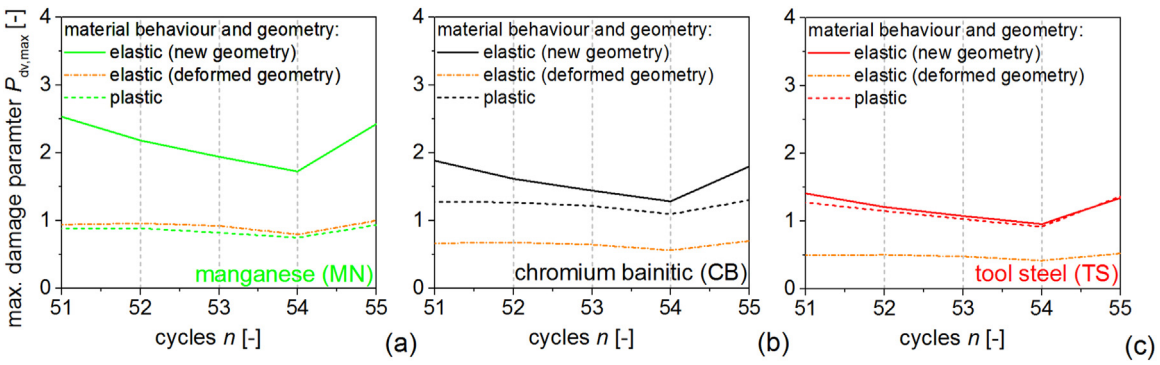

Fig. 22. The maximum damage $P_{dv,max}$ for cycle 51–55 for (a) manganese steel, (b) chromium-bainitic steel and (c) tool steel with a new geometry (solid line), worn geometry (dashed-dotted orange) and after 50 cycles (dotted)).

If high deformations occur, it turned out that it is very important to include plastic material description in the calculations as they influence the stress situation and thus the P_{dv} values and their positions. If this is not considered, a run-in geometry for simulations should be used. Taking these points into account, the DV damage criterion represents a useful method for evaluating damage in crossing noses.

Acknowledgements

Financial support by the Austrian Federal Government (in particular from Bundesministerium für Verkehr, Innovation und Technologie and Bundesministerium für Wissenschaft, Forschung und Wirtschaft) represented by Österreichische Forschungsförderungsgesellschaft mbH and the Styrian and the Tyrolean Provincial Government, represented by Steirische Wirtschaftsförderungsgesellschaft mbH and Standortagentur Tirol, within the framework of the COMET Funding Programme is gratefully acknowledged. Furthermore, we want to thank A. Ekberg for his help during the implementation of the damage criterion.

References

[1] H. Hertz, Über die Berührung fester elastischer Körper, J. für die reine und Angew. Math. 92 (1881) 156–171.
[2] A. Ekberg, E. Kabo, Fatigue of railway wheels and rails under rolling contact and thermal loading—an overview, Wear 258 (7–8) (2005) 1288–1300.
[3] E. Kassa, C. Andersson, J.C.O. Nielsen, Simulation of dynamic interaction between train and railway turnout, Veh. Syst. Dyn. 44 (3) (2006) 247–258.
[4] W.Y. Yan, T. Antretter, F.D. Fischer, H. Blumauer, Numerical Analysis of the Cyclic Response of a Crossing Component in a Switch, Verformungskundliches Kolloquium XIX, Leoben, Austria, 2000.
[5] M. Wiest, W. Daves, F.D. Fischer, H. Ossberger, Deformation and damage of a crossing nose due to wheel passages: contact Mechanics and Wear of Rail/Wheel Systems - CM2006, Wear 265 (9–10) (2008) 1431–1438.
[6] M. Pletz, W. Daves, H. Ossberger, A wheel set/crossing model regarding impact, sliding and deformation—Explicit finite element approach, Wear 294–295 (2012) 446–456.
[7] Ossberger, U., Pletz, M., Eck, S., Daves, W. (eds) (2013) Validation of a finite element crossing model using measurements at an instrumented turnout in: Proceedings of the 23rd Symposium on Dynamics of Vehicles on Roads and Tracks, Qingdao, China.
[8] M. Pletz, W. Daves, W. Yao, H. Ossberger, Rolling contact fatigue of three crossing nose materials—Multiscale FE approach in: Proceedings of the 9th International Conference on Contact Mechanics and Wear of Rail / Wheel Systems, Chengdu, 2012. Wear, **314** (1–2), pp. 69–77, 2014.
[9] L. Xin, V.L. Markine, I.Y. Shevtsov, Numerical analysis of the dynamic interaction between wheel set and turnout crossing using the explicit finite element method, Veh. Syst. Dyn. 54 (3) (2016) 301–327.
[10] J. Wiedorn, W. Daves, U. Ossberger, H. Ossberger, M. Pletz, Simplified explicit finite element model for the impact of a wheel on a crossing – Validation and parameter study, Tribol. Int. 111 (2017) 254–264.
[11] J. Wiedorn, W. Daves, H. Ossberger, M. Pletz, A Simplified Dynamic Finite Element Model for the Impact of a Wheel on a Crossing: Validation and Parameter Study, in: Proceedings of the Third International Conference on Railway Technology: Research, Development and Maintenance (ed J. Pombo), Cagliari, Sardinia, Italy. Civil-Comp PressStirlingshire, UK, 2016.
[12] Y. Ma, A.A. Mashal, V.L. Markine, Modelling and experimental validation of dynamic impact in 1: 9 railway crossing panel, Tribol. Int. 118 (2018) 208–226.
[13] K. Dang Van, B. Griveau, On a New Multiaxial Fatigue Limit Criterion: Theory and Application, EGF3, Mechanical Engineering Publications, *London*, 1989, pp. 476–496.
[14] W. Daves, W. Kubin, S. Scheriau, M. Pletz, A finite element model to simulate the physical mechanisms of wear and crack initiation in wheel/rail contact, Wear 366–367 (2016) 78–83.
[15] K. Dang Van, M.H. Maitournam, B. Prasil, Elastoplastic analysis of repeated moving contact application to railways damage phenomena, Wear 196 (1–2) (1996) 77–81.
[16] K. Dang Van, M.H. Maitournam, On some recent trends in modelling of contact fatigue and wear in rail, Wear 253 (1–2) (2002) 219–227.
[17] K. Dang Van, M.H. Maitournam, Z. Moumni, F. Roger, A comprehensive approach for modeling fatigue and fracture of rails, Eng. Fract. Mech. 76 (17) (2009) 2626–2636.
[18] A. Ekberg, E. Kabo, H. Andersson, An engineering model for prediction of rolling contact fatigue of railway wheels, Fat. Frac Eng. Mat. Struct. 25 (10) (2002) 899–909.
[19] A. Ekberg, B. Åkesson, E. Kabo, Wheel/rail rolling contact fatigue – Probe, predict, prevent, Wear 314 (1–2) (2014) 2–12.
[20] H. Desimone, A. Bernasconi, S. Beretta, On the application of Dang Van criterion to rolling contact fatigue, Wear 260 (4–5) (2006) 567–572.
[21] M. Ciavarella, F. Monno, G. Demelio, On the Dang Van fatigue limit in rolling contact fatigue, Int. J. Fatigue 28 (8) (2006) 852–863.
[22] M. Ciavarella, F. Monno, A comparison of multiaxial fatigue criteria as applied to rolling contact fatigue, Tribol. Int. 43 (11) (2010) 2139–2144.
[23] W. Weibull, A statistical distribution function of wide applicability, J. Appl. Mech. 18 (3) (1951) 293–297.
[24] J. Wiedorn, W. Daves, H. Ossberger, U. Ossberger, M. Pletz Using stress-based damage models to describe subsurface damage in crossings, Paper presented to in: Proceedings of the 11th International Heavy Haul Association Conference 2017, Cape Town, South Africa.
[25] A. Bernasconi, Efficient algorithms for calculation of shear stress amplitude and amplitude of the second invariant of the stress deviator in fatigue criteria applications, Int. J. Fatigue 24 (6) (2002) 649–657.
[26] Practice for Statistical Analysis of Linear or Linearized Stress-Life (S-N) and Strain-Life (-N) Fatigue Data (2015), E08 Committee, West Conshohocken, PA.
[27] Wolfram Research Mathematica, Version 11.0, Champaign, Illinois, 2016.
[28] ABAQUS 6.12 Documentation. ⟨www.simulia.com⟩.
[29] J. Kunz, Kontaktprobleme und ihre praktische Lösung, Konstruktion 61 (2009) 54–58.
[30] X. Zhao, Z. Li, The solution of frictional wheel–rail rolling contact with a 3D transient finite element model: Validation and error analysis in: Proceedings of the 8th International Conference on Contact Mechanics and Wear of Rail / Wheel Systems, Florence, 2009. *Wear*, 271 (1–2), 444–452, 2011.
[31] U. Ossberger, S. Eck, E. Stocker Performance of different materials in a frog of a turnout, in: Proceedings of the IHHA 2015 - International Heavy Haul Association Conference2015.

Paper C

Finite element model for predicting the initiation of subsurface damage in railway crossings - A parametric study

AUTHORS

Julian Wiedorn[1], Werner Daves, Uwe Ossberger, Heinz Ossberger, Martin Pletz

[1] **corresponding author**

JOURNAL

Published in Journal of Rail and Rapid Transit (ISSN: 0954-4097).

ABSTRACT

In this study, the initiation of subsurface damage due to the impact of new and worn wheels on differently deformed crossing nose geometries is calculated using the Dang-Van criterion. Three crossings with different materials (manganese steel, chromium-bainitic steel, and tool steel) were cyclically loaded in an FE crossing model reported in a previous study to evaluate the run-in state of plastic deformation. The impacts of the wheels on the deformed crossings were then calculated by considering the behavior of an elastic material. This parametric study showed the effects of different velocities, axle loads, and wheel types on the vertical contact forces, contact pressures, and Dang-Van damage parameters. Additionally, the ability of manganese steel crossings to withstand unfavorable load situations was observed by including plastic material behavior and considering material history, such as residual stresses and hardening.

CONTRIBUTION

Responsible for the development of the method.
Carried out the numerical simulations.
Wrote most parts of the paper.

Original Article

Institution of MECHANICAL ENGINEERS
Journal of RAIL AND RAPID TRANSIT

Proc IMechE Part F:
J Rail and Rapid Transit
0(0) 1–15

DOI: 10.1177/0954409718797039
journals.sagepub.com/home/pif
SAGE

Finite element model for predicting the initiation of subsurface damage in railway crossings—A parametric study

Julian Wiedorn[1], Werner Daves[1], Uwe Ossberger[2], Heinz Ossberger[2] and Martin Pletz[3]

Abstract

In this study, the initiation of subsurface damage due to the impact of new and worn wheels on differently deformed crossing nose geometries is calculated using the Dang-Van criterion. Three crossings with different materials (manganese steel, chromium-bainitic steel, and tool steel) were cyclically loaded in an FE crossing model reported in a previous study to evaluate the run-in state of plastic deformation. The impacts of the wheels on the deformed crossings were then calculated by considering the behaviour of an elastic material. This parametric study showed the effects of different velocities, axle loads, and wheel types on the vertical contact forces, contact pressures, and Dang-Van damage parameters. Additionally, the ability of manganese steel crossings to withstand unfavorable load situations was observed by including plastic material behavior and considering material history, such as residual stresses and hardening.

Keywords

Simulation, crossing, subsurface damage, finite elements, plasticity, wheel/rail contact, contact forces, contact pressures, plastic adaption

Date received: 31 March 2018; accepted: 28 July 2018

Introduction

Railroad switches are components of the railway track which guide trains from one track to the other. The crossing (or frog) is a part of the turnout—the intersection of two rails, see Figure 1. The figure shows a typical 1:12 crossing with the wing rail and crossing nose marked green and red, respectively. This type of crossing is a fixed crossing, as it contains no movable part. In the facing direction, the wheel initially runs on the wing rail and transitions to the crossing nose.

Due to its construction, the crossing acts as an interruption of the continuous track system and is heavily loaded during the transition, which can cause severe damage. The main reason is the downward and upward movement of the wheel during the transition from the wing rail to the crossing nose (impact) and the high contact pressures at the crossing nose when the wheel impacts onto the crossing nose.

Different types of materials can be used—low strength and high strength steels, such as manganese steel or tool steel (experimental), respectively. Their concepts of application are very different: manganese steel enables plastic deformation to lower the occurring stresses and tool steels have very high yield stresses and withstand the impact loads with small plastic deformation.

To evaluate the tendencies for damage initiation, the Dang-Van (DV) damage criterion[1] can be used. The criterion was first introduced by Van who attempted to predict damage, such as crack initiation. It is based on stress fields for loading in the elastic shakedown regime and indicates the location and direction of the damage initiation. The criterion is used in a variety of ways: for typical rail damage, such as head-checks,[2] in combination with crack propagation,[3] or as part of a larger damage model.[4] Desimone et al.[5] and Ciavarella and Monno,[6] however, criticized the criterion of being too conservative for wheel/rail rolling contact fatigue in particular cases and proposed modifications of the damage locus of the criterion.

[1]Materials Center Leoben Forschung GmbH, Leoben, Austria
[2]voestalpine VAE GmbH, Zeltweg, Austria
[3]Department of Polymer Engineering and Science, Montanuniversitaet Leoben, Leoben, Austria

Corresponding author:
Julian Wiedorn, Materials Center Leoben Forschung GmbH, Rlseggerstraße 12, Leoben 8700, Austria.
Email: Julian.wiedorn@mcl.at

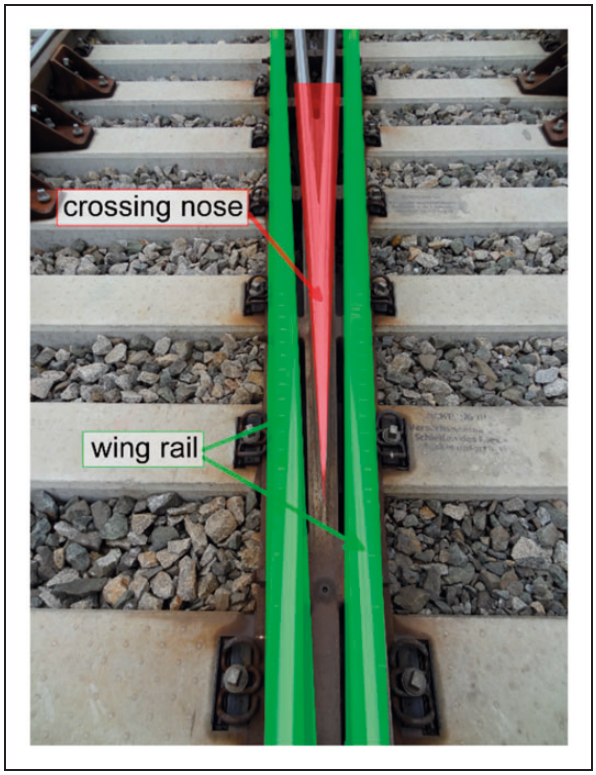

Figure 1. Typical fixed crossing in a track.

As mentioned before, stresses are needed to calculate the subsurface damage parameter values. A method to evaluate the stress and strain fields during the impact on a crossing is the explicit finite element (FE) method. Wiest et al.[7] and Pletz et al.[8] introduced different models based on this method. Furthermore, Pletz already calculated cyclic deformation and crack propagation using different materials.

Another method is the multibody simulation, which is fast but does not directly calculate stress fields nor plastic deformation. Interesting work using this method on crossings was done by Kassa et al.[9] and extended by Andersson and Abrahamsson[10] Just recently, Skrypnyk et al. added further simplifications regarding plastic deformation.[11]

In this work, the authors use an FE crossing model simplifying some features of the real geometry based on the work of Pletz et al.,[8] which was introduced and validated.[12,13] It contains a wheel, which runs on a contact spring (wing rail) and a simplified crossing nose geometry, which uses parameters extracted from a given geometry. The authors extended this model to describe a more realistic contact geometry and validated its plastic surface deformation.[2]

They showed the importance of considering plastic deformation for the evaluation of damage initiation during the impact of differently worn wheels on crossing noses.

In this paper, the model from Wiedorn et al.[2] is used to perform a comprehensive parametric study on the subsurface damage initiation for three crossing nose materials: manganese steel, chromium-bainitic steel, and tool steel. The parameters include different worn wheels, axle loads, and velocities. The previously calculated deformed geometries for the selected materials are taken and the linear-elastic material behavior is assumed. Additionally, we perform a case study to show the ability of manganese steel crossings to handle unfavorable load situations (high axle load and high velocity) in the run-in state using plasticity.

Damage: Concept, materials, and experimental evaluation

To consider multiaxial fatigue, Dang Van and Griveau[1] introduced a criterion for the high cycle fatigue regime, which is based on the macroscopic stresses in the body. Two material parameters that are evaluated experimentally by bending and torsion experiments are needed to consider the multiaxiality in the criterion. The equivalent stresses $\tau_{\mathrm{eq,dv}}$ are defined as

$$\tau_{\mathrm{eq,\,dv}}(t) = \tau_{\mathrm{a}}(t) + \alpha_{\mathrm{dv}}\sigma_{\mathrm{h}}(t) < \tau_{\mathrm{f}} \tag{1}$$

with the shear stress amplitude τ_{a}; the hydrostatic stress σ_{h}; the current time t during one loading cycle; the DV material parameter α_{dv} and τ_{f}, the shear–torsion fatigue limit.

By transforming equation (1), we introduce the DV damage variable P_{dv} with

$$P_{\mathrm{dv}} = \max_{0 \leqslant t \leqslant T_{cycle}} \frac{\tau_{\mathrm{a}}(t)}{\tau_{\mathrm{f}} - \alpha_{\mathrm{dv}}\sigma_{\mathrm{h}}(t)} \tag{2}$$

Subsurface damage is evaluated for every wheel impact with the total time period T_{cycle} for one impact ($t \in T_{\mathrm{cycle}}$). A P_{dv} value above 1 indicates subsurface damage initiation and a P_{dv} value below 1 indicates no damage initiation.

The criterion calculates damage using shear stress amplitudes. Therefore, a median stress σ_{mid} has to be found. We do this by using a min–max optimization, which minimizes the largest von Mises stress occurring during the total time period T. A detailed explanation and validation of the routine is done by Bernasconi.[2]

With the stress amplitude $\sigma_{\mathrm{ij,a}}(t)$ for every time t the shear stress amplitude $\tau_{\mathrm{a}}(t)$ can be calculated as

$$\tau_{\mathrm{a}}(t) = \frac{1}{2}\max\left(\left|\sigma_{1,\mathrm{a}}(t) - \sigma_{2,\mathrm{a}}(t)\right|, \left|\sigma_{1,\mathrm{a}}(t) - \sigma_{3,\mathrm{a}}(t)\right|, \left|\sigma_{2,\mathrm{a}}(t) - \sigma_{3,\mathrm{a}}(t)\right|\right) \tag{3}$$

The calculation is performed in Wolfram Mathematica© as part of postprocessing for a chosen number of FEs around the impact position.

In a previous work,[13] we investigated three different materials in this paper: manganese steel, chromium-bainitic steel, and tool steel.[2,14] From a

mechanical point of view, the main difference between the tested materials is their yield stress and hardening behavior: Manganese steel has a low yield stress but a distinct work hardening behavior; tool steel and chromium-bainitic steel, however, have higher yield stresses, but less work hardening.

Fatigue testing to evaluate the SN curves was done with 25 polished specimens for each material: rotational bending using an experimental setup similar to the one in Khalid et al.[15] and alternating torsion similar to the one in Shimizu et al.[16]

The manganese steel was rolled, solution annealed, and quenched; the tool steel forged, quenched, and tempered; and the chromium bainitic steel rolled, naturally cooled, and tempered. The fatigue parameters were evaluated according to the ASTM E739 standard[17] with the arcsine-sqrt(P) method in the fatigue endurance regime. The parameters are based on 50% probability and the results are shown in Table 1.

The negative α_{dv} (see Table 1) is changed to 0.0, as negative values do not confirm the common observation that increasing hydrostatic stresses decrease the damage initiation value P_{dv}.

Figure 2 shows the graphical representation of the threshold limit of the damage criterion. The solid lines represent the damage locus for each material. Shear stress values above the damage loci have P_{dv} damage values larger than 1, which indicates subsurface damage initiation. Bending and torsion experiments allow us to create this damage locus and consider a multiaxial loading regime. For each experimental evaluation, a different multiaxial loading occurs, which means different shear and hydrostatic stresses. This gives us two points and enables us to create a damage locus by assuming a linear relationship between them.

The green, black, and red lines in Figure 2 represent the different materials: manganese, chromium-bainitic, and tool steel, respectively. The uncorrected manganese steel is shown as a dotted line in the figure. The increasing max. shear stresses in the negative (compressive) hydrostatic stress region indicate an increased strength against fatigue damage. At $\sigma_h = 0$ MPa, the max. shear stresses represent the shear–torsion fatigue limit τ_f, evaluated from the experiments. "General results" section gives a detailed explanation on how the criterion is applied to evaluate a crossing nose.

Table 1. The parameters for the DV damage criterion.

	DV parameters	
Materials	τ_f (MPa)	α_{dv} (–)
Chromium bainitic steel (CB)	375	0.07
Tool steel (TS)	500	0.11
Manganese steel (Mn)	278	0 (−0.06)

DV: Dang-Van.

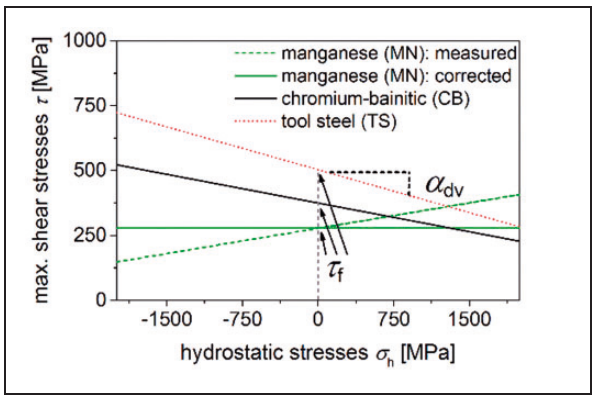

Figure 2. Graphical representation of the damage criteria for all three materials: manganese steel, chromium-bainitic steel, and tool steel.

Simulation model

The stresses occurring during the impact of a wheel on a crossing depend on different parameters, such as the loading conditions and material behavior (yield stresses and hardening). To calculate the stresses and strain fields we introduce a simplified FE model, where a wheel impacts onto the crossing nose. The simplifications of the FE model are taken from Wiedorn et al.[2,12] The input parameters of the model, which mimic different wheel types (impact position, wing rail downward angle and radius, crossing nose height, and head radii) are expanded to consider slip due to the transition of the wheel from the wing rail to the crossing nose.

Evaluation of input parameters

Figure 3 shows the vertical displacement Δh of a wheel with a new, worn, and hollow-worn profile on

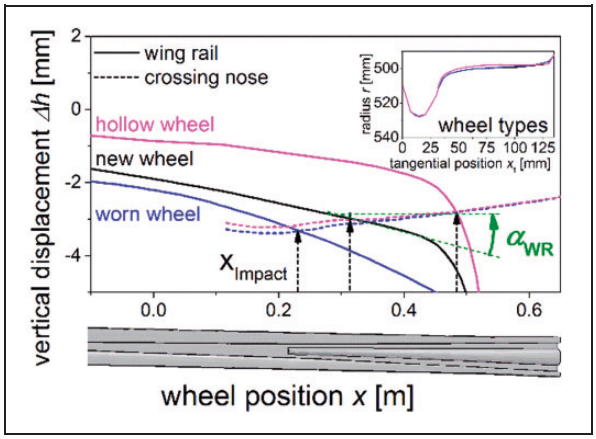

Figure 3. The trajectories of the three wheel profiles running along the wing rail and the crossing nose geometry with two input parameters: x_{Impact} and α_{WR}.

a 60E1-500-1:12 CENTRO crossing type. The new wheel is based on an ORE S1002 profile. The different profiles due to wear are shown in the embedded figure in the right corner, referred to as new, worn, and hollow wheel. The evaluation of the vertical displacement is done as preprocessing statically with a routine stated in Wiedorn et al.[12]

The wheels initially run on the wing rail (solid line) and transition to the crossing nose (dotted line)—its intersection is called impact position x_{Impact}. x_{Impact} and the wing rail downward angle α_{WR} are different for the chosen wheels and can describe the impact of a wheel on the crossing nose:

- The worn wheel has the lowest impact position and a downward angle between the new and the hollow wheel.
- The hollow wheel continues to run on the wing rail, which means a belated impact and a rather large wing rail downward angle.
- The impact position x_{Impact} of the new wheel is in between those two and has the lowest wing rail downward angle.

Figure 4(a) shows the wing rail downward angle α_{WR} and their evaluated impact positions. To increase the variation, we select five points (dots in Figure 4(b)), which depend on the three different wheel profiles. Furthermore, as the model simplifies the wing rail, the wing rail head radius r_{WR} is evaluated at the impact positions. r_{WR} is then used as the parameter of a nonlinear contact spring k_{WR} (see Figure 6). α_{WR} and r_{WR} are evaluated on the undeformed wing rail with the routine stated in a previous work.[2]

In this paper, we use a run-in geometry with the impact loads stated before (solid lines in Figure 4(b)). The resulting initial crossing nose geometries are shown in Figure 4(b).

The undeformed geometry (gray dotted in Figure 4(b)) uses

- the vertical displacement Δh (Figure 3) as input for the crossing nose height h and
- the wheel/crossing nose contact radius as the crossing nose head radius r_{cn} (see Figure 6).

In Wiedorn et al.,[2] we use the plastic material behavior of three different materials (manganese, chromium-bainitic, and tool steel) and simulate 55 impact cycles of the wheel on the crossing nose. Due to the different material behavior, the deformations are different for all materials. The deformed geometries define the initial crossing nose geometries for the simulations in this paper.

In addition to previous works,[2,12] we include the slip of the wheel due to the transition from the wing rail to the crossing nose in a simplified way. Figure 5 shows the model used for the parameter evaluation (a) and the used creepage–traction relationship and the change of the wheel rolling radius in contact.

The system shown in Figure 5(a) can be described with

$$I_{\text{wheel}}\dot{\omega} = -T_R\, r_{wc} \tag{4}$$

where I_{wheel} is the wheel inertia, $\dot{\omega}$ is the angular acceleration, and T is the frictional force at the contact position with the wheel rolling radius r_{wc}. T_R depends on the normal force Q and the current creepage of the system with the relationship shown in Figure 5(b). We assume quasi-static creepage and define the creepage c with

$$c = \frac{r_{wc}\,\omega - v}{v} \tag{5}$$

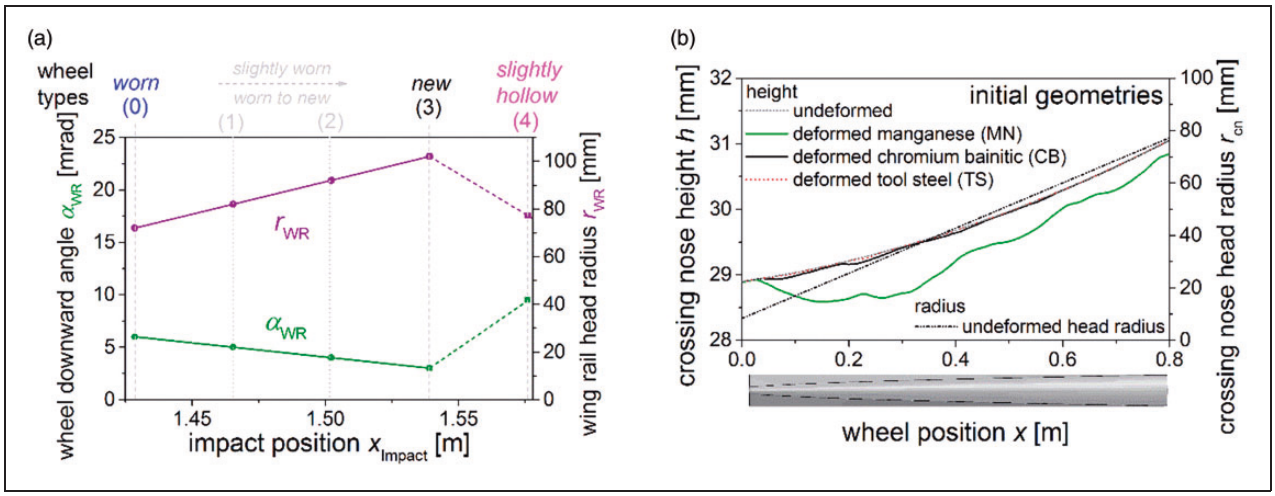

Figure 4. (a) The impact positions, wing rail downward angle, and wing rail head radius for the selected wheels and (b) the initial crossing nose geometries for the manganese steel, chromium-bainitic, and tool steel crossing.

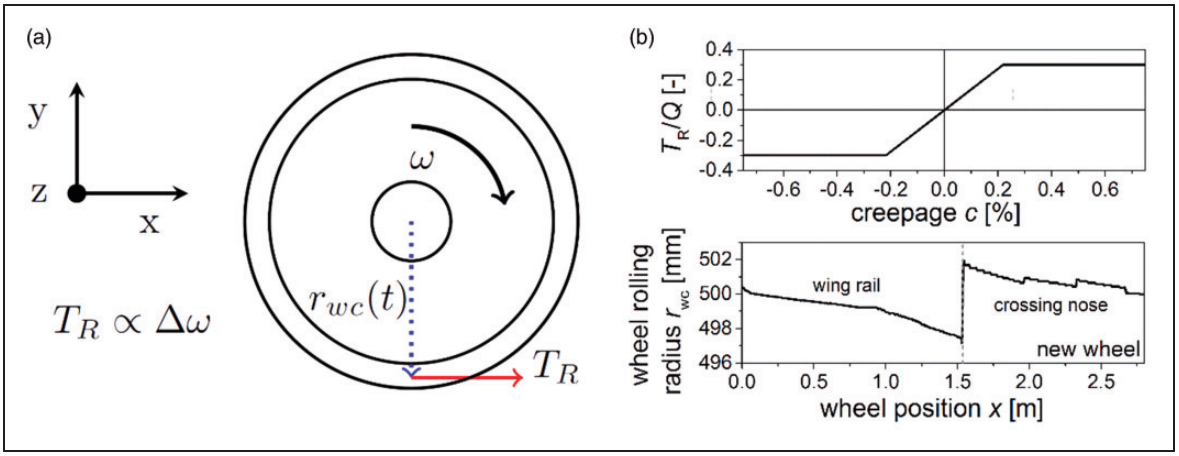

Figure 5. (a) The simplified model to evaluate the input parameter slip s, (b) the used creepage c and tangential force T_R/normal force Q relationship, and (c) the changing radius in contact of a new wheel r_{wc}.

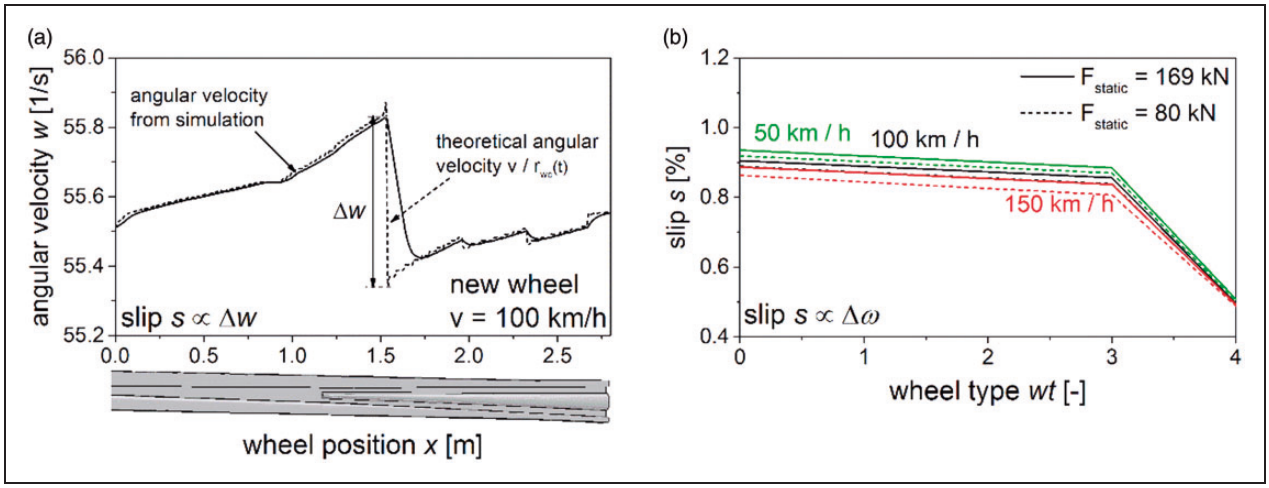

Figure 6. (a) The result of the slip model, the angular velocity change $\Delta\omega$, which is needed for calculating the slip s. (b) The slip due to different wheel types. The green, black, and red lines represent $v = 50$, 100, and 150 km/h, and the solid and dotted lines the F_{static} of 160 and 80 kN, respectively.

where v is the velocity of the wheel and ω the angular velocity. For the normal force, we take the static wheel load F_{static} of the system.

The rolling radius r_{wc} is evaluated in preprocessing and changes due to the changing contact position in the z-direction. The wheel rolling radius r_{wc} is evaluated with a similar routine as one of the evaluations of the vertical wheel displacements. When running on the wing rail r_{wc} becomes smaller as the contact position moves away from the flange. The sudden increase (gray dotted line in Figure 5(b) at $x = 1.5$ m) of the wheel radius in contact indicates the transition of the wheel from the wing rail to the crossing nose. The contact position changes from the field side of the wheel to a position closer to the wheel flange, which increases the rolling radius r_{wc} due to the wheel geometry. The equations are solved numerically using an explicit algorithm in Wolfram Mathematica©.

Figure 6(a) shows the typical angular velocities calculated by the simplified slip model. The solid line represents the calculated angular velocity of the wheel during the transitions and the dotted lines represent the theoretical angular velocity calculated with

$$\omega_{\text{th}} = \frac{v}{r_{wc}} \tag{6}$$

The difference $\Delta\omega$ of the maximum angular velocity of the simulation to the lowest theoretical angular velocity at the transition point is then used to calculate the input parameter slip s of the model (see Figure 6(a)). Equation (5) is then simplified and the creepage c_{init} is defined as

$$s = c_{\text{init}} = \frac{\Delta\omega}{\omega_{\text{th, impact}}} \tag{7}$$

where $\Delta\omega$ is the difference described above and $\omega_{\text{th,impact}}$ is the theoretical angular velocity, that

corresponds to the rolling radius when rolling without slip, at the impact position.

Figure 6(b) shows the calculated slip s for different velocities (50, 100, and 150 km/h), static loads (solid and dotted lines for 169 and 80 kN, respectively), and wheel types. The slip s decreases from the worn to the hollow wheel due to the worn regions of the wheel profiles (see Figure 3). Furthermore, the slip s is lower at higher velocities and increases with increasing static loads. The implementation of the FE model is described in the following section.

FE model

The authors introduce a fast and simplified FE model,[12] which considers the impact of different worn wheels with its crucial parameters (see "Evaluation of input parameters" section). The model simplifies the wing rail to a nonlinear contact spring and the wheel moves downward according to the wing rail downward angle α_{WR}. The authors then introduce a more realistic crossing nose geometry by using more geometrical data. The contact radius of the crossing nose at the contact position of the wheel and the vertical displacement of the wheel evaluated over a longer distance are used to define the crossing nose geometry. Figure 7 shows a reduced mechanical model of the FE model with its crucial parameters:

- the wing rail downward angle α_{WR},
- the wing rail contact radius r_{wr},
- the impact position x_{Impact},
- the crossing nose head radius $r_{cn}(x)$ and
- the crossing nose height $h(x)$.

α_{WR} and r_{wr} describe the wing rail and $r_{wr}(x)$ and $h(x)$ the crossing nose geometry; x_{Impact}, however, is the position, where the wheel transitions from the wing rail to the crossing nose and acts as a link between both of them (see Figure 3).

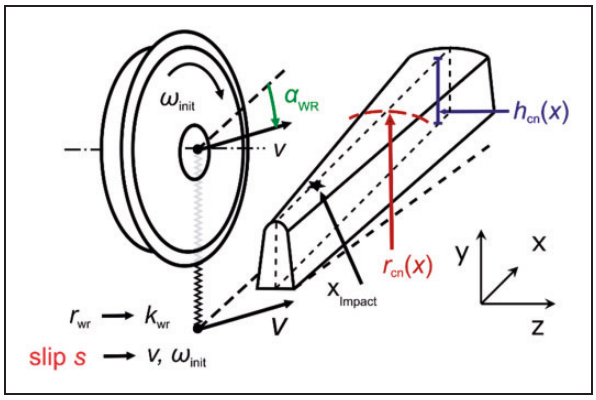

Figure 7. A schematic diagram of the mechanical system of the FE model and its main input parameters. The spring/dashpot support in the vertical direction at the bottom of the crossing nose is not shown.

The slip s is included by increasing the initial angular velocity of the wheel ω to ω_{init} with

$$\omega_{init} = \omega(1 + s) \tag{8}$$

ω is calculated with $\omega = \frac{v}{r_{Wheel}}$, where v is the velocity and r_{Wheel} is the radius of the simplified wheel with 0.478 m. The boundary conditions, the masses, the wheel damping coefficient d_w (primary suspension), the spring-dashpot support d_r/k_r and the non-linear wing-rail contact spring k_{wr} are taken from Wiedorn et al.[13] The wheel damper acts as the suspension in the center of the wheel and the spring/dashpot support is modeled at the bottom of the crossing nose. For the parameter study, the velocity of the wheel is varied between 50 and 150 km/h and the vertical static load between 80 and 180 kN, which represents axle loads between 14 and 26 t. The values are summarized in Table 2.

The impact positions and downward angles of the different wheels are shown in Figure 4(a). Furthermore, each wheel type, axle loads, and velocity have different slip values, which are taken from Figure 5(b).

The simplified wheel initially runs on the pretensioned contact spring which moves downward according to the wing rail downward angle α_{WR}. The y-direction of this nonlinear contact spring is connected to the spring of the crossing nose, as the wing rail and crossing nose are one component. The start position is chosen so that it impacts on the undeformed crossing nose at the impact position x_{Impact}. Depending on the state of wear of the crossing nose, this impact position changes slightly. When the wheel touches the crossing nose, the load is transferred to the crossing nose and the nonlinear spring unloaded and its stiffness goes to zero.

Three different crossing nose geometries are investigated in this work with a different extent of plastic deformation, as explained in the "Evaluation of input parameters" section: the deformed crossing for manganese steel, chromium-bainitic steel, and tool steel (see Figure 4(b)). They have the same initial geometry

Table 2. The chosen model parameters for the parametric study.

Parameter	Values
Wheel damper constant d_w as primary suspension (N s/m)	53,000
Spring constant k_r (at the bottom of the crossing nose) (kN/mm)	90
Damper constant d_r (at the bottom of the crossing nose) (N s/m)	250,000
Velocity v (km/h)	50, 100, 150
Static loads F_{static} (kN)	80, 124, 180

and the same initial mesh: C3D8R elements, 105,000 for the rail and 83,000 for the wheel, with an edge length for the elements in contact of about 1 mm. Their deformed geometry is considered by using the deformed mesh after 55 impact cycles.[2] For the contact between the wheel and the crossing nose, a kinematic contact algorithm and a coefficient of friction of 0.3 is used.

For both, the wheel and the crossing nose, the model uses linear-elastic material behavior with a Young's modulus of 210 GPa, a Poisson's ratio of 0.3, and a density of 7800 km/m^3.

In the "Contact stresses" section, a case study, which investigates the positive effect of plastic deformation of the manganese steel on very unfavorable loading conditions (high axle loads), is done. There, the model uses the cyclic Chaboche model with combined isotopic and kinematic hardening with three backstresses[2] (see Table 3). Furthermore, not only the deformed geometry is used for the calculation, but also the material state of the run-in crossing nose is transferred.

Results and discussion

In this section, the influence of the velocity, static loads, and wheel types on contact forces, pressures, and subsurface damage initiation is explained. Furthermore, we show that contact pressures and the damage initiation have similar trends and explain the tendency for subsurface damage initiation for each crossing nose by considering their deformed geometry and plastic deformation.

General results

Figure 8 shows the vertical contact forces F and the contact pressures p over the longitudinal position of the wheel. The results show the impact of a new wheel with a velocity v of 100 km/h and a static load F_{static} of 80 kN on an elastic crossing nose with a deformed geometry of a manganese steel crossing. The wheel initially runs on the wing rail (contact spring), denoted by the dashed line, until it reaches the deformed crossing nose at the wheel position at about 0.1 m. There, the dynamic response increases the contact forces and pressures and the wheel continues to run on the crossing nose (solid lines). For this paper, only a short region after the impact position is investigated, as this area is crucial in terms of damage. It has a total length of about 230 mm and starts at the impact position x_{Impact} of the undeformed crossing nose. The area is marked by gray dashed lines and is different for each wheel, as the x_{Impact} changes.

To describe the vertical contact forces F and contact pressures p in the parameter study, one value was chosen for each output: the maximum of the contact force F called the impact force $F_{\max}$ and of the contact pressure p called the impact pressure $p_{\max}$. They are evaluated between the dashed lines around the impact position of the wheel. In Figure 8, F increases up to a maximum of about $F_{\max} = 125$ kN and p up to $p_{\max} = 1.4$ GPa between those limits. Due to the deformation of the crossing and the dynamic response, it sometimes happens that the maximum force or pressure on the crossing nose appears outside the evaluated area. Since we are only interested in the first impact of the wheel on the crossing nose, those values are not considered.

To assess the subsurface damage initiation, a post-processing routine is used. Figure 9 shows a sketch of the evaluation routine of the maximum subsurface initiation damage value $P_{\text{dv,max}}$.

The subsurface damage P_{dv} is evaluated according to the routine stated in the "Damage: Concept, materials, and experimental evaluation" section. We evaluate the damage initiation value P_{dv} on the same distance as $p_{\max}$ and $F_{\max}$ and down to a depth of

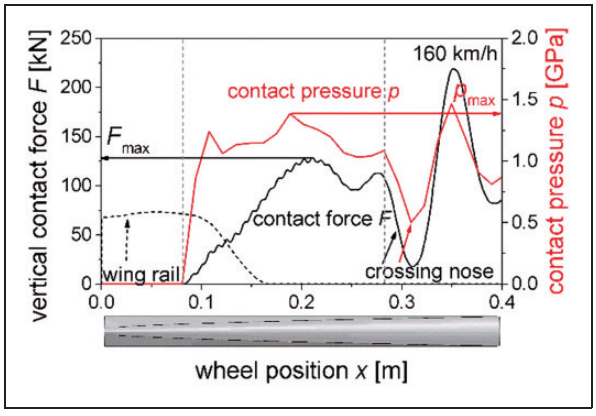

Figure 8. Dynamic result of the simulation model: black represents the vertical contact forces F and red the contact pressure p.

Table 3. The material parameters of manganese steel for the case study.

Young's modulus (GPa)	Poisson's ratio (–)	Density (kg/m^3)	R_0 (MPa)	Q (MPa)	B (–)	C_1 (GPa)	D_1 (–)	C_2 (GPa)	D_2 (–)	C_3 (GPa)	D_3 (–)
Property 201	0.3	7800	200	250	3	1000	10,000	40	400	2	3

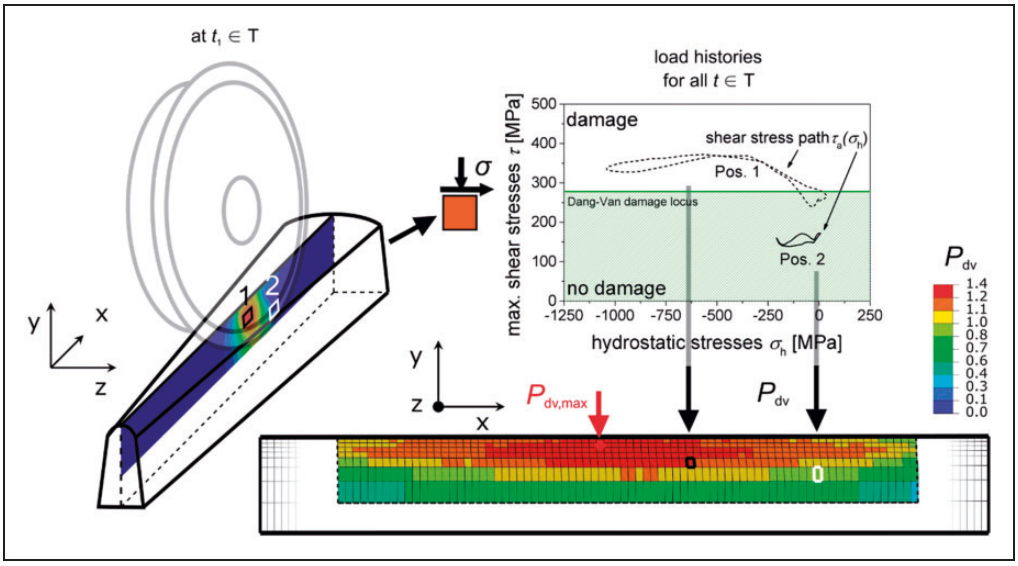

Figure 9. Exemplary sketch of the calculation of the damage initiation P_{dv} for two elements and the maximum $P_{dv,max}$ for all elements. The routine is carried out for all impact cycles.

about 3 cm. All elements in this area are regarded and P_{dv} is investigated separately. The 3D sketch on the left side of Figure 9 shows an exemplary snapshot at $t_1 \in$ T during the impact on a wheel on the crossing nose. Two elements are chosen (1—black and 2—white) and their stresses at every $t \in$ T are evaluated. As described in the "Damage: Concept, materials, and experimental evaluation" section, we then calculate the mid stress for those elements to evaluate the shear stress amplitude $\tau_a(t)$ (see equation (2)). The plot in the upper right corner shows the hydrostatic stresses $\sigma_h(t)$ and the shear stress amplitude $\tau_a(t)$, see dotted and solid lines for the element at position 1 and 2, respectively. With equation (3), the subsurface damage P_{dv} is then calculated. The model repeats this routine for every element in the evaluation area. The result of this evaluation is then shown in the contour plot at the bottom. The exemplary elements are marked black and white. As the last step, we then evaluate the maximum subsurface damage initiation parameter $P_{dv,max}$ from all elements with $P_{dv,max} = \max_{e \in \text{elements}} P_{dv,e}$, where "elements" is the list of all elements within the defined area.

Contact forces

Figure 10 shows the maximum contact forces F_{max} obtained for the three investigated crossing geometries with elastic material behavior: the deformed geometry of manganese crossing in (a) to (c), the chromium-bainitic steel crossing in (d) to (f), and the tool steel crossing in (g) to (i). The results are shown for different static loads F_{static}, wheel types, and velocities. Table 1 and Figure 10(a), (d), and (g) give an overview of all investigated cases in a 3D plot: the surfaces represent the different velocities (50, 100, and 150 km/h). Furthermore, two colored planes are added for all crossing geometries: (b) and (c) for the crossing with the deformed manganese geometry, (e) and (f) for the chromium-bainitic steel geometry, and (h) and (i) for the tool steel geometry. They represent a cut through the surfaces and show the maximum vertical contact forces. The former shows F_{max} for a new wheel and all loads and the latter F_{max} for all wheel types and a static load $F_{static} = 124$ kN.

The different wheel types are marked with numbers: 0 for the worn wheel, 1 for the slightly worn wheel #1, 2 for the slightly worn wheel #2, 3 for the new wheel, and 4 for the hollow wheel. All geometries show increasing maximum contact forces F_{max} when increasing the static load F_{static}.

When comparing the new wheel for all materials, the manganese steel crossing (cp. Figure 10(b)) shows higher maximum contact forces than the chromium-bainitic steel crossing (see Figure 10(e)) and tool steel (see Figure 10(h)). These differences are due to the differently deformed geometries, which are a result of previous calculations with plastic material behavior. For the new wheel and the deformed manganese crossing geometry, the increase of F_{max} with increasing F_{static} is low but reaches a maximum of about 310 kN for $v = 150$ km/h and a static load of 170 kN. For chromium-bainitic steel and tool steel, the maximum values for the new wheel are lower, about 280 and 240 kN, respectively. In both cases, the results with $v = 100$ and 150 km/h and $F_{static} = 170$ kN are very close together. For low static loads, the maximum contact forces F_{max} are similar for chromium-bainitic steel and tool steel and about 50 kN and up to 100 kN lower than the results of the model with the deformed manganese geometry for $v = 50$ and 150 km/h, respectively. For other wheel types, especially the worn and hollow wheels, the deformed geometry of the manganese crossing shows similar, and lower, maximum contact forces F_{max} than the other geometries. When comparing the different

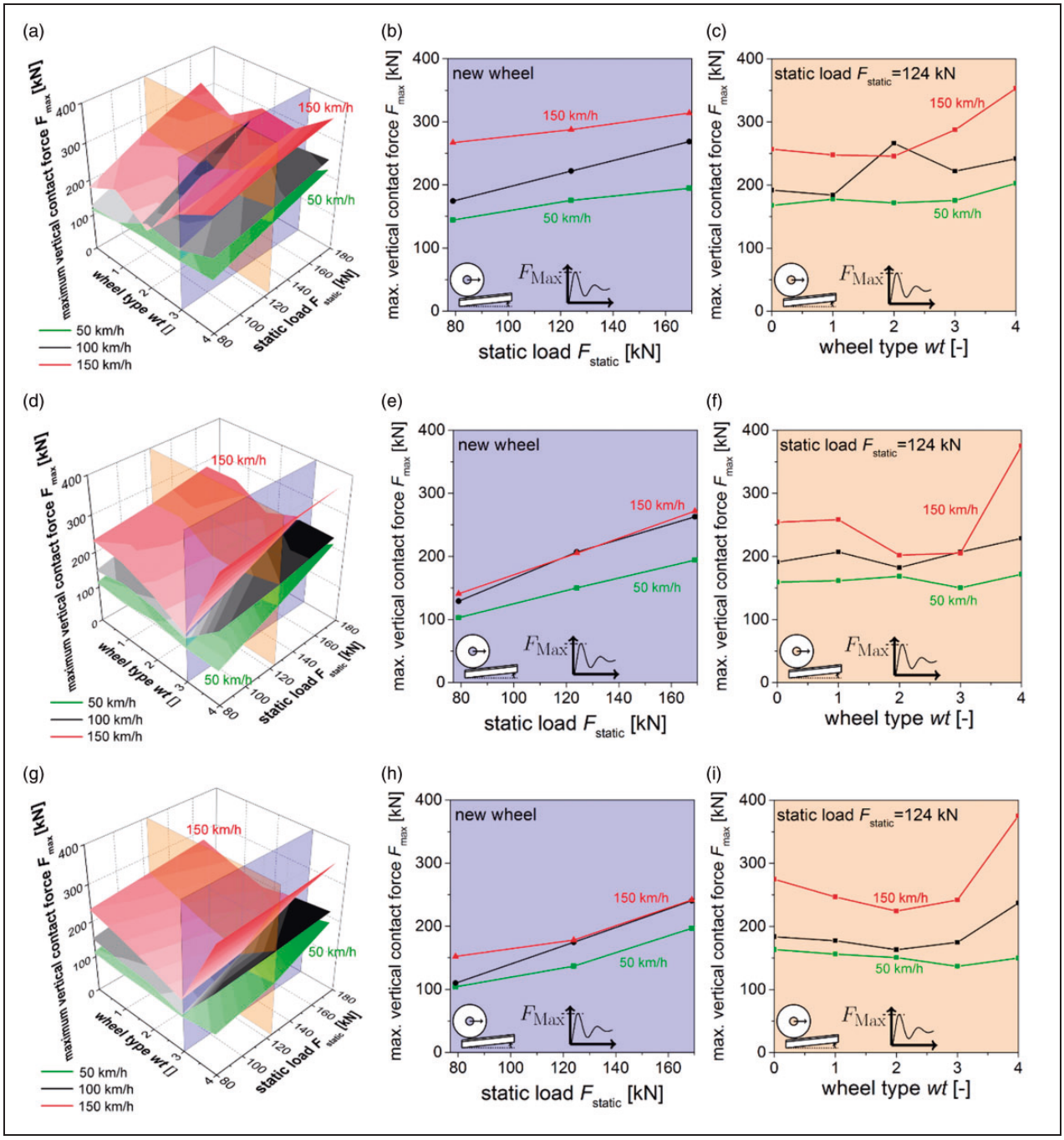

Figure 10. The maximum contact forces F_{max} for the manganese crossing—(a) to (c), the chromium-bainitic crossing—(d) to (f), and the tool steel crossing—(g) to (i). (a), (d), and (g) show a 3D plot of all results, whereas (g) to (i) show detailed results at the planes indicated in the 3D plot.

wheel types of the manganese crossing in Figure 10(c) to the chromium-bainitic and tool steel crossing in Figure 10(f) and (i), this tendency can be seen clearly. There the worn and hollow wheel have maximum values between 170–270 and 150–370 kN for all velocities and geometries. The impact of the hollow wheel at $v = 150$ km/h on the manganese crossing geometry, however, has the lowest maximum contact force F_{max} with 350 kN.

For the slightly worn wheel #2 (wheel type 2), the manganese steel crossing shows an unexpected result (see Figure 10(a) and (c)): the maximum contact forces F_{max} are higher for $v = 100$ km/h than for $v = 150$ km/h. The reasons are the limited evaluation area (about 25 cm around the impact position) and the arising dynamics caused by the deformed geometry.

Contact stresses

In this section, the results of the model in terms of maximum contact pressures p_{max} for all materials and elastic material behavior are shown. Similar to Figure 10, Figure 11(a) to (c) shows the results of the crossing with the deformed manganese

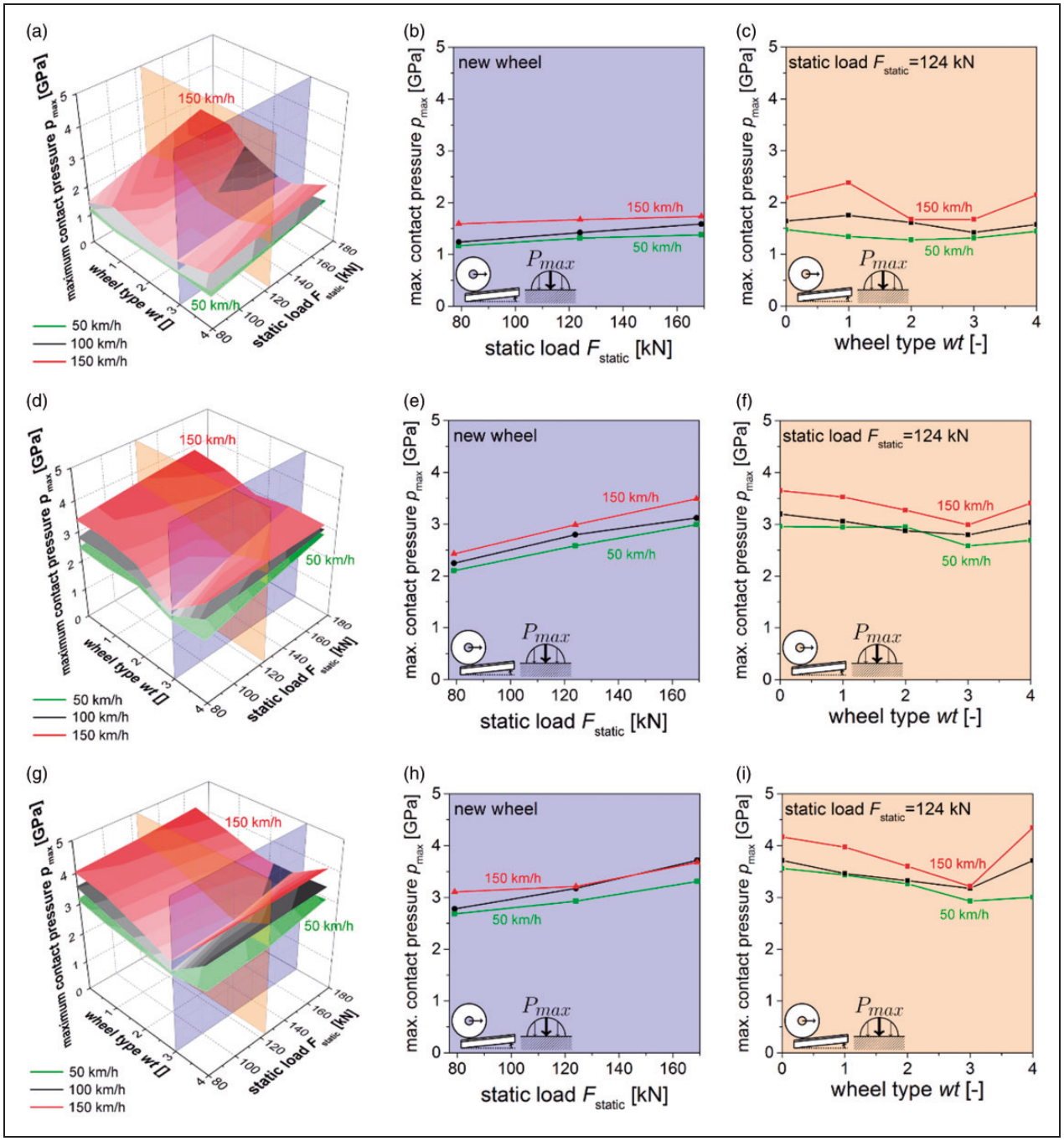

Figure 11. The maximum contact pressure p_{max} for the manganese crossing —(a) to (c), the chromium-bainitic crossing—(d) to (f), and the tool steel crossing—(g) to (i). (a), (d), and (g) show a 3D plot of all results, whereas (b), (c), (e), (f), (h), and (i) show detailed results at the planes indicated in the 3D plot.

geometry, Figure 11(d) to (f) of the chromium-bainitic geometry, and Figure 11(g) to (i) of the tool steel geometry. The surfaces in the 3D plot represent different velocities (see Figure 11(a), (d), and (e)), and the two planes are at the same position as in Figure 10. The calculated values are given as supplemental material and shown in Table A1 to A3. For all three crossing geometries, the maximum contact pressure p_{max} increases with increasing static loads F_{static} (see Figure 11(b), (e), and (h)), and—with a few exceptions—also velocities v. For higher velocities and the slightly worn or new wheel, the maximum values of the manganese steel and tool steel geometry are similar and the surface for $v = 100$ and 150 km/h begins to overlap, see Figure 11(a) and (g), respectively.

The manganese steel has a lower maximum p_{max} with values at about 2.5 GPa than the chromium-bainitic steel and tool steel with values close to 4 GPa. These values arise for a velocity v of 150 km/h, a static load of 180 kN and for the worn—in case of the tool steel, also for the hollow—wheel. When comparing the wheel profiles at $F_{static} = 124$ kN in Figure 11(c), (f), and (i), the lowest p_{max} values can be found for the slightly

worn wheel #2 or new wheel with values of about 1.5 GPa for the manganese crossing, 2.8 GPa for the chromium-bainitic, and 3 GPa for the tool steel crossing for $v = 50$ km/h. This trend continues for the other investigated loads F_{static}.

The selected cuts in Figure 11(b), (c), (e), (f), (h), and (i) confirm the overall lower contact pressures of manganese steel for all velocities and loads. The previous plastic deformation changes the contact geometry between the wheel and the rail and influences the arising contact pressures. In case of the manganese steel, the high deformation (see Figure 4(b)) increases the contact radius. As a result, a larger contact area is available for the contact force, which decreases the maximum contact pressure $p_{\max}$.

Damage parameter $P_{dv,max}$

In this section, we show the results of the maximum subsurface damage initiation parameter $P_{\text{dv,max}}$ for the investigated crossing geometries and impact loads. It is calculated with elastic material behavior.

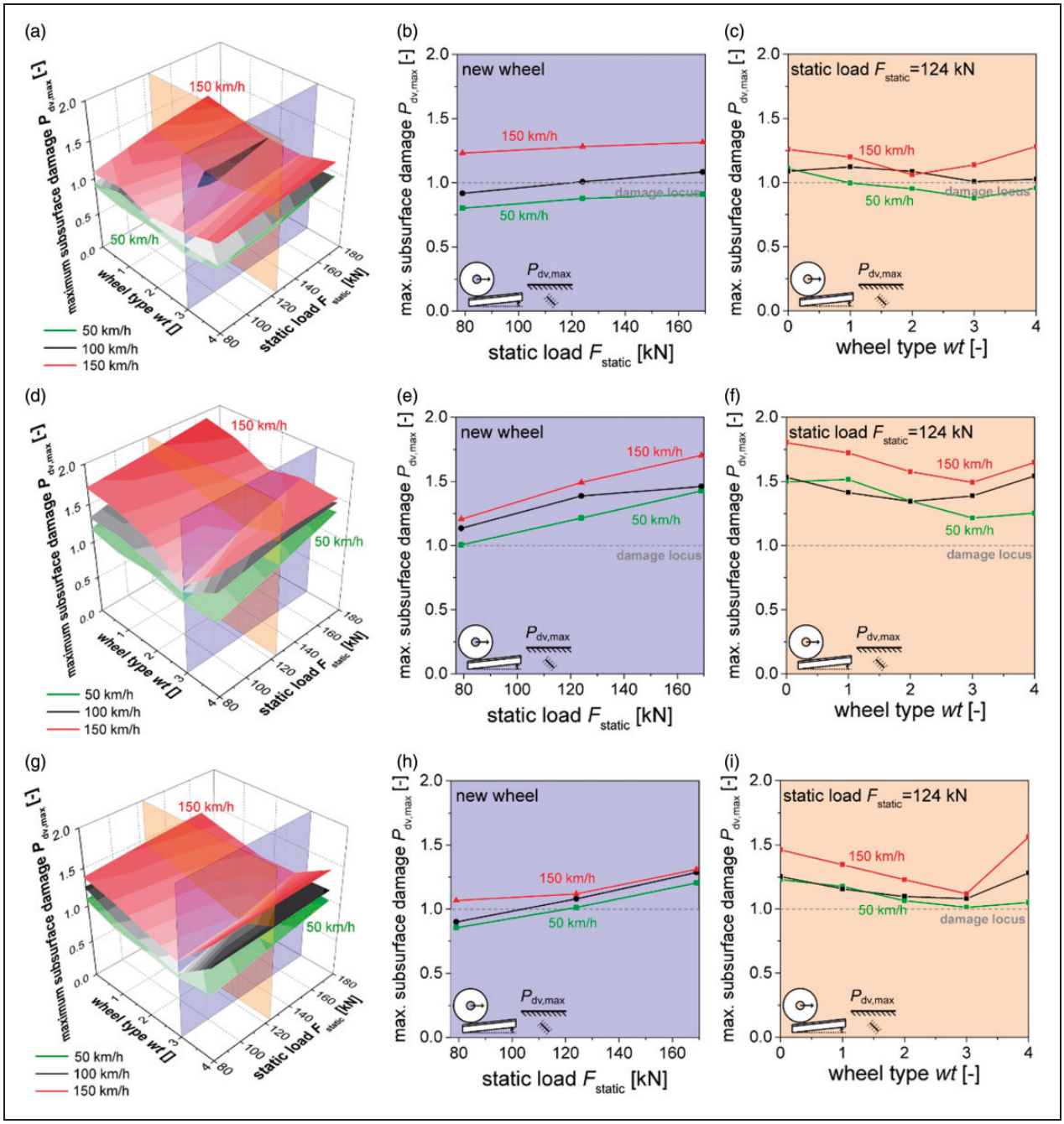

Figure 12. The maximum subsurface damage initiation $P_{\text{dv,max}}$ for the manganese crossing—(a) to (c), the chromium-bainitic crossing—(d) to (f), and the tool steel crossing—(g) to (i). (a), (d), and (g) show a 3D plot of all results, whereas (g) to (i) show the detailed results at the planes indicated in the 3D plot.

Figure 12 presents the evaluated data in a similar way as Figures 10 and 11: (a) to (c), (d) to (f), and (g) to (h) show $P_{dv,max}$ for the deformed manganese steel, chromium-bainitic steel, and tool steel geometry. The cuts of the 3D plot are at the same position: at the new wheel and at a static load of about 124 kN. We calculated $P_{dv,max}$ according to the routine stated in the ''Damage: Concept, materials, and experimental evaluation'' and ''General results'' sections.

The calculated values are given as supplemental material and shown in Table A4 to A6. As already stated in a previous work,[2] the contact pressures are strongly connected to the arising subsurface damage initiation values: they depend on the shear stress amplitudes in the body. Therefore, similar trends for the evaluated parameters can be seen in Figure 12: increasing static loads and—with some exceptions—increasing velocities v increase the maximum subsurface damage parameter $P_{dv,max}$. The highest and lowest maxima for all geometries can be found for the slightly worn and new wheel (see Figure 12(a), (d), and (f) or (c), (f), and (i)) for $F_{static} = 124$ kN.

Nevertheless, in terms of maximum values for the damage variable of the investigated materials, the trends for p_{max} (see Figure 11) are different: higher contact pressures do not necessarily mean high subsurface damage initiation values: The tool steel crossing has very high contact pressures and $P_{dv,max}$ values between 1 for $v = 50$ km/h and 1.5 for $v = 150$ km/h. In comparison, the manganese crossing is in a similar range ($P_{dv,max}$ between 1 and 1.4), but has the lowest maximum contact pressures p_{max}. The chromium-bainitic steel, however, has values of $P_{dv,max}$, max up to 2, but p_{max} values similar to or lower than tool steel.

The reason is the influence of the material parameters in the DV damage criterion and the deformed geometries. Next to the shear and hydrostatic stresses, the evaluated DV material parameters influence the subsurface damage parameter P_{dv}: higher DV material parameters (α_{dv} and mean τ_f) mean higher resistance against fatigue and, therefore, lower damage values (see equation (3)). Manganese steel has the lowest and tool steel the highest DV parameters (see Table 1). Low arising stresses on the manganese steel crossing and the high stresses on the tool steel cause similar subsurface damage initiation values. The chromium-bainitic steel, however, has contact pressures p_{max} nearly as high as for the tool steel, a similar geometry, but lower DV material parameters.

Study: Influence of plastic deformation in unfavorable load situations

Manganese steel has a relatively low initial yield stress but distinct work hardening. This enables the crossing to adapt to a loading by reducing the occurring stresses until it reaches a state of no or less plastic deformation.[2] Furthermore, it was shown that the geometry change due to plastic deformation is the main reason for the reduction of the subsurface damage initiation values.

Considering the run-in geometry and material history, a material behavior similar to high strength steels can be assumed: an adapted geometry with less or no deformation. But, the material behavior of the manganese steel enables the crossings to react positively to unfavorable load situation, such as high axle loads or severely worn wheels. Additional plastic deformation due to the overload reduces the contact stresses and therefore the damage-inducing stresses in the body. To show this effect, we compare a crossing with run-in geometry and (a) elastic material behavior to (b) plastic behavior and the calculated material history.[2]

We choose a load scenario, which is not realistic, but underlines the ability of manganese steel to react to that loading with plastic deformation. Therefore to show this ability, we combine a very high axle load with a high velocity and create a hypothetical scenario, which is obviously unfavorable for the crossing. Table 4 shows the input parameters for this scenario.

The run-in geometry is shown in Figure 4(b). The plastic calculation, however, uses the material parameters from Table 3 and the calculated material state (residual stresses, hardening, etc.) after 55 cycles.[2] We calculate the impact of the five different worn wheels from Figure 4(b). For the plastic calculation, the crossing is loaded successively, which means that the cycles of the chosen scenario are added to the former 55 cycles: cycle 56–60.

Figure 13 shows the vertical contact forces F ((a) and (b)) and the contact pressures p ((c) and (d)) for the crossing with elastic material behavior ((a) and (c)) and plastic material behavior ((b) and (d)). The dotted line represents the worn wheel, the gray solid line the slightly worn wheel #1, the dashed-dotted line the slightly worn wheel #2, the black solid line the new wheel, and the dashed-dotted line the slightly hollow wheel.

The vertical contact force F of the model with elastic material behavior (Figure 13(a)) is slightly higher than the force of the model with plastic material behavior (Figure 13(b)). The plastic deformation reduces the maximum vertical contact forces and the arising dynamic forces, especially for the worn

Table 4. Chosen scenario for the case study.

Parameter	Value
Crossing nose materials	(1) Elastic, (2) manganese cyclic plastic
Wheel types *wt*	Worn, slightly worn #1 and #2, new, slightly hollow
Velocity v (km/h)	200
Static load F_{static} (kN)	250 (axle load 48.9 t)

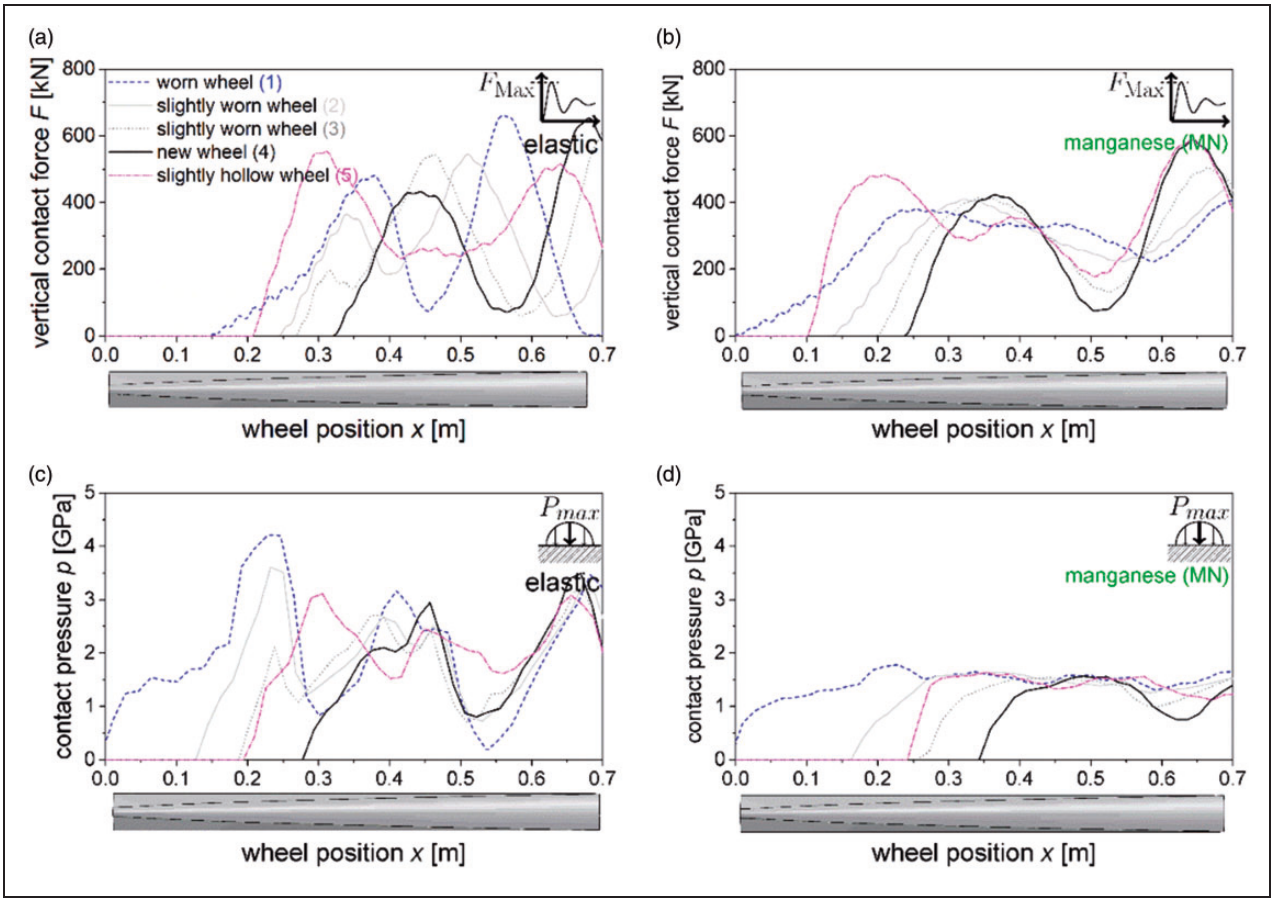

Figure 13. The vertical contact forces F for a static load of 250 kN and a velocity of 200 km/h for the crossing with (a) elastic and (b) plastic material. (c) and (d) show the contact pressure p during the impact of the wheel for the elastic and plastic material, respectively.

wheels. When comparing the contact pressures, however, a larger difference between the wheels can be observed. The worn wheel has the largest maximum contact pressures and shows values of about 4 GPa and 1.8 GPa for the elastic and plastic material behavior, respectively.

A decrease of more than 40% can be seen when comparing p_{max} with elastic and plastic material behavior. The lowest values are found for the new wheel for both, F_{max} and p_{max}.

The reason for the reduction of the maximum contact forces F_{max} and pressures p_{max} is the instant reaction of the manganese steel crossing to the loading. Especially for p_{max} this difference is significant as it is strongly influenced by the contact geometry. The surface deformation caused by the wheel impact increases the contact radius—flattens the contact surface—and, thus, reduces the contact pressures.

Figure 14 shows the maximum subsurface damage $P_{dv,max}$ for the different wheel types.

When comparing the maximum $P_{dv,max}$ values of the crossing with plastic material behavior (dashed line in Figure 14) to the crossing with elastic material behavior (solid line in Figure 14), a reduction of more than 25% is calculated for all wheel types. The $P_{dv,max}$ values during the impact of the slightly worn wheel #1 drop from about 1.5 to 1.1.

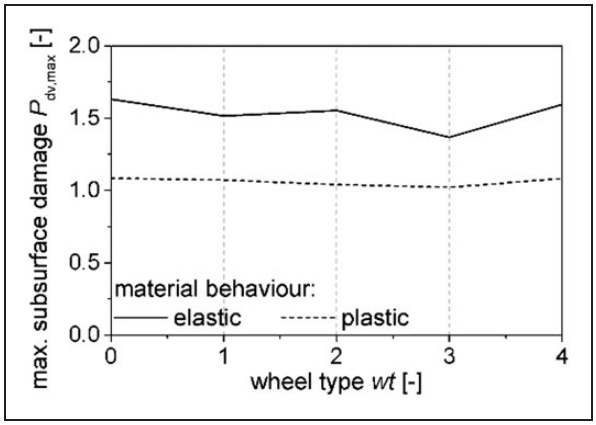

Figure 14. The maximum subsurface damage initiation $P_{dv,max}$ for the impact of differently worn wheels on the manganese crossing. The results are shown for the model with elastic (solid line) and plastic (dashed line) material behavior.

We can explain this behavior by the reduction of the p_{max} values due to plastic deformation as mentioned before: The lower contact pressures induce lower stresses in the crossing and, thus, reduce the P_{dv} values.

Although the model used a run-in geometry and material, the manganese steel crossing uses additional

plastic deformation as a protection mechanism for damage initiation.

Conclusions

An FE crossing model was used to determine stresses in the crossing nose during the impact of worn and new wheels. Damage initiation was then calculated for three different materials (manganese steel, chromium-bainitic steel, and tool steel) and their run-in geometries, which were calculated before using their plastic material behavior.

- The maximum vertical contact forces F_{max}, the maximum contact pressures p_{max}, and the maximum DV damage initiation value $P_{dv,max}$ are shown as a function of the wheel velocity v, the axle load, and the wheel type. In addition to already known tendencies, such as increasing F_{max} and p_{max} with increasing velocity or axle loads, it is shown that this also applies to the damage value $P_{dv,max}$. The highest $P_{dv,max}$ values occur for the worn and hollow wheel, the lowest for the slightly worn and new wheel. Decreasing velocity lowers p_{max} and $P_{dv,max}$ for the hollow wheel, significantly.
- The tendency for damage initiation is determined by the occurring stresses and the DV material parameters. Manganese steel shows the lowest tendency for subsurface damage initiation. It has the lowest contact pressures due to its deformation, but also the lowest DV material parameters. Tool steel, however, has the highest DV material parameters and p_{max}, but slightly higher $P_{dv,max}$ values. Chromium-bainitic steel shows the highest DV damage initiation values $P_{dv,max}$, but contact pressures slightly lower than tool steel.
- Manganese steel crossings are able to adapt very well to unfavorable load situations (high axle load, high velocity) by plastic deformation. Run-in manganese crossings with plastic material behavior showed significantly lower contact pressures p_{max} and damage initiation $P_{dv,max}$ than the crossing with elastic material behavior. Manganese crossings enable additional plastic deformation to reduce the occurring stresses, although the crossing had an adapted geometry and hardened run-in material.

Acknowledgements

We wish to thank Anders Ekberg (Chalmers University of Technology, Gothenburg, Sweden) for pointing out the ability of manganese steel crossings to react against severe load conditions.

Declaration of Conflicting Interests

The author(s) declared no potential conflicts of interest with respect to the research, authorship, and/or publication of this article.

Funding

The author(s) disclosed receipt of the following financial support for the research, authorship, and/or publication of this article: Financial support by the Austrian Federal Government (in particular from Bundesministerium für Verkehr, Innovation und Technologie and Bundesministerium für Wissenschaft, Forschung und Wirtschaft) represented by Österreichische Forschungsförderungsgesellschaft mbH and the Styrian and the Tyrolean Provincial Government, represented by Steirische Wirtschaftsförderungsgesellschaft mbH and Standortagentur Tirol, within the framework of the COMET Funding Programme is gratefully acknowledged.

ORCID iD

Julian Wiedorn http://orcid.org/0000-0002-5129-637X

References

1. Dang Van K and Griveau B. On a new multiaxial fatigue limit criterion: theory and application. In: Brown MW and Miller KJ (eds), *EGF3*. London: Mechanical Engineering Publications, 1989, pp.476–496.
2. Wiedorn J, Daves W, Ossberger U, et al. Numerical assessment of materials used in railway crossings by predicting damage initiation – validation and application. submitted. *Wear* 2018; 414–415: 136–150.
3. Dang Van K, Maitournam MH, Moumni Z, et al. A comprehensive approach for modeling fatigue and fracture of rails. *Eng Fract Mech* 2009; 76: 2626–2636.
4. Ekberg A, Kabo E and Andersson H. An engineering model for prediction of rolling contact fatigue of railway wheels. *Fat Frac Eng Mat Struct* 2002; 25: 899–909.
5. Desimone H, Bernasconi A and Beretta S. On the application of Dang Van criterion to rolling contact fatigue. *Wear* 2006; 260: 567–572.
6. Ciavarella M and Monno F. A comparison of multiaxial fatigue criteria as applied to rolling contact fatigue. *Tribol Int* 2010; 43: 2139–2144.
7. Wiest M, Daves W, Fischer FD, et al. Deformation and damage of a crossing nose due to wheel passages: contact mechanics and wear of rail/wheel systems – CM2006. *Wear* 2008; 265: 1431–1438.
8. Pletz M, Daves W and Ossberger H. A wheel set/crossing model regarding impact, sliding and deformation – explicit finite element approach. *Wear* 2012; 294–295: 446–456.
9. Kassa E, Andersson C and Nielsen JCO. Simulation of dynamic interaction between train and railway turnout. *Veh Syst Dyn* 2006; 44: 247–258.
10. Andersson C and Abrahamsson T. Simulation of interaction between a train in general motion and a track. *Veh Syst Dyn* 2010; 38: 433–455.
11. Skrypnyk R, Nielsen JCO, Ekh M and Pålsson BA. Metamodelling of wheel–rail normal contact in railway crossings with elasto-plastic material behaviour. *Engineering with Computers* 2018. DOI: 10.1007/s00366-018-0589-3.12.
12. Wiedorn J, Daves W, Ossberger H, et al. A simplified dynamic finite element model for the impact of a wheel on a crossing: validation and parameter study. In: *Proceedings of the Third International Conference on Railway Technology: research, development and*

maintenance (ed J Pombo), Cagliari, Sardinia, Italy, 2016. Stirlingshire, UK: Civil-Comp Press. DOI: 10.4203/ccp.110.116.

13. Wiedorn J, Daves W, Ossberger U, et al. Simplified explicit finite element model for the impact of a wheel on a crossing – validation and parameter study. *Tribol Int* 2017; 111: 254–264.
14. Wiedorn J, Daves W, Ossberger H, et al. Using stress-based damage models to describe subsurface damage in crossings. In: *Paper presented at 11th International Heavy Haul Association conference 2017*, Cape Town, South Africa, 2017.
15. Khalid YA, Mutasher SA, Sahari BB, et al. Bending fatigue behavior of hybrid aluminum/composite drive shafts. *Mater Des* 2007; 28: 329–334.
16. Shimizu S, Tsuchiya K and Tosha K. Probabilistic Stress-Life (P-S-N) study on bearing steel using alternating torsion life test. *Tribol Trans* 2009; 52: 807–816.
17. ASTM E739-10. Standard Practice for Statistical Analysis of Linear or Linearized Stress-Life (S-N) and Strain-Life (ε-N) Fatigue Data. West Conshohocken, PA: ASTM International, 2015. Available at: www.astm.org.

Paper D

Investigation of deformation mechanisms in manganese steel crossings using FE models

AUTHORS

Julian Wiedorn[1], Werner Daves, Uwe Ossberger, Heinz Ossberger, Martin Pletz

[1] **corresponding author**

JOURNAL

Published in Tribology International (ISSN: 0301-679X).

ABSTRACT

A finite element model is introduced to investigate the deformation mechanisms of manganese steel crossings: (i) the plastic adaptation after installation and (ii) the long-term behavior in track with ongoing plastic deformation. The model uses measured geometries and plastic material behavior adapted to hardness measurements of a new and run-in explosion-depth hardened crossing nose. The plastic deformation is calculated and validated with measurements in track. To show the influences of the deformation due to repeated wheel impacts, contact forces and pressures are calculated. A detailed investigation of the geometric degradation in terms of surface deformation and plastic deformation in depth explains the observed behavior: they are described over the calculated impact cycles with its local position on the crossing nose.

CONTRIBUTION

Responsible for the development of the method.
Carried out the numerical simulations.
Wrote most parts of the paper.

Tribology International 138 (2019) 424–434

Contents lists available at ScienceDirect

Tribology International

journal homepage: www.elsevier.com/locate/triboint

Investigation of deformation mechanisms in manganese steel crossings using FE models

Julian Wiedorn[a,*], Werner Daves[a], Uwe Ossberger[b], Heinz Ossberger[b], Martin Pletz[c]

[a] Materials Center Leoben Forschung GmbH, Leoben, Austria
[b] voestalpine VAE GmbH, Zeltweg, Austria
[c] Department of Polymer Engineering and Science, Montanuniversitaet Leoben, Austria

ABSTRACT

A finite element model is introduced to investigate the deformation mechanisms of manganese steel crossings: (i) the plastic adaptation after installation and (ii) the long-term behaviour in track with ongoing plastic deformation. The model uses measured geometries and plastic material behaviour adapted to hardness measurements of a new and run-in explosion-depth hardened crossing nose. The plastic deformation is calculated and validated with measurements in track. To show the influences of the deformation due to repeated wheel impacts, contact forces and pressures are calculated. A detailed investigation of the geometric degradation in terms of surface deformation and plastic deformation in depth explains the observed behaviour: they are described over the calculated impact cycles with its local position on the crossing nose.

1. Introduction

To switch between railway tracks, trains are guided through crossings. One commonly used crossing type is the fixed crossing. Depending on its features, a more or less distinct impact of the wheel occurs during the passing of the train, which increases the contact forces. There, the wheel is forced to move downwards and upwards, which goes along with a sudden change of the radii in contact. This change causes slip to arise. Furthermore, the small head radii of the crossing nose cause high contact pressures and traction stresses. The geometric design of the crossing, the loading of the train and its velocity can multiply these effects and cause severe damage and wear [1].

Although the loads are known to be rather high, no uniform guideline for crossing material selection exist. A common material for rigid crossing noses is steel with high manganese content (> 12%) – manganese steel (or mangalloy or Hadfield steel after Robert Hadfield) [2]. In contrast to other common crossing materials, manganese steel experiences large plastic deformations due to repeated wheel impacts, see Fig. 1.

The deformation and its behaviour in track is mainly influenced by its low yield strength and high work hardening capacity. In Ref. [3], the authors review the deformation behaviour of manganese steels and explain its excellent formability (adaption) due to twinning-induced plasticity (TWIP). The relationship between its mechanical properties and microstructure is reviewed in Ref. [4]. Increasing the temperature during deformation, however, is found to decrease the strain hardening capacity [5]. The effect of rolling contact loading conditions on the mechanical behaviour of manganese steel is discussed in Ref. [6]: the authors investigated the influence of load, rolling speed and number of cycles.

A method that takes advantage of the deformation behaviour of manganese steel and increases the wear resistance and strength is pre-hardening by explosives. During explosive hardening (higher strain-rate) the twinning mode is accompanied by a slipping mode, which reduces the minimum deformation threshold for strain hardening significantly [7]. The influence of the thickness of the explosives and the amount of explosions on lifetime and hardness is investigated in Refs. [8,9]. They showed the microstructure before and after explosion hardening of a manganese crossing and found a limiting thickness for the explosives because of micro-crack formation.

As a result of these properties, manganese steel shows an extraordinary performance in track. In Refs. [10–12], the authors compare different types of materials and show the positive influence of the plastic deformation of manganese steel crossings on impact forces and pressures. Furthermore, subsurface damage using the Dang-Van damage parameter [13] is evaluated. Manganese steel performs best, but the authors also discuss the positive effects of using the – to the loads – adapted manganese geometry for higher strength steels in Ref. [12]. Another feature of manganese steel crossings is the ability to react to unfavourable load situations with plastic deformation, which is discussed in Ref. [14].

In general, two stages of plastic deformation can be defined for

* Corresponding author.
E-mail address: julian@wiedorn.at (J. Wiedorn).

https://doi.org/10.1016/j.triboint.2019.06.016
Received 15 January 2019; Received in revised form 12 May 2019; Accepted 9 June 2019
Available online 13 June 2019
0301-679X/

Fig. 1. A deformed manganese crossing in track.

manganese crossing noses:

(1) The positive adaption of the geometry and material to (and due to) the loading in the first few cycles and
(2) the long-time behaviour with continuing deformation.

Pletz et al. [15] use measured geometries for an explicit FE model and compares a new and worn geometry. They show this geometric adaption in terms of contact forces and pressures. In Ref. [16], the authors investigate damage of a Hadfield steel crossing due to rolling contact: For different wheel velocities they evaluated the positions of maximum deformation using hardness measurements of a failed and degraded crossing to describe the material response.

In this paper, we utilize an FE model on the basis of the FE model introduced in Ref. [12] to explain the two deformation mechanisms of explosion-depth hardened (EDH) manganese steel crossings. The model was first published in Ref. [17] and further developed in Ref. [18]. The FE method enables us to evaluate stress and strain fields and the deformation using cyclic plasticity. However, high computational times limit the number of cycles we are able to simulate.

To describe the two stages of plastic deformation, we choose two relevant times in the lifecycle of a manganese crossing, see Fig. 2. A specific combination of measured geometries and material states for these models allow us to investigate the deformation behaviour:

(a) For the plastic adaption, the *new* crossing model uses a geometry measured after installation in track with a material behaviour due to explosion hardening. It describes the initial situation of manganese crossings and can show the adaption to the loads and thus the reduction of the contact stresses in the first few cycles.
(b) For the long-time behaviour, the *run-in* crossing model uses a geometry after 2 years in track (11.9 MGT) with a material behaviour of a crossing after years in track. This model allows us to make statements about proceeding plastic deformations.

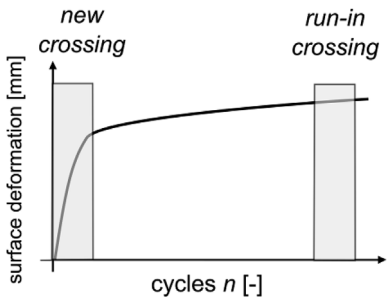

Fig. 2. A schematic diagram of the deformation of manganese crossings over impact cycles. *New* crossing and *run-in* crossing represent two instants during the life of a crossing: the plastic adaption at the beginning and the long-time behaviour after millions of loadings.

The material of the new and run-in EDH crossing model is already hardened due to the pre-deformation: either only by explosion hardening or additionally by the cyclic impacts of the wheel. The local hardness is then implemented in the FE model via a yield stress field.

The pre-deformation is recorded by performing hardness measurements on cross-sectional cuts of a new, EDH rail and a worn EDH crossing taken from the track. With simple tension tests of flat specimen with different hardness, a correlation between hardness and yield stress is found.

To include the material response (EDH and run-in + EDH) in the simulation models, we then adapt the cyclic plasticity model by changing the yield stresses for each finite element. Measured hardness profiles are considered by setting the yield stress of the elements according to the hardness value measured at the same position in depth.

The model then calculates the surface deformation, accumulated equivalent plastic strains and the dynamic behaviour (contact forces and stresses) over 40 impact cycles of a new wheel. By showing the evolution of those outputs over impact cycles, we are able to show the plastic adaption of a new crossing. Furthermore, statements are made about the long-time behaviour of manganese steel crossings.

2. Deformed manganese crossings: geometries, simulation and effects

2.1. Measured geometries & simulation model

Manganese crossings show severe material degradation during their lifetime: Displacement of the surface over several millimetres is normal and goes along with the good adaptability of this type of steel. Fig. 3a and b shows worn geometries of manganese steel crossings after 11.9 million gross tons (MGT) and 46.8 MGT, which were measured in track. The reference state of the shown surface change is an initial measurement of the surface geometry after installation in track.

The red and blue colours represent areas of missing and added material in comparison to the initial measurements, respectively. For both measurements, the highest values can be seen at the position where the wheel transits from the wing rail to the crossing nose (impact position). There, the red area indicates the start of the flattening, which usually increases the contact radii. The material is either removed due to wear or moved by plastic deformation. The latter mechanism seems to be dominant for manganese crossings – especially at the beginning, after the installation in track. The deformation pushes the material to another position, which appears as a blue area in the figure. The highest

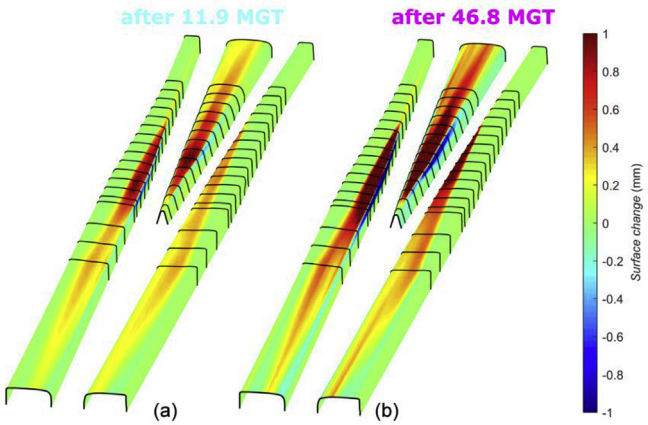

Fig. 3. Measured deformation of a crossing after (a) 11.9 MGT and (b) after 46.8 MGT.

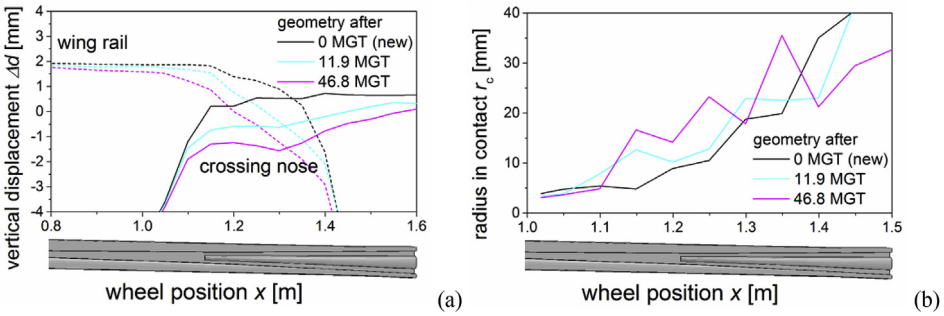

Fig. 4. (a) Displacement of an unworn (type ORE 1002) wheel on the wing rail (solid) and crossing nose (dashed) and (b) contact radii of a crossing nose on an unworn (black) crossing geometry and worn geometries after 11.9 MGT (cyan) and after 46.8 MGT (magenta). (For interpretation of the references to colour in this figure legend, the reader is referred to the Web version of this article.)

surface displacement is at similar positions for both measurements: Fig. 3b mainly reveals the continued degradation at the positions of the passing wheel, shown by the increased maximum and decreased minimum values from the measured geometry after 11.9 MGT to the one after 46.8 MGT.

This surface degradation affects the wheel movement significantly. Fig. 4a shows the vertical displacement of an unworn wheel when passing a new (black) and the two worn crossings of Fig. 3 – after 11.9 MGT and 46.8 MGT. The vertical displacements are evaluated geometrically by moving an unworn type ORE 1002 wheel over the measured surfaces and tracking its downwards and upwards movement. For this evaluation, the lateral wheel displacement was not considered and set to 0.

With increasing MGT passing the turnout, the height of wheel trajectories on the wing rail (dotted) and crossing nose (solid) shifts downwards. Furthermore, the inclination of the wheel trajectory on the wing rail decreases and a dent-like structure seems to develop on the crossing nose. Together, this means an increased downward and upward movement of the wheel when moving from the wing rail to the crossing nose (impact). Besides, the position where the dotted and solid trajectories for each geometry intersect (the impact positions) moves opposite the running direction of the wheel – closer to the start of the crossing nose.

Fig. 4b shows the change of the radius in contact when moving an unworn wheel over the three investigated geometries: new and run-in after 11.9 and 46.8 MGT with black, cyan and magenta lines, respectively. A radius is interpolated on and over the whole distance of the crossing nose at the positions where the wheel contacts the crossing nose. Especially at the beginning of the crossing nose where contact radii were smaller than 30 mm (wheel position x less than 1.4 m), an apparent increase of the contact radii by increasing the gross tons is evident ("flattening" of the crossing nose). Despite the few measuring points and the associated measurement inaccuracies, a clear trend can be recognized. These changes affect the contact forces and pressures during the passing of the wheel on the crossing, which is discussed in Section 2.3. The model used in this paper to calculate the dynamic response is described in Section 2.2.

2.2. Simulation model

A simplified FE model calculates the impact of a wheel on a crossing nose having the measured geometries from Section 2.1. It was introduced in Ref. [18] and adapted by the authors in Ref. [12] to calculate cyclic wheel impacts on different crossing nose materials using a plastic material model. The simplifications include.

- a non-linear contact spring instead of the wing rail, which depends on the contact radii of the wing rail and wheel and
- a crossing nose geometry calculated using the wheel displacements and contact radii as shown in Fig. 4a and b.

In the model, the wheel moves downwards on the non-linear contact spring according to the wheel displacements in Fig. 4a (dotted lines) on the wing rail and impacts on the crossing nose at the impact position (the intersection of the dotted and solid line). The wheel displacements and impact positions are different for new and worn wheels and, as seen in Fig. 4a, for measured geometries.

The crossing nose is simulated using finite elements and a geometry according to the solid lines in Fig. 4a and b. The wheel displacements represent the height and the contact radii the surface radii of the crossing nose model. A detailed explanation of the model, including the mechanical system, such as the wheel damper and the bedding, is shown in Ref. [12].

The wheel impacts of the simulations in this paper have a velocity of 90 km/h and a static load of 79 kN. In Section 2.3, we show the dynamic response of the new and worn geometries from Section 2.1 using this concept.

2.3. Effects on contact forces and pressures (elastic)

The changing displacements of the wheel and its contact situation due to geometrical material degradation have a significant influence on contact forces and pressures. In addition, the strong plastic adaption of the manganese steel during the first load cycles determines and limits the resulting contact forces and pressures. To show these influences, the vertical contact forces F and the contact pressures p are calculated using a new and two run-in geometries (11.9 MGT and 46.8 MGT) with elastic

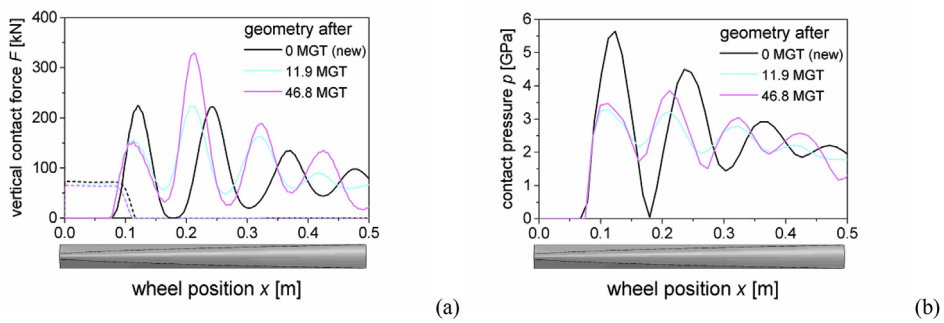

Fig. 5. (a) Contact forces F and (b) contact pressures p of a crossing nose with an unworn (black) geometry and worn geometries after 11.9 MGT (cyan) and after 46.8 MGT (magenta) using a model with elastic material behaviour. (For interpretation of the references to colour in this figure legend, the reader is referred to the Web version of this article.)

material behaviour, see Fig. 3a and b. The model uses a Young's modulus of 201 GPa, a Poisson's ratio of 0.3 and a density of 7800 kg/m^3 for the simulation.

Fig. 5 shows (a) the vertical contact forces and (b) pressures during the impact of an unworn wheel on the crossing nose (solid lines). For the contact forces in Fig. 5a, the unworn wheel reaches maximum contact forces of about 210 kN for the new geometry in track (0 MGT) and values of less than 210 kN and more than 300 kN for the early run-in (11.9 MGT) and the late run-in (46.8 MGT) geometry, respectively.

In comparison to the contact forces, the contact pressures in Fig. 5b show a slightly different behaviour. The maximum contact pressures are higher than 5 GPa (new geometry), decrease to about 3.5 GPa for the early run-in crossing and increase slightly at the second peak for the late run-in geometry.

These results show very well the typical behaviour of manganese crossings and allow to define different stages during the life of crossings. Comparing the results for the new and early run-in crossing, the adaption of the manganese crossing can be seen very well. Both, the contact forces and contact pressures clearly drop during the transition of the wheel. This effect is more significant for the contact pressures. The reason is the adapted geometry of the early run-in geometry, which, in case of the contact forces, allows the wheel to transit smoothly from the wing rail to the crossing nose. For the contact pressures the drop is due to the changed contact situation – the higher contact radii on the crossing nose, see Fig. 4b.

Considering the high contact pressures (5 GPa) and the low yield stresses of manganese steel, it is obvious that the process of the plastic adaption takes place immediately, preventing the high contact pressures to arise. Therefore, calculating the new geometry elastically cannot represent the realistic behaviour of manganese crossings – the driving deformation mechanisms are not considered. The early and the later degradation of manganese crossings, which is measured in track, strengthen this observation: the highest deformation/degradation is observed at the first measurements after the installation in track. They were taken after 1 month in track and 0.5 MGT of loads. In Section 3.2 we use this measurement to validate the calculated deformation of the simulation model. The comparison of the wheel displacements of the new to the early worn and the early worn to the late worn geometry confirms this behaviour, see Fig. 4: The difference of the curves is similar although the number of cylces is 3 times higher (10 MGT to 30 MGT).

Furthermore, it can be observed, that there is an ongoing degradation from the early to the late run-in geometry, see Fig. 3a and b, which effects the contact forces and pressures in Fig. 5. After the positive adaption from the new to the early run-in geometry, the forces and pressures rise again, which describes a deteriorating condition after the adaption of the crossing.

To consider all these effects and show its mechanisms – especially at the beginning – it is important to consider the real material behaviour of the crossings. This paper focuses on the degradation due to plastic deformation, as this seems to be an important mechanism for manganese steel crossings. Section 3 explains the used material model and the implementation concept to consider explosion-depth hardened manganese crossings.

3. Plastic response: measurements, numerical implementation and validation

To understand the deformation behaviour, two main mechanisms are distinguished – the plastic adaption at the beginning and the long-time behaviour, see Fig. 2. Two models describe this behaviour: a crossing model with a *new* geometry and a model with a *run-in* geometry (using the material behaviour of a run-in crossing). Both are explosion-hardened. With hardness measurements and simple tension tests, we show a concept how to consider this material behaviour and how to implement it in an FE model.

3.1. Material model

For the description of the material in the simulation model, a cyclic hardening model is used. It can describe typical behaviour of rail steel, which is caused by the complex loading situation, such as the Bauschinger effect, ratcheting and plastic or elastic shakedown. Especially manganese steel shows a distinct work hardening behaviour, which is responsible for its good performance in track.

A von Mises yield surface with an associated flow rule forms the basic structure of the model. For the cyclic behaviour, mixed isotropic and kinematic hardening is considered [19]. The yield surface F can be described with

$$F = f(\sigma - \alpha) - \sigma_s \tag{1}$$

where σ_s is the yield stress, σ are the ocurring stresses, α the backstresses and $f(\sigma-\alpha)$ the equivalent Mises stresses with respect to the backstresses α. The isotropic hardening uses a simple exponential law describing the evolution of the yield stress in dependence of the equivalent plastic strains ε_{pl}, the scalar representative of the plastic strains ε_p:

$$\dot{\varepsilon}_{pl} = \sqrt{\dot{\varepsilon}_p : \dot{\varepsilon}_p} \tag{2}$$

The exponential law follows with

$$\sigma_s = \sigma_s + Q\left(1 - e^{-B\,\varepsilon_{pl}}\right) \tag{3}$$

σ_y is the yield stress at zero plastic strain, Q defines the maximum change in size and B defines the rate at which the yield surface develops. For the kinematic part, the model uses a non-linear kinematic hardening law. It describes the evolution of the backstress α with

$$\alpha_k = \frac{C_k}{D_k}\left(1 - e^{-D_k\,\varepsilon_{pl}}\right) + \alpha_{k,1}\, e^{-D_k\,\varepsilon_{pl}} \tag{4}$$

k is the number of backstresses, which the model needs to describe the

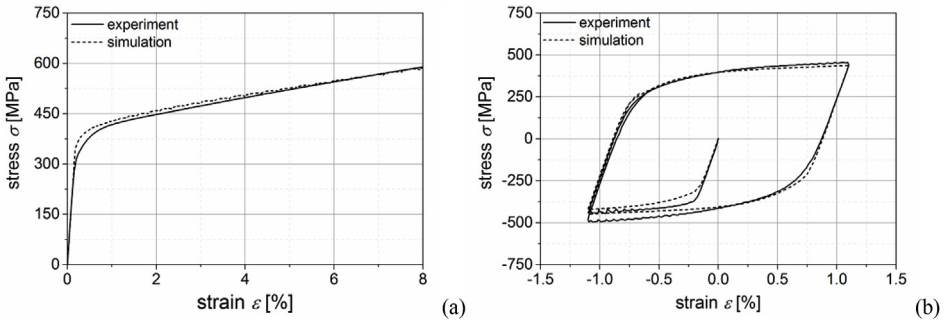

Fig. 6. Experimental and simulated stress-strain curve for (a) a tensile test and (b) one cycle of load with a strain amplitude of 1.1% for manganese steel. A Chaboche-type material model is used for the material fit.

Table 1
The material parameters of manganese steel.

Young's modulus [GPa]	Poisson's ratio [−]	Density [kg/m³]	σ_y [MPa]	Q [MPa]	B [−]	C_1 [GPa]	D_1 [-]	C_2 [GPa]	D_2 [-]	C_3 [GPa]	D_3 [-]
Property											
201	0.3	7800	200	250	3	1000	10000	40	400	2	3

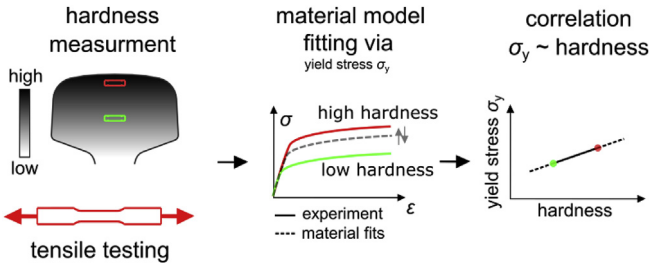

Fig. 7. Methodology of implementing the material behaviour of deformed manganese steel in the material model.

behaviour and C_k and D_k are material parameters, which are calibrated to experimental data. Fig. 6 shows the calibrated curves for a simple tension and one cycle of a tension-compression test of a virgin (not pre-deformed) manganese steel.

The simulated curves agree very well to the simulated ones. The calibrated model uses three backstresses with 6 parameters. Table 1 shows the material parameters of manganese steel in this paper.

To implement the material behaviour of an explosion depth hardened (EDH) and run-in crossing, we adapt the material model from Table 1. Fig. 7 shows the conceptual sketch of the implementation into the given material model. It imitates hardened material behaviour by changing the yield stress parameter σ_y of the material model.

To describe the material state of a hardened crossing we use hardness measurements. Based on those measurements, we get a first idea of the material predeformation into depth, see Fig. 7. With specimens, which have a different hardness, i.e. the red and green boxes in Fig. 7, tensile tests are performed: The results show shifted stress-strain curves (green and red curves). By adjusting the yield stress values and keeping all the other parameters constant – see Eqs. (3) and (4) and Table 1 – the model is fitted to the experimental stress-strain curves. However, it has to be considered that due to this method the material model is fitted using isotropic hardening only. As we do not have any data about the occurring backstresses, but have experimental data about the actual yield stresses, we choose to change the yield stresses of the material model only. For pre-hardening, this method seems reasonable but other typical mechanisms, such as ratchetting due to repeated wheel impacts, may be reduced.

We now have two different hardness values for the specimen and two corresponding (shifted) yield stresses σ_y. A linear fit then correlates the measured hardness with the fitted yield stresses σ_y. Fig. 8 and Fig. 9 show the measured hardness into depth, the experimental and simulated stress-strain curves and the yield stress σ_y – hardness correlation in detail.

Vickers hardness measurments with a load of 0.5 kp (HV0.5) are performed on a cross-sectional cut on a not pre-deformed – referred as “standard” – and an explosion depth hardened (EDH) manganese rail, see Fig. 8a. The results are shown in Fig. 8b: the black and grey line show the not pre-deformed (new) and EDH material, respectively. The high surface hardness is due to the manufacturing process of the crossings. Casted crossings are sandblasted directly after casting, which increases the surface hardness.

Ignoring the surface region, the EDH rail shows higher hardness than the standard one (increase of 150 HV0.5). Then, flat tensions specimen are cut at three positions underneath the surface for both rails, the not pre-deformed and EDH one, marked as red rectangles in Fig. 8a. The hardness values of the specimens are 220 HV0.5 and 340 HV0.5 for the standard and EDH rail, respectively. Fig. 9a shows the results of the tensile tests as solid lines: the black represents the not pre-deformed and the grey one the EDH rail.

The hardening due to the explosion shifts the curve upwards, increasing the yield stress by more than 200 MPa.

As a next step the material model, see Eq. (3) – (4) and Table 1, is fitted to the experiments by changing the yield stress σ_y, as explained in Fig. 7. The dotted curves in Fig. 9 show the simulated stress-strain curves for both rails: For the standard (black) and EDH rail (grey), the fit resulted in values of 200 MPa and 440 MPa, respectively. By including the hardness of the specimen, two points specify the yield stress and hardness correlation: 220 HV0.5 hardness with a yield stress of 200 MPa and 340 HV0.5 with a yield stress of 440 MPa, see Fig. 9b. These points – marked green in Fig. 9b – define a linear function, which allows us to relate hardness values to the yield stress σ_y of the material model.

As written above, two models describe the deformation mechanisms of EDH manganese crossings in this paper: one for the plastic adaption in the beginning and one for the long-time behaviour. The measured hardness in-depth defines the material properties for each model. For the plastic adaption, the model uses the measured geometry after installation in track and the measured hardness in depth of Fig. 8. The model for the long-time behaviour uses the measured geometry after

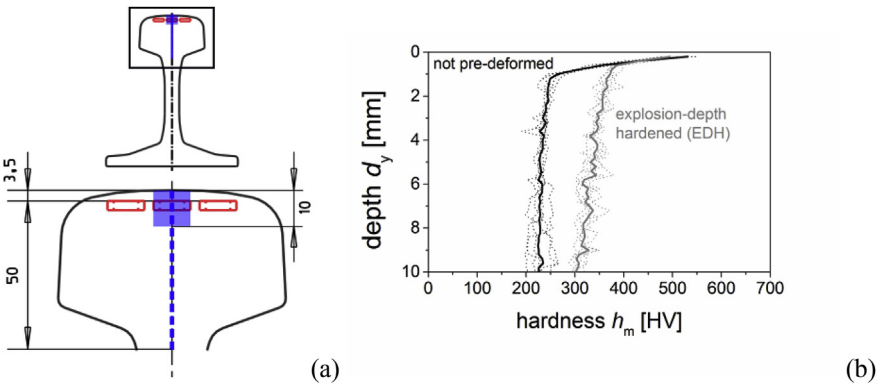

Fig. 8. a) the evaluated area for the hardness measurements and (b) the measured values (HV 0.5) into a depth of 10 mm for manganese steel without pre-deformation and explosion-depth hardened taken at 5 positions in the indicated area.

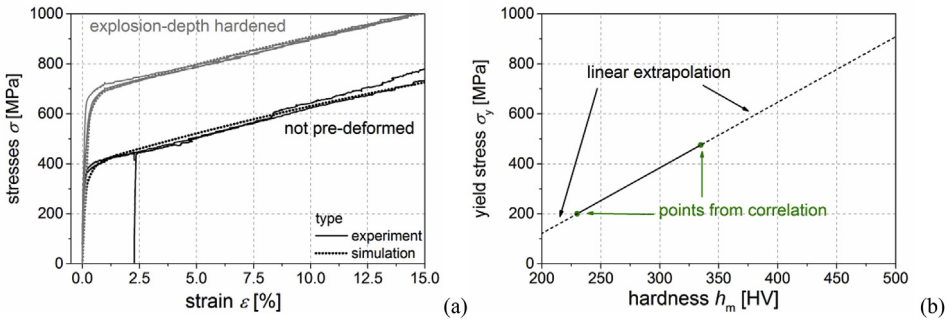

Fig. 9. a) Results of the flat tension tests (solid) and the adapted material model (dashed) for manganese steel without pre-deformation and explosion-detonation hardened (EDH). The measured hardness for the samples (taken from Fig. 8b) is 220 HV and 340 HV. (b) shows a linear fit between the adapted yield stress of the material model and the measured hardness.

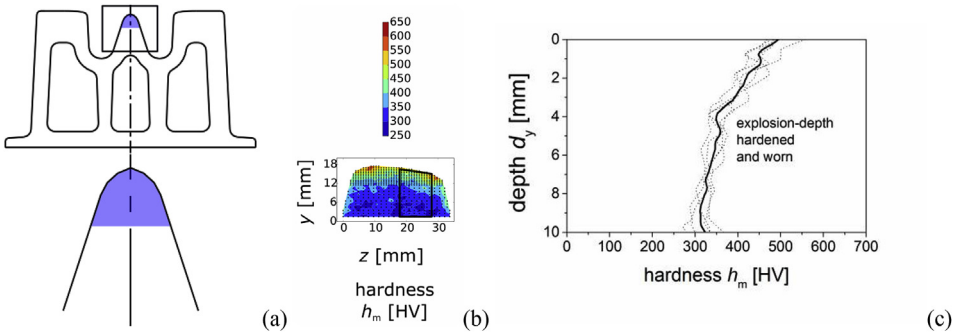

Fig. 10. (a) Cross-sectional view of the hardness map measured on a run-in and EDH manganese crossing nose with the position of the extracted hardness data and (b) the measured hardness (HV 1) into depth.

46.8 MGT and the hardness of a run-in crossing in track, see Fig. 10. As mentioned before, the simplified material model does not capture kinematic hardening properly. The limited description of the actual material (i.e. missing backstresses) introduces an additional uncertainty. This is more significant for the run-in crossing as its material model uses hardness maps of a pre-deformed crossing after millions of wheel impacts.

A worn crossing in track was removed and a hardness mapping on a cross-sectional cut performed. It was in service for about 12 years with an annual load of 22 MGT. In comparison to the measurements of the new EDH rail, the hardness mapping for the run-in crossing was done with a pound load of 1 (HV1) instead of 0.5 (HV0.5). The blue coloured area in Fig. 10a shows the position of the hardness mapping on a schematical cut of a crossing nose. In Fig. 10b, the results of the hardness mapping for the blue area in Fig. 10a can be seen: In some areas close to the highest deformation, the hardness reaches values of up to 600 HV0.5. For the hardness in the simulation model, 5 paths into the depth y between z = 17.5–27.5 mm are chosen, see the black rectangle in Fig. 10b. They are plotted in Fig. 10c as dotted lines, similar to the measurements of the rails in Fig. 8b. The solid black line represents the mean of the 5 chosen paths and defines the hardness into depth relation for the simulation model.

As the last step, by using the relationship shown in Fig. 9b, the material of both simulation models has to be adapted according to the hardness measurements in Figs. 8b and 10c. Fig. 11 shows the material implementation concept for the finite element model in this paper.

Fig. 11 shows the implementation concept of the material for the finite element model simplified for a 2-dimensional mesh. Based on an arbitrary finite element mesh, all elements undergo the same procedure. The concept is shown for one exemplary element, see the green marked element in Fig. 11. With information about the height and depth (from the surface) of the element, it can be related to a hardness value: We calculate the mean hardness over the height and position in depth of the element using the depth-hardness relation as shown in Step 1. Figs. 8b and 10c represent this relationship for the plastic adaption (new, unworn crossing) and long-time (run-in crossing) simulation model, respectively. Step 2 includes the calculation of the yield stress σ_y based on the hardness value of Step 1. Fig. 9b represents this relationship based on the experimental evaluation mentioned before. For each hardness value (and finite element) a new material model is created using the σ_y parameter. As the last step, the material model with the new yield stress σ_y is assigned to the element. By repeating this procedure for each element a mesh with elements having different material models is defined, see the blue coloured mesh in Fig. 11: Dark coloured areas represent elements with high yield stresses (due to high hardness) and light coloured areas elements with low yield stresses.

However, this implementation may introduce additional plastic deformation to the simulation due to element height and hardness

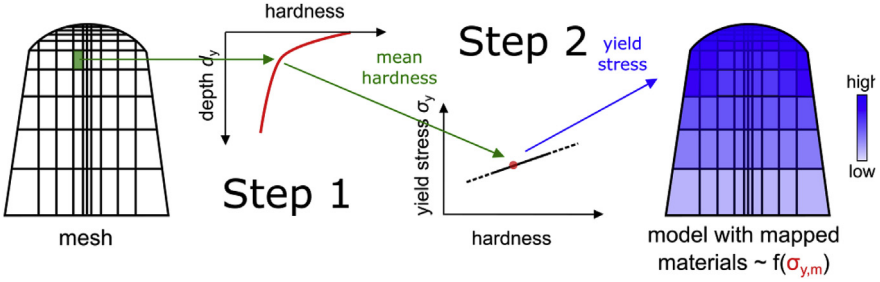

Fig. 11. The material implementation concept for the simulation model.

gradient. The depth and especially the height of the elements determine the hardness: the measured hardness values are averaged over the height and a mean is determined for each element. Therefore, the higher the hardness gradient and the height of the element, the more difference of the mean hardness value to the measured maximum value, especially at the surface (due to the high gradient). For near-surface loads, this means that there is less resistance to deformation (smaller yield stress) in the simulation model than actually measured. We describe this behaviour as “material run-in” as it should be negligibly small after a few impact cycles.

3.2. Validation

The *new* crossing model in this paper investigates the early deformation behaviour (plastic adaptation) of manganese crossings due to cyclic wheel impacts. To validate the calculated deformations due to plastic deformation in the simulation model, we compare the deformation at the surface to measurements of a manganese crossing in track. Therefore, the simulation uses the *new* crossing model, which has a measured geometry of an EDH crossing after placement in track, and the material model due to EDH with the concept shown in Section 3.1. The model then calculates the surface deformation after 80 impact cycles of differently worn wheels (worn, new and hollow) to reach a state where the plastic deformation increments have decreased significantly. Fig. 12a shows the height change Δy due to the calculated deformation compared to early measurements after placement in track (0.5 MGT).

The simulated height change Δy is shown as a solid line and the measured Δy values as grey dots. Similar to the worn geometries in Fig. 3, the measurements are taken from Ref. [20]. Δy is taken at the contact position of the measured, unworn manganese crossing and an unworn (new) wheel in the region of 0.4 m after the impact on the crossing nose. The same validation concept is used in Ref. [12]. The simulated deformation agrees with the measured one: In all areas around the impact positions, similar tendencies with respect to increasing and decreasing Δy can be seen. Also the magnitude of the values are at a similar level: they deviate in the beginning impact area between x = 0.1 and 0.2 m.

In our model we calculate the first 80 impact cycles which is equivalent to a load of less than 0.002 MGT. The measurements, however, are taken after 0.5 MGT. Considering the evolution of the highest height change during the simulation, representing the crossing deformation and referred to as “bump”, see Fig. 12b, it is still reasonable to compare these results: the depth of the bump is increasing at rather small rates after 80 cycles (1.23E-5 mm per cylce). The simulation overestimates the deformations but trends can be shown well. To sum up, the reason for the deviations can be explained as follows:

1. The lack of available data concerning the history of passing loads and wheels and the exact material definition (hardening).
2. Limits of the simulation models in terms of computational effort and simplifications, especially concerning the material implementation. The former does not allow an accurate reproduction of the impact cycles (number of cycles, different loads and wheel types), the latter introduces inaccuracies in the deformation.

Considering the limits of the simulations and the available data, it shows that the considered wheel impacts and the simplified implementation of the material behaviour in this way represent a realistic scenario. Since the paper describes the driving mechanism qualitatively it is a reasonable accuracy.

4. Deformation mechanisms: results and discussion

In this section, the deformation behaviour of a *new* and *run-in* manganese EDH crossing is explained by showing the development of the contact forces, contact pressures, geometric degradation and plastic deformation. The cyclic loading of the wheel causes plastic deformation of the crossing nose, especially on the new crossing (plastic adaption). This influences the contact forces and pressures and shows a significant reduction in comparison to the results of a crossing with a linear elastic material response. We then show the surface deformation for both crossings and explain the mechanisms by showing the development of the plastic deformation into the depth over the cyclic impacts of an unworn wheel. In contrast to simulations in the validation section, the calculations in this section only consider the impact of an unworn wheel. This introduces other effects, such as increased dynamic forces after the impact position due to the concentrated deformation. Since the main point of interest were the deformations at the impact position, any subsequent effects have not been considered. Due to the concentrated deformation the number of impact cycles can be reduced.

4.1. Contact forces

Fig. 13a and c shows the contact forces during the impact of a wheel on a manganese crossing nose elastic material behaviour (green) and for the 1st (red) and 40th (red) plastic cycle for a new and run-in EDH crossing, respectively. The development of the maximum contact forces for every simulated cycle is plotted in Fig. 13c and d.

The dynamic response of the new EDH crossing nose clearly changes over the cycles, see Fig. 13a. Comparing the vertical contact forces of the elastic crossing (grey) to the plastic response at the 1st cycle (red), a similar behaviour with a significant drop of the maximal contact forces from 225 kN to 175 kN can be seen. This drop is due to the plastic deformation, and – with further load cycles - shifts the maximum contact forces to the second peak, see the green line in Fig. 13a. There, the first contact of the wheel with the crossing nose happens more smoothly due to the adaption of the geometry to the cyclic loading of the new wheel. The development of the maximum contact force shows a clear drop for the first cycle – as shown in Fig. 13a – but then rises again, see the green line in Fig. 13b. After the first cycles, it nearly reaches the maximum contact forces of the elastic crossing (black line).

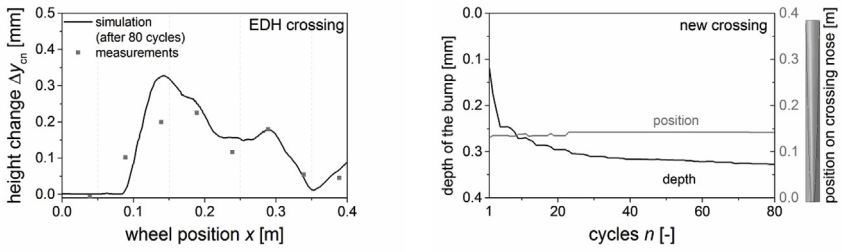

(a) (b)

Fig. 12. Validation of the simulation results: (a) the height change Δy_{cn} after 80 impact cycles and (b) the developed bump (depth) due to the impact of a new wheel over the calculated cycles.

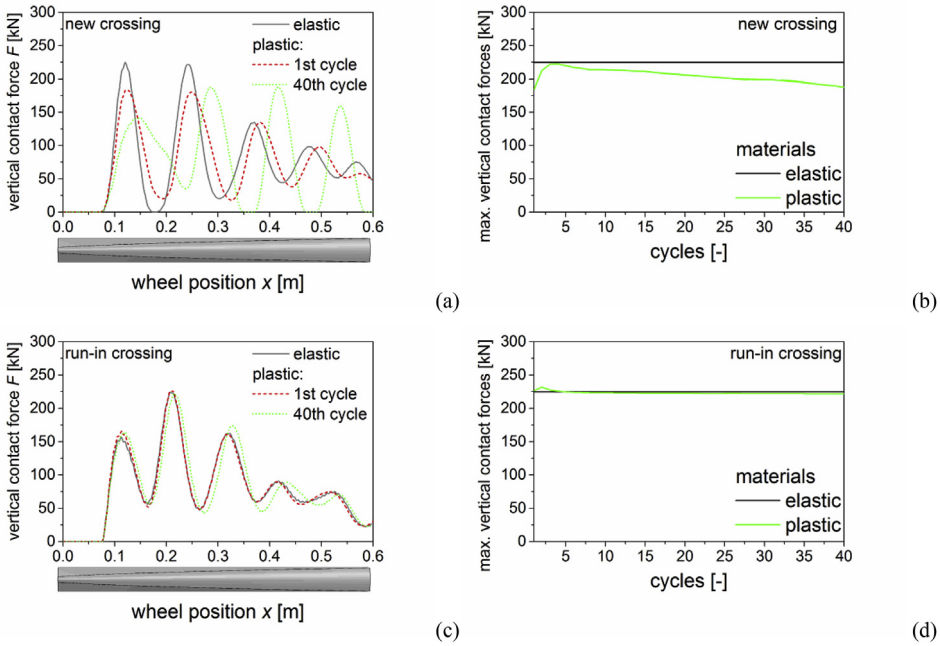

Fig. 13. (a,c) The vertical contact forces F during the passing of the wheel on a crossing nose with elastic material behaviour (gray) and plastic material behaviour after the 1st (red) and 40th impact cycle. (c, d) The development of the maximum contact forces over the calculated cycles. (a) and (b) show the results for a new, (c) and (d) for a run-in EDH crossing nose. (For interpretation of the references to colour in this figure legend, the reader is referred to the Web version of this article.)

Then it starts to drop until the last simulated cycle – the 40th cycle – when it reaches its minimum with 175 kN.

The run-in EDH crossing shows a completely different behaviour over the cycles: in comparison to the new crossing, the contact forces and its maxima stay nearly constant. Although the maximum contact forces of both elastic crossings (the new and run-in) are similar (about 225 kN), the contact forces F over the wheel position x are completely different see Fig. 13c. There, similar to the new crossing after 40th cycle (Fig. 13a), the maximum is shifted to the second peak. This shift is already visible after less cycles in Fig. 13a and has become more dominant with the run-in crossing in Fig. 13c. Fig. 13d confirms the observed behaviour: The maximum contact forces do not change over the cycles – they behave nearly the same way as the elastic response.

4.2. Contact stresses

Similar to Figs. 13 and 14 shows the contact pressures for the impact of a new wheel on a manganese crossing nose. Fig. 14a and c shows the contact pressures p during the impact of a new wheel for a new and run-in EDH crossing and Fig. 14c and d shows the development of the maximum contact pressures plotted over the impact cycles. The grey line in Fig. 14a and c represents the results calculated with elastic material behaviour and the red and green line the results for the 1st and 40th cycle with plastic material behaviour, respectively.

In comparison to the drop of the contact forces due to the plastic deformation in Fig. 13, the drop of the contact pressures p is more significant, see Fig. 14. On the new EDH crossing, they drop from 5.5 GPa for the elastic cycle to about 2.5 GPa after the 1st plastic cycle, see the grey and red line in Fig. 14a, respectively. Due to the ongoing

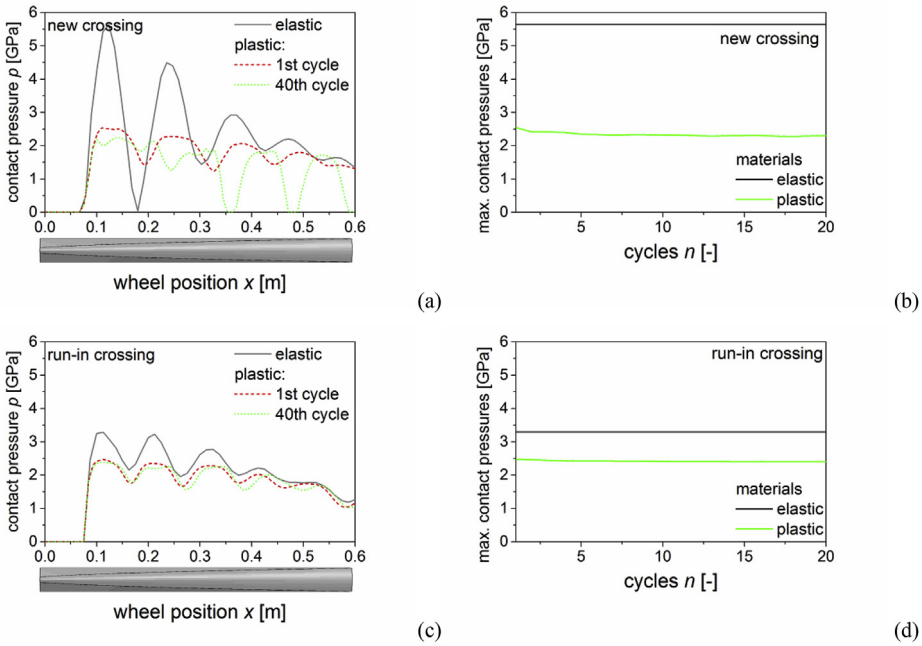

Fig. 14. (a,c) The max. contact pressures p during the passing of the wheel on an nose with elastic material behaviour (gray) and plastic material behaviour after the 1st (red) and 40th (green) impact cycle. (c, d) The development of the maximum contact pressures over the calculated cycles. (a) and (b) show the results for a new, (c) and (d) for a run-in EDH crossing nose. (For interpretation of the references to colour in this figure legend, the reader is referred to the Web version of this article.)

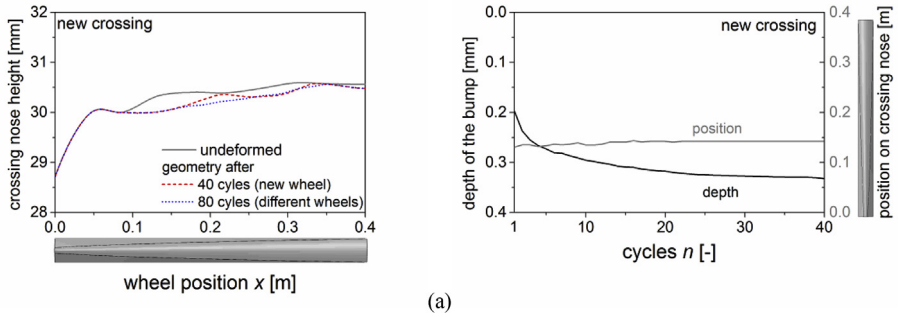

Fig. 15. (a) The crossing nose height after 40th impact cycle due to the impact of different wheels (blue) and an unworn wheel (red) on an EDH crossing nose. (b) The development of the bump depth as indicated in (a) over the calculated cycles. (For interpretation of the references to colour in this figure legend, the reader is referred to the Web version of this article.)

plastic deformation, the contact pressures p decrease to about 2 GPa after 40 cycles. Fig. 15b shows this development over the simulated impact cycles. As seen in Fig. 15a, the first cycles shows the highest drop, but the maximum contact pressures p are still decreasing after 40 cycles. This behaviour was to be expected since a change in the contact geometry due to the plastic deformation affects the contact pressures significantly [21].

Fig. 14c and d shows the contact pressures p for the run-in EDH crossing. Similar to the new crossing, the most significant drop of the maximum p values takes place in the first cycle: it drops from about 3.2 GPa to 2.5 GPa, see the grey and green line in Fig. 14c. After that, the contact pressure p does not change significantly. The change in the first cycle and the constant values afterwards indicates the material is run-in behaviour as discussed in Section 3.1.

Of course, this effect is also present with the new crossing, but because of the overall increased hardness due to the previous plastic deformation, especially near the surface, it is more significant for the run-in crossing.

4.3. Deformationss

To explain the deformation mechanisms the results are shown in terms of deformations of the surface (permanent displacements) and plastic deformation underneath the surface.

4.3.1. Surface deformation

Fig. 15a shows the undeformed (grey) and the deformed crossing nose geometry of a new EDH crossing after 40 impact cycles of an unworn wheel (red) and 80 impact cycles of different wheels (blue). The simulation of the different wheels is used for the validation of the deformation in Section 3.2. Changes of the crossing nose height (from undeformed to deformed due to wheel impacts) represent the geometric degradation of the surface. The crossing nose height is evaluated along the wheel position x in the middle of the crossing nose.

Comparing the height of the undeformed geometry to the deformed geometries, the maximum deformation is in the area between x = 0.08 and 0.18 m. The maximum deformation is similar for the simulated impacts of 40 unworn wheels (dashed) and 80 different wheels (dotted). Therefore, only the results of the simulation with the 40 impact cycles of an unworn wheel are considered for the evaluation, as mentioned in the section introduction. We refer to the deformed area around the maximum deformation as “bump”. For the new crossing nose it has a total depth of about 0.33 mm at the end of the simulated wheel impacts.

Fig. 15b shows the development of the bump: The highest deformations happen at the first cycle, which form a depth of about 0.2 mm. The deformation increments then decrease with increasing cycles and nearly reach a steady value after 40 cycles.

Fig. 16a shows the crossing nose height of the *run-in* crossing model, without simulated impacts of wheels (grey) and after the impact of 40 unworn wheels (red).

In comparison to Fig. 15a, the deformation of the run in crossing nose is less than 0.1 mm. Furthermore, it does not change after less than 10 cycles, see Fig. 16b. Similar to the new crossing nose, the biggest deformation increment happens in the first cycle.

However, for both models, the deformation at the beginning of the simulation may be slightly overestimated. A mean hardness is used for the material definition for each element, as explained in the validation section, which may introduce additional deformation, as it is lower as the measured hardness at the top of the rail. This effect is more significant for the run-in crossing nose as there is a higher hardness measured close to the surface. The fact that the depth of the bump does not change after just several cycles, supports the assumption that additional plastic deformation is introduced due to the decreased hardness.

4.3.2. Plastic deformation

Fig. 17 shows a sketch of the evaluation scheme for the accumulated equivalent plastic strain increment for one simulation cycle. As a first step the accumulated plastic deformation after each simulation cycle is taken for all finite elements, and the difference to the previous step is calculated. The calculated increment shows us if and how much – in comparison to the previous cycle – plastic deformation occurs. With the routine in Fig. 17, the maximum equivalent plastic strain increments into the depth for each impact cycle are then evaluated.

The routine evaluates the maximum equivalent plastic. strain increment for each row of elements. The 2-dimensional cross-sections represent an arbitrary 3-dimensional finite element mesh. The green and the blue areas mark two element rows. For each element row, the routine finds the element with the highest equivalent plastic strain increment. After having found the maximum, the depth of the integration point is calculated by using its position (coordinates) and the height of the surface above the element. For the chosen element rows, the element with the maximum value is shown and its depth marked with d_1 and d_2. The maximum equivalent plastic strain increments and its depth can be plotted in a graph, see the green and blue lines in ‘Step 2’ in Fig. 17. By including all other element rows the shown strain increment and depth graph can be completed for the chosen impact cycle. This routine is then repeated for all other impact cycles. Fig. 18 shows the maximum strain increments into depth for the new EDH and run-in EDH crossing using the routine mentioned above. The 1st, 10th, 20th, 30th and 40th impact cycle are plotted for the new and run-in EDH crossing.

For all cycles, the highest plastic strain increments are in the area close to the surface. For the strain increments of the new crossing, see Fig. 18a, the values drop immediately from about 0.05 underneath the surface to values between 0.005 and 0.015 at the surface. The maximum values are decreasing with increasing cycles but are clearly visible at the 40th, impact cycle. For the run-in crossing, the accumulated equivalent plastic strain increments drop from 0.015 at the first cycle to about 0 after just several impact cycles, see 10th to 40th cycle.

Assuming that the plastic deformation causes a hardening of the material, the calculated plastic deformation agrees very well with the hardness measurements in Fig. 10: the ongoing plastic deformation and

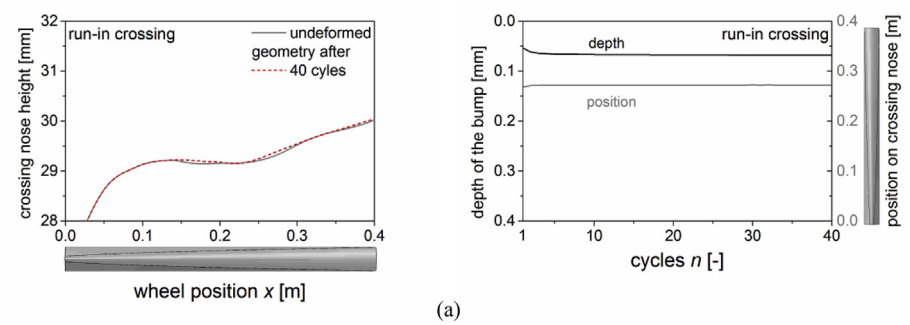

(a) (b)

Fig. 16. (a) The displacement of the run-in crossing nose surface height after the 40th impact cycle due to the impact of an unworn wheel (red) on a run-in crossing nose. (b) The developedbump (depth) due to a new wheel over the calculated cycles. (For interpretation of the references to colour in this figure legend, the reader is referred to the Web version of this article.)

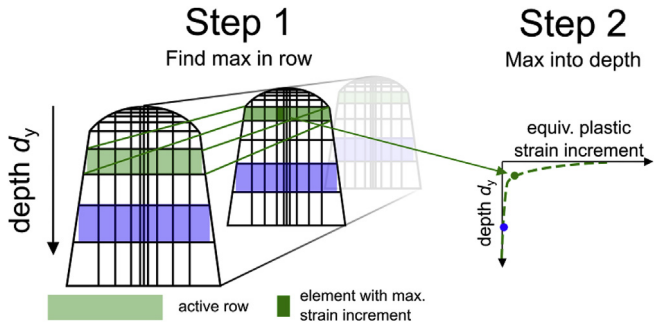

Fig. 17. Schematic figure of the evaluation of the equivalent plastic strain increment into depth for one simulation cycle.

the increased hardness due to the impacts of the wheel reach a depth of about 5 mm. Below 5 mm depth, see Fig. 10, the measured hardness is similar to the one of the new (undeformed) crossing, see Fig. 8. This confirms that most of the effects due to the cyclic wheel impacts are in this area and depth, which is also seen in the simulation.

The deformation of the run-in crossing behaves slightly different to observations in track. While it is clear from the comparison of the measured geometries, see Figs. 3 and 4, that the degradation decreases, it still happens. The calculated plastic deformation in the simulation underestimates the real behaviour, as it reaches values close to zero (equivalent plastic strain increments of less than 1E-6).

Due to the high computational effort, it is not possible to consider all degradation mechanisms in one model. In addition, there are no exact observations of crossings in the field describing the ongoing deformation. This does not allow to make a proper selection of the considered mechanisms in front but may show that there are other, more important mechanisms for the existing long-term degradation. Some of those missed details due to the simplifications that may explain the difference of the simulations to observations are:

- Variety of loadings: a wider range of different wheels and axle loads
- Direction of the passing wheels: changing directions of the trains can result alternating stress and deformation in a horizontal direction
- Symmetry of the simulation model: this causes a modified contact pressures (symmetric wheel) and may miss different contact positions on the crossing nose (symmetric crossing nose)
- Number of simulated cycles: as mentioned in Section 1, we are limited in numbers of covered simulation cycles due to the high computational effort
- Simplified material model: as mentioned in previous sections, the pre-deformed material is using yield stresses only (isotropic hardening). Ongoing deformation due to kinematic hardening, i.e. ratchetting, will be underestimated.

For a precise prediction of the long-term behaviour these details may be added.

5. Conclusions

The two stages of the deformation of manganese steel crossings are investigated using finite element simulation models. The simulation models use geometries taken from measurements in track and a material model, which combines conventional material testing and hardness measurements. This allow us to describe the adaption of a new and the long-time behaviour of a run-in manganese steel crossing. Therefore, a methodology is presented, which allows to include pre-deformed material behaviour on the basis of hardness measurements. This is done for the explosion depth hardening (EDH) of a new and for the hardening caused by the predeformation due to impact loads of a run-in crossing nose. The major findings of the investigation of the deformation mechanisms are:

(a) In comparison to the run-in crossing, the contact forces of the new EDH crossing change over the cyclic wheel impacts. Therefore, the maximum conctact forces of a run-in crossing with plastic material behaviour are similar to the results with elastic material behaviour due to the hardening. For the new crossing, the maximum contact forces decrease slightly when considering plastic material behaviour accompanied by a change of the dynamic response. This

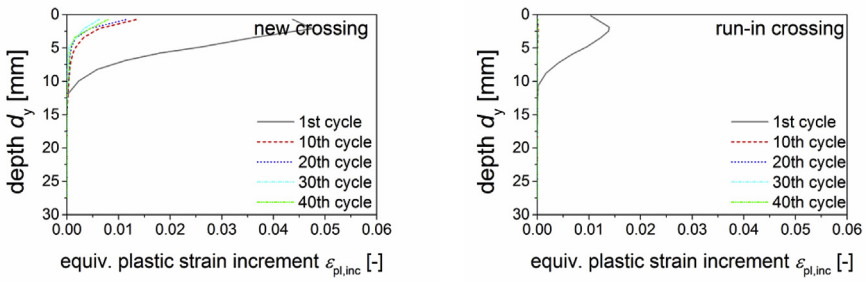

(a) (b)

Fig. 18. The equivalent plastic strain increment in depth of the crossing nose at the 1st, 10th, 20th, 30th and 40th impact cycle for (a) an EDH crossing nose and (b) a run-in crossing nose.

tendency is confirmed when calculating the contact forces of the worn geometry: A similar dynamic response is evident.

(b) For both crossing models, the contact pressures drop due the plastic deformation. This effect is more distinct for the new EDH crossing, but decreases rapidly after a few cycles.

(c) The plastic adaption of a new EDH and run-in crossing is shown in terms of surface displacements and plastic deformation into depth. For both, the largest deformation increments are calculated for the first impact cycles. For the new crossing, the plastic deformation incremenet then drops to less than half of the initial impact cycle. The measurements of the geometry and a comparison to hardness measurments into depth of a run-in crossing confirm these tendencies. The run-in crossing does almost show no deformation after the first impact cycles.

The mechanisms during the plastic adaption of a new manganese crossing are explained and its tendencies confirmed with different measurements. To describe the long-time behaviour of manganese steel crossing in more detail, the simulation model can be modified, especially in terms of the number of impact cycles, viarity of impact loads and plastic material model.

Acknowledgments

The authors gratefully acknowledge the financial support under the scope of the Shift2Rail Joint Undertaking Project “IN2TRACK”, H2020 Project number 730841. The authors further gratefully acknowledge the financial support under the scope of the COMET program within the K2 Center “Integrated Computational Material, Process and Product Engineering (IC-MPPE)” (Project No 859480). This program is supported by the Austrian Federal Ministries for Transport, Innovation and Technology (BMVIT) and for Digital and Economic Affairs (BMDW), represented by the Austrian research funding association (FFG), and the federal states of Styria, Upper Austria and Tyrol.

References

[1] Ekberg A, Åkesson B, Kabo E. Wheel/rail rolling contact fatigue – probe, predict, prevent. Wear 2014;314(1–2):2–12.
[2] Tweedale G, Jones RV, Paton WDM. Sir Robert Abbott Hadfield F. R. S. (1858-1940) and the dicovery of manganese steel. Notes Rec. R. Soc. Lond. 1985;40(1):63–74.
[3] Chen L, Zhao Y, Qin X. Some aspects of high manganese twinning-induced plasticity (TWIP) steel, a review. Acta Metall Sin 2013;26(1):1–15.
[4] Bouaziz O, Allain S, Scott CP, Cugy P, Barbier D. High manganese austenitic twinning induced plasticity steels: a review of the microstructure properties relationships. Curr Opin Solid State Mater Sci 2011;15(4):141–68.
[5] Bayraktar E, Khalid FA, Levaillant C. Deformation and fracture behaviour of high manganese austenitic steel. J Mater Process Technol 2004;147(2):145–54.
[6] Harzallah R, Mouftiez A, Felder E, Hariri S, Maujean J. Rolling contact fatigue of Hadfield steel X120Mn12. Wear 2010;269(9–10):647–54.
[7] Zhang M, Lv B, Zhang F, Feng X. Explosion deformation and hardening behaviours of Hadfield steel crossing. ISIJ Int 2012;52(11):2093–5.
[8] Zhang F, Lv B, Wang T, Zheng C, Zhang M, Luo H, et al. Microstructure and properties of purity high Mn steel crossing explosion hardened. ISIJ Int 2008;48(12):1766–70.
[9] Zhang FC, Lv B, Wang TS, Zheng CL, Zhang M, Luo HH, et al. Explosion hardening of Hadfield steel crossing. Mater Sci Technol 2013;26(2):223–9.
[10] Pletz M, Daves W, Yao W, Kubin W, Scheriau S. Multi-scale finite element modeling to describe rolling contact fatigue in a wheel–rail test rig. Tribol Int 2014;80:147–55.
[11] Wiedorn J, Daves W, Ossberger H, Ossberger U, Pletz M. Using stress-based damage models to describe subsurface damage in crossings. Paper presented to 11th international heavy haul association conference 2017, cape town, South Africa. 2017.
[12] Wiedorn J, Daves W, Ossberger U, Ossberger H, Pletz M. Numerical assessment of materials used in railway crossings by predicting damage initiation - validation and application. Wear 2018;414–415:136–50.
[13] Dang Van K, Griveau B. On a new multiaxial fatigue limit criterion: theory and application. London: EGF3, Mechanical Engineering Publications; 1989. p. 476–96.
[14] Wiedorn J, Daves W, Ossberger U, Ossberger H, Pletz M. Finite element model for predicting the initiation of subsurface damage in railway crossings—a parametric study. Proc Inst Mech Eng - Part F J Rail Rapid Transit 2018. https://doi.org/10.1177/0954409718797039.
[15] Pletz M, Ossberger U, Ossberger H, Daves W. Dynamic finite element model-impact force and contact pressure for measured geometries of fixed crossings. In: Rosenberger M, Plöchl M, Six K, Edelmann J, editors. Dynamics of vehicles on roads and tracks: proceedings of the 24th symposium of the international association for vehicle system dynamics (IAVSD 2015), graz, Austria, 17-21 august 2015. Leiden, The Netherlads: CRC Press, Taylor & Francis Group; 2016. p. 1337–46.
[16] Guo SL, Sun DY, Zhang FC, Feng XY, Qian LH. Damage of a Hadfield steel crossing due to wheel rolling impact passages. Wear 2013;305(1–2):267–73.
[17] Wiedorn J, Daves W, Ossberger H, Pletz M. A simplified dynamic finite element model for the impact of a wheel on a crossing: validation and parameter study. In: Pombo J, editor. The third international conference on railway Technology: research, development and maintenance. UK: Civil-Comp PressStirlingshire; 2016.
[18] Wiedorn J, Daves W, Ossberger U, Ossberger H, Pletz M. Simplified explicit finite element model for the impact of a wheel on a crossing – validation and parameter study. Tribol Int 2017;111:254–64.
[19] Chaboche JL. Time-independent constitutive theories for cyclic plasticity. Int J Plast 1986;2(2):149–88.
[20] Eck S, Oßberger H, Oßberger U, Marsoner S, Ebner R. Comparison of the fatigue and impact fracture behaviour of five different steel grades used in the frog of a turnout. Proc Inst Mech Eng - Part F J Rail Rapid Transit 2014;228(6):603–10.
[21] Hertz H. Über die Berührung fester elastischer Körper. J für die Reine Angewandte Math (Crelle's J) 1881;92:156–71.